VILNIUS UNIVERSITY

JEVGENIJ CHMELIOV

EXCITATION EVOLUTION AND SELF-REGULATION ABILITY OF PHOTOSYNTHETIC LIGHT-HARVESTING SYSTEMS

Doctoral dissertation
Physical sciences, Physics (02P)

Vilnius, 2015

Doctoral dissertation was prepared at Vilnius University in 2011 – 2015, Vilnius, Lithuania

Scientific supervisor:

prof. habil. dr. Leonas Valkūnas (Vilnius University, Physical sciences, Physics – 02P)

VILNIAUS UNIVERSITETAS

JEVGENIJ CHMELIOV

SUŽADINIMO EVOLIUCIJA IR SAVIREGULIACIJOS GEBA FOTOSINTETINĖSE ŠVIESĄ SURENKANČIOSE SISTEMOSE

Daktaro disertacija
Fiziniai mokslai, fizika (02P)

Vilnius, 2015 metai

Disertacija rengta 2011 – 2015 metais Vilniaus universitete

Mokslinis vadovas:

prof. habil. dr. Leonas Valkūnas (Vilniaus universitetas, fiziniai mokslai, fizika – 02P)

Acknowledgments

I would like to express my sincere gratitude to a number of people without whom this Thesis would not be completed. First of all, I express the deepest appreciation to my supervisor professor Leonas Valkūnas, who brought me into the field of theoretical Physics and altruistically shared his knowledge, experience, and enthusiasm, always providing exceptional support and unceasing encouragement. Many thanks go to Gediminas Trinkūnas, who introduced me into the amazing world of photosynthesis and learned me not to be afraid of any difficulties.

I am proud that during my research I have met and collaborated with many outstanding people, particularly Graham R. Fleming, Rienk van Grondelle, Herbert van Amerongen, Bruno Robert, and Alexander V. Ruban—the respected specialists and leaders in their field. Their comments and stimulating discussions contributed a lot to the results presented in this Thesis. I am also very grateful to the brilliant experimentalists—J. Michael Gruber, Tjaart P. J. Krüger, Erica Belgio, Ramūnas Augulis, and Egidijus Songaila—whose measurements provided the background for my research work. Special thanks go to Christopher D. P. Duffy and Andrius Gelžinis for their theoretical contribution, and to all the fellow students and researchers in the Department of Theoretical Physics for an extremely creative and friendly atmosphere.

I would also like to thank the unknown reviewers of my publications for their valuable comments and positive feedback and to acknowledge the financial support from the Research Council of Lithuania and European Social Fund.

Finally, I express my infinite gratitude and love to all my family for supporting me spiritually throughout the research work and my life in general.

Jevgenij Chmeliov
Vilnius, 2015

Common notations

AOM	acousto-optic modulator
Car	carotenoid
CG	coarse-grained (model)
Chl	chlorophyll
CT	charge transfer
DAS	decay-associated spectra
DOS	density of states
EET	excitation energy transfer
ERPE	excitation radical-pair equilibrium (model)
FWHM	full width at half maximum
IC	internal conversion
IRF	instrument response function
ISC	intersystem crossing
LHCII	major light-harvesting complex of photosystem II
Lut	lutein

Neo	neoxanthin
NPQ	non-photochemical quenching
PSI	photosystem I
PSII	photosystem II
QD	quantum dot
QY	quantum yield
RC	reaction center
RP	radical pair
SMS	single-molecule spectroscopy
ST	singlet–triplet (annihilation)
TDC	transition density cube
TTL	transfer-to-trap limiting (model)
Vio	violaxanthin
WT	wild-type
Zea	zeaxanthin

Contents

> “ *Human ingenuity will never devise an invention more beautiful, more simple or more direct than does Nature because in her inventions nothing is lacking, and nothing is superfluous.*
>
> LEONARDO DA VINCI

Introduction

During billions of years of evolution, the Sun has always remained the main source of energy for all living beings inhabiting the Earth. Even nowadays, the amount of solar energy that reaches the Earth’s surface during one day is sufficient to sustain all the imaginable human activities for about two decades [1]. The absolute majority of this energy is utilized and then stored in a form of the energy of chemical bonds during the process of *photosynthesis*, one of the most important metabolic reactions occurring *in vivo*. Green plants, algae, and cyanobacteria are not only responsible for the primary step of biomass production, but also fill the Earth’s atmosphere with oxygen, a byproduct of photosynthesis required for the vast majority of the heterotrophic living organisms, including humans.

The “molecular oxygen factories” of photosynthesis are hidden deeply inside the plant leaves, in the intracellular organelles of several micrometers in diameter, known as *chloroplasts* (see Fig. 1a). Surrounded with a double envelope membrane, chloroplasts are filled with an extensive system of internal membranes, called *thylakoids*, that are the place for the light reactions of photosynthesis [2–4]. The outer space of the thylakoids is filled with an aqueous medium, stroma, and is responsible for the carbon fixation reactions. Thylakoids are closely associated with each other and form stacked regions, grana, interconnected with stroma lamellae. Thylakoid membrane itself is a lipid bilayer with a wide variety of proteins embedded into it (see Fig. 1b). The majority of them, namely photosystem I (PSI) and photosystem II (PSII) together with their peripheral antenna complexes, are responsible for light harvesting, excitation energy transfer (EET) towards the reaction center (RC) of each photosystem, and charge separation therein, while other enzymes participate in electron transfer between both photosystems (like cytochrome b_6f) and synthesis of the adenosine triphosphate (ATP) molecules (performed by ATP synthase). Oxygen-evolving complex, closely associated with the RC of PSII, oxidizes water molecules thus generating molecular oxygen.

Both photosystems are not evenly distributed across the thylakoid membrane: while PSIIs are mainly found within the stacked grana lamellae, PSIs are located almost exclusively in the stroma lamellae. These photosynthetic units contain hundreds of pigment molecules—chlorophylls (Chls) and carotenoids (Cars)—

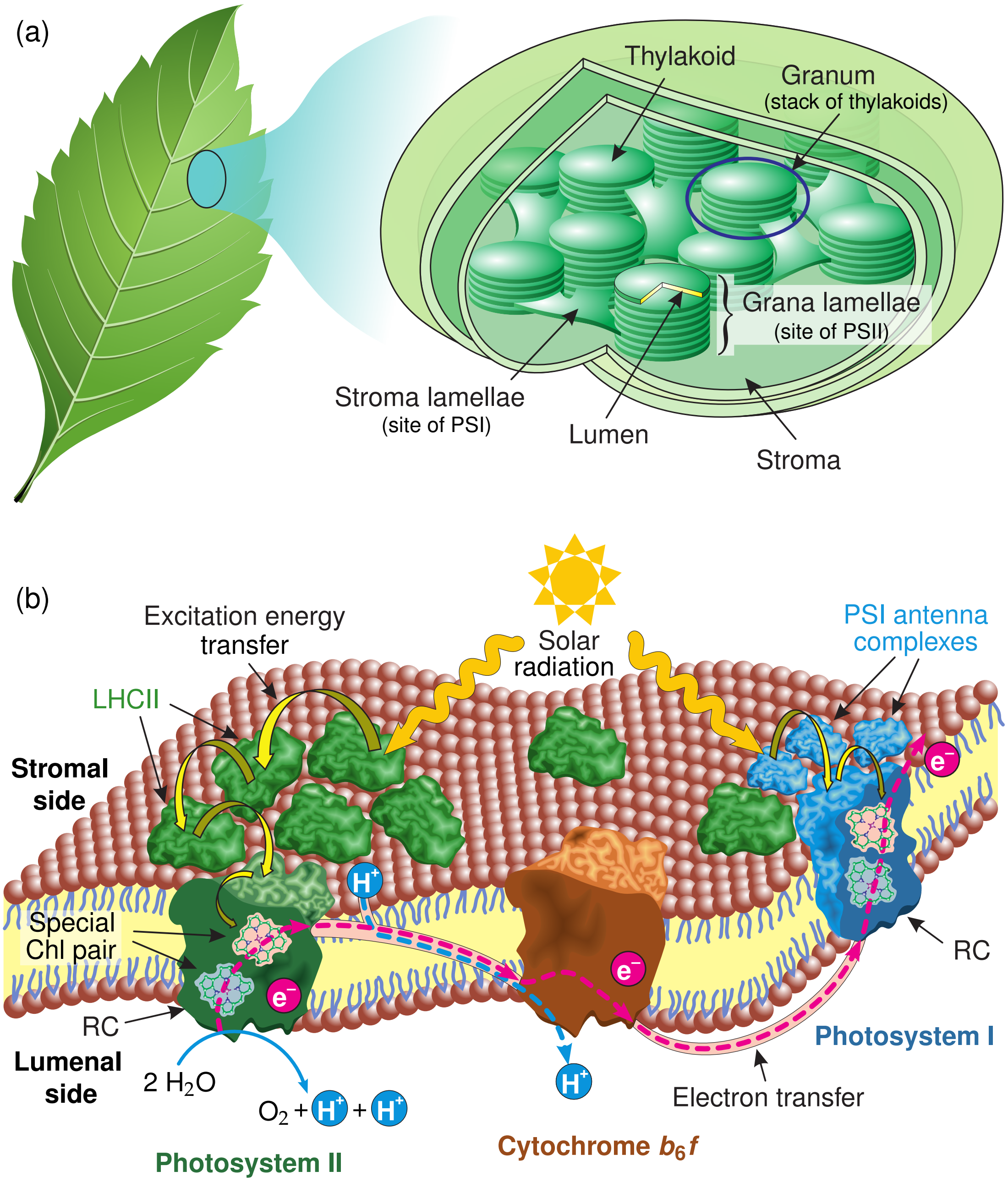

Figure 1 | Schematic organization of the photosynthetic apparatus of green plants. (**a**) Internal structure of the chloroplast—an “oxygen factory” of plant’s leaf, where all the main photosynthetic reactions take place. An extensive system of internal membranes, known as thylakoids, is highly folded and forms stacked regions (grana), interconnected with stroma lamellae. (**b**) Composition of the thylakoid membrane, where incoming solar radiation is captured and stored in the form of trans-membrane electrochemical potential. The reaction centers of both photosynthetic units—PSI and PSII—are surrounded by peripheral light-harvesting complexes, some of which are loosely bound to the RCs and, when needed, can diffuse through the membrane from one photosystem to another. Oxidation of water molecules and production of the molecular oxygen is performed in the RC of PSII, and cytochrome $b_6 f$ is an enzyme participating in electron transfer from PSII to PSI.

all bound to the protein scaffold, and operate in sequence to convert the energy of the incident solar radiation into a storable chemical form. In order to increase the absorption cross-section of both photosynthetic units, their reaction centers are surrounded by the so-called pigment–protein antenna complexes. The size of the antenna system varies considerably in different organisms, ranging from about 20–30 pigments per RC in some photosynthetic bacteria to generally 200–300 chlorophylls per RC in higher plants or even to a few thousands of pigments per RC in some types of algae and green sulfur bacteria [2]. In green plants, the most abundant pigment–protein complex, binding roughly half of the all terrestrial Chl molecules, is the major light harvesting complex of PSII (LHCII) [5].

The mutual arrangement of the pigment molecules within the light-harvesting antenna of the photosystem, as well as their spectroscopic properties, ensures an optimal absorption of the incoming photons and extremely efficient (up to 99 %) transfer of the generated electronic excitations towards the reaction center, where excitation energy is stabilized in the form of a trans-membrane electrochemical potential necessary for the subsequent stages of photosynthesis [4]. Despite extensive research taken over the last few decades (reviewed, *e.g.*, in [6–11]), the specific underlying molecular mechanisms responsible for such an efficient excitation energy transfer within the light-harvesting antenna are still not fully understood. The phenomenon becomes even more remarkable if one takes into account the intrinsic structural disorder of biological systems and continuous spatial rearrangement of the pigment–protein complexes occurring within the photosynthetic membrane [3, 10].

While such an outstanding quantum efficiency of light harvesting helps photosynthetic organisms to survive and to successfully function at very low levels of illumination, like in aquatic environment or in deep continuous shadow, under bright sunlight it has a negative impact and can lead to the photodamage. Indeed, although being rather fast, the turnover rate of the RC is still finite. As a result, intense illumination saturates its operation and leads to the over-excitation of the light-harvesting antenna thus threatening the formation of free radicals or conversion of molecular oxygen, produced in PSII, into its highly reactive singlet species capable to “burn out” the whole photosystem. However, over long ages of evolution, photosynthetic organisms, particularly higher plants, have developed various self-regulatory mechanisms that help them to deal with the excess excitation energy even at the molecular level and, when needed, safely dissipate it as heat [12]. Firstly, the RC itself is capable of adapting to varying external illumination by efficiently regulating the process of charge separation [13, 14]. Additionally, other reversible regulatory processes take place in the light-harvesting antenna and make up part of the observed non-photochemical quenching (NPQ) of Chl fluorescence in PSII. On a macroscopic thylakoid-level, the most slowly appearing and relaxing form of NPQ, qI, is attributed to actual photoinhibitory damage of a fraction of the RCs in PSII, can take several hours to reverse and is seriously detrimental to the viability of the organism. On a timescale of tens of minutes, the flow of excitation energy towards the RC can be controlled by the reorganization of the antenna complexes thus adjusting the overall absorption cross-section of the RCs [15, 16]. The major part of NPQ—so-called energy-dependent quenching, qE,—is another example of the feedback regulation in photosynthesis [17] that is triggered by ΔpH across the thylakoid membrane, increasing during the bright sunlight [12]. This most important component of the photoprotective NPQ forms and relaxes within seconds to minutes and operates on a molecular level, though there is still no consensus regarding its underlying molecular mechanism(s) [18–22]. Finally, non-linear processes like singlet–singlet or singlet–triplet (ST) annihilation, naturally occurring in molecular aggregates under high excitation conditions, also contribute to the faster relaxation of the excess excitation energy.

Over the last two decades, advances in experimental techniques have attracted a lot of attention to the field of photosynthetic light harvesting and non-photochemical quenching. Many breakthrough discoveries have been made, arising new questions and leading to even more intensive studies, but not everything has been clarified yet. It has been shown that rational, artificial adjustment of the NPQ process could improve the global crop yield by up to 30 % [23,24], thus indicating the potential rewards associated with understanding the molecular mechanism(s) involved in NPQ and the unprecedented photochemical quantum efficiency of the RCs. Inspired by lessons from Nature, first efforts towards artificial photosynthesis have already been done, mimicking the function of the RC [25–27], light-harvesting antenna [27, 28], water-splitting complexes [29–31], or even the two-photosystem tandem architecture [32–35]. But still a lot of work have to be done in order to attain at least similar level of efficiency that Nature has leisurely achieved after billions of years of evolution.

Main goal and tasks of the research work

The main goal of the research work presented in this thesis is to analyze excitation energy dynamics in photosynthetic light-harvesting systems exhibiting different levels of structural organization—from the inter-pigment interactions within the same antenna complex to the processes occurring in the large aggregates of LHCII trimers, variously sized photosystems, or even whole thylakoid membranes—paying a special attention to the self-regulatory abilities of the photosynthetic pigment–proteins. In order to achieve this goal, the following tasks are formulated:

- ➢ Calculate the inter-pigment excitation transfer rates within the LHCII complex and evaluate the quenching efficiency of each carotenoid molecule.
- ➢ Develop theoretical models describing the features of the fluorescence intermittency and singlet–triplet annihilation observed in single light-harvesting complexes.
- ➢ Reveal the molecular origin of distinct functional states of the LHCII complexes by analyzing the temperature-dependent time-resolved fluorescence arising from LHCII trimers and aggregates.
- ➢ Develop the fluctuating antenna model that describes the non-exponential fluorescence decay kinetics observed in various photosynthetic systems.
- ➢ Analyze the fluorescence induction kinetics observed in thylakoid membranes and evaluate the macroscopic structural changes occurring therein during the reversible formation of the non-photochemical quenching.

Statements presented for the defense

1. The non-photochemical quenching state in the LHCII complex is one of the intrinsic states of the pigment–protein that randomly becomes available as a result of the protein's slow conformational dynamics. Exposure to any ambient stress modulates the energy landscape of the pigment–protein complex thus shifting the dynamic equilibrium towards one or another pre-existing state.

2. The LHCII complex can be in one of at least three distinct intrinsic states. The dominating one exhibits strong fluorescence around the 680-nm spectral region. The red-emitting state, specified by the fluorescence spectrum shifted towards the longer wavelengths, is related to the partial mixing of excitonic and chlorophyll–chlorophyll charge transfer states. The origin of the quenched state responsible for NPQ is the incoherent excitation transfer from chlorophylls to the short-lived carotenoid excited states, most probably that of lutein pigments.

3. The dynamic increase of the light-harvesting antenna during short-term acclimation to the high light conditions ensures better photoprotection due to higher probability for the generation of NPQ centers within the antenna and, at the same time, minimizes the drop in excitation delivery to the open reaction centers. Slow traps capable of being generated anywhere in the antenna provide a flexible way to gradually adjust the overall efficiency of NPQ thus providing sufficient photoprotection while not interfering with the photosynthetic productivity.

4. The origin of the multi-exponential fluorescence decay kinetics observed in various systems—from single LHCII trimers to their aggregates, variously sized photosystems, or whole thylakoid membranes—is caused by the fluctuating nature of the light-harvesting antenna and not by the exciton–radical pair equilibration at the side of the excitation quencher.

Organization of the thesis

The thesis consists of 5 chapters, in which excitation dynamics and relaxation are analyzed at different levels of the structural organization of the light-harvesting antenna: from the inter-molecular excitation energy transfer within the same pigment–protein complex to the global excitation evolution in their large aggregates, variously sized photosynthetic units, or the whole thylakoid membrane. In the first chapter, molecular structure of the major light-harvesting complex, LHCII, is introduced followed by the first structure-based all-pigment model for excitation energy transfer and relaxation in an LHCII monomer, which allowed the identification of the dominating excitation quenching pathways. In Chapter 2, we focus on the spectroscopic features of the single LHCII complexes and present theoretical description for the observed processes of fluorescence intermittency and singlet–triplet annihilation. Then, in Chapter 3, excitation evolution in an LHCII aggregate is studied by analyzing the corresponding temperature-dependent time-resolved fluorescence spectra. We identify several distinct intrinsic states of the pigment–protein complexes and associate each of them with the underlying molecular mechanism. In Chapter 4, we further focus on the fluctuating properties of the light-harvesting antenna and show that these properties and not the radical pair equilibration at the site of the excitation trap are at the heart of the multi-exponential fluorescence decay kinetics observed in various photosynthetic systems. Finally, the study of fluorescence induction kinetics in thylakoid membranes, undertaken in the last chapter, reveals the dynamic increase of the antenna size during short-term adaptation to the increased light density, which gives us another example of the outstanding design principles of light harvesting and photoprotection implemented in the natural photosynthesis.

Author's contribution and presentation of the results

The author of the thesis has calculated inter-pigment excitation transfer rates and the resulting exciton evolution in Chapter 1; formulated the theoretical models, derived all the analytic expressions and performed the numeric calculations in Chapters 2, 4, and 5; and provided multivariate curve resolution analysis of the experimental results, formulated the coarse-grained model and the final conclusions in Chapter 3.

The results of the dissertation are presented in 9 scientific publications:

1. J. Chmeliov, A. Gelzinis, E. Songaila, R. Augulis, C. D. P. Duffy, A. V. Ruban, L. Valkunas, "The Nature of Self-Regulation in Photosynthetic Light-Harvesting Antenna", under review in *Nature*.
2. J. M. Gruber, J. Chmeliov, T. P. J. Krüger, L. Valkunas, R. van Grondelle, "Singlet–Triplet Annihilation in Single LHCII Complexes," *Physical Chemistry Chemical Physics*, 2015, **17**, 19844–19853.
3. J. Chmeliov, W. P. Bricker, C. Lo, E. Jouin, L. Valkunas, A. V. Ruban, C. D. P. Duffy, "An 'All Pigment' Model of Excitation Quenching in LHCII," *Physical Chemistry Chemical Physics*, 2015, **17**, 15857–15867.
4. J. Chmeliov, G. Trinkunas, H. van Amerongen, L. Valkunas, "Excitation Migration in Fluctuating Light-Harvesting Antenna Systems," *Photosynthesis Research*, 2015, doi:10.1007/s11120-015-0083-3.
5. E. Belgio, E. Kapitonova, J. Chmeliov, C. D. P. Duffy, P. Ungerer, L. Valkunas, A. V. Ruban, "Economic Photoprotection in Photosystem II That Retains a Complete Light Harvesting System with Slow Energy Traps," *Nature Communications*, 2014, **5**, 4433.
6. J. Chmeliov, G. Trinkunas, H. van Amerongen, L. Valkunas, "Light Harvesting in a Fluctuating Antenna," *Journal of the American Chemical Society*, 2014, **136**, 8963–8972.
7. J. Chmeliov, L. Valkunas, T. P. J. Krüger, C. Ilioaia, R. van Grondelle, "Fluorescence Blinking of Single Major Light-Harvesting Complexes," *New Journal of Physics*, 2013, **15**, 085007.
8. C. D. P. Duffy, J. Chmeliov, M. Macernis, J. Sulskus, L. Valkunas, A. V. Ruban, "Modeling of Fluorescence Quenching by Lutein in the Plant Light-Harvesting Complex LHCII," *The Journal of Physical Chemistry B*, 2013, **117**, 10974–10986.
9. L. Valkunas, J. Chmeliov, T. P. J. Krüger, C. Ilioaia, R. van Grondelle, "How Photosynthetic Proteins Switch," *The Journal of Physical Chemistry Letters*, 2012, **3**, 2779–2784.

Other author's publications not covered within the dissertation:

1. J. Chmeliov, J. Narkeliunas, M. W. Graham, G. R. Fleming, L. Valkunas, "Exciton–Exciton Annihilation and Relaxation Pathways in Semiconducting Carbon Nanotubes", under review in *Nanoscale*.
2. J. Chmeliov, E. Songaila, O. Rancova, A. Gall, B. Robert, D. Abramavicius, L. Valkunas, "Excitons in the LH3 Complexes from Purple Bacteria", *The Journal of Physical Chemistry B*, 2013, **117**, 11058–11068.
3. D. Rutkauskas, J. Chmeliov, M. Johnson, A. Ruban, L. Valkunas, "Exciton Annihilation as a Probe of the Light-Harvesting Antenna Transition into the Photoprotective Mode," *Chemical Physics*, 2012, **404**, 123–128.
4. G. Trinkunas, O. Zerlauskiene, V. Urboniene, J. Chmeliov, A. Gall, B. Robert, L. Valkunas, "Exciton Band Structure in Bacterial Peripheral Light-Harvesting Complexes", *The Journal of Physical Chemistry B*, 2012, **116**, 5191–5198.
5. L. Valkunas, J. Chmeliov, G. Trinkunas, C. D. P. Duffy, R. van Grondelle, A. V. Ruban, "Excitation Migration, Quenching and Regulation of Photosynthetic Light Harvesting in Photosystem II," *The Journal of Physical Chemistry B*, 2011, **115**, 9252–9260.
6. M. Graham, J. Chmeliov, Y. Ma, H. Shinohara, M. Hersam, A. Green, L. Valkunas, G. Fleming, "Exciton Dynamics in Semiconducting Carbon Nanotubes", *The Journal of Physical Chemistry B*, 2011, **115**, 5201–5211.
7. L. Valkunas, G. Trinkunas, J. Chmeliov, A. V. Ruban, "Modeling of Exciton Quenching in Photosystem II, *Physical Chemistry Chemical Physics*, 2009, **11**, 7576–7584.

The author has also presented the dissertation results at 12 conferences:

1. J. Chmeliov, L. Valkūnas, J. M. Gruber, T. P. J. Kruger, R. van Grondelle, "Pavieniai fotosintetiniai anteniniai kompleksai ir jų fluorescencijos ypatumai", *41-oji Lietuvos Nacionalinė Fizikos konferencija*, Vilnius, Lithuania, June 17–19, 2015.
2. J. Chmeliov, M. Gruber, R. van Grondelle, L. Valkunas, "Singlet–Triplet Annihilation in Single Light-Harvesting Complexes," *Light-harvesting processes: an interdisciplinary conference on novel concepts of light-harvesting phenomena and related topics*, Banz Monastery, Germany, March 8–12, 2015.
3. J. Chmeliov, G. Trinkunas, H. van Amerongen, L. Valkunas, "Light Harvesting in a Fluctuating Antenna," *Workshop on Ultrafast Processes in Photosynthesis. New Vistas at ELI-ALPS*, Szeged, Hungary, October 18–21, 2014.

4. J. Chmeliov, G. Trinkunas L. Valkunas, “Fluctuating Antenna as an Origin of Multi-Exponential Fluorescence Kinetics in Photosystem II,” *11th Nordic Femtochemistry Conference*, Vilnius, Lithuania, May 26–27, 2014.
5. J. Chmeliov, “Regulation and Adaptation Processes in Photosynthetic Light-Harvesting Complexes,” *International Conference “Biophysics of Photosynthesis”*, Rome, Italy, October 28–30, 2013.
6. J. Chmeliov, L. Valkūnas, C. D. P. Duffy, E. Belgio, A. V. Ruban, “Augalų antrosios fotosistemos molekuliniai apsaugos mechanizmai,” *40-oji Lietuvos Nacionalinė Fizikos konferencija*, Vilnius, Lithuania, June 10–12, 2013.
7. J. Chmeliov, L. Valkunas, G. Trinkunas, “Excitation Energy Transfer and Regulation in Photosynthetic Light-Harvesting Complexes,” *Light-harvesting processes: an interdisciplinary conference on novel concepts of light-harvesting phenomena and related topics*, Banz Monastery, Germany, April 7–11, 2013.
8. J. Chmeliov, L. Valkunas, “Excitation Energy Quenching in Photosynthetic Light-Harvesting Antenna,” *Vilnius Workshop on Non-Linear Spectroscopy and Open Quantum Systems*, Vilnius, Lithuania, October 22–23, 2012.
9. J. Chmeliov, L. Valkunas, G. Trinkunas, T. P. J. Krüger, R. van Grondelle, “Excitation Energy Transfer and Regulation in Photosynthetic Light-Harvesting Antenna,” *10th International Conference on Excitonic Processes in Condensed Matter, Nanostructured and Molecular Materials*, Groningen, The Netherlands, July 2–6, 2012.
10. J. Chmeliov, L. Valkūnas, “Pavienių fotosintetinių anteninių kompleksų trūkinėjančioji fluorescencija,” *Fizinių ir technologijos mokslų tarpdalykiniai tyrimai: 2-oji LMA Jaunųjų mokslininkų konferencija*, Vilnius, Lithuania, February 14, 2012.
11. J. Chmeliov, L. Valkunas, G. Trinkunas, “Excitation Energy Transfer and Fluorescence Quenching in Photosynthetic Light-Harvesting Antenna,” *Vilnius Workshop on Non-Linear Spectroscopy and Open Quantum Systems*, Vilnius, Lithuania, November 7–10, 2011.
12. J. Chmeliov, L. Valkūnas, T. P. J. Krüger, C. Ilioaia, R. van Grondelle, “Pavienių fotosintetinių anteninių kompleksų trūkinėjančioji fluorescencija,” *39-oji Lietuvos Nacionalinė Fizikos konferencija*, Vilnius, Lithuania, October 6–8, 2011.

> “ *It is structure that we look for whenever we try to understand anything.*
>
> LINUS PAULING

Chapter 1

Microscopic organization and function of major light-harvesting complexes

As it was already mentioned in the Introduction, major light-harvesting complexes from plants, LHCII, are the most prevalent photosynthetic pigment–protein complexes that bind about half of all the terrestrial chlorophyll molecules [5]. This fact explains the special attention that photosynthetic community focuses on LHCIIs, their internal structure, function, and macroscopic organization within the thylakoid membranes. In fact, well-established procedure of the purification of LHCII complexes provides a good background for the detailed studies of inter-pigment interactions and excitation energy transfer in either separate LHCII trimers or in their aggregates and extends our current understanding of the light-harvesting processes and the non-photochemical quenching taking place *in vivo*.

In this chapter, the structural organization of LHCII complexes and its influence on the EET as well as possible attribution to the NPQ mechanism are reviewed. Based on the known crystal structure of LHCII trimers [36–38] and the detailed quantum chemistry calculations of the electronic properties of the pigment molecules [39–41], excitation dynamics in LHCII complexes is then investigated in Section 1.3. Particularly, the influence of the carotenoid molecules is examined and possible channels for the excitation quenching are revealed[1].

1.1 LHCII: structure determines function

The internal atomic structure of the LHCII complexes was first determined from the electron microscopy and electron crystallography measurements [36, 37] and was refined later by means of X-ray crystallography with a sub-3-Å resolution [38]. Structurally, the basic functional unit of LHCII complexes was found to be an almost cylindrically shaped pigment–protein of about 7.3 nm in diameter and consisting of three noncovalently associated subunits. In their turn, each monomeric subunit contains three trans-membrane polypeptide chains (α-helices)

---

[1] The modeling results presented in this chapter are based on the works published in [42, 43].

that coordinate 8 molecules of Chl *a*, 6 Chls *b*, and 4 carotenoids: 2 luteins (Lut), neoxanthin (Neo), and a xanthophyll cycle carotenoid—violaxanthin (Vio) or zeaxanthin (Zea). The chemical structures of the chromophores found in LHCII complexes are presented in Fig. 1.1a, and the overall spatial composition of LHCII trimer is shown in Fig. 1.1b.

Chlorophylls are the major light-harvesting pigments that govern the whole plant photosynthesis. Large absorption cross-section (~4 Å^2) and long excited state lifetime (~5 ns) make them very effective light captors as well as excitation energy transmitters to the reaction center [3]. The Chl molecule consists of a planar chlorin ring, being about 10 Å in diameter and containing a Mg atom in the center, with a long hidrophobic phytyl tail attached to it (Fig. 1.1a). The latter is very flexible and can adopt to various positions and orientations available within the protein "pocket", whereas the chlorin ring incorporates an extended conjugated system of the π-electrons, delocalized across the alternating single and double C–C bonds. This property makes the chlorin ring the actual light-absorbing part of the Chl molecule and simplifies quantum chemistry calculations, during which non-absorbing phytyl tail is usually replaced with a simple methyl group [42–44].

The absorption spectrum of the Chl molecule consists of two major bands in the visible light spectrum: the red one corresponds to the two lowest-energy transitions—the so-called Q_y (S_1) and much weaker Q_x sub-bands—while the blue one (the Soret band) produces a short-lived higher excited states that very rapidly (~1 ps) via internal conversion (IC) relaxes to the S_1. In plants, two types of Chl molecules are found, namely Chl *a* and Chl *b*, that differ by a single radical denoted as "R" in Fig. 1.1a, where a formyl group of Chl *b* replaces a methyl group of Chl *a*. Such a small change in chemical composition, however, results in a notable shift of the Chl *b* absorption spectrum to shorter wavelengths in the red spectral region and to the longer wavelengths in the blue one (*cf.* Fig. 1.1c). As a result, the main function of Chl *b* pigments is to absorb the light that is spectrally not accessible for Chls *a* and then to transfer the generated electronic excitation to the nearby Chl *a* molecules, thus extending the absorption cross-section of the latter. This property explains why Chls *b* are found only in the peripheral antenna complexes and not in the PSII core complexes.

Other pigment molecules found in LHCIIs and mentioned above belong to a wide class of carotenoids, which comprises over 600 fully characterized and naturally occurring molecular species [45, 46]. Although carotenoids are biosynthesized only by plants and some microorganisms, they are eventually distributed over the whole biosphere and are known to be responsible for many vital functions: they can act as vitamin precursors or powerful antioxidants, natural colorants or odorants. In fact, countless colors of the surrounding world, from flow-

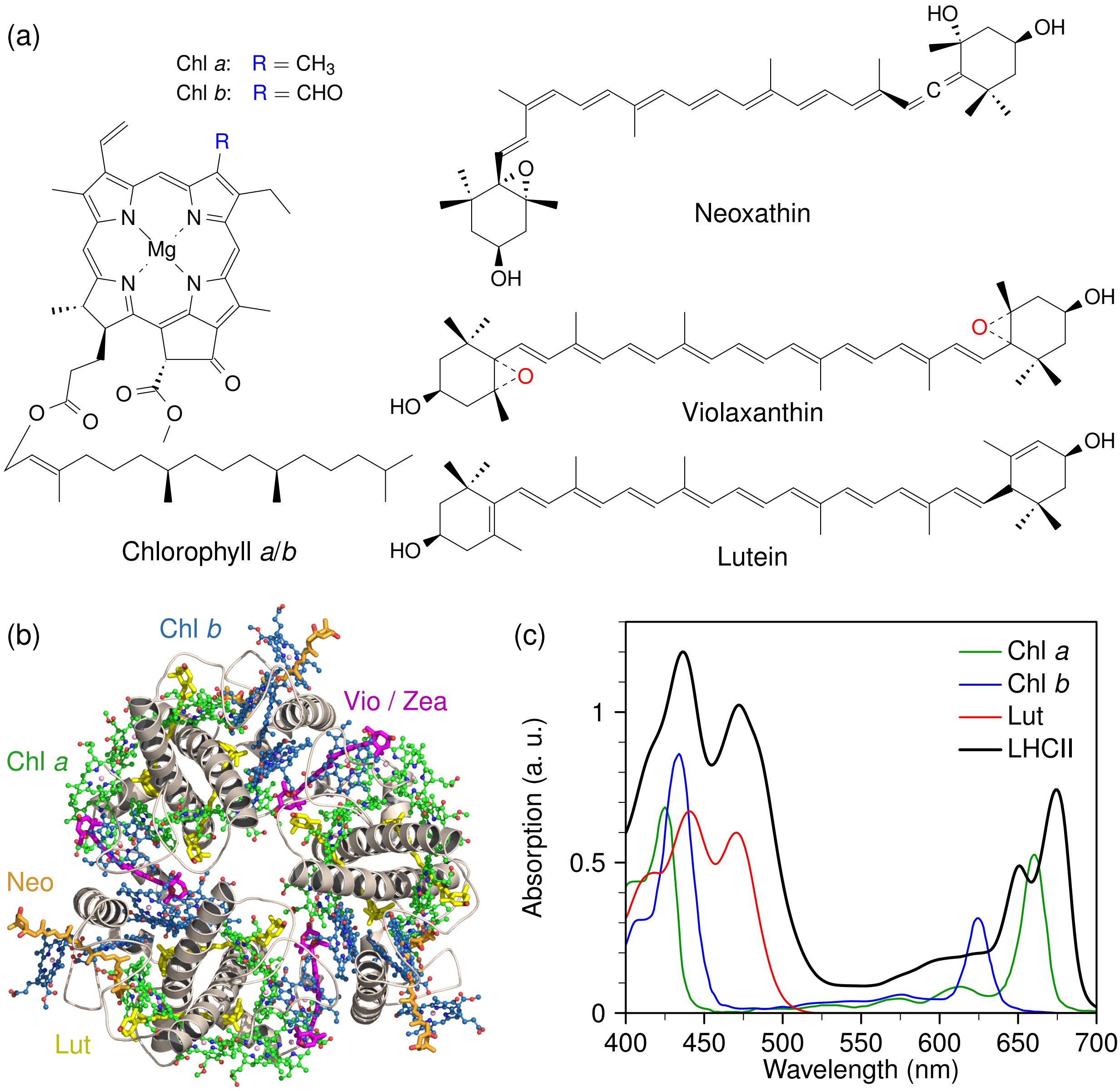

Figure 1.1 | (**a**) Light-harvesting pigments found in LHCII complexes—chlorophylls (left) and carotenoids (right). Chl *a* and Chl *b* differ by the single group denoted with blue color. The de-epoxidation of violaxanthin (loss of the two oxygen atoms denoted with red color) converts it into zeaxanthin. (**b**) Crystal structure of the LHCII trimer [38], as viewed from the stromal side of the thylakoid membrane. Each monomeric subunit contains 8 Chls *a* (green), 6 Chls *b* (blue), 2 Luts (yellow), 1 Neo (orange), and 1 xanthophyll cycle carotenoid—Vio or Zea (magenta). (**c**) Room-temperature absorption spectra (not mutually scaled) of the solubilized Chl *a*, Chl *b*, and Lut pigments as well as LHCII trimer. Data taken from [3].

ers, fruits and vegetables to plumage of birds and markings of fishes or amphibians, arise from various types of carotenoids.

The functional diversity of the carotenoid pigments is related to their unique spectroscopic properties that arise from their structure. The characteristic structural pattern of all carotenoids is a polyene hydrocarbon chain—a backbone consisting of alternating single and double C–C bonds. The carotenoids found in the light-harvesting antenna of higher plants—lutein, neoxanthin, violaxanthin, and zeaxanthin—belong to a class of oxygenated carotenoids, known as xanthophylls. Additionally, these photosynthetic Cars contain ring structures at each end (*cf.* Fig. 1.1a). Neoxanthin is the most polar and asymmetric of these Cars in LHCII [3, 4]. In contrast, violaxanthin is the most symmetric one and contains two epoxy oxygen atoms at each ring. This Car, located on a periphery of LHCII complex, is known to participate in the *xanthophyll cycle*, a process during which under high light conditions Vio is reversibly de-epoxidated into zeaxanthin [47]. During this reversible cycle another Car—antheraxanthin, having only one epoxy group—is transiently formed. The remaining two Cars in the LHCII complex, luteins, are isomers of Zea and are terminated with two ring groups that have different double bond positions within the ring. Both Luts are arranged in a cross pattern (see Fig. 1.1b) and provide a strong link between the two protein helices, thus holding the LHCII complex together [38]. These Cars were determined to be essential for proper *in vitro* folding into stable LHCII complexes [48].

An extended π-conjugated system of Cars results in their unusual energetic and electronic properties. Since the ground state (S_0) and the first singlet excited state (S_1) both posses the same symmetry, the corresponding transition is optically dipole-forbidden [45]. Therefore an intense 3-peak absorption band, typically lying in the 400–500 nm region (see Fig. 1.1c for Lut[2]), corresponds to a direct excitation into the lowest three vibrational levels of a second electronic excited state, S_2. Despite the sub-ps lifetime of this state [45], its excitation energy can be transferred to the nearby Chl molecule, so in this case Cars act as an accessory light-harvesting pigments, further extending absorption cross-section of LHCII into blue-green optical region not available for Chls. Excitation energy can also reach Chls via intermediate population of the Car S_1 state following internal conversion from its S_2 state. However, this channel for EET can become active only for some particular values of the Car S_1 energy that should be higher than that of Chl S_1 state. Otherwise, energy will flow in the opposite direction, and short-living (~10 ps [45]) Car S_1 state will act as an effective quencher of the Chl fluorescence. Nevertheless, because of its dipole-forbidden nature, knowledge about the Car S_1 state energetics is still limited. Direct fluorescence measurements at different

---

[2] Other LHCII xanthophylls have very similar absorption spectra to that of Lut, just slightly shifted to the shorter (Vio and Neo) or to the longer (Zea) wavelengths [3].

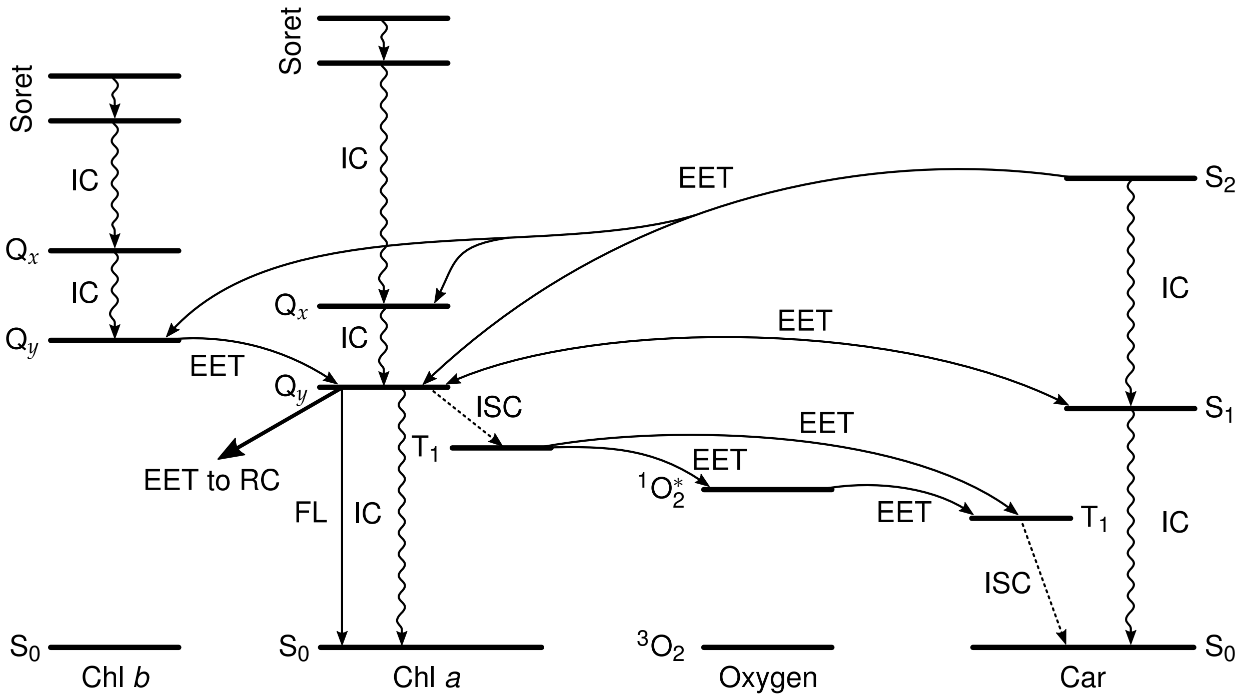

Figure 1.2 | Schematic diagram of the dominating excitation energy transfer and relaxation pathways in light-harvesting antenna: internal conversion (IC), intersystem crossing (ISC), fluorescence (FL), and excitation energy transfer (EET).

temperatures and in different environments revealed various S_1 energies, from 14 550 to 14 610 cm^{-1} for Zea and from 14 880 to 15 580 cm^{-1} for Vio [49, 50]. Later, excited state absorption measurements on LHCII mutants containing only single Car species were performed, revealing the S_1 energy of 13 900 cm^{-1}, the same for Lut, Vio, and Zea [51]. Alternatively, during the two-photon absorption measurements of solubilized Lut the corresponding S_1 peak was found to be located at 14 350 cm^{-1} [52]. In addition to all these inconsistencies, the *in vivo* situation becomes even more unclear since the local protein/pigment environment inside LHCII is known to strongly affect the transition energies of all the pigment molecules (note, *e.g.*, the red-shift of the absorption spectrum of the LHCII trimer compared with that of the solubilized Chls, shown in Fig. 1.1c). The reported existence of additional states of Cars, energetically lying between the S_1 and S_2 states and promoting Car→Chl excitation energy transfer [45, 53], makes the whole story even more complicated.

Besides participating in the light-harvesting processes, carotenoids also play an important role in *photoprotection*. At low light conditions, the quantum yield (QY) of Chl triplet state, T_1, formation (see Fig. 1.2) in the light-harvesting antenna is about 30 % [54] and is even larger at higher excitation densities, when the reaction centers become closed and cannot photochemically utilize the incoming excitation. At such conditions, the QY of intersystem crossing (ISC) can approach 60–80 %, the values determined for the isolated Chl molecules [55]. The generated triplet Chl states decay on a millisecond timescale [56, 57] and therefore readily react with molecular oxygen produced in the RC of PSII. As a result, the highly reactive species of singlet oxygen are formed [58] that can potentially damage the whole photosynthetic apparatus. In carotenoids, due to fast relaxation to the ground state the ISC is very inefficient. Nevertheless, Car triplet states are known to successfully scavenge this reactive oxygen species and dissipate its energy as heat [59]. Moreover, it was found that in LHCII more than 90 % of Chl triplets are at room temperature also efficiently quenched by Cars, primarily by two lutein molecules [60, 61]. Carotenoids are also supposed to participate in a non-photochemical quenching, a process when over-excitation of the antenna chlorophylls is very efficiently dissipated as heat, thus even avoiding the formation of the triplet Chl states [18–20]. This topic is further discussed in the following section.

The dominating pathways of excitation energy relaxation and inter-molecular transfer in light-harvesting antenna complexes discussed above are summarized in Fig. 1.2.

1.2 Proposed mechanisms of NPQ

It is known that natural, *in vivo* NPQ is driven by the interplay of three factors: a strong trans-membrane ΔpH resulting ultimately from a high rate of photosynthetic charge separation [62, 63], the enzymatic de-epoxidation of the violaxanthin to zeaxanthin in the PSII antenna (the so-called xanthophyll cycle mentioned above) [64], and the presence of the PsbS protein within the photosynthetic membrane [65]. It has been proposed that the collective action of these three mechanisms induces a subtle reversible conformational change in the antenna pigment–protein complexes, thereby altering the landscape of inter-pigment interactions and leading to the formation of exciton quenching states [12]. However, despite extensive research, there is still no consensus concerning the exact molecular nature of the quenching sites, their precise location within the PSII antenna, and the exact physical mechanism(s) by which they are activated. Significantly reduced fluorescence lifetime, observed in the *in vitro* aggregates of the solubilized LHCII complexes [66, 67] as well as in LHCII crystals [19], compared to that in separated LHCII trimers have raised the hypothesis of the aggregation-induced quenching. However, it is still not clear whether the aggregation process itself leads to the generation of the excitation quenching states or it is just an indicator that helps to observe such states.

Regarding the nature and physical location of the NPQ sites, several possible models have been suggested so far, each indirectly supported by some experimental observations [12]. Most of them ascribe the leading role to the carotenoid molecules and their short-lived optically dark S_1 state. First of all, the close association between NPQ and the xanthophyll cycle raised the idea of a "molecular gearshift mechanism" [68]. According to it, the energy of the S_1 state of Vio lies above the Chl S_1 state. In this scenario, the absorption of light energy by the dipole-allowed S_2 state of Vio is followed by rapid IC and subsequent downhill energy transfer to the Chl molecule. As a result, Vio plays merely a light-harvesting role. On the other hand, the S_1 state of Zea was predicted to lie below that of Chl, thus promoting the backward excitation energy transfer (Chl→Zea) and its rapid non-radiative dissipation.

Later, the Zea cation signal was detected in thylakoid membranes under NPQ conditions [18]. As a result, the formation of Zea–Chl charge transfer (CT) state followed by the non-radiative charge recombination was proposed as an origin for NPQ. Initially, the location of this CT state was assumed to be within LHCII, although other PSII antenna complexes should also not be excluded. Indeed, the same Zea cation signal was also observed in the isolated minor light-harvesting complex CP29 [21]. On the other hand, the presence of the Zea cation has not yet been shown to be associated with any significant fluorescence quenching compared to the Vio-containing complexes [21, 69]. At the same time, other experiments have demonstrated almost instantaneous population of the Car S_1 state upon excitation of Chls [70] as well as Chl fluorescence signal appearing shortly after the two-photon excitation of the Car S_1 state [71]. Both these observations suggest strong interaction between some particular Car and Chl pigments resulting in excitation delocalization over Car–Chl heterodimer, which is also able to operate as an excitation energy trap. Finally, incoherent excitation energy transfer from Chls to Cars, luteins in particular, has also been proposed [20]. Recently, similar mechanism involving direct EET from the Chl *a* pigment to the S_1 state of β-carotene has been shown to be responsible for photoprotection in cyanobacteria [72]. Meanwhile, in opposite to all these carotenoid-involving mechanisms of NPQ, excitation energy trapping via a low-lying Chl–Chl CT state has also been proposed [22].

In order to distinguish between all these possible mechanisms of NPQ, microscopic modeling of excitation energy transfer and quenching in light-harvesting antenna is required. Such theoretical calculations became possible after crystal structure of most photosynthetic pigment–protein complexes—LHCII [38], CP29 [73] and PSII core complexes [74]—had been obtained with a resolution higher than 3 Å, providing essential information on the structural organization and mutual arrangement of the pigment molecules in these systems. That also provided possibility to calculate interaction energies between different Chl pigments in LHCII in the dipole–dipole approximation and then to simultaneously fit absorption, linear- and circular-dichroism, and steady-state fluorescence spectra as well as transient absorption kinetics [75, 76]. Later, highly accurate *ab initio* quantum chemistry methods were used to calculate Chl–Chl interaction energies, at the same time accounting for the effects of the protein, membrane, and water environment [40, 44]. These studies contributed significantly to understanding of inter-chlorophyll EET. However, due to difficulties in the quantum chemistry calculations of the strongly correlated S_1 excited state of the Car pigments, their influence has not yet been studied thoroughly, even though crystal structure of LHCII complexes [38] represents highly quenched species [19] that manifests the presence of some excitation energy traps resembling NPQ *in vivo*.

In the following sections, this drawback is eliminated and an "all-pigment" model of LHCII is formulated. As a result, a reasonable estimation of the quenching ability of various carotenoids is obtained.

1.3 An all-pigment model of LHCII

1.3.1 Inter-pigment interactions

In order to quantitatively study inter-molecular excitation energy transfer within LHCII, interaction strength between different pigments has to be calculated. Electrostatic coupling between the transition densities of a "donor" (D) and an "acceptor" (A) molecules is composed of two components arising from the Coulomb, J_{DA}, and the exchange, K_{DA}, interactions:

$$W_{\mathrm{DA}} = J_{\mathrm{DA}} - K_{\mathrm{DA}}.$$

The exchange interaction requires significant overlap between the atomic orbitals of the donor and acceptor transition densities and as such falls off exponentially with increasing inter-molecular distance. Therefore its contribution is usually neglected, so that $W_{\mathrm{DA}} \approx J_{\mathrm{DA}}$.

In the first theoretical works that appeared shortly after the determination of the high-resolution crystal structure of LHCII [38], the Coulomb coupling was approximated as an interaction between two point transition dipole moments $\mathbf{d}$ [75–77]:

$$J_{\mathrm{DA}} \simeq \frac{1}{4\pi\varepsilon\varepsilon_0}\left(\frac{\mathbf{d}_{\mathrm{D}}\cdot\mathbf{d}_{\mathrm{A}}}{R^3} - \frac{3\left(\mathbf{d}_{\mathrm{D}}\cdot\mathbf{R}\right)\left(\mathbf{d}_{\mathrm{A}}\cdot\mathbf{R}\right)}{R^5}\right),$$

where R is the center-of-mass separation of the molecules D and A, and ε is the mean dielectric constant of the protein environment. At the heart of the dipole approximation is the assumption that the inter-molecular distance between donor and acceptor is much greater than the spatial extent of either molecule. This is clearly not a case in a densely packed pigment–protein complex such as LHCII. As a result, excitation energy to the dipole-forbidden ($\mathbf{d} \approx 0$) S_1 state of the carotenoids becomes possible. Therefore, a more accurate description of the transition density should be employed. Based on the quantum chemistry calculations, such a description can be achieved in several different approaches. In the *transition charges* method, some partial electric charge q_α is assigned to each atom of the molecule by fitting the overall electrostatic potential of the transition density of the pigment, calculated by using, *e.g.*, time-dependent density functional theory [40,44,78]. The coupling between the molecules D and A is then evaluated as Coulomb interaction of all the transition charges of one molecule, $q_\alpha^{(\mathrm{D})}$, described by a radius–vector $\mathbf{r}_\alpha^{(\mathrm{D})}$, with the total electrostatic potential created by the another molecule, $\varphi_\mathrm{A}(\mathbf{r})$ [40]:

$$J_\mathrm{DA} = \sum_{\alpha\in\mathrm{D}} \varphi_\mathrm{A}\left(\mathbf{r}_\alpha^{(\mathrm{D})}\right) \cdot q_\alpha^{(\mathrm{D})}.$$

This method also allows accounting for the inhomogeneous dielectric properties of the protein environment and was successfully applied to Chl and bacteriochlorophyll molecules, in which S_1 transition exhibits predominantly single-excitation character. However, this theory cannot account for the double-excitation character of the Car S_1 transition [79].

To evade this issue, computationally more expensive semi-empirical quantum chemistry methods should be used [80]. By expressing the transition dipole moment for a transition between the ground state, $|\mathrm{GS}\rangle$, and the first excited state, $|\mathrm{EX}\rangle$, of the molecule in terms of its atomic orbitals:

$$\mathbf{d}_\mathrm{A} = \left\langle \mathrm{EX} \middle| \hat{\mathbf{d}}_\mathrm{A} \middle| \mathrm{GS} \right\rangle = \sum_{\alpha\in\mathrm{A}} \mathbf{r}_\alpha T_\alpha,$$

the inter-pigment interaction can be easily calculated in the so-called *transition monopole* approach [42]:

$$J_\mathrm{DA} = \sum_{\substack{\alpha\in\mathrm{A}\\ \beta\in\mathrm{D}}} \frac{1}{4\pi\varepsilon\varepsilon_0} \frac{T_\alpha T_\beta}{\left|\mathbf{r}_\alpha - \mathbf{r}_\beta\right|}.$$

Here α and β label atoms of the molecules A and D, positioned at $\mathbf{r}_\alpha$ and $\mathbf{r}_\beta$, respectively, and T_α is the total transition density associated with the α-th atom. Alternatively, the *transition density cube* (TDC) method [81] can be formulated by approximating the true transition densities of the molecules as a discrete three-dimensional grid of volume elements (or "cubes"). The transition density, $M_\mathrm{A}(i)$, associated with a cube of volume $\delta V = \delta x\, \delta y\, \delta z$, positioned at $\mathbf{r}_i$, is given as follows [82]:

$$M_\mathrm{A}(i) = \int_{x_i}^{x_i+\delta x} \int_{y_i}^{y_i+\delta y} \int_{z_i}^{z_i+\delta z} \Psi_\mathrm{EX}^{(\mathrm{A})*}\, \Psi_\mathrm{GS}^{(\mathrm{A})}\, \mathrm{d}x\mathrm{d}y\mathrm{d}z, \tag{1.1}$$

where $\Psi_{\mathrm{GS}}^{(\mathrm{A})}$ and $\Psi_{\mathrm{EX}}^{(\mathrm{A})}$ are the quantum-chemically calculated ground and excited state wave functions of the molecule A, respectively. The TDC method is known to better represent the transition density in regions out of the plain of the molecule than both previously discussed approaches: the only approximations involved in this calculation are the predetermined grid size and the accuracy of the quantum mechanical wave functions that the TDCs are constructed from. As the number of grid points increases, the Coulomb couplings calculated from the donor and acceptor TDCs approach their exact values based on the donor and acceptor wave functions [81]. As a result, the latter can be approximated as the sum of all pairwise interactions between the TDCs of the donor and acceptor molecules:

$$J_{\mathrm{DA}} = \sum_{i,j} \frac{e^2}{4\pi\varepsilon\varepsilon_0} \frac{M_{\mathrm{D}}(i)\, M_{\mathrm{A}}(j)}{\left|\mathbf{r}_i - \mathbf{r}_j\right|}. \tag{1.2}$$

Although being completely different in their formulations, all these three methods were shown to produce similar Chl–Chl couplings within LHCII [40, 42, 43]. Even though for some more distant and weakly interacting molecules the obtained couplings differ up to 5 times, a good correlation and better match was demonstrated for more strongly interacting Chl pairs [43], indicating that the differences of the results produced by utilizing various theories probably do not exceed the uncertainties arising due to influence of protein environment and its possible dynamic fluctuations.

The pairwise inter-molecular interaction energies, obtained for 18 pigment molecules (14 Chls and 4 Cars) from an LHCII monomer using TDC method, are listed in Table 1.1, where pigments are labeled according to the Liu *et al.* notation of the crystal structure [38]. For all the pigments, both Cars and Chls, the S_1 transitions were computed using the MNDO-CAS-CI method [83] with an active space consisting of 6 π-orbitals, as implemented by the MOPAC2006 semi-empirical quantum chemistry package[3] [84]. For the Car molecules this method yields a dipole-forbidden ($d \simeq 0\,\mathrm{D}$) S_1 transition as well as a dipole-allowed ($d \simeq 20\,\mathrm{D}$) S_2 transition, in line with the common properties of carotenoids discussed above. The correct properties of the S_1 transition of the Chl molecules are also attained. However, in the later case the calculated transition dipole moments were somewhat larger compared to the reported vacuum-extrapolated values [85]. Therefore, transition densities in Eq. 1.1 were rescaled by a factor of 0.7. For consistency, the same rescaling factor was also applied for the Car transition densities, though due to vanishing dipole moment it cannot be further verified by comparing to some experimental values. The protein environment was accounted for with a

---

[3] These calculations were carried out by C. D. P. Duffy and W. P. Bricker from Queen Mary University of London, UK. Further details are presented in [43].

simple continuum model, in which pigment molecules are embedded in a uniform dielectric material with relative dielectric constant of $\varepsilon = 2$ [40]. In spite of such simplifications, the obtained Chl–Chl couplings, shown in Table 1.1, reasonably match those calculated using a more sophisticated protein model [40], while newly computed Chl–Car interaction energies in Table 1.1 allow evaluating the possible role of each carotenoid in excitation energy relaxation.

Closer look at the obtained Chl–Chl interaction energies reveals that the majority of the pigments are weakly-to-moderately coupled, with the $J_{\mathrm{DA}} < 20\,\mathrm{cm}^{-1}$. It means that in most cases, Förster regime of incoherent excitation energy transfer [86–88] can be readily used to describe excitation dynamics. Somewhat larger couplings (between 30 and $80\,\mathrm{cm}^{-1}$) can be noted for the neighboring pigments in the Chl*b*601–Chl*a*602, Chl*a*604–Chl*b*606, Chl*a*603–Chl*b*609, and Chl*b*608–Chl*a*610 pairs. However, each of these pairs is composed of the chlorophyll pigments of different types, Chl *a* and Chl *b*, so that due to poor spectral overlap one can still consider incoherent EET within these pairs. As a result, only two clusters of strongly interacting pigments of the same type can be observed—the pair Chl*a*613–Chl*a*614 and the triplet Chl*a*610–Chl*a*611–Chl*a*612. The latter, known as LHCII *terminal emitter*, was determined to be responsible for the reddest part of LHCII fluorescence spectrum [40,75] and therefore was proposed to act as a local excitation energy sink, transferring its energy to the nearby lutein molecule [20].

With regard to the Chl–Car couplings, much weaker values were obtained. One can see that Lut620 is only appreciably coupled ($J = 12\,\mathrm{cm}^{-1}$) with Chl*a*612 (see also Fig. 1.3 for the enlarged mutual arrangement of the pigment molecules). Despite the close cofacial geometry of the Lut620 and Chl*a*612 pigments, their interaction energy is significantly weaker than that of the Chl*a*611–Chl*a*612 pair ($J = 131\,\mathrm{cm}^{-1}$). This can be attributed to the dipole-forbidden nature of the Car S_1 transition. The coupling between Lut620 and more distant neighboring Chls is significantly weaker. Due to the symmetry of the two lutein domains in LHCII [38] another lutein, namely Lut621, was found to be similarly coupled to Chl*a*603 ($J = 11\,\mathrm{cm}^{-1}$). In fact, the Chl*a*603–Lut621 heterodimer has essentially the same close, cofacial geometry as Chl*a*612–Lut620, albeit with some minor differences in the overall conformation of carotenoid [89]. Interestingly, other two xanthophylls, Vio622 and Neo623, were found to be very weakly coupled to their Chl neighbors, that indicates their weak contribution to both light harvesting and photoprotection. Indeed, it was shown that a xanthophyll with an absorption maximum at 486 nm, attributed to Neo, does not play a significant role in either light-harvesting or triplet quenching in this complex [90]. Later studies, based on spectroscopic analysis, suggested that Vio in LHCII does not transfer excitation energy to neighboring chlorophylls and therefore also does not participate in light-harvesting [91]. Recent quantum chemistry calculations of the Car S_2–Chl S_2

Table 1.1 | Inter-pigment couplings in LHCII monomer (in cm^{-1}). Diagonal values represent Chl site energies determined by Müh *et al.* [40].

Pigments	Chl*b*601	Chl*a*602	Chl*a*603	Chl*a*604	Chl*b*605	Chl*b*606	Chl*b*607	Chl*b*608	Chl*b*609	Chl*a*610	Chl*a*611	Chl*a*612	Chl*a*613	Chl*a*614	Lut620	Lut621	Vio622
Chl*b*601	15 405																
Chl*a*602	-35.6	14 940															
Chl*a*603	-5.4	18.1	14 850														
Chl*a*604	-1.9	6.3	5.0	14 820													
Chl*b*605	0.4	-0.5	-0.9	-3.1	15 465												
Chl*b*606	1.6	-5.5	-9.5	77.6	11.3	15 385											
Chl*b*607	-1.6	5.0	1.0	-17.6	1.1	13.2	15 225										
Chl*b*608	-1.7	4.8	3.4	-2.5	-3.4	3.0	-3.0	15 215									
Chl*b*609	-2.4	18.2	62.7	-6.6	-0.2	13.1	-6.3	-14.0	15 475								
Chl*a*610	-4.1	-10.0	-8.9	4.5	-1.5	-3.4	-0.5	39.8	-1.0	14 790							
Chl*a*611	-8.9	-1.8	-1.0	-2.4	1.0	2.3	-1.7	-3.1	-2.5	-29.6	14 950						
Chl*a*612	3.2	11.2	1.9	0.3	2.2	2.9	-1.8	-0.6	-1.2	-12.3	131.4	14 940					
Chl*a*613	-6.7	-5.5	0.9	-0.3	0.9	1.5	-1.2	-1.4	-1.4	-6.9	-5.6	4.0	14 840				
Chl*a*614	-3.1	-1.9	-6.8	-3.3	0.4	1.9	-2.5	-1.1	-1.8	-2.0	-3.9	0.7	-60.0	14 940			
Lut620	0.2	-0.1	0.0	0.5	0.0	-0.3	0.2	0.1	0.2	3.6	1.3	12.2	-2.8	-0.6	?		
Lut621	0.3	-2.8	10.8	-5.4	0.2	2.0	-1.9	0.3	0.8	0.4	0.2	-0.6	0.2	0.4	0.0	?	
Vio622	1.1	0.0	0.1	0.0	0.0	0.0	0.0	0.0	0.0	0.1	0.4	0.0	3.2	2.4	0.0	0.0	?
Neo623	0.2	-0.4	-0.3	3.9	-0.8	-3.9	0.2	-3.1	0.6	-0.4	0.3	0.9	0.2	0.2	0.0	0.1	0.0

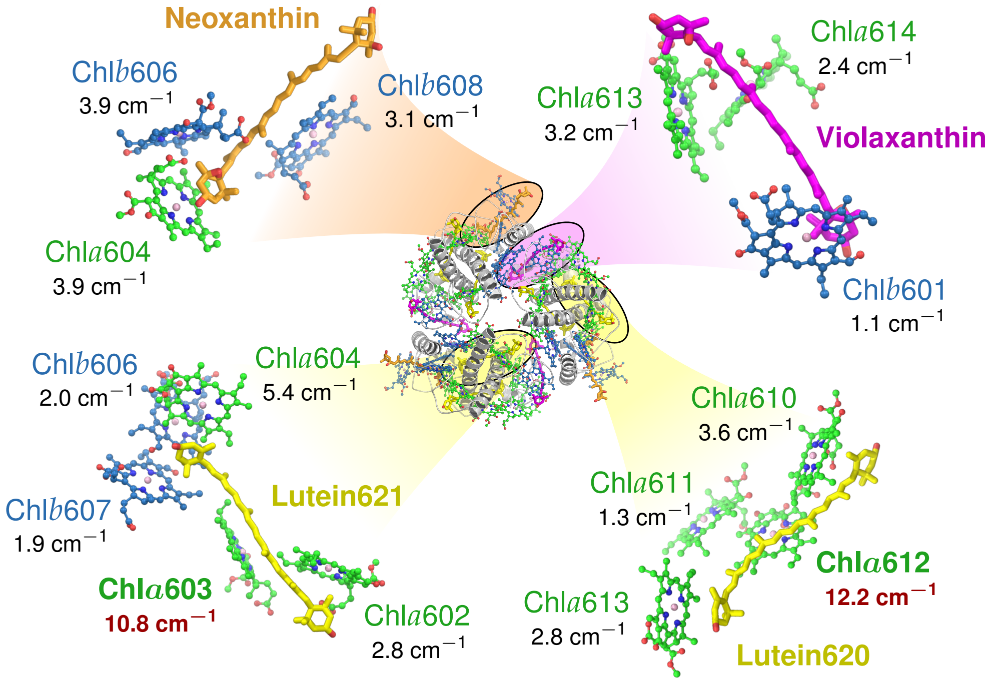

Figure 1.3 | Crystal structure of the LHCII trimer [38] and the mutual arrangements of the 4 carotenoid molecules and their neighboring Chls. Numbers represent the coupling strengths between the corresponding Chls and Cars.

couplings in LHCII have also revealed that Vio and Neo are significantly less energetically connected to the Chl pool than the two lutein molecules [41].

One point that needs to be mentioned at this stage concerns the absolute value of the calculated Chl–Car couplings. As mentioned above, the vanishingly small transition dipole moment of the Car S_1 state prevents accurate empirical rescaling or phase fixing of the raw calculated transition densities. A compromise was to subject the Car transition densities to the same rescaling factor as obtained empirically for the Chl molecules, but this is only an approximation. The calculated Chl–Car couplings are qualitatively reasonable and are consistent with the observed differences between Vio–Chl, Neo–Chl and Lut–Chl couplings. However, they are only strictly meaningful in a relative sense. For the same reason it is not possible to assign a particular phase to the Car transition densities based on the overall phase of a vanishingly small transition dipole moment. However, since the Chl–Car couplings are much weaker than the inter-chlorophyll ones, it is reasonable to assume that energy transfer between the two pigment pools proceeds incoherently and any excitonic Chl–Car interactions would be subject to rapid disruption by polaronic effects. As a result, Chl-to-Car energy transfer depends only on the magnitude of the coupling, in accordance to Förster theory [86–88].

1.3.2 Förster theory of excitation energy transfer

Quantum chemistry calculations of all the inter-pigment couplings allow constructing a full excitonic Hamiltonian for LHCII monomer, which in the site basis is expressed as

$$\hat{H} = \sum_{n=1}^{N} E_n \left|n\right\rangle \left\langle n\right| + \sum_{n \neq m}^{N} J_{nm} \left|n\right\rangle \left\langle m\right| . \tag{1.3}$$

Here $N = 18$ is the number of pigments in the LHCII monomer (8 Chls *a*, 6 Chls *b*, and 4 Cars), E_n is the energy of the S_1 level of the nth pigment, and J_{nm} is the interaction energy between the nth and mth molecules, as defined above in Eq. 1.2. For the site energies of Chl pigments one can use those obtained by Müh *et al.* [40] from the detailed calculations of the influence of the protein environment and simultaneous fit of the absorption, linear and circular dichroism as well as fluorescence spectra. However, as discussed above, the site energies for the S_1 transition of Cars are not known. Therefore, the effect of possible variations in these energies has also to be investigated. The resulting Hamiltonian of Eq. 1.3 is presented in Table 1.1.

Assuming the Förster regime of incoherent excitation energy transfer, the inter-pigment transfer rates from the mth to the nth site, k_{nm}, are calculated according to the following equation [76,92]:

$$k_{nm} = \frac{2\left|J_{nm}\right|^2}{\hbar^2}\mathrm{Re}\int_0^\infty A_n\left(t\right)F_m^*\left(t\right)\,\mathrm{d}t, \tag{1.4}$$

where

$$A_n\left(t\right) = \mathrm{e}^{-\mathrm{i}E_n t/\hbar - g_n(t)}, \tag{1.5}$$

$$F_m\left(t\right) = \mathrm{e}^{-\mathrm{i}(E_m/\hbar - 2\lambda_m)t - g_m^*(t)} \tag{1.6}$$

are the Fourier-transforms of the absorption and fluorescence lineshapes, respectively; $g_n\left(t\right)$ is the line-broadening function, and $\hbar\lambda_n$ is the Stokes shift for the corresponding pigment. In terms of the spectral density $C''\left(\omega\right)$, the latter two quantities are expressed as

$$g_n\left(t\right) = \int_0^\infty \frac{\mathrm{d}\omega}{\pi\omega^2}C_n''\left(\omega\right)\left[\left(1-\cos\left(\omega t\right)\right)\coth\left(\frac{\hbar\omega}{2k_\mathrm{B}T}\right) + \mathrm{i}\left(\sin\left(\omega t\right) - \omega t\right)\right],$$

$$\lambda_n = \int_0^\infty \frac{\mathrm{d}\omega}{\pi\omega}C_n''\left(\omega\right),$$

where k_B is Boltzmann constant and T denotes the absolute temperature.

The conventional (based on dipole–dipole interactions) Förster theory predicts no excitation energy transfer between Chls and dark (dipole-forbidden) S_1 state of the carotenoids. However, due to relatively small inter-pigment distances in the photosynthetic light-harvesting complexes, energy transfer to the dipole-forbidden states becomes possible [93,94]. In this case the "absorption spectrum" of the Car S_1 state in Eq. 1.4 should be treated as a density-of-states (DOS) distribution. Two-photon absorption spectrum of lutein [52] reveals a very broad DOS of the S_1 transition with a full width at half maximum (FWHM) being about $3\,000\,\mathrm{cm}^{-1}$, see dots in Fig. 1.4. Currently, no empirical spectral density has been determined for the vibronic structure of the Car S_1 state. However, such a broad lineshape can be obtained by postulating the spectral density of the overdamped Brownian oscillator with large reorganization energy λ_0:

$$C_n''\left(\omega\right) = 2\lambda_0\frac{\omega\gamma}{\omega^2+\gamma^2}, \qquad n \equiv \text{Carotenoid}. \tag{1.7}$$

For the following calculations of EET, the parameter γ, determining the correlation time of the site energy fluctuation, was assumed to be equal $\gamma = 53\,\mathrm{cm}^{-1}$ (or $\gamma^{-1} = 100\,\mathrm{fs}$), a typical value usually used for the light-harvesting pigments. In order to describe the broad two-photon absorption spectrum of solubilized lutein [52], the reorganization energy λ_0 then should be chosen to be of the order of $\lambda_0 = 3\,520\,\mathrm{cm}^{-1}$ (if static disorder due to inhomogeneous broadening is ne-

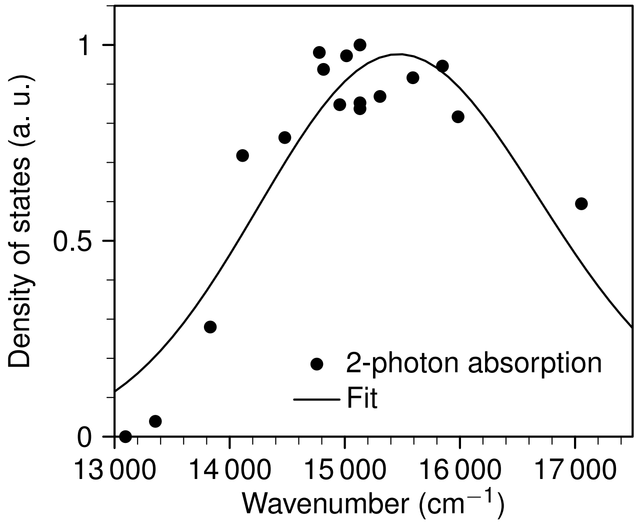

Figure 1.4 | Density-of-states for the Lut S_1 transition. Dots represent two-photon excitation spectrum of lutein in octanol solution (data taken from [52]) while solid line corresponds to DOS lineshape, fitted by calculating the inverse Fourier transform of Eq. 1.5 and assuming spectral density of the overdamped Brownian oscillator (Eq. 1.7).

glected), *cf.* Fig. 1.4 for the resulting fit of the DOS distribution. Other parameter pairs ($\gamma^{-1} = 50\,\text{fs}$, $\lambda_0 = 3\,360\,\text{cm}^{-1}$ and $\gamma^{-1} = 200\,\text{fs}$, $\lambda_0 = 3\,610\,\text{cm}^{-1}$) yield approximately the same DOS function of the above-mentioned FWHM. Evidently, in the Förster regime of the excitation energy transfer only the shape of the DOS distribution is important. Therefore, in all three cases of the λ_0 and γ pairs the obtained transfer rates did not differ more than by 1 %. For simplicity, the same spectral density was assumed for other xanthophylls as well. Meanwhile, for the chlorophylls the spectral density suggested by Renger *et al.* was used:

$$C''_n(\omega) = \frac{\pi S_0 \omega^5}{s_1 + s_2} \sum_{i=1}^{2} \frac{s_i}{7!2\omega_i^4} \mathrm{e}^{-\sqrt{\omega/\omega_i}}, \qquad n \equiv \text{Chlorophyll},$$

where $S_0 = 0.5, s_1 = 0.8, s_2 = 0.5, \omega_1 = 0.56\,\text{cm}^{-1}$, and $\omega_2 = 1.94\,\text{cm}^{-1}$ [40,44,95].

Given the inter-pigment excitation hopping rates k_{nm} defined in Eq. 1.4, the total excitation dynamics in LHCII can be simulated by solving the system of Pauli Master equations

$$\frac{\mathrm{d}}{\mathrm{d}t} P_n(t) = \sum_{m \neq n} \left[k_{nm} P_m(t) - k_{mn} P_n(t) \right] - (k_\mathrm{f} + k_\mathrm{nr}) P_n(t), \tag{1.8}$$

where $P_n(t)$ is the time-dependent probability for the excitation to reside on the nth pigment, k_f is the fluorescence rate, and k_nr is the rate of non-radiative decay. Typical values of $k_\mathrm{f}^{-1} = 16\,\text{ns}$ and $k_\mathrm{nr}^{-1} = 5.3\,\text{ns}$ were chosen for chlorophylls yielding excitation mean lifetime of Chl S_1 state $\tau_{\text{Chl}} = (k_\text{f} + k_\text{nr})^{-1} \approx 4\,\text{ns}$ [5]. On the other hand, for the dipole-forbidden S_1 state of Cars one should choose $k_\text{f} = 0$ and very fast non-radiative relaxation of $k_\text{nr}^{-1} \approx 10\,\text{ps}$.

The model outlined above can be slightly transformed in order to account for the effect of exciton delocalization over several pigments. This can be easily done by performing block diagonalization of the Hamiltonian and thus introducing domains of strongly-coupled molecules (with a coupling greater than some threshold energy, J_cutoff) [40,76,96]. A range of various cutoff values (15–120 cm^{-1}) has been used in recent studies on pigment–protein complexes [40,76,78,96–98]. Obviously, since many inter-pigment electronic couplings are expected to be comparable to the electron–phonon couplings, no single threshold energy resulting in such a simple division of the molecules into domains can be considered precise. In fact, it can be shown that the total calculated excitation decay rate in LHCII is almost insensitive to whether Chl–Chl coherence effects are accounted or or not. Therefore, in order to be consistent with previous studies [42,44,76,96], in the following calculations the excitonic delocalization will be considered only between those molecules, for which the calculated incoherent excitation transfer occurs on a sub-ps timescale. Then, assuming instantaneous thermalization of the excitation within the same domain, the net inter-domain hopping rates are evaluated as follows [96]:

$$k_{\text{dom}\,a \leftarrow \text{dom}\,b} = \sum_{\substack{n \in \text{domain}\,a \\ m \in \text{domain}\,b}} k_{nm} \cdot W_m^{(\text{dom}\,b)}, \tag{1.9}$$

where $W_m^{(\text{dom}\,b)}$ is the Boltzmann factor describing the probability of the corresponding mth excitonic state within the domain b:

$$W_m^{(\text{dom}\,b)} = \frac{\mathrm{e}^{-E_m/(k_\text{B}T)}}{\sum_{j \in \text{domain}\,b} \mathrm{e}^{-E_j/(k_\text{B}T)}}.$$

This simplified domain model has been recently demonstrated to closely reproduce the full model combining Modified Redfield and Generalized Förster approaches [96].

1.3.3 Excitation energy transfer in LHCII monomer

Calculations of the incoherent excitation hopping rates between different pigments at room temperature, carried out according to Eq. 1.4 by using the Hamiltonian from Table 1.1, yielded sub-ps timescales for the excitation transfer between Chl*a*610 and Chl*a*611, between Chl*a*611 and Chl*a*612, and between Chl*a*613 and Chl*a*614. This observation is fully in line with our previous qualitative discussion about the strength of the inter-pigment interactions. Therefore the pair Chl*a*613–

Chl*a*614 and the triplet Chl*a*610–Chl*a*611–Chl*a*612 were considered to form two separate domains with instantaneous equilibration of the excitation within each of them, in consistency with earlier studies of various pigment contribution to the excitonic states [40, 44]. After making these adjustments to the model, total excitation dynamics in LHCII monomer was calculated. The resulting pairwise excitation transfer times between various pigments are shown in Table 1.2. Chl→Car transfer times, presented in this table, were calculated by assuming Car site energies ensuring the strongest overall excitation quenching (see below).

With regard to inter-chlorophyll excitation transfer, Table 1.2 reveals that it takes at most 6 ps for the excitation to be transmitted from Chl *b* pigment to the nearby Chl *a* molecule. The slowest transfer is exhibited from Chl*b*607 while for other Chl *b* pigments EET is even faster. The backward transfer, from Chl *a* to Chl *b*, is about an order of magnitude slower. Excitation energy transfer between the Chl *a* molecules is also rather fast, taking just several ps; the longest time (about 15 ps) is needed for excitation to escape from Chl*a*604, but that fact becomes clear if one takes into account its rather low S_1 energy (see Table 1.1) and distant location from other Chl *a* pigments (*cf.* Fig. 1.3),

In the absence of Chl→Car excitation transfer pathway, the total fluorescence kinetics in LHCII decays in a single-exponential way with a mean lifetime of 4 ns and fluorescence quantum yield being $\varphi_\mathrm{f} = k_\mathrm{f} / \left(k_\mathrm{f} + k_\mathrm{nr}\right) = 0.25$. However, inclusion of carotenoids significantly reduces both the fluorescence quantum yield and the mean excitation lifetime. This effect obviously depends on the energy of the S_1 transition of each xanthophyll.

As already mentioned in Section 1.1, the site energies of Cars are difficult to define as the dipole-forbidden nature of the Car S_1 state prevents its direct experimental measurements, although it is known that it exhibits some overlap with the spectral band of the Chl S_1 transition. For this reason S_1 energies of all 4 Cars were treated as (relatively) free parameters. In particular, the dependence of the Chl→Car excitation transfer rates on the Car site energies was investigated. This dependence for the most significant Chl-to-Car energy transfer pathways is demonstrated in Fig. 1.5. We see that the weak Chl–Neo623 and Chl–Vio622 couplings result in very slow energy transfer (about 180 and 270 ps, respectively). Conversely, Chl→Lut620 and Chl→Lut621 energy transfer times are by an order of magnitude faster, a result of their stronger interaction and closer association between these Cars and their neighboring Chls. The fastest energy transfer rate, $(23\,\mathrm{ps})^{-1}$, is between Chl*a*603 and Lut621. The calculated rate of incoherent energy transfer from Chl*a*612 to Lut620 was very similar to the one of Chl*a*603→Lut621 pathway; however, exciton delocalization over the terminal emitter Chl*a*610–Chl*a*611–Chl*a*612 notably reduces the net efficiency of this quenching channel. Due to the broad nature of the Car S_1 transition all these

Table 1.2 | Inter-pigment excitation transfer times (in ps) from the pigment labeling the column to the pigment labeling the row of the corresponding cell, calculated according to Eq. 1.4 by assuming Förster regime and two domains of strongly-coupled Chls. Excitation energy transfer rates from Chls to Cars were calculated by taking Car site energies from Table 1.3. Values longer than 1 ns are not shown.

Pigments	Chl*b*601	Chl*a*602	Chl*a*603	Chl*a*604	Chl*b*605	Chl*b*606	Chl*b*607	Chl*b*608	Chl*b*609	Chl*a*610–611–612	Chl*a*613–614	Lut620	Lut621	Vio622	Neo623
Chl*b*601	–	26.8	–	–	–	147	476	460	57.9	–	–	–	–	–	–
Chl*a*602	2.7	–	1.7	17.5	–	97.8	38.5	39.3	17.8	8.4	26.8	–	–	–	–
Chl*a*603	236	1.1	–	15.7	–	65.5	–	140	3.0	10.7	24.9	–	–	–	–
Chl*a*604	–	9.7	13.5	–	–	1.2	7.2	327	341	35.4	90.4	–	–	–	–
Chl*b*605	–	–	–	–	–	4.0	–	224	–	–	–	–	–	–	–
Chl*b*606	133	869	906	19.8	2.7	–	5.8	123	2.1	–	–	–	–	–	–
Chl*b*607	197	156	–	52.7	587	2.6	–	40.0	19.1	923	–	–	–	–	–
Chl*b*608	181	151	846	–	65.7	53.8	38.1	–	4.2	18.1	–	–	–	–	–
Chl*b*609	81.7	245	64.9	–	–	3.2	65.2	14.9	–	–	–	–	–	–	–
Chl*a*610–611–612	48.9	2.2	4.1	15.1	323	65.0	71.9	1.4	317	–	4.4	–	–	–	–
Chl*a*613–614	168	11.9	13.3	57.5	–	964	176	625	–	6.9	–	–	–	–	–
Lut620	–	–	–	–	–	–	–	–	–	61.5	498	–	–	–	–
Lut621	–	349	23.0	91.5	–	707	762	–	–	–	–	–	–	–	–
Vio622	–	–	–	–	–	–	–	–	–	–	255	–	–	–	–
Neo623	–	–	–	177	–	189	–	293	–	–	–	–	–	–	–

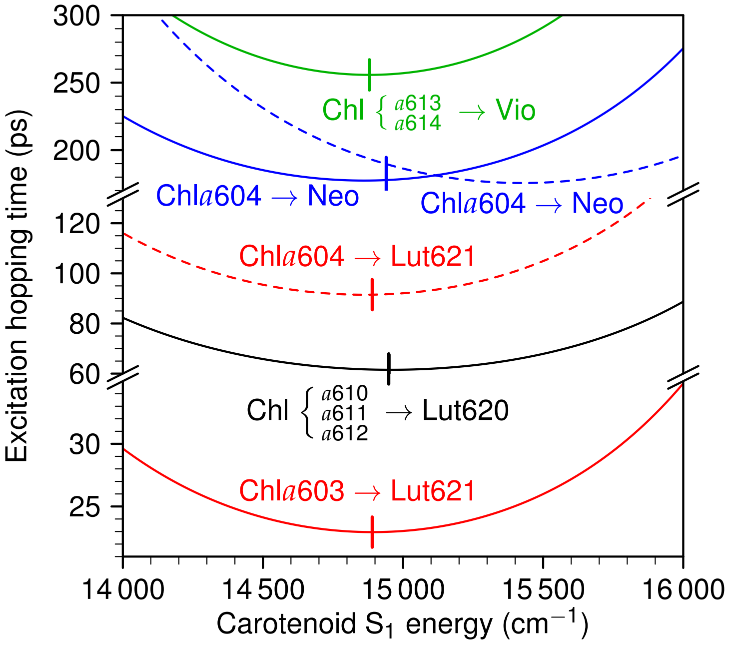

Figure 1.5 | Chl→Car excitation transfer times *vs.* Car S_1 energy level, obtained for different excitation pathways. Vertical bars indicate energy levels minimizing mean excitation lifetime (see also Table 1.3).

Table 1.3 | Energies of Car S_1 transitions ensuring fastest excitation relaxation in LHCII monomer and the resulting quantum yields (QY) of quenching by particular Car. The total IC and fluorescence quantum yield of all the Chls is 0.01.

Carotenoid	S_1 energy	QY
Lut620	14 950 cm^{-1}	0.37
Lut621	14 890 cm^{-1}	0.49
Vio	14 880 cm^{-1}	0.06
Neo	14 940 cm^{-1}	0.07

hopping times are rather insensitive to the variations in the Car site energy. For example, the Chl*a*603→Lut621 hopping time varies between ~23 and ~30 ps over a wide range of energies between 14 000 and 16 000 cm^{-1}. However, in all cases we see that there are two dominating channels for Chl→Car energy transfer, both incorporating lutein molecules.

The two Chl→Lut energy transfer pathways result in significant excitation quenching. To quantitatively evaluate the efficiency of each xanthophyll acting as a quencher, excitation dynamics in LHCII monomer was calculated by solving Eq. 1.8. The initial condition for this equation was chosen to represent a single exciton per LHCII, with equal probabilities to be localized over any of 14 chlorophylls. The strongest possible excitation energy quenching, resulting in mean excitation lifetime of $\tau = 65\,\mathrm{ps}$, was obtained with the S_1 energy levels of xanthophylls indicated with vertical bar in Fig. 1.5 and listed in Table 1.3. These energies differ from those determined from the two-photon absorption measurements of the corresponding Cars in solution. This is not surprising, since the protein scaffold is known to introduce notable shifts of energy levels of the pigments compared with their energies *in vacuo* or in solution. In the same Table 1.3, quantum yields of excitation quenching by the specific Car is also given, calculated as an amount of the initial excitation being "utilized" by this Car. In such conditions, the fluorescence QY has dropped about 60 times, from 25 % down to 0.4 %, compared to the unquenched state. Our model implies that quenching proceeds mainly via Chl→Lut energy transfer (total quenching efficiency of both Luts is 86 %), while the other Chl–Car channels do not contribute significantly to the overall excitation quenching. Finally, the contribution of different Chls to the total excitation decay kinetics is shown in Fig. 1.6, which again illustrates very fast (within several ps) excitation transfer from Chl *b* to Chl *a* pigments. After ~10 ps excitation totally equilibrates over the whole LHCII and then quickly decays with a lifetime of about 65 ps. This observation raises the idea of the so-called *coarse-grained* (CG) model that is usually used to describe excitation dynamics in larger photosynthetic antenna (LHCII aggregates or whole photosystems) [99–103]. In

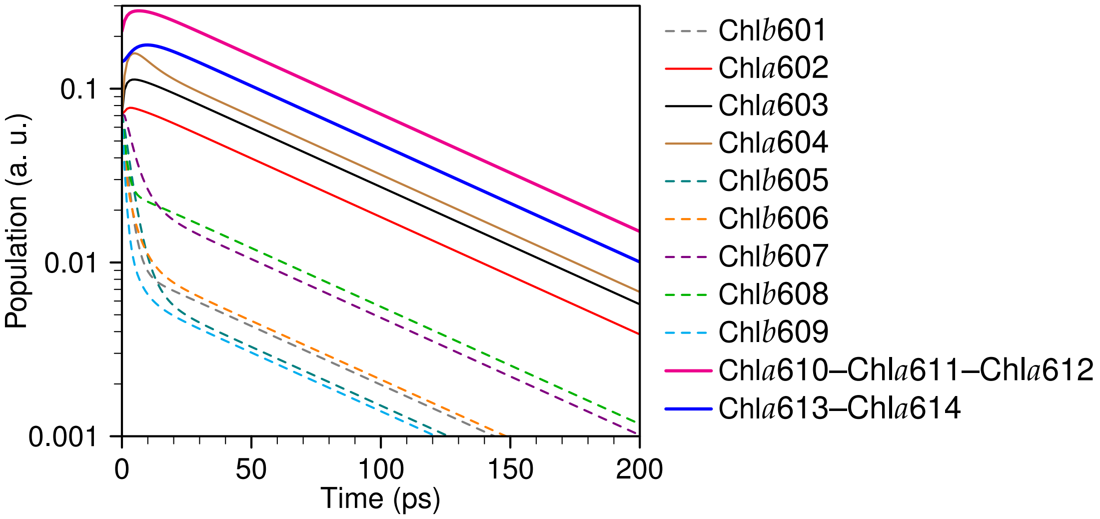

Figure 1.6 | Evolution of the excitation population of different Chl pigments, calculated by assuming the equal probabilities for the initial excitation. Solid and dashed lines correspond to Chls *a* and *b*, respectively, with inter-Chl couplings calculated by Müh *et al.* [40] and the Car site energies optimized for the best quenching (see Table 1.3). For comparison, excitation kinetics calculated from our-obtained inter-Chl couplings are indicated with dotted lines.

this model, excitation equilibration within the same antenna complex is assumed to happen infinitely fast compared with the mean rate of excitation "hopping" from one complex to another. We will face CG model once again in the following chapters and apply it to study excitation dynamics and quenching in LHCII aggregates.

At this point, several things regarding our obtained results should be noted. First of all, the overall (the fastest possible) quenching predicted by our model exceeds the actual quenching observed in LHCII crystals by an order of magnitude. Indeed, the crystallized LHCIIs had a very broad distribution of fluorescence lifetimes centered at ~800 ps compared to the ~4 ns lifetime of the solubilized (unquenched) trimers [19]. There are several possible sources of this discrepancy. Firstly, due to the absence of rigorous experimental scaling of the Car S_1 transition densities and the lack of a detailed description of the protein/solvent environment it is likely that the calculated Chl–Car couplings represent some over-estimates of the actual physical couplings. Secondly, the Car site energies were chosen to promote the strongest possible quenching rather than to match (relatively poorly defined) *in situ* experimental values. Therefore our model inherently provides a lower limit for excitation lifetime. Longer excitation lifetime may also naturally arise if only one monomer per LHCII trimer is in its quenched state. However, one important conclusion we can draw is that, even given the most favorable site energies and over-estimated couplings, Vio and Neo do not appear to contribute to the excitation quenching. This conclusion confirms an earlier proposal [20] that lutein and not violaxanthin or neoxanthin is responsible for fast excess excitation energy dissipation.

Another interesting result is the fact that, according to the presented model, both Lut620 and Lut621 contribute similarly to the energy dissipation. This contradicts the originally suggested NPQ mechanism [20] proposing that quenching proceeds via the Chl–Lut620 channel only. However, the structural symmetry of the two lutein domains means that one would expect (as was obtained in the presented model) very similar coupling profiles for the two molecules. Meanwhile, it was shown that these two lutein molecules have different conformations within LHCII and therefore might have different functions in the NPQ mechanism [89]. Due to the fact that the "dark" nature of the Car S_1 state is largely a product of the well-defined inversion and particle–hole symmetries of the molecule, non-planar distortions can be expected to have a strong effect on the Chl–Car couplings. To some extent, the differences in geometry were preserved during the quantum chemistry calculations by utilizing some geometry-constrained optimization, but this procedure itself is not as accurate as obtaining the *real* geometry by optimizing the pigments within their protein binding pockets. It is possible that a more "natural" treatment of these different non-planar distortions may predict some more pronounced variations in quenching abilities of both luteins.

Finally, the presented model demonstrates that simple accounting for Car molecules in LHCII crystals does add pathways that can result in strong fluorescence quenching, without the need for more non-trivial mechanisms such as the formation of charge transfer states [104] or Chl–Car excitonic interactions [105]. However, given that both of these features have been unambiguously observed experimentally, it is not possible (or even correct) to exclude these as playing some role in the quenching mechanism. Additionally, recent single-molecule studies have revealed that LHCII possesses multiple distinct quenching conformations and therefore several quenching pathways may co-exist [106].

1.4 Summarizing remarks

Natural photosynthesis has proven to be a perfect example of the self-sustaining molecular machine which, depending on situation, is able to perform totally different tasks that, nevertheless, help to achieve the maximal net efficiency. At ordinary light conditions, the spectroscopic properties of the light-harvesting pigments and their structural organization ensure an optimal absorption of the incoming solar radiation and subsequent excitation energy transfer to the reaction center. Meanwhile, at the saturating light intensities, the light-harvesting antenna exhibits a reversible switch into the photoprotecting mode during which excess energy is safely dissipated as heat and the formation of dangerous chemical species is avoided. This is achieved with the help of the same pigments participating in light harvesting—the carotenoid molecules.

The microscopic model of the excitation energy dynamics in the known LHCII crystal structure, presented in Section 1.3, has proven to correctly capture the dissipative nature of this configuration. The crystals from which the LHCII structure was obtained exhibit considerable fluorescence quenching relative to the (unknown) *in vivo* light-harvesting conformation [19]. This is a feature of the LHCII crystal structure that *chlorophyll-only* models have failed to capture. To address this issue, the first *all-pigment* microscopic model of the LHCII was formulated. This model, at least qualitatively, was able to explain the dissipative character of the known crystal structure and therefore to provide some insight into one of the possible NPQ mechanisms for *in vivo* LHCII. It was shown that two centrally-located lutein molecules interact with their closely-associated Chl neighbors in such a way as to yield slow but significant Chl-to-Car energy transfer followed by rapid relaxation of the lutein S_1 state. Additionally, this model can provide us some information about the conformational switch that forms/relaxes these quenching pathways: the dramatic differences between the Chl–Lut couplings and those of Vio and Neo imply that only modest changes in molecular associations can have a profound impact on the quenching ability of the Cars.

In the next chapters, excitation energy transfer and quenching in larger systems will be analyzed. Thorough analysis of various experimentally collected data will help to validate the ideas presented in this chapter regarding possible quenching mechanism(s) that governs photoprotection *in vivo*.

> “*Two souls, alas! reside within my breast,*
> *And each withdraws from, and repels, its brother...*
>
> JOHANN WOLFGANG VON GOETHE,
> “FAUST”

Chapter 2

Spectroscopic features of single light-harvesting complexes

Determination of the crystal structure of major light harvesting complexes [38] shed light on the structural organization of the pigment molecules and, accompanied with the theoretical structure-based calculations, contributed to the deeper understanding of the nature of extremely efficient excitation energy transfer. As described in the previous chapter, extension of these calculations by including optically dark S_1 state of the carotenoid molecules provided quantitative evidences that incoherent “hopping” of excitation energy from chlorophyll to the lutein molecule can be one of the most probable mechanisms of non-photochemical quenching. However, all these studies were not able to answer the most important question: how does the light-harvesting antenna switch into its photoprotective mode? Is such a transition of LHCII from a very efficient light-harvester into a very efficient excitation quencher controlled by some specific environmental force or by the intrinsic properties of LHCII itself? Conventional experimental measurements, collecting spectral or time-resolved information simultaneously from a huge number of the pigment–proteins, could not answer these questions either.

Some clue was provided when new experimental techniques allowed detecting properties of a single LHCII complex and visualizing how these properties evolve in time [106–109]. As a result, the effects like fluorescence blinking or spectral diffusion were observed. In this chapter, a short description of the experimental observations on a level of single LHCII complexes, particularly fluorescence intermittency under continuous illumination and bi-exponential fluorescence decay behavior, is provided. In order to quantitatively explain these effects and understand the underlying mechanisms, corresponding theoretical interpretation is suggested—the diffusion-controlled model that describes essential protein dynamics underlying blinking mechanism and the statistical model of single–triplet annihilation giving rise to the bi-exponential fluorescence kinetics[4].

---

[4] The modeling results presented in this chapter are based on the works published in [110–112].

2.1 Looking at single LHCII complexes

Already by the first experimental observations [113] single-molecule spectroscopy (SMS) has proven to be a valuable tool to inspect various subtle properties of the optical transitions of the individual molecules that are not obscured by the ensemble average. Indeed, traditional spectroscopic methods usually allow researchers to measure only some statistically averaged quantities, describing the whole system as a single unit. In this case the probability distribution of various quantities that describe the system, their dynamic and/or static variations caused by the heterogeneity of the system characteristics, such as fundamental interactions between distinct molecules and their proximate environment, remain undetermined. The ability to reveal such properties using SMS and therefore to obtain much more new information resulted in growing interest in possible applications of SMS techniques not only to simple fluorophores like dye molecules [114,115] or colloidal semiconductor quantum dots (QDs) [116], but also to much more complex biological systems such as green fluorescent proteins [117] or even pigment–protein light-harvesting complexes [106–109, 118–122]. SMS methods were also successfully applied in labeling experiments incorporating simple fluorophores being attached to complex macromolecules, thus providing valuable information about molecular interactions, reaction kinetics, conformational dynamics or molecular motion [123, 124].

SMS measurements revealed several unexpected properties of the individual molecule, such as spectral diffusion—the phenomenon when transition frequencies of a molecule change due to some variations of its local surroundings. Another intriguing effect discovered by SMS is the so-called fluorescence intermittency, or blinking. In virtually all fluorescing systems studied to date at the single-molecule level, the measured fluorescence intensity fluctuates rapidly and abruptly despite the continuous illumination [125, 126]. The sudden and uncorrelated fluctuations occur mostly between two well-defined strongly and non- or weakly emitting levels (the corresponding states are commonly referred to as *on*- and *off*-states, respectively) and usually serve as a simple signature of single emitters. In the early studies of fluorescence blinking of single molecules in molecular crystals [127] it was found out that the probability of various time intervals spent by the system in the *on*- and *off*-states (*on*- and *off*-times) to a large extent could be described by a single-exponential distribution, as predicted by the quantum jump theory of transitions between singlet and metastable triplet states [128]. Later, blinking behavior with much longer *off*-times that could not arise from intersystem crossing was also discovered [126]. In most cases *off*-times varied across almost all experimentally accessible time scales, typically spanning over 4 orders of magnitude or even from microseconds to several hours in the case of semiconducting QDs [129]. Moreover, almost in all these very diverse systems the dwell times t of both *on*- and *off*-states were not exponentially distributed: their probability densities $P(t)$ followed an inverse power law of the form $P(t) \propto t^{-m}$, with the exponent m typically lying between 1 and 2 [126]. Despite many studies in this field, the explanation for probably one of the most intriguing riddles of SMS—why do all these diverse systems of various complexity exhibit very similar blinking statistics leading to the absence of a typical time scale and even to weak ergodicity breaking [128]?—still remains unanswered.

In order to resolve (at least partially) this problem, several models describing fluorescence blinking in semiconducting QDs have been proposed so far. In these models the dark state of the QD is associated with the photoejection of an electron. According to the so-called trap models [125, 130, 131], the electron can tunnel through a barrier to a trap located nearby, and the dark period ends when the trapped electron hops back. Alternatively, power-law blinking statistics naturally arises if one considers a 1- or 2-dimensional random walk involving a first-passage time. As another alternative, a diffusion-controlled electron transfer model was suggested [132,133], where a light-induced 1-dimensional diffusion in energy phase space was considered. Additionally, some more models of power-law statistics have been proposed, but none of the existing theories can explain all the experimental observations of the phenomenon of blinking. Moreover, no or very limited theoretical background regarding fluorescence blinking in other—biological—systems exists.

Recently, new data on fluorescence intermittency in the LHCII complexes from green plants has been collected [108, 109]. By immobilizing the LHCII trimers from a dilute solution onto a polymer substrate and implementing a confocal microscopy, a raster-scanned image of the fluorescence intensity spatial distribution was constructed to identify separate fluorescing objects (see Fig. 2.1a). In this fluorescence map, each peak corresponds to a single fluorescing unit, generally an LHCII trimer. However, some dimmest peaks might arise either from an LHCII monomer or from the partially quenched fluorescence of the small LHCII aggregates that could be accidentally formed during the sample preparation procedures. Alternatively, the strongest peaks likely correspond to more than one separate LHCII trimer. As a result, the observed heterogeneity of the fluorescence intensity peaks provided possibility to exclude from the subsequent analysis the signals potentially coming not from a single LHCII trimer, thus reducing any possible statistical artifacts.

Surprisingly, SMS fluorescence measurements of single LHCII trimers with a very complex internal biomolecular structure revealed very similar blinking behavior, as in structurally much simpler fluorescent dyes or QDs [108, 109]. An example trace of the time evolution of fluorescence intensity, observed for a sin-

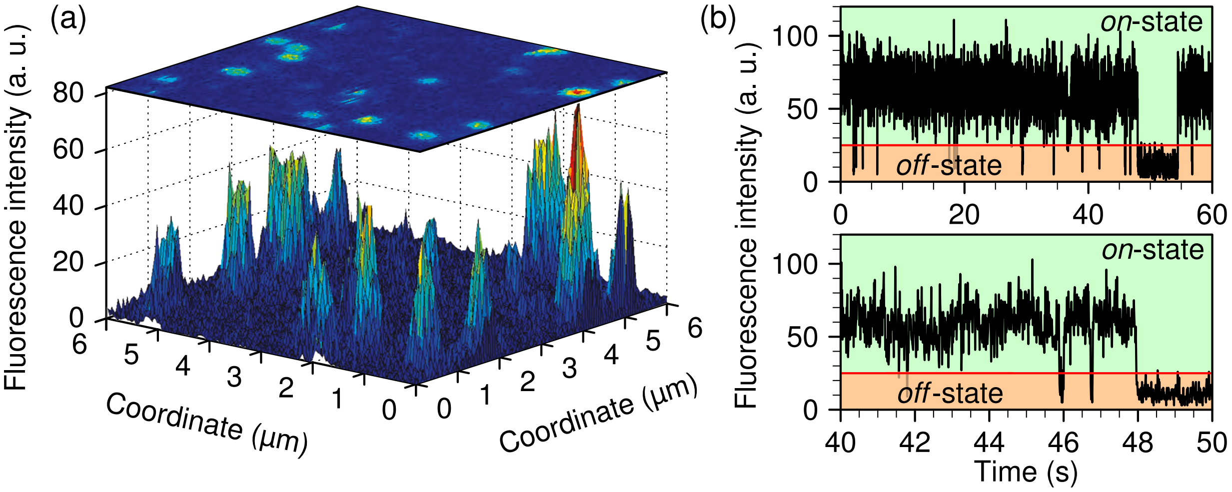

Figure 2.1 | (**a**) Raster-scanned image of fluorescence intensity distribution in a 6 µm × 6 µm sample region containing well-separated immobilized LHCII complexes [108]. Each spot represents a single fluorescing unit (or a small group of closely arranged fluorescing objects. (**b**) An example trace of the time evolution of the integral fluorescence intensity originating under continuous illumination from one of the spots depicted in panel (a). Rapid reversible transitions between the highly and weakly fluorescing states can be observed on different timescales (lower panel depicts an excerpt from the upper one). Red lines indicate threshold intensity separating these bright and dark states. Figure adapted with permission from [108]. © 2011 American Chemical Society.

gle LHCII trimer being under continuous illumination, is shown in Fig. 2.1b and clearly reveals the random rapid transitions between the strongly and weakly fluorescing states that are observed on various timescales. By introducing some threshold intensity value (indicated with red lines in Fig. 2.1b), two major states—the bright and dark ones—were determined. Statistical analysis of these states showed that, like in other systems mentioned above, the dwell times of both *on*- and *off*-states were distributed according to a power law statistics (*cf.* symbols in Fig. 2.4a–b) and strongly depended on various environmental conditions, such as acidity level or illumination intensity [109, 122]. Taking into account the important physiological functions of LHCII complexes—very efficient light harvesting and excitation energy transfer as well as regulation via non-photochemical quenching—it is therefore very unlikely that this functional significance and fluorescence properties of LHCIIs can be unrelated. Since the models describing fluorescence intermittency in QDs cannot be directly applied to these biological complexes, the physical mechanisms underlying power-law blinking of single LHCII still remained unclear. To solve this issue, a conceptual model based on the dynamic self-organization of the intrinsic structure of LHCII is introduced in the following section.

2.2 How photosynthetic proteins switch

2.2.1 Model formulation

In order to describe fluorescence intermittency in LHCII complexes, we assume that as a consequence of the precise protein structural arrangement and dynamics, the LHCII trimer can be found in two equilibrium states: either in a bright (*on*) state, in which the fluorescence signal from the irradiated LHCII trimer is clearly detected, or in a dark (*off*) state, in which fluorescence is strongly quenched. The switching between these two states is probably related to a subtle conformational change of the protein which disturbs the energy balance between different pigments. Based on the results demonstrated in the previous chapter, variability of the distance between one (or both) of the lutein molecules and the nearby chlorophylls a can be considered as the dominant modulation factor of this energy balance. Another possible effect could be the adjustment of the energies of the dark S_1 state of Luts [71, 105], resulting in their values approaching the optimal ones, listed in Table 1.3 and ensuring the fastest Chl→Lut excitation energy transfer. Of course, other mechanisms proposed to govern NPQ [12] can also be reversibly activated and deactivated. In any case, the self-regulating process of the formation of centers responsible for excitation energy quenching would shorten (or prolong) the mean excitation lifetime of Chl molecules, and, consequently, the intensity of the measured fluorescence would vary in time.

To summarize, when LHCII is in the *on*-state, its structural and/or energetic configuration is unfavorable for excitation quenching to occur. Due to fast intramolecular dynamics of the Chls and their interactions with the protein vibrations the total energy of this state fluctuates rapidly in the vicinity of the minimum of the potential well of the *on*-state. Let us denote the generalized coordinate which describes the manifold of all these fast vibrations as X. As a result of a "slow" deformation of the protein (let us introduce another generalized slowly varying coordinate Y representing the slow structural change of the protein), the protein configuration in the vicinity of some Chl molecules changes, resulting in a formation of the intrinsic quencher and, therefore, the decrease of the mean fluorescence intensity. Thus the system undergoes a transition into the *off*-state, corresponding to another potential well in the phase space of the coordinates X and Y. Since the LHCII trimer can be in only one state at the same time, the random-walk in phase space will lead to a random and rapid switching between the *on*- and *off*-states, which will qualitatively resemble the experimentally obtained effect of fluorescence intermittency (a somewhat similar concept was employed to describe the fluorescence blinking in semiconducting QDs [133] and structural regulation in biological macromolecules [134, 135]).

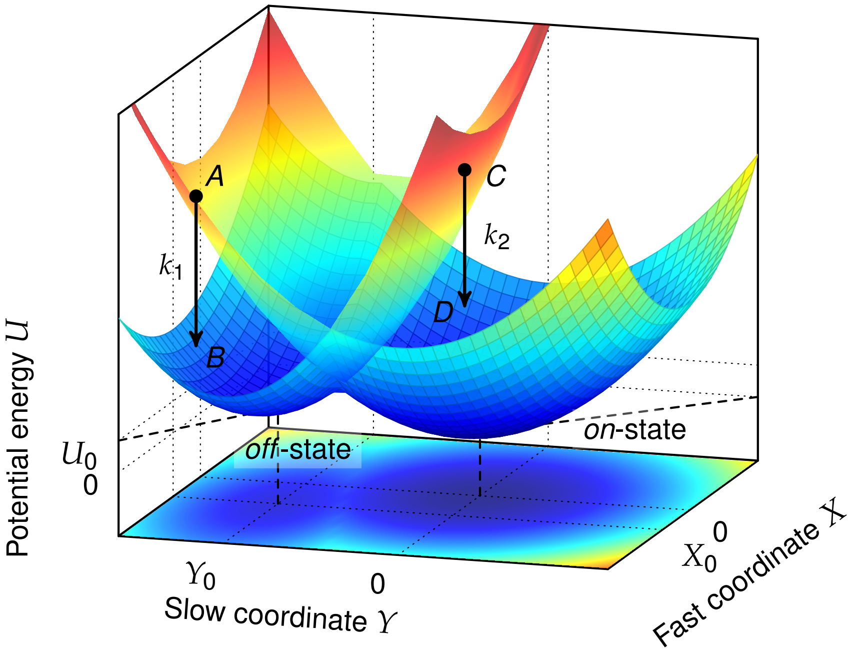

Figure 2.2 | Potential energy surfaces of the *on*- and *off*-states in the phase space of the X and Y coordinates. Arrows, denoted as k_1 and k_2, represent the downward relaxation rates of the *on* → *off* and *off* → *on* transitions, respectively.

In the simplest harmonic approximation the potentials of light and dark states can be written as

$$U_1\left(X,Y\right) = \tfrac{1}{2}\lambda_1 X^2 + \tfrac{1}{2}\gamma_1 Y^2,$$
$$U_2\left(X,Y\right) = \tfrac{1}{2}\lambda_2\left(X - X_0\right)^2 + \tfrac{1}{2}\gamma_2\left(Y - Y_0\right)^2 + U_0,$$

where indices "1" and "2" denote the *on*- and *off*-states, respectively; X and Y are the generalized coordinates responsible for the fast intramolecular vibrations of the Chls and slow structural conformations of the protein, respectively; λ_i and γ_i describe reorganization energies in the ith potential along the corresponding coordinate; X_0 and Y_0 determine the equilibrium position of the second potential surface; and U_0 is the vertical shift between the potential minima. The schematic relative position of these potentials is presented in Fig. 2.2. If $Y \approx 0$, a common set of parameters will yield $U_1\left(0,0\right) < U_2\left(X_0,0\right)$, so that the system will more probably be in the *on*-state. The vanishing probability of the excitation quenching in this scheme corresponds to the activated transition from the phase space point $\left(X,Y\right) \approx \left(0,0\right)$ with the energy $U_1\left(0,0\right)$ on the *on*-state potential to the same point with the energy $U_2\left(0,0\right) \gg U_1\left(0,0\right)$ on the potential of the *off*-state. After such a transition only the coordinate X changes rapidly (variations of Y occur on a much longer time scale), thus the system, keeping the Y coordinate at fixed position $Y = 0$, quickly "diffuses" to the potential minimum $U_2\left(X_0,0\right)$. From here the system will rapidly "fall" back to the *on*-state potential with the energy $U_1(X_0, 0) \ll U_2(X_0, 0)$ and finally "diffuse" to the initial phase space point with the energy $U_1(0, 0)$, that will lead to the recovery of the fluorescence intensity.

Due to some specific, environmentally induced conformational change of the protein the Y value can increase, and in the vicinity of the $Y \approx Y_0$ configuration we will get $U_1(0, Y_0) > U_2(X_0, Y_0)$. As a result, the system will switch to the *off*-state and therefore the fluorescence signal from the LHCII trimer will be quenched. Similarly to the case discussed above, there exists a very small probability that due to some reason the excitation energy quenching will terminate, which is represented by the activated transition $U_2(X_0, Y_0) \to U_1(X_0, Y_0)$ followed by the rapid diffusion along the X coordinate to $U_1(0, Y_0)$. However, at that point there is a very high probability for the system to relax to the lower energy $U_2(0, Y_0)$ and "diffuse" back to the potential minimum $U_2(X_0, Y_0)$.

For the sake of simplicity we can also assume that transitions between the *on*- and *off*-states occur strictly vertically, *i.e.* during the transition the coordinates X and Y do not change. These transitions are shown with arrows in Fig. 2.2. In addition, let us also assume that the rate of relaxation (downward transition) from the phase space point A on the *on*-state potential to the phase space point B with the same coordinates on the *off*-state potential is equal to k_1 and does not depend on the position of the points A and B. Similarly, the rate of downward transition $C \to D$ from the *off*- to the *on*-state is denoted as k_2. The rates of the upward transitions are renormalized by taking into account the corresponding Boltzmann factor $\exp\left(-|\Delta U| / (k_\mathrm{B}T)\right)$, which introduces the dependency on the coordinates of the points A and B as well as C and D. To summarize, the rates of the downward and upward transitions are assumed to be given as follows:

$$\begin{cases} A \to B: & k_1, \\ C \to D: & k_2, \end{cases} \quad \text{and} \quad \begin{cases} B \to A: & k_1 \exp\left(-\frac{U_1(X_A,Y_A)-U_2(X_B,Y_B)}{k_\mathrm{B}T}\right), \\ D \to C: & k_2 \exp\left(-\frac{U_2(X_C,Y_C)-U_1(X_D,Y_D)}{k_\mathrm{B}T}\right), \end{cases} \tag{2.1}$$

where k_B is Boltzmann constant and T is the absolute temperature.

From the energy gap law [136], which describes non-radiative transitions between different energy levels by taking into account the interactions with the environmental phonons, it follows that in order to calculate the real (effective) transition rates, the ones defined in Eq. 2.1 should be multiplied by the factor $\exp\left(-\alpha |\Delta U| / (\hbar\omega_0)\right)$, where ω_0 is the dominating frequency of the phonons taking part in the transitions between the *on*- and *off*-states, and α is some function, weakly (logarithmically) depending on the potential energy difference $|\Delta U|$, so that it can be treated as some constant parameter ($\alpha \cong 1$–3) [136]. This exponential factor ensures that both upward and downward transitions occur mainly in the vicinity of the line $\left(X^{(\mathrm{s})}, Y^{(\mathrm{s})}\right)$, which corresponds to the intersection of the two potentials: $U_1\left(X^{(\mathrm{s})}, Y^{(\mathrm{s})}\right) = U_2\left(X^{(\mathrm{s})}, Y^{(\mathrm{s})}\right)$. Upon moving away from this line the potential energy difference $|\Delta U|$ increases rapidly, so that the number of phonons taking part in the transition also rises, resulting in exponentially decreasing transition probability.

In order to reduce the number of unknown parameters and to simplify the set of equations, let us scale the potential energy in thermal units and thus introduce dimensionless potentials $V_i\left(X, Y\right) = U_i\left(X, Y\right) / \left(k_\mathrm{B}T\right)$ as well as dimensionless coordinates

$$x = \sqrt{\tfrac{k_\mathrm{B}T}{\lambda_1}}X, \quad x_0 = \sqrt{\tfrac{k_\mathrm{B}T}{\lambda_1}}X_0, \qquad y = \sqrt{\tfrac{k_\mathrm{B}T}{\gamma_1}}Y, \quad y_0 = \sqrt{\tfrac{k_\mathrm{B}T}{\gamma_1}}Y_0.$$

Now, by denoting $\lambda_1/\lambda_2 = \lambda$, $\gamma_2/\gamma_1 = \gamma$, and $U_0/\left(k_\mathrm{B}T\right) = V_0$ we obtain the simplified expressions for the potential wells:

$$V_1\left(x, y\right) = \tfrac{1}{2}x^2 + \tfrac{1}{2}y^2, \tag{2.2}$$

$$V_2\left(x, y\right) = \tfrac{1}{2}\lambda\left(x - x_0\right)^2 + \tfrac{1}{2}\gamma\left(y - y_0\right)^2 + V_0. \tag{2.3}$$

The time-dependent probability density $\rho_i\left(x, y, t\right)$ for finding values x and y at time t, when the system is either in the *on*- or in the *off*-state, obey slightly modified Smoluchowski diffusion equations in the potential field [133,137]:

$$\begin{aligned}\frac{\partial}{\partial t}\rho_1\left(x, y, t\right) &= \left(D_x\mathcal{L}_x + D_y\mathcal{L}_y\right)\rho_1\left(x, y, t\right) + \exp\left(-\alpha\frac{|\Delta U|}{\hbar\omega_0}\right)\\ &\times\begin{cases} k_2\rho_2\left(x, y, t\right) - k_1\mathrm{e}^{V_1(x,y) - V_2(x,y)}\rho_1\left(x, y, t\right), & V_1\left(x, y\right) \leq V_2\left(x, y\right),\\ k_2\mathrm{e}^{V_2(x,y) - V_1(x,y)}\rho_2\left(x, y, t\right) - k_1\rho_1\left(x, y, t\right), & V_1\left(x, y\right) > V_2\left(x, y\right),\end{cases}\end{aligned} \tag{2.4}$$

$$\begin{aligned}\frac{\partial}{\partial t}\rho_2\left(x, y, t\right) &= \left(D_x\mathcal{L}_x + D_y\mathcal{L}_y\right)\rho_2\left(x, y, t\right) + \exp\left(-\alpha\frac{|\Delta U|}{\hbar\omega_0}\right)\\ &\times\begin{cases} k_1\mathrm{e}^{V_1(x,y) - V_2(x,y)}\rho_1\left(x, y, t\right) - k_2\rho_2\left(x, y, t\right), & V_1\left(x, y\right) \leq V_2\left(x, y\right),\\ k_1\rho_1\left(x, y, t\right) - k_2\mathrm{e}^{V_2(x,y) - V_1(x,y)}\rho_2\left(x, y, t\right), & V_1\left(x, y\right) > V_2\left(x, y\right),\end{cases}\end{aligned} \tag{2.5}$$

where D_x and D_y are the diffusion coefficients along x and y directions, respectively, while $\mathcal{L}_x$ and $\mathcal{L}_y$ are the corresponding diffusion operators:

$$\mathcal{L}_z\rho_i(x, y, t) = \left[\frac{\partial^2}{\partial z^2} + \frac{1}{k_\mathrm{B}T}\frac{\partial}{\partial z}\frac{\partial U_i(x, y)}{\partial z}\right]\rho_i(x, y, t), \qquad i = 1, 2; \quad z = x, y. \tag{2.6}$$

The coupled diffusion-controlled rate equations 2.4 and 2.5 describe the *unconditional* evolution of the probability density of the *on*- and *off*-states after some initial population. However, during the experiment the exact dwell times of bright and dark states are measured. Therefore to obtain the blinking statistics for an *on* (or *off*) event, we need to calculate the *conditional* probability density $P_1(t)$ (or $P_2(t)$) for the system to remain in the *on*- (or *off*-) state during the whole period t. These conditional probability densities can be obtained if we de-couple Eqs. 2.4 and 2.5 by setting the population of the *off*-state in Eq. 2.4 and the population of the *on*-state in Eq. 2.5 to zero during the whole observation time interval t:

$$\begin{aligned}
\frac{\partial}{\partial t}\rho_1(x,y,t) &= \left(D_x\mathcal{L}_x + D_y\mathcal{L}_y\right)\rho_1(x,y,t) - k_1\mathrm{e}^{-|\Delta V|/\Omega}\rho_1(x,y,t) \\
&\qquad\qquad \times \begin{cases} \mathrm{e}^{V_1(x,y)-V_2(x,y)}, & V_1(x,y) \le V_2(x,y), \\ 1, & V_1(x,y) > V_2(x,y) \end{cases} \\
&\equiv \left(D_x\mathcal{L}_x + D_y\mathcal{L}_y - k_1H_1(x,y)\right)\rho_1(x,y,t); \qquad (2.7) \\
\frac{\partial}{\partial t}\rho_2(x,y,t) &= \left(D_x\mathcal{L}_x + D_y\mathcal{L}_y\right)\rho_2(x,y,t) - k_2\mathrm{e}^{-|\Delta V|/\Omega}\rho_2(x,y,t) \\
&\qquad\qquad \times \begin{cases} 1, & V_1(x,y) \le V_2(x,y), \\ \mathrm{e}^{V_2(x,y)-V_1(x,y)}, & V_1(x,y) > V_2(x,y) \end{cases} \\
&\equiv \left(D_x\mathcal{L}_x + D_y\mathcal{L}_y - k_2H_2(x,y)\right)\rho_2(x,y,t), \qquad (2.8)
\end{aligned}$$

where we denoted $\Omega = \hbar\omega_0/(\alpha k_\mathrm{B}T)$ and introduced the new functions

$$\begin{aligned}
H_1(x,y) &= \mathrm{e}^{-|\Delta V|/\Omega}\cdot\min\left\{1,\mathrm{e}^{V_1-V_2}\right\}, \\
H_2(x,y) &= \mathrm{e}^{-|\Delta V|/\Omega}\cdot\min\left\{1,\mathrm{e}^{V_2-V_1}\right\}.
\end{aligned} \qquad (2.9)$$

Equations 2.7 and 2.8 can be further simplified by taking into account the different timescales for the diffusion along the coordinates x and y. Indeed, by assuming that $D_x \gg D_y$ (in our formulation, the former describes fast intramolecular vibrations whereas the latter—slow protein conformations) and denoting

$$\eta = D_x/D_y \gg 1, \qquad \tau = D_yt, \qquad K_i = k_i/D_y,$$

one can rewrite Eq. 2.7 as

$$\frac{\partial}{\partial\tau}\rho_1(x,y,\tau) = \left(\eta\mathcal{L}_x + \mathcal{L}_y - K_1H_1(x,y)\right)\rho_1(x,y,\tau). \qquad (2.10)$$

Since $\eta \gg 1$, the dependence of ρ_1 on x can be evaluated in terms of adiabatic approximation. In the zero-order approximation, the motion along the y coordinate can be considered completely frozen, so, by taking into account the definition of $\mathcal{L}_x$ (see Eq. 2.6) and potential $V_1(x,y)$ (Eq. 2.2), the last equation 2.10

is reduced:

$$\frac{\partial}{\partial \tau}\rho_1(x,y,\tau) \simeq \eta \mathcal{L}_x \rho_1(x,y,\tau) = \eta \frac{\partial}{\partial x}\left(x + \frac{\partial}{\partial x}\right)\rho_1(x,y,\tau). \tag{2.11}$$

Due to large η the solution of this equation very quickly converges to a stationary (Gaussian) distribution along the x coordinate, so that we can approximate it as

$$\rho_1(x,y,\tau) \simeq \frac{1}{\sqrt{2\pi}}\mathrm{e}^{-\frac{1}{2}x^2}\bar{\rho}_1(y,\tau),$$

where $\bar{\rho}_1(y,\tau)$ satisfies the equation

$$\frac{\partial \bar{\rho}_1(y,\tau)}{\partial \tau} \equiv \frac{\partial}{\partial \tau}\int \mathrm{d}x\, \rho_1(x,y,\tau) = \left(\mathcal{L}_y - \kappa_1(y)\right)\bar{\rho}_i(y,\tau). \tag{2.12}$$

Similarly, for the *off*-state we obtain

$$\frac{\partial \bar{\rho}_2(y,\tau)}{\partial \tau} \equiv \frac{\partial}{\partial \tau}\int \mathrm{d}x\, \rho_2(x,y,\tau) = \left(\mathcal{L}_y - \kappa_2(y)\right)\bar{\rho}_2(y,\tau). \tag{2.13}$$

Here, the new functions $\kappa_1(y)$ and $\kappa_2(y)$ were introduced:

$$\kappa_1(y) = K_1\frac{1}{\sqrt{2\pi}}\int \mathrm{d}x\, \mathrm{e}^{-\frac{1}{2}x^2}H_1(x,y), \tag{2.14}$$

$$\kappa_2(y) = K_2\sqrt{\frac{\lambda}{2\pi}}\int \mathrm{d}x\, \mathrm{e}^{-\frac{1}{2}\lambda(x-x_0)^2}H_2(x,y). \tag{2.15}$$

The initial conditions needed to solve Eqs. 2.12 and 2.13 should be chosen as follows. First we define the stationary solution of Eq. 2.12, $\bar{\rho}_1^{(\mathrm{st})}(y)$, when transition to the *off*-state is inactive. Then we multiply this steady-state (Gaussian) distribution by the effective rate $\kappa_1(y)$ given in Eq. 2.14. The obtained function determines the initial distribution of the population of the *off*-state: $\bar{\rho}_2(y,\tau=0) \propto \bar{\rho}_1^{(\mathrm{st})}(y)\cdot\kappa_1(y)$. Similarly, the initial probability density for the population of the *on*-state is given by the product $\bar{\rho}_2^{(\mathrm{st})}(y)\cdot\kappa_2(y)$. Interestingly, after substituting expressions for $H_i(x,y)$ (see Eq. 2.9) and normalizing, both initial distributions coincide:

$$\bar{\rho}_i(y,\tau=0) \propto \int \mathrm{d}x\, \mathrm{e}^{-|\Delta V|/\Omega}\cdot\min\left\{\mathrm{e}^{-V_1(x,y)}, \mathrm{e}^{-V_2(x,y)}\right\}. \tag{2.16}$$

A more detailed numerical analysis reveals that Eq. 2.16 defines a very sharp distribution with the maximum located at the intersection point $y^{(0)}$ of the one-dimensional functions $V_1(x=0,y)$ and $V_2(x=x_0,y)$ (see Fig. 2.3).

After Eqs. 2.12 and 2.13 have been solved numerically, the survival probabil-

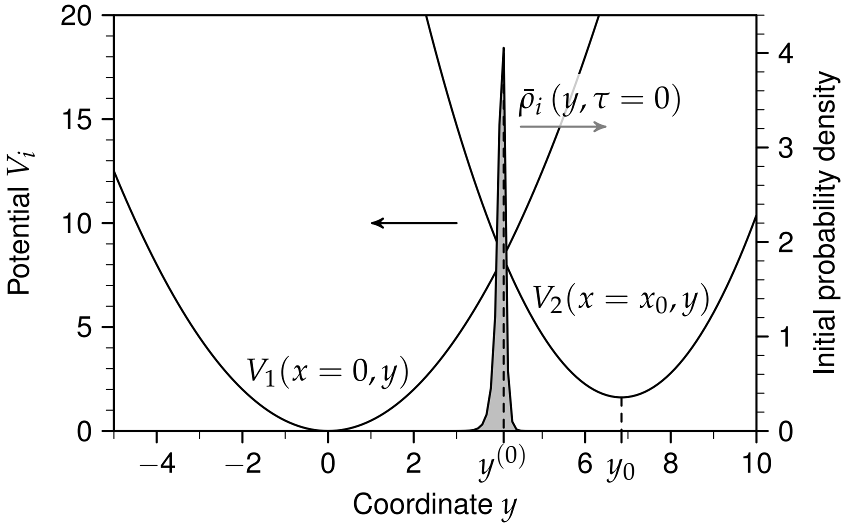

Figure 2.3 | Potential energies V_i (left axis) and initial probability density $\bar{\rho}_i\,(y,\tau=0)$ (right axis), calculated according to Eq. 2.16 using the parameters obtained by fitting the experimental data collected at pH 8 (see Figs. 2.4 and 2.5).

ities of the *on*- and *off*-states, $S_i\,(\tau)$, which define the probability that after the transition the system is still in the same *on*- or *off*-state during the whole observation period τ, can be found by integrating $\bar{\rho}_i\,(y,\tau)$ over y:

$$S_i(\tau) = \int \mathrm{d}y\, \bar{\rho}_i(y,\tau).$$

Finally, the density of this survival probability, which corresponds to the experimentally gathered blinking statistics and determines the probability $P_i(\tau)$ that a transition from one state to another occurs within the time interval $(\tau;\tau+\mathrm{d}\tau)$, is defined as

$$P_i(\tau) = -\frac{\mathrm{d}S_i(\tau)}{\mathrm{d}\tau}, \qquad i = 1,2.$$

These quantities can be fitted to the distributions of blinking events, obtained by analyzing the fluorescence time traces, similar to the ones shown in Fig. 2.1.

2.2.2 Calculated blinking statistics and properties of the *on*- and *off*-states

As follows from the model description, after the introduction of the dimensionless variables only 8 undefined parameters are left: 5 of them describe the potential surfaces (λ, γ, x_0, y_0, and V_0) while the other 3 determine the transitions between the *on*- and *off*-states (k_1, k_2, and Ω). All these parameters were varied by fitting the experimental data of the pH-dependent blinking statistics [109]. Since the diffusion coefficient D_y only determines the time scale of the protein conformation dynamics, it does not change the shape of the $P_i\,(t)$ distributions on a logarithmic scale, but just shifts these distributions along the time and probability density axes:

$$\lg P_i\left(\lg t\right) = \lg\left(-\tfrac{\mathrm{d}}{\mathrm{d}t}S_i\left(\lg t\right)\right) = \lg P_i\left(\lg \tau - \lg D_y\right) + \lg D_y.$$

Thus, after calculating the blinking statistics with a particular set of the 8 mentioned parameters, the obtained curves were additionally shifted along both logarithmic axes to match the experimental distributions, and from the magnitude of this shift the diffusion coefficient was determined. The obtained fitting results for the data collected under different acidity conditions of the environment (which mimics various trans-membrane ΔpH values of the intact thylakoids) are shown in Fig. 2.4a–b, and the corresponding fitting parameters are presented in Fig. 2.5. The value of pH 8 represents natural physiological conditions corresponding to the state of strong fluorescence of the isolated trimers, while the lower pH values reflect NPQ conditions. Finally, the survival probabilities of both states, $S_i\left(t\right)$, are depicted in Fig. 2.4c. We see that at first they rapidly decrease (the survival probability in the *off*-state decreases much faster than that in the *on*-state), but after several seconds they approach an almost constant value.

Potential energy surfaces. By analyzing the parameters describing the potential surfaces of the bright and dark states, one can note that the slopes of these surfaces along the x coordinate differ several times, and this difference becomes less pronounced as the environmental acidity increases (see blue line in Fig. 2.5a representing the ratio of these slopes, λ). On the other hand, the ratio of the slopes of the potential surfaces along the slow y coordinate, γ, in the near-neutral environment (around pH 6–8) is almost insensitive to the pH variations and approximately equals 1.3 (red line in Fig. 2.5a). A very weak pH-dependence in that region is also obtained for y_0, which describes the position of the minimum of the potential energy of the dark state (see red line in Fig. 2.5b). These results lead to the assumption that the generalized coordinate y, describing slow conformational changes of the protein, should be related to the distance between some particular pigments. Indeed, protonation of some specific protein residues does not directly influence the interaction between the pigments, which mostly depends on their relative arrangement. In such a case neither the γ parameter, which describes the reorganization energy relating to the change of the inter-molecular distances, nor y_0, defining the inter-pigment arrangement that corresponds to the most effective excitation energy quenching, should exhibit any notable sensitivity to the acidity of the environment. On the other hand, when the environmental acidity increases further, approaching pH 5.5, both γ and y_0 change noticeably, which can be a manifestation of some kind of phase transition. The almost 2-fold increase of λ at this pH just confirms this conclusion. The pH-dependencies of x_0 and V_0 are slightly non-monotonic (see blue and black lines in Fig. 2.5b), which is probably

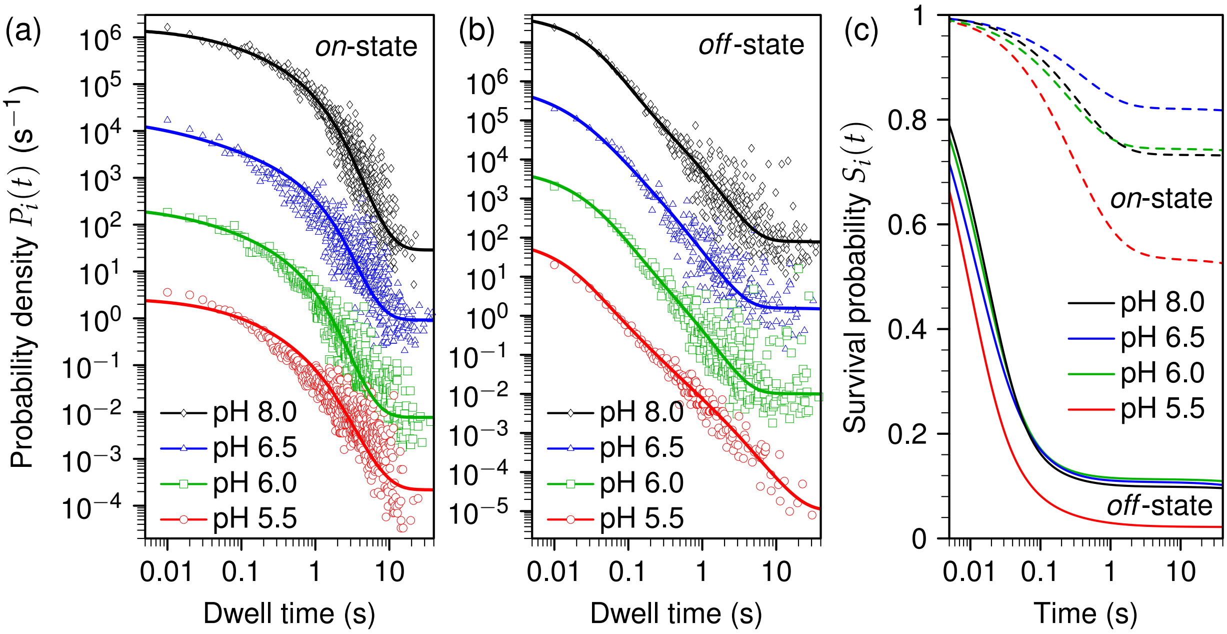

Figure 2.4 | (a–b) Experimental (symbols) [109] and simulated (lines) probability densities $P_i(t)$ of the dwell times t in bright (a) and dark (b) states for 4 different acidity levels of the environment. For visual clarity, each data set (except that corresponding to pH 5.5) is offset upwards by a factor of 100. (**c**) Survival probabilities of the *on*-states (dashed lines) and *off*-states (solid lines), $S_i(t)$.

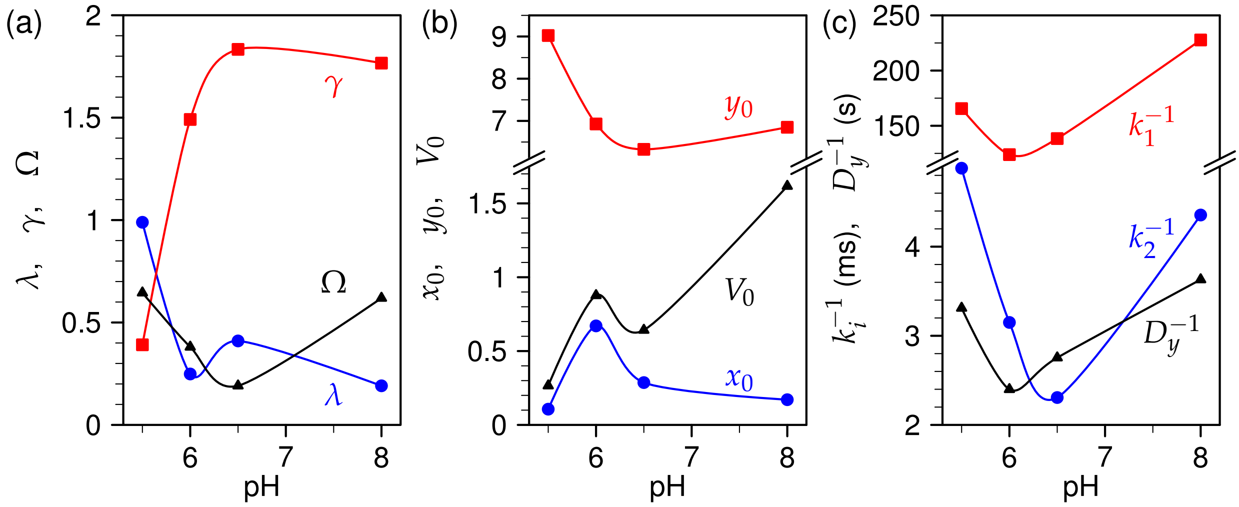

Figure 2.5 | Fitted model parameters that correspond to the fitted probability densities of the dwell times, shown in Fig. 2.4.

due to some uncertainties in the obtained values. However, we see that generally in the more acid environment the energy difference between both minima of potential energy decreases more than 3 times when compared with the physiological conditions. Obviously that corresponds to the increased probability for the system to switch to the non-fluorescing dark state.

Diffusion and transitions between the states. The remaining model parameters determine the transitions between the *on*- and *off*-states. From the pH-dependence of Ω we first notice that the energy $\hbar\omega_0$ of the dominating phonon mode participating in the transitions is of the order of $k_B T$ and is almost insensitive to the pH level. This relatively high value of Ω can also explain the mentioned steadying of the survival probabilities of the *on*- and *off*-states. Indeed, while modeling the diffusion in the potential wells, the initial probability distribution position $\bar{\rho}_i(y, t = 0)$ was chosen near the intersection point $y^{(0)}$ of the *on*- and *off*-potentials (*cf.* Fig. 2.3). As a result, the exponential factor in Eqs. 2.7 and 2.8 is $\exp\left(-\left|\Delta V\right|/\Omega\right) \approx 1$, so that the initial transition probability is rather high. That is reflected in the fast drop of the survival probabilities to reside in each state (*cf.* Fig. 2.4c). During the following time periods the distribution is not only broadening along the y coordinate, but also the position of its maximum is shifting toward the minimum of the corresponding potential. Since the distance $y_0 \approx 7$ is rather big, after some time $\bar{\rho}_i(y, t)$ diffuses far away from $y^{(0)}$, and wherever $\bar{\rho}_i(y, t)$ differs from zero, the factor $\exp\left(-\left|\Delta V\right|/\Omega\right) \to 0$. As a result, the transition probability drops almost to 0 and the corresponding survival probability approaches its steady-state regime. On the other hand, due to diffusion $\bar{\rho}_i(y, t)$ is still expanding, and when the far wing of the probability density reaches $y^{(0)}$, the transition probability will rise again, leading to a further decrease of the population of both *on*- and *off*-states. With the current diffusion rates this effect would only become apparent after several tens of minutes, so due to photobleaching it was not possible to reveal it during SMS experiments.

As shown in Fig. 2.5c, the rates of transitions from the *on*- and *off*-states differ significantly. The rate of the *on*→*off* transition quickly increases upon lowering the pH level while the rate of the backward transition remains virtually the same, so that the ratio varies from 30 at lower pH values to 60 at higher ones. Such a high ratio of the transition rates in opposite directions obtained for the whole studied pH range reveals why the population of the *off*-states, $S_2(t)$, decreases in time much faster than that of the *on*-states ($S_1(t)$, see Fig. 2.4c). After the transition to the dark state the system generally lives there only for a very short time, so that the measured fluorescence intermittency resembles very short blinking rather than short flashes. At first glance, the higher rate of the *on*→*off* transitions in the more acidic environment would indicate an increased number of short-lived *on*-states. However, the ~1.4-fold increase of the diffusion coefficient (in pH 6–6.5 region) determines faster diffusion of the $\bar{\rho}_i(y, t)$ towards the corresponding potential minimum, so that the overall effect is the experimentally observed stabilization of long-lived bright states. This fact is also supported by the slightly higher value of the steady-state survival probability of the *on*-state (Fig. 2.4c).

On the other hand, in very acidic surroundings (pH 5.5) the rate of diffusion again decreases very notably, giving another confirmation to the mentioned phase transition occurring in such environment conditions. Qualitatively, the trends of the pH-dependence of the diffusion coefficient could be explained in the following way. In the near-neutral environment (around pH 7) the decrease of pH results in the protonation of those protein residues which are most intimately related to the transitions between the *on*- and *off*-states, and therefore electrostatic repulsion might increase the rate of those specific deformations responsible for such transitions. However, in a much more acidic environment the protein becomes almost homogeneously protonated, which mitigates the mentioned effect; moreover, the increased protein mass also slows down its deformations, so that finally the diffusion coefficient is reduced. The absolute value of the inverse diffusion coefficient (several seconds) determines the timescale of the conformational dynamics of the protein scaffold. The time needed for the system to completely switch from one conformational state to another (the diffusion time) can be evaluated as $T = y_0^2 / \left(2D_y\right) \approx 7\,\mathrm{s}$, which is of the same order of magnitude as times required for conformational changes observed in other photoactive pigment–protein complexes [138]. Rapid forward an backward switching between these two states, observable on much shorter timescale, is achieved due to fast molecular fluctuations.

2.2.3 Dynamic self-organization of LHCII

It is clear that the description of all the possible conformational changes that can occur in the LHCII trimer by using only one generalized coordinate as well as simple harmonic potential wells cannot reveal all the subtle details of the fluorescence intermittency. However, the rather good fitting results presented in Fig. 2.4 suggest that the major properties of the blinking phenomenon are preserved even in such a simplified model. The slight misfitting obtained for the *on*-state at shorter dwell times implies that several minima corresponding to the bright state might be expected to co-exist on the potential energy surface. This assumption is supported by the experimental observations [108, 109] that revealed several distinct mean fluorescence intensities which were attributed to the same bright state, with many transitions occurring just among them without switching to the *off*-state. Further experimental investigation of the temporal evolution of the fluorescence spectrum of the single LHCII complexes have additionally revealed several fluorescing states with the red-shifted fluorescence maxima [107]. Particularly, it was found that not only the overall fluorescence intensity but also the fluorescence spectrum exhibits rapid reversible fluctuations. While the LHCII complexes fluoresce generally at 680 nm, occasionally fluorescence peak position shifts to 700–

720 nm or to even redder spectrum region. We will discuss this in more details in the next chapter.

As it was already mentioned above, our obtained ratio of the transition rates, k_2/k_1, varies between 30 (at lower pH levels) and 60 (at higher ones). On the other hand, this ratio should also represent the dynamic equilibrium between the *on*- and *off*- states. That observation means that even under ordinary light-harvesting conditions on average one per 60 LHCII trimers is quenched. Such a conclusion can partially explain the experimentally observable excitation energy quenching as well as the heterogeneity of the fluorescence lifetimes in LHCII aggregates [139–142]. Indeed, there is nonzero probability that in the aggregated supercomplex one or several LHCII trimers will be in their quenching state, therefore due to the inter-trimer excitation transfer the mean fluorescence lifetime is expected to be essentially shorter compared to the case of the disconnected trimers. Under more adverse environmental conditions the average number of quenchers should exhibit a ~2-fold increase.

Another interesting outcome of our model is the ability to precisely represent the power-law behavior of the probability density for the *off*-events with the exponents close to -2 [109]. Since ordinary models that are based on a one-dimensional random-walk and consider the distributions of the first-passage times predict this exponent to be equal roughly $-3/2$ [143], one needs to assume anomalous diffusion to obtain different exponents [133, 144]. Over the last 20 years it was discovered that many disordered systems, especially biological ones, exhibit either a faster or slower increase in time of the mean variance than predicted by the classical Brownian motion, corresponding to the so-called super- and subdiffusion, respectively [143, 145]. It was demonstrated, for example, that in living cells membrane proteins experience subdiffusive behavior [146] since due to interaction with other particles their mobility decreases. However, the asymptotic distribution of the first-passage times in the case of one-dimensional subdiffusion is proportional to either $t^{-1-\mu}$ or $t^{-1-\mu/2}$, depending on whether diffusion is bounded or unbounded [143]. Here, μ describes the rate of diffusion: $\left\langle (\Delta x)^2 \right\rangle \propto t^{\mu}$ with $0 < \mu < 1$ (classical diffusion corresponds to $\mu = 1$). We see, that even anomalous diffusion could not explain the power-law blinking of the single LHCII trimers with the exponent being slightly greater (in absolute value) than 2 [109]. However, the model proposed in this work and based on dynamic self-organization processes in the pigment–protein complexes is able to overcome such difficulties and reproduce experimental observations reasonably well. Interestingly, the drop of the absolute value of the mentioned exponent below 2 (as observed at pH 5.5 [109]), when anomalous diffusion can in principle be applied, indirectly confirms our previous assumption about the possible phase transition taking place in the very acidic environment.

2.3 Singlet–triplet annihilation in single LHCII

Techniques of single-molecule spectroscopy can be combined with ordinary spectroscopic methods, *e.g.* by performing correlated measurements of fluorescence intensity (like those demonstrated in Fig. 2.1), fluorescence spectrum (revealing the already mentioned spectral diffusion), and fluorescence lifetime of individual LHCII complexes [106]. The simultaneous measurements of multiple spectroscopic quantities not only reveal the existence of multiple functional states of the pigment–proteins that differ either in fluorescence intensity [108, 109], emission spectral region [107], or excited state lifetime [106], but also allow picking out the complexes being in some particular state for the subsequent more detailed analysis of their intrinsic properties. Recently, such correlated measurements of integral fluorescence intensity and fluorescence decay kinetics of single immobilized LHCII complexes were performed, demonstrating some details of the non-linear exciton relaxation pathways in light-harvesting complexes arising from another regulatory self-quenching mechanism known as singlet–triplet (ST) annihilation[5].

2.3.1 Bi-exponential excitation intensity-dependent fluorescence decay kinetics

As followed from the time-resolved fluorescence measurements of single unquenched LHCII complexes, their fluorescence decay kinetics at excitation intensities below $50\,\mathrm{W/cm^2}$ can be satisfyingly described with a single-exponential function: $F(t) \propto \exp(-t/\tau_{\mathrm{slow}})$. The obtained mean value of the excitation lifetime, $\tau_{\mathrm{slow}} = (3.4 \pm 0.3)$ ns, which was measured individually in about 100 single unquenched complexes, was the same as in an ensemble of solubilized complexes, $\tau = (3.45 \pm 0.02)$ ns, measured on the same setup [112]. This implies that neither surface attachment nor any other SMS-related measuring condition (*e.g.*, large detergent-to-protein ratio) systematically affects any of the radiative and nonradiative decay rates. However, under considerably higher excitation intensity an additional fast decay component appears, $\tau_{\mathrm{fast}} = (35 \pm 10)$ ps, whereas the slower component remains unchanged (see Fig. 2.6a). Additional measurements at the intermediate excitation intensities revealed that in all cases the normalized fluorescence kinetics exhibits a bi-exponential decay behavior:

$$F(t) = A_{\mathrm{slow}} \mathrm{e}^{-t/\tau_{\mathrm{slow}}} + A_{\mathrm{fast}} \mathrm{e}^{-t/\tau_{\mathrm{fast}}},$$

where τ_{slow} and τ_{fast} time components remain the same as listed above while their relative amplitudes A_{slow} and A_{fast} heavily depend on the excitation intensity. As

---

[5] The experimental measurements described in this section were performed by J. M. Gruber from Vrije Universiteit in the Netherlands. Further details are presented in [112].

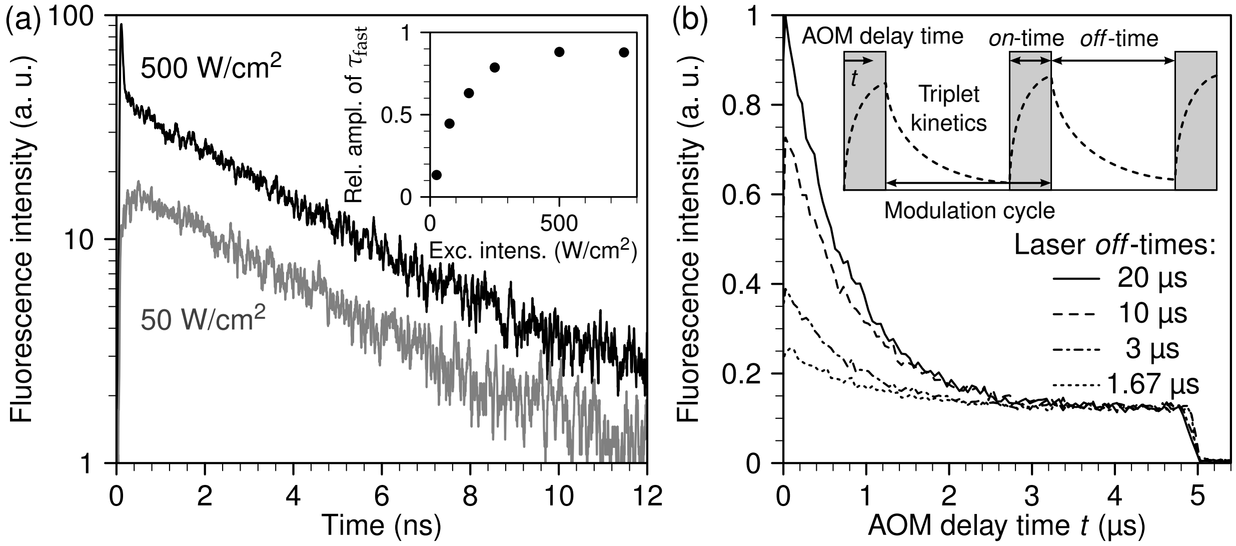

Figure 2.6 | (a) Fluorescence decay kinetics in a single LHCII complex at different excitation intensities of 50 and 500 W/cm^2. At higher intensity, a fast 35-ps decay component becomes apparent. **Inset**: dependence of the relative amplitude of a fast 35-ps component on the excitation intensity. (**b**) Fluorescence kinetics, measured at a µs timescale using an acousto-optic modulator with $t_{\text{on}} = 5\,\mu\text{s}$ and different t_{off} values at an excitation intensity of 500 W/cm^2. **Inset**: illustration of the stepwise amplitude modulation of excitation pulses applied via an acousto-optic modulator to probe the µs time range and resulting in varying concentration of triplet states, as schematically shown with the dashed line.

demonstrated in the inset of Fig. 2.6a, the relative amplitude of the fast decay component exhibits approximately linear increase with the excitation intensity followed by a saturation behavior at higher illumination levels. The initial amplitude of the non-normalized fluorescence kinetics, however, was found to correlate with the excitation power at the whole intensity range, meaning that absorption cross-section of the LHCII trimer does not change.

The obtained value of the fast decay component, ~35 ps, lies within the time range of less than 40 ps, reported for the annihilation processes, and within the limits of slow inter-monomer excitation energy transfer in an LHCII trimer [76, 147–149]. This result, together with the intensity-dependent fluorescence kinetics and high repetition rate (76 MHz) of the laser pulses used in the experimental setup, suggests that the fast decay component seen in this experiment in principle might be connected to singlet–triplet annihilation: the used excitation power was still too low to simultaneously create 2 excitons within LHCII, meaning vanishing probability for singlet–singlet annihilation to occur. Currently existing model for ST annihilation in molecular aggregates [150], however, cannot explain the appearance of excitation intensity-dependent bi-exponential decay kinetics. Therefore, in order to validate this assumption, additional measurements by utilizing an acousto-optic modulator (AOM) as a fast shutter were performed. The inset in Fig. 2.6b demonstrates how the stepwise modulation of the excitation laser power can be used to measure variations of fluorescence intensity on a µs timescale. If the fast 35-ps decay component correlates with the ST annihilation, the overall fluorescence intensity should notably depend on the concentration of the triplet states within the LHCII trimer. The latter should obviously increase in time during the illumination period (denoted as *on*-time, t_{on}, in the inset of Fig. 2.6b), while it should naturally drop during the subsequent dark period (*off*-time (t_{off}), respectively), as schematically demonstrated with the dashed line in the inset of Fig. 2.6b. The corresponding time evolution of the fluorescence intensity was indeed observed experimentally. As demonstrated in Fig. 2.6b, the total fluorescence intensity notably decreases during several µs until it reaches some constant value corresponding to a particular maximal concentration of the generated triplet states. The rate of fluorescence drop was found to correlate with the excitation intensity [112] since the latter naturally determines the rate of the triplet state generation. On the other hand, by changing the duration of the *off*-time period of the modulation cycle, the initial triplet concentration prior subsequent illumination period can by varied (*cf.* different kinetics in Fig. 2.6b). From the resulting initial fluorescence amplitude, the lifetime of the triplet state can be evaluated, which resulted in a time constant $K_{\mathrm{T}}^{-1} \approx 6.6$ µs. This value lies within the range of 2–9 µs, reported for the lifetimes of the carotenoid triplet states [60,151], thus providing an additional support for the dominating role of ST annihilation in these measurements.

2.3.2 ST annihilation in LHCII trimers: a statistical approach

As discussed in Section 1.1 and schematically shown in Fig. 1.2, carotenoids not only participate in light harvesting and non-photochemical quenching, but are also able to effectively quench the generated triplet states of the chlorophyll pigments. In fact, it is known that in LHCII more than 90 % of Chl triplets are efficiently quenched by Cars, primarily by lutein molecules [60, 61]. Indeed, due to fast excitation energy transfer from Chls *b* to Chls *a*, occurring on a timescale of several ps (*cf.* Table 1.2 and Fig. 1.6) and much slower excited state decay and inter-system crossing, mainly Chl *a* triplet states are formed. As follows from the structural organization of LHCII (Fig. 1.1b), all the Chl *a* pigments are, in their turn, in close proximity with either one of two central luteins or neoxanthin, leading to the active role of these Cars in quenching Chl triplet states[6]. Therefore it is not surprising that the lifetime of the triplet state in LHCII, evaluated from

---

[6] The fourth Car, either Vio or Zea depending on the stress conditions of plants before protein purification, is located at the periphery of the protein backbone and was shown not to contribute to triplet quenching [91, 152].

the AOM measurements, is in line with the reported Car triplet lifetimes and not those of chlorophylls that are of the order of several ms. The resulting triplet states of Car molecules can also act as another intrinsic photo-protection mechanism, which under higher photon flux conditions quenches singlet excited states of Chls via non-linear exciton–exciton annihilation [153]. The efficiency of this ST annihilation process depends on the excitation intensity, the exciton diffusion radius, the number of pigments within the system, and their connectivity [154–157].

The annihilation kinetics in large molecular aggregates are usually well-described with a rather simple kinetic model [150]:

$$\frac{\mathrm{d}n(t)}{\mathrm{d}t} = G(t) - [k + k_{\mathrm{ISC}}]\, n(t) - \gamma N(t) n(t), \tag{2.17}$$

$$\frac{\mathrm{d}N(t)}{\mathrm{d}t} = k_{\mathrm{ISC}} n(t) - K_{\mathrm{T}} N(t), \tag{2.18}$$

where $n(t)$ and $N(t)$ denote the time-dependent concentrations of singlet and triplet states, respectively; k and K_{T} are the rate constants of the linear singlet and triplet exciton decay, respectively; γ is the rate constant of ST annihilation; k_{ISC} is the rate of inter-system crossing in a chromophore molecule; and $G\,(t)$ is the singlet generation rate (pumping rate). Since k and K_{T} usually differ by several orders of magnitude, variations of triplet concentration in the steady-state regime between two subsequent laser pulses are almost negligible compared to the already accumulated triplet concentration. As a result, $N(t)$ in Eq. 2.17 can be replaced by its stationary value, $N\,(t) \approx N_0$, which is derived from the following equation [150]:

$$N_0 = \frac{k_{\mathrm{ISC}}}{k + k_{\mathrm{ISC}} + \gamma N_0} \cdot \frac{n_0}{K_{\mathrm{T}} \tau},$$

here τ is the time interval between two subsequent excitation pulses whereas $n_0 = \int G\,(t)\,\mathrm{d}t$ is the total initial concentration of singlet excitons generated by a single pump pulse. The concentration of singlets decreases therefore faster in the annihilation regime than in annihilation-free conditions, but still in a simple single-exponential way:

$$n(t) = n_0 \mathrm{e}^{-(k + k_{\mathrm{ISC}} + \gamma N_0) t}.$$

Such a single-exponential behavior is indeed observed in, *e.g.*, polymer films, where a large concentration of singlet and/or triplet excitons is possible [150,158]. Similar kinetic approach has also been successfully applied to the LHCII aggregates [142,148]. It has also been used to describe the saturation of the steady-state fluorescence with increasing excitation intensity of single LHCII complexes [109]. However, this kinetic model did not give correct solutions for the bi-exponential fluorescence decay kinetics of LHCII trimers, shown in Fig. 2.6a.

One of the reasons for the successful application of this kinetic model to describe ST annihilation in polymer films was the fact that the final triplet concentration in the system could be up to three orders of magnitude larger than that of singlet excitons. Such a situation, however, does not hold in the case in small photosynthetic antenna units like single LHCII complexes, where the maximum number of excitons is limited to the number of available pigments. This implies that the simple kinetic model outlined above might (and should) be violated. Therefore, to account for the limited amount of available exciton states and their discrete nature, a more detailed statistical model has to be developed.

In small aggregates of pigment molecules like single LHCII trimers, distances between the most-remote chromophores are usually much smaller than the actual excitation diffusion length. As a result, the whole aggregate can be viewed as a single supermolecule which is fully characterized by a manifold of various accessible energy levels reflecting single and multiple excitations [154, 155, 159, 160]. The resulting statistical model describing possible transitions between these energy levels has been successfully used to describe non-linear singlet–singlet annihilation in LHCII trimers [142, 148]. At a high repetition rate of the excitation laser, the formation of triplet states should also be considered, which requires the extension of the statistical model of an LHCII supermolecule.

When the formation of triplet states is taken into account, the overall state of the system is fully described by two numbers, i—the actual number of singlets, and j— the actual number of triplets. If we denote the probability of this state as $P_{i,j}$, the transitions between various states obey the following Pauli Master equations (see Fig. 2.7 for illustration):

$$\begin{aligned}\frac{\mathrm{d}P_{i,j}(t)}{\mathrm{d}t} &= G(t)\cdot P_{i-1,j}(t) + (i+1)\,k_{\mathrm{ISC}}\cdot P_{i+1,j-1}(t)\\ &+ \left[(i+1)\,k + (i+1)\,j\gamma\right]\cdot P_{i+1,j}(t)\\ &+ (j+1)\,K_{\mathrm{T}}\cdot P_{i,j+1}(t) - \left[G(t) + ik_{\mathrm{ISC}} + ik + ij\gamma + jK_{\mathrm{T}}\right]\cdot P_{i,j}(t),\\ &\qquad i = 0,1,\ldots,n_{\max};\quad j = 0,1,\ldots N_{\max},\end{aligned} \tag{2.19}$$

here all the rates are denoted in the same way as in Eqs. 2.17 and 2.18, whereas $n_{\max}$ and $N_{\max}$ represent the maximum number of the available singlet and triplet states, respectively. In the case of LHCII, all the rates in Eq. 2.19 are at least two orders of magnitude slower than the typical inter-pigment excitation transfer rates, which allows us to totally neglect the latter. The numerical pre-factors of the transition rates in Eq. 2.19 reflect the statistical number of possible relaxation pathways contributing to a particular transition in the supermolecule. The system of Eq. 2.19 should be modified slightly at the boundaries of the network depicted in Fig. 2.7 in order to account for the lack of some transitions if $i = 0$ or $n_{\max}$ and

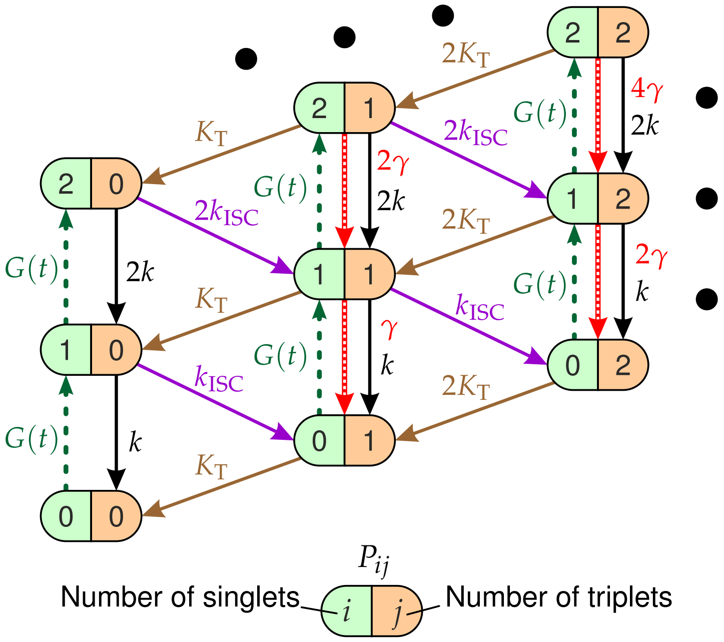

Figure 2.7 | Statistical model of ST annihilation. Color ovals represent various possible states of the system containing different numbers of singlets and triplets. The probability of each state is P_{ij} and arrows demonstrate possible transition between these states. k and K_T are the relaxation rates of singlet and triplet states, respectively; k_{ISC} is the rate of inter-system crossing; γ is the rate of ST annihilation; and $G(t)$ denotes the generation rate of singlet states by laser excitation. The black dots indicate that the model can be farther extended to higher numbers of singlet and triplet states.

$j = 0$ or N_{max}. Since excitation intensities used in fluorescence measurements of single LHCII were rather low, the states corresponding to $i \geq 2$ are expected to remain almost unpopulated. Therefore, for the sake of simplicity we neglect the terms describing singlet–singlet annihilation in Eq. 2.19 and Fig. 2.7; the model, however, can be easily adjusted to account for this additional relaxation channel that becomes available at higher excitation densities [142, 161].

By numerically solving the system of differential equations 2.19, the time-dependent probabilities $P_{i,j}(t)$ of every state can be easily obtained. Then the mean number of singlets, $n(t)$, is defined as a weighted sum:

$$n(t) = \sum_{i=0}^{n_{max}} \sum_{j=0}^{N_{max}} i \cdot P_{i,j}(t) . \tag{2.20}$$

Analogically, the mean number of triplets is

$$N(t) = \sum_{i=0}^{n_{max}} \sum_{j=0}^{N_{max}} j \cdot P_{i,j}(t) . \tag{2.21}$$

If we analytically calculate the sums in Eqs. 2.20 and 2.21 by taking the Pauli

Master equations (Eq. 2.19) into account, we obtain two simple relations:

$$\frac{\mathrm{d}n(t)}{\mathrm{d}t} = \sum_{i=0}^{n_{\max}} \sum_{j=0}^{N_{\max}} i \cdot \frac{\mathrm{d}}{\mathrm{d}t} P_{i,j}(t)$$

$$= G(t) - [k + k_{\mathrm{ISC}}]\, n(t) - \gamma \sum_{i=0}^{n_{\max}} \sum_{j=0}^{N_{\max}} i \cdot j \cdot P_{i,j}(t), \qquad (2.22)$$

$$\frac{\mathrm{d}N(t)}{\mathrm{d}t} = \sum_{i=0}^{n_{\max}} \sum_{j=0}^{N_{\max}} j \cdot \frac{\mathrm{d}}{\mathrm{d}t} P_{i,j}(t) = k_{\mathrm{ISC}} n(t) - K_{\mathrm{T}} N(t). \qquad (2.23)$$

These equations are exactly the same as Eqs. 2.17 and 2.18, except for the last term in Eq. 2.22. This term is in fact the reason for the deviation from the mono-exponential decay kinetics of singlet excitons. For short excitation pulses (compared to other characteristic time scales), the exact form of the generating function $G(t)$ is not important—the only significant quantity is the initial population of the generated singlet states, $n_0 = \int G(t)\, \mathrm{d}t$. Starting from the initial distribution $P_{0,0}(t) = 1$ and $P_{i,j}(t) = 0$ for $i > 0$ or $j > 0$, the system of Eq. 2.19 can be solved for a large sequence of laser excitations until the quasi-stationary distribution of triplets is obtained, *i.e.* until the probabilities $P_{i,j}(t)$ prior to two subsequent pulses become indistinguishable.

The same model can also be used to calculate triplet accumulation and the resulting fluorescence drop observed during the AOM measurements (*cf.* Fig. 2.6b). Indeed, the number of detected photons during a specific time bin interval Δt at the AOM delay time t is proportional to the integral of the singlet kinetics:

$$F(t) \propto \int_{t}^{t+\Delta t} n(t')\, \mathrm{d}t'. \qquad (2.24)$$

For simplicity, if the binning time interval Δt in Eq. 2.24 is small compared to the timescale of formation of the triplet state, it can be substituted with the time interval τ between two subsequent excitation pulses while the proportionality in Eq. 2.24 is still approximately preserved.

2.3.3 Calculated ST annihilation kinetics

As discussed above, fluorescence kinetics in single LHCII trimers exhibit a two-exponential decay behavior with a fast lifetime of $\tau_{\mathrm{fast}} \approx 35\,\mathrm{ps}$ and a slow one of $\tau_{\mathrm{slow}} \approx 3.4\,\mathrm{ns}$. In terms of the statistical description this indicates that on average less than one triplet state per LHCII is formed: the fast kinetics represents the situation when exactly one triplet is generated, so that the corresponding lifetime is $\tau_{\mathrm{fast}} \approx (k + k_{\mathrm{ISC}} + \gamma)^{-1} \approx \gamma^{-1}$. The slower counterpart, on the other hand,

Table 2.1 | Model parameters used to fit the fluorescence decay kinetics at a µs timescale, obtained from AOM measurements and shown in Figure 2.6b.

Model parameter	Value
S–T annihilation rate	$\gamma^{-1} = 36$ ps
Singlet linear relaxation rate	$k^{-1} = 5.81$ ns
Triplet linear relaxation rate	$K_{\mathrm{T}}^{-1} = 6.99$ µs
Inter-system crossing rate	$k_{\mathrm{ISC}}^{-1} = 8.54$ ns
Initial excitation per 1 kW/cm^2 of laser intensity	$n_0 = 0.073/1\,\frac{\mathrm{kW}}{\mathrm{cm}^2}$

can be attributed to the case when triplet states are not generated at all, yielding $\tau_{\mathrm{slow}} \approx (k + k_{\mathrm{ISC}})^{-1}$. The observed two-exponential decay is therefore a time-averaged sum of the statistical interchange of both scenarios. From these measurements, only the ST annihilation rate $\gamma \approx 1/\,(35\,\mathrm{ps})$ can be evaluated precisely, whereas all the other transition rates present in Eq. 2.19 remain uncertain. It can be shown that various sets of the parameters k, K_{T}, k_{ICS}, and n_0 can equally well reproduce the experimentally observed fluorescence kinetics. To avoid ambiguity, it is necessary to obtain additional information on the rate of triplet formation.

This additional information is provided by the time-dependent AOM experiments illustrated in Fig. 2.6b, revealing the process of triplet generation. To verify the proposed statistical model of ST annihilation, we used Eqs. 2.19 and 2.24 to simultaneously fit all four µs-timescale fluorescence kinetics shown in Fig. 2.6b just by using different laser pulse *off*-time periods t_{off}. In order to avoid any possibly remaining uncertainty in the fitting results, we also used slow and fast lifetimes extracted from the steady state fluorescence kinetics as additional constrains for the model parameters. Other variables like $t_{\mathrm{on}} = 5\,\mu\mathrm{s}$, $\tau = 1/f = 13.16\,\mathrm{ns}$ (here $f = 76\,\mathrm{MHz}$ is the laser repetition rate) and the excitation intensity of 500 W/cm^2 were fixed to represent the experimental conditions.

The obtained model parameters are outlined in Table 2.1 while the corresponding best-fitted fluorescence kinetics are shown with red lines in Fig. 2.8. The calculated steady state fluorescence kinetics indeed demonstrate bi-exponential behavior, as shown in Fig. 2.8a–b for two different excitation intensities of 300 and 750 W/cm^2. In both cases, the concentration of triplets almost does not change between two subsequent laser pulses and is indeed smaller than 1 (on average 0.85 and 0.98 per LHCII trimer, respectively), as discussed above. As a result, the total observed singlet excitation kinetics is expressed as a statistical average of all possible triplet numbers present in the system. At an excitation intensity of 300 W/cm^2 there is, for example, a 1.9 % probability for the system to contain two triplets, a 80.7 % probability for one triplet, and a 17.4 % probability for no triplets. The probability for two triplets is almost negligible (and it is even smaller

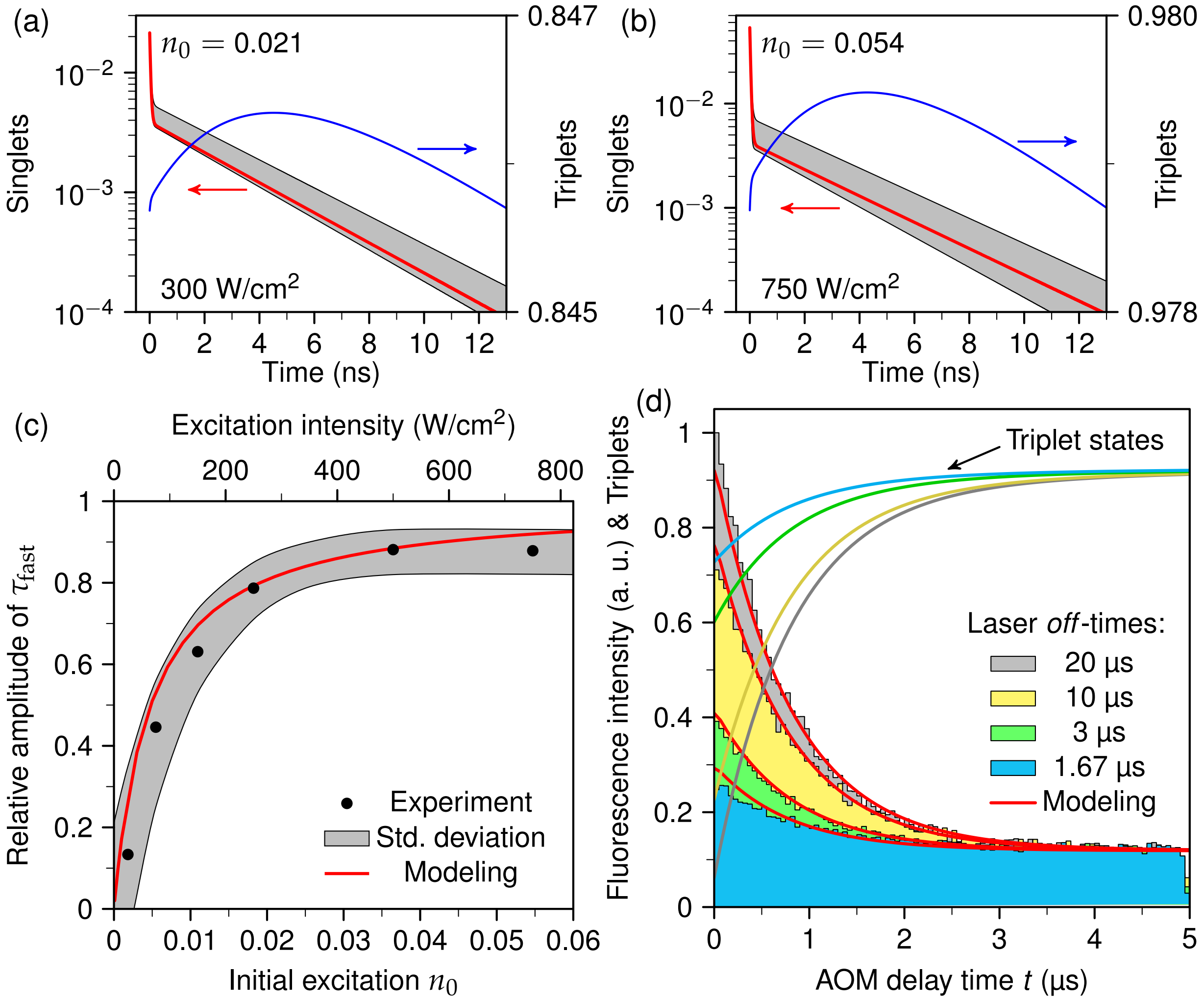

Figure 2.8 | Verification of the statistical model of ST annihilation in single LHCII trimers. (**a**–**b**) Calculated steady-state fluorescence kinetics of singlets (red line, left axis) and triplets (blue line, right axis) in single LHCII complexes for excitation intensities of 300 W/cm^2 (a) and 750 W/cm^2 (b). n_0 denotes the initial number of generated singlets and the gray shading indicates the boundary values of the standard deviation in the experimental measurements. (**c**) Measured (dots, top axis) and calculated (red line, bottom axis) dependence of the relative amplitude of a fast 35-ps component of the fluorescence decay kinetics on the excitation intensity. Shaded region demonstrates standard deviation in the experimental measurements of about 20 LHCIIs. (**d**) Fluorescence decay kinetics at a µs timescale, obtained from AOM measurements with $t_{\mathrm{on}} = 5\,\mu\mathrm{s}$ and different t_{off} values (filled curves, the same as in Fig. 2.6b). Red lines indicate the corresponding best-fitted re-normalized kinetics, calculated according to Eq. 2.24 using the parameters listed in Table 2.1. The calculated time evolution of the triplet states accumulation is shown with lines of the same color as the corresponding AOM experimental traces.

at lower excitation intensities), therefore it cannot be resolved due to limited time resolution of the experimental setup utilized in the current measurements. In fact, by slightly changing the lifetimes in the exponents as well as their relative amplitudes, the calculated kinetics can be perfectly fitted with a bi-exponential decay. By comparing kinetics shown in Fig. 2.8a–b we see that the relative amplitudes of the fast and slow components strongly depend on the excitation intensity. This dependence was further investigated and the obtained results fully agree with the experimental measurements, as illustrated by the red line in Fig. 2.8c that demonstrates the increase of the relative amplitude of the fast decay component with the initial excitation n_0, calculated using the parameters listed in Table 2.1.

Finally, the calculated µs-scale fluorescence kinetics are shown in Fig. 2.8d and match the experimentally measured ones pretty well. Slight deviations of the fitted curves from the experimental data could have various reasons. The experimental AOM kinetics shown in Fig. 2.8d were obtained from different single LHCII complexes, that could give rise to the effect of some static disorder or slight structural heterogeneity of various pigment–proteins. Further differences could arise from the presence of an additional quenching mechanism that on average slightly decreases the probability of ST annihilation. Fast blinking events that cannot be resolved in fluorescence intensity traces might also be an explanation [108]. These could be caused by conformational changes of the pigment–protein complex, but the reported presence of a low number of unquenched Chl triplets within LHCII [61, 162] could also contribute, especially at higher excitation intensities.

In the same Fig. 2.8d, the calculated rise kinetics of the triplet population are also presented. As expected and qualitatively described above, a higher amplitude of the AOM kinetics at the onset of a modulation cycle corresponds to a lower initial average concentration of triplets and thus a slower decay of singlet states of Chl molecules. As a result, the longer lasting singlet states yield higher fluorescence intensity. Therefore the presented statistical model can fully explain all the experimentally observed features of ST annihilation in single LHCII complexes.

At this point, several remarks regarding the obtained model parameters can be made. First of all, the obtained ST annihilation rate $\gamma \approx (35\,\mathrm{ps})^{-1}$ contains information about the inter-pigment excitation energy transfer processes and can be understood as the mean diffusion time of a singlet excitation until its energy is transferred to a Car triplet state followed by the annihilation. As a result, this value indicates the upper limit for the mean inter-monomer excitation hopping time within the LHCII trimer. It is somewhat slower than the singlet–singlet annihilation rate extracted in earlier studies [148] due to additional time needed for excitation transfer from the Chl *a* pigment to the particular Car in triplet state located nearby. Furthermore, this defined time constant for annihilation in an LHCII trimer implies a well-connected and structurally unchanged trimeric structure of the immobilized protein complex.

The obtained initial excitation at 1 kW/cm^2 laser intensity, $n_0 = 0.073$, represents the number of absorbed photons per laser pulse, which agrees well with the evaluated absorption rate of ~0.06 photons per pulse based on the given excitation intensity and the reported absorption cross-section of an LHCII trimer, $\sigma = 1.4 \cdot 10^{-15}\,\mathrm{cm}^2$ [107]. Such a small number of generated excitation, even at the highest laser intensities used during the measurements, totally excludes the possibility for the singlet–singlet annihilation. Therefore, the latter was not accounted for in Eq. 2.19. Nevertheless, the proposed statistical model can be straightforwardly generalized to include both non-linear processes.

The lifetime of the Car triplet state, directly extracted from the measured AOM kinetics and evaluated as $K_{\mathrm{T}}^{-1} \approx 6.6\,\mu\mathrm{s}$, is just slightly faster than the values of 7–9 μ*s* found in literature for Cars in anaerobic conditions [60, 151]; the deviation of the fitted value, $K_{\mathrm{T}}^{-1} \approx 6.99\,\mu\mathrm{s}$ (see Table 2.1), is even smaller. This discrepancy could be caused by the trace amounts of oxygen; however, that seems unlikely due to the high photo-stability of complexes (typically more than one minute). Another possibility is that ST annihilation may intrinsically shorten the lifetime of Car triplet states via the frequent access of higher excited triplet states. Meanwhile, the obtained timescale for the Chl inter-system crossing of $k_{\mathrm{ISC}}^{-1} \approx 8.54\,\mathrm{ns}$ agrees with the published range of $\sim 10\,\mathrm{ns}$ [55, 60] and results in an absolute triplet generation yield of 40 %. This is somewhat higher than the value of 30 % found for PSII with closed reaction centers in chloroplasts [54]. However, such a discrepancy can be explained by the difference in the slightly quenched long lifetime component of about ~2 ns in the latter case.

2.4 Summarizing remarks

Single-molecule spectroscopy-based measurements have revealed many unexpected properties of the photosynthetic light-harvesting complexes. In spite of its complicated internal structure, an LHCII trimer, containing more than half a hundred photoactive pigment molecules, behaves as a single unit and demonstrates behavior that earlier was observed only in the case of single emitters like simple dye molecules or quantum dots. Particularly, it was found that single LHCII trimer is able to reversibly switch between several distinct states corresponding to various fluorescence intensity levels, the peak position of fluorescence spectrum, or mean fluorescence lifetime. In this chapter, it was demonstrated that such a blinking behavior is an intrinsic property of LHCII complexes that is governed by subtle conformational changes in the protein scaffold, disturbing the inter-pigment energetic pattern. As a result, even under ordinary light-harvesting conditions some antenna complexes are quenched, and their fraction can vary in response to the external exposure like pH level or excitation intensity. Such intrinsic ability of proteins to act as an environmentally controlled switch makes them a suitable candidate to govern non-photochemical quenching and fast reversible transitions between the almost perfect energy-transfer and the quenching states of the light-harvesting antenna. Similar switching mechanisms therefore can also be expected to exist for other biologically important proteins liable to some conformational changes that have an effect on their functional properties.

In combination with more conventional spectroscopic techniques, SMS measurements also provide possibility to disentangle quenching and/or bleaching effects and thus to focus solely on the properties of individual highly fluorescent unquenched LHCII trimers, which is not possible during usual ensemble measurements. As demonstrated in Section 2.3 of this chapter, this approach allowed us to thoroughly study the process of singlet–triplet annihilation, another self-quenching mechanism that manifests itself at high excitation density conditions. In terms of the proposed statistical model, the experimentally observed biexponential fluorescence decay in single LHCII complex can intuitively be understood as fast switching between an annihilation and a non-annihilation regimes, corresponding to the presence and absence of a Car triplet state. This model, being able to perfectly describe ST annihilation in a rather small molecular system, can potentially spark off new studies on the larger molecular aggregates, *e.g.* on PSII supercomplexes that fall into the intermediate range between a statistical and kinetic mathematical description.

In the following chapter, we will utilize the determined switching ability of individual LHCII trimers by formulating model for excitation energy dynamics in large LHCII aggregates. Starting from the SMS data on single light-harvesting complexes, we will be able to explain both the spectral features and the multi-exponential decay behavior of the fluorescence kinetics in the aggregated state of pigment-proteins.

> “ *Don’t I feel in my soul that I am part of this vast harmonious whole?*
>
> LEV NIKOLAYEVICH TOLSTOY,
> “WAR AND PEACE”

Chapter 3

Excitation dynamics in LHCII aggregates

In the previous chapters, the main attention was payed to the spectroscopic properties of single separated light-harvesting complexes and excitation dynamics therein. This situation, however, is obviously different from the *in vivo* thylakoid membranes, where pigment–protein complexes build up a well-interconnected network designed to efficiently deliver excitation energy to the photosynthetic reaction centers. As a result of charge separation in the RCs, the observed fluorescence signal in photosystem II becomes significantly quenched: the mean excitation lifetime drops down to ~300–400 ps [163–165] comparing to that of ~3.5 ns in separated LHCII trimers (*cf.* Section 2.3). The closure of all the RCs slows the fluorescence decay down to ~2 ns [166], which is still far below the mentioned 3.5 ns. The presence of photosystem I as well as the formation of non-photochemical quenching at higher light intensities additionally affect the observed spectroscopic signatures and the measured excitation decay kinetics in the thylakoid membranes; the structural heterogeneity [167] of the latter makes the interpretation of the experimental results even more complicated.

In order to avoid these difficulties, studies of the artificially formed LHCII aggregates have been undertaken widely [61,66,67,142,148,149,168–173], revealing many spectroscopic similarities to the intact thylakoid membranes. The results of single-molecule spectroscopy, applied to LHCII trimers [107–109] and discussed in the previous chapter, provided possibility to interpret the experimental observations from a different point of view than it was done earlier. To demonstrate this new approach, in the current chapter we present recent time-resolved fluorescence measurements on LHCII aggregates, performed over a wide temperature range. The thorough analysis of the experimental data revealed several distinct functional states of the LHCII complexes, one of which is responsible for excitation quenching while another is characterized by the red-shifted fluorescence spectrum. Different temperature behavior of both states allowed us to identify the underlying molecular origin of these states, thus providing insight into the photoprotective mechanisms implemented *in vivo*[7].

---

[7] The results presented in this chapter are based on the work submitted for publication [174].

3.1 Time-resolved fluorescence from LHCII aggregates

Studies of isolated LHCII complexes are conventionally performed by preparing their aqueous solution at high detergent concentration. Under such conditions, micelles around LHCII trimers are formed that prevent any clustering of the pigment–protein complexes. Systematic fluorescence measurements of separated LHCIIs unexpectedly demonstrated a considerable fluorescence decrease when detergent was removed [175] and LHCII aggregates were formed. This observation led to the hypothesis that the aggregated state of the light-harvesting antenna is intrinsically quenched and is responsible for NPQ occurring *in vivo* [66]. To some extent, this suggestion was indirectly supported by the observed enhanced energetic contact between pigment–proteins of thylakoid membranes under NPQ conditions [15]. Recently, an important role of zeaxanthin acting in between the complexes and helping to create a variety of quenching sites within the aggregated light-harvesting antenna was verified [176].

Measurements, performed on LHCII aggregates [168,173,177] and LHCII crystals [19] at the temperatures below 100 K, have additionally demonstrated the appearance of a new strong peak in the spectral region around 700 nm of the steady-state fluorescence spectrum, resembling red-shifted chlorophyll fluorescence in the 77 K thylakoid membranes [66, 178]. Interestingly, both effects of LHCII clustering and red-shifted fluorescence were also observed during the studies of the overwintering evergreen plants [179–181]. All these observations imply complex dynamics that occurs in LHCII aggregates as well as in the intact thylakoid membranes. By studying two limiting cases of the light-harvesting antenna—single LHCII trimers and their large clusters—the obtained results can be generalized to the *in vivo* PSII, composed on average of 3–4 LHCII trimers per RC [5]. Thus *in vitro* studies of the LHCII aggregates still do not lose their relevance and, as will be shown below, may solve some puzzles of self-regulation in photosynthesis.

To examine excitation energy dynamics in LHCII aggregate and its relationship to NPQ, high-resolution time-resolved fluorescence measurements were performed recently by taking advantage of the streak-camera-based spectrograph which enables simultaneous temporal and spectral decomposition of the detected fluorescence signal[8]. Since the molecular mechanisms proposed so far to govern NPQ (*cf.* Section 1.2) are expected to demonstrate different behavior at various temperatures, the fluorescence signal was measured over a wide temperature range from 273 K down to 15 K. A typical time-resolved fluorescence spectrum, observed at 150 K temperature, is shown in Fig. 3.1a as a two-dimensional

---

[8] The experimental measurements described in this chapter were performed by E. Songaila and R. Augulis from Center for Physical Sciences and Technology in Lithuania. Further details are presented in [174].

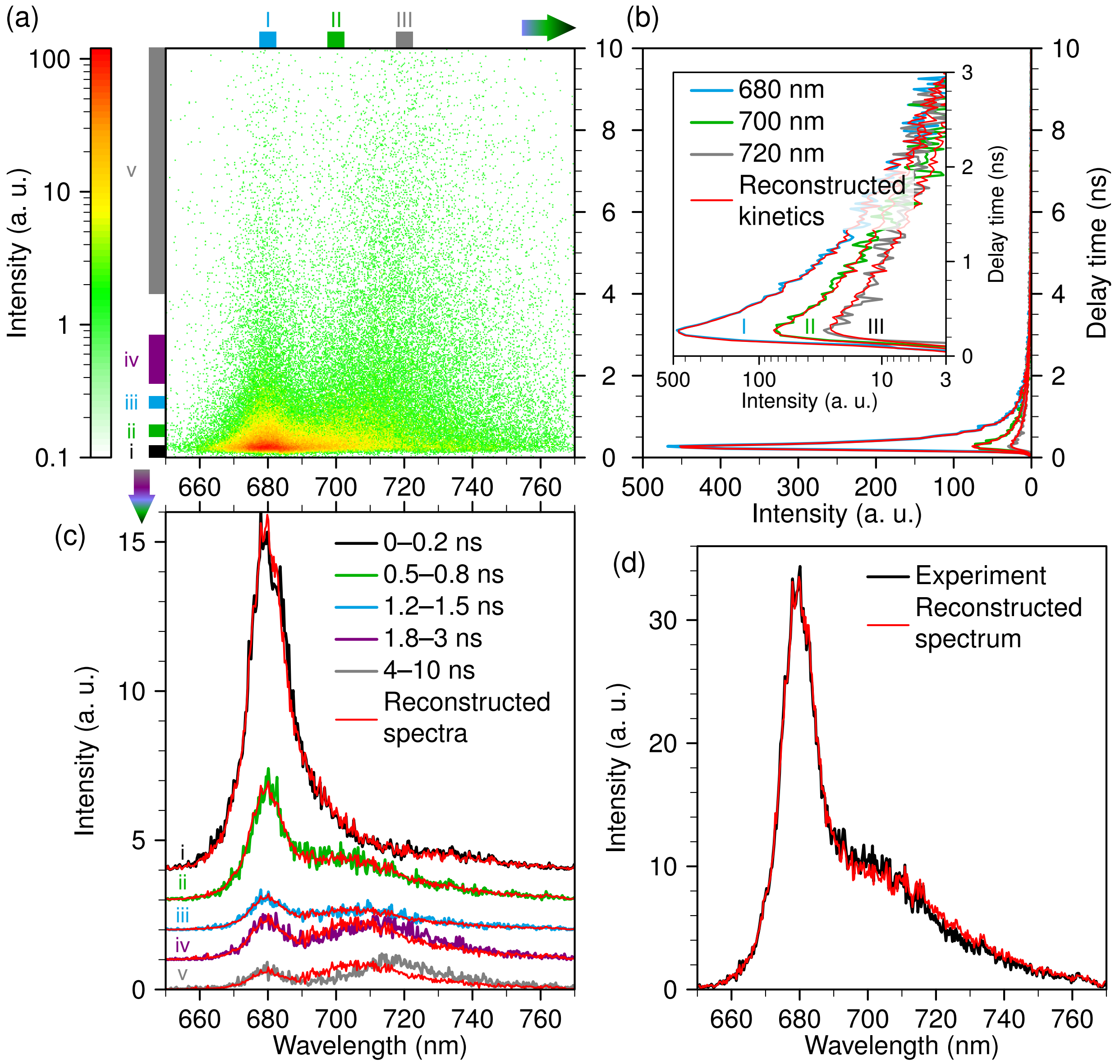

Figure 3.1 | Time-resolved fluorescence measurements of the LHCII aggregates at 150 K. (**a**) Two-dimensional plot illustrating evolution of fluorescence intensity $F(\lambda, t)$. (**b**) Vertical slices (fluorescence kinetics) of panel (a) obtained by integrating the fluorescence intensity map over a 5-nm-wide regions around 680, 700, and 720 nm (indicated with color bars I–III). **Inset**: the same kinetics on a semi-logarithmic scale. (**c**) Horizontal slices (fluorescence spectra) of panel (a) obtained by integrating the fluorescence intensity map over different time intervals (indicated with color bars i–v). (**d**) Steady-state fluorescence spectrum of LHCII aggregate, obtained by integrating the fluorescence intensity map from panel (a) over the whole time region. Red lines in panels (b), (c), and (d) illustrate corresponding fluorescence kinetics and spectra, reconstructed from the sum of the two major components shown in Fig. 3.2.

map and reveals a notable difference of the fluorescence decay kinetics at various wavelengths (compare, *e.g.*, vertical slices at 680, 700, and 720 nm, shown in Fig. 3.1b). We see that, as a result of aggregation, fluorescence over the whole spectral region is significantly quenched (mean lifetimes vary from ~250 ps at 680 nm to ~650 ps at 720 nm) compared to the case of isolated trimers. Fluorescence kinetics at longer wavelengths exhibit much slower decay, so in spite of their small initial amplitude, their corresponding spectral region starts to dominate after several ns following the initial excitation, see Fig. 3.1c. As a result, in the course of time in addition to the 680 nm peak, another peak at ~710 nm appears, resulting in a typical above-mentioned wing in the far red region of the steady-state fluorescence spectra of LHCII aggregates (Fig. 3.1d). Similar results were obtained at other temperatures as well [174]. These observations indicate an effective and only slightly reversible excitation transfer from the whole aggregate into some particular centers responsible for the long-lived red-shifted Chl fluorescence. Since the maximum amplitude of the excitation kinetics at 700 nm is almost an order of magnitude smaller than that of the dominating spectral component at 680 nm, not all the excitations reach these specific "red" centers. Thus additional excitation quenching centers should co-exist within the aggregate. These observations are in line with single-molecule spectroscopy experiments [107], where it was shown that on a micro- to millisecond timescale the same LHCII trimer can reversibly switch between several spectrally different states: although most of the time the fluorescence spectrum exhibited a strong peak at 680 nm, sometimes the position of this peak shifted to ~700 nm, or the fluorescence signal was disappearing at all.

3.2 Identifying distinct emitting states of LHCIIs

Time-resolved fluorescence spectra are often analyzed in terms of the decay-associated spectra (DAS). The observed non-exponential time dependence is then described by a number of states with distinct lifetimes. The more exponentials are needed to describe the kinetics, the more intermediate states are obtained. While this type of analysis is suitable for small molecular systems and transitions between multiple electronic states of the same or neighboring pigments, it is not the case for the aggregates with constituents possessing different spectroscopic properties. Indeed, in the later case the measured kinetics is a sum of the kinetics arising from individual complexes, each of which might be described with different timescales. Therefore, analysis in terms of DAS could give intermediate states that have no physical origin.

To avoid unnecessary intermediate states appearing in DAS analysis and to unambiguously distinguish between spectral components arising from the LHCII

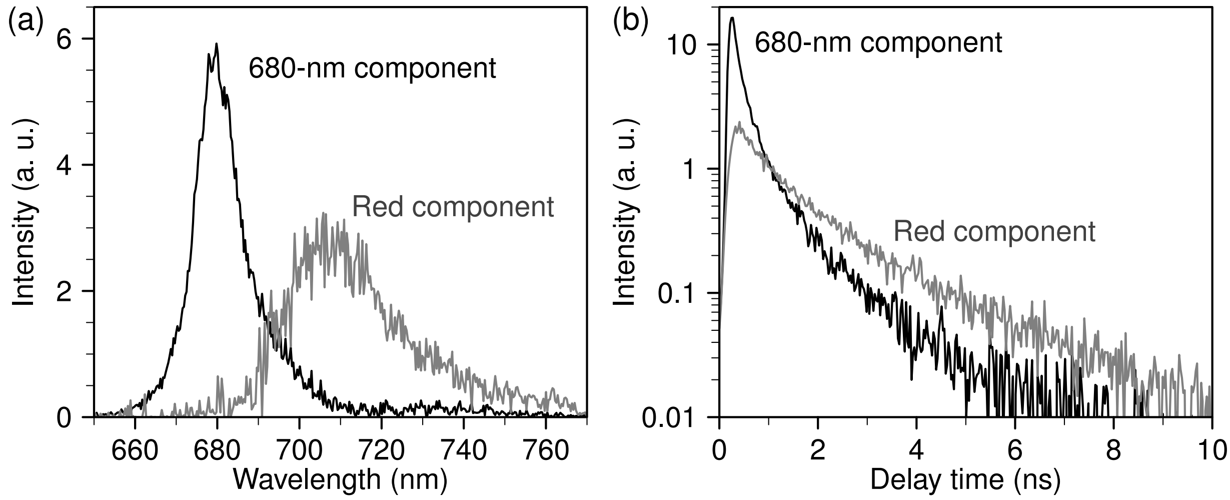

Figure 3.2 | Steady-state fluorescence spectra (**a**) and fluorescence decay kinetics (**b**) of the two major components that were extracted from the fluorescence intensity map presented in Fig. 3.1a by means of multivariate curve resolution. Fluorescence spectra are normalized to have equal area below them. The obtained two spectral components correspond to two distinct emitting states in LHCII aggregates.

trimers being in different states, the collected time-resolved fluorescence spectra $F(\lambda, t)$ were analyzed by implementing the multivariate curve resolution approach [182]. The main idea of this factorization method is to express the initial data matrix as the product of two non-negative matrices, one for the lineshapes of the distinct spectral components, $S_i(\lambda)$, and another for their relative time-dependent weights, $W_i(t)$:

$$F(\lambda, t) \approx \sum_{i=1}^{N} W_i(t)\, S_i(\lambda),$$

or, in a matrix form,

$$\mathbf{F} = \mathbf{W} \cdot \mathbf{S} + \mathbf{E}, \tag{3.1}$$

where the residual matrix **E** should be minimized. The number of the lineshapes, N, should be kept minimal but sufficient to reproduce the experimental data and is usually chosen based on the singular value decomposition analysis. In our case, this analysis revealed two dominating singular values for the time-resolved fluorescence spectra recorded at all the temperatures except the two highest ones (see below). The factorization in Eq. 3.1 was done according to the multiplicative update algorithm [183] by using an additional unimodality constraint ensuring that each spectral component has only one dominating peak, thus minimizing any possible ambiguity of the obtained results. All the optimizations were carried out for 10 000 times starting from random non-negative initial matrices **W** and **S**.

As an example, the obtained best factorization results for the fluorescence spectra, measured at 150 K and shown in Fig. 3.1a, are presented in Fig. 3.2. Here we see that fluorescence from the LHCII aggregate can indeed be attributed to just two distinct emitting states: the dominating one has a strong fluorescence maximum at 680 nm and quickly decays with a mean lifetime of ~250 ps whereas the second one exhibits much broader fluorescence spectrum centered at 707 nm and considerably slower decay behavior (the mean lifetime is about 1 ns). Rather high ratio of the fluorescence kinetics amplitudes of both components indicates that there are relatively few red-emitting states within the whole aggregate. The quality of such spectral decomposition was validated by reconstructing total fluorescence kinetics at various wavelengths and fluorescence spectra at different time delays, see red lines in Fig. 3.1b–d. Although a perfect reproduction is achieved for the time delays $<$ 3 ns, some discrepancies can be noted at later times that can be attributed to the formation of additional states, emitting even in the redder spectral region. Nevertheless, the fluorescence intensities at such long delay times are almost negligible and have little effect to the integral fluorescence spectrum of the LHCII aggregate (*cf.* Fig.3.1d).

Fluorescence signal from the LHCII aggregates at other temperatures was analyzed in a similar way, and the obtained results are summarized in Fig. 3.3. As was already mentioned, just one spectral component was sufficient to reproduce the recorded fluorescence data at 250 and 273 K while two components were needed at all lower temperatures. As expected, the fluorescence lineshapes of both the 680-nm and the red components become notably narrower as temperature drops, though in all cases the spectrum of the red component is much broader. More interesting is the fact that while the peak maximum of the 680 nm component stays roughly at the same position at all considered temperatures, its counterpart exhibits considerable blue shift upon cooling: from ~707 nm at 200 K down to 688 nm at 15 K. This shift results in a very strong overlap of the spectra of both components and the disappearance of the second peak in the steady-state fluorescence spectra of LHCII aggregates under temperatures below 50 K [168, 173].

For reference, time-resolved fluorescence spectra of the LHCII trimers prior their aggregation were also measured and analyzed in a similar way. Differently from the case of the aggregates, only one spectral component was sufficient to perfectly reproduce all the experimental data at all the temperatures (the obtained normalized spectra and kinetics are summarized in Fig. 3.4). This means that (i) the concentration of the red-emitting species of the LHCII trimers is relatively low, as already noted from the fluorescence kinetics of both components in the LHCII aggregates, and (ii) the intrinsic excitation decay rate in both 680-nm and red species is very similar. Fluorescence spectra of the trimers were found to be very similar to those of the 680-nm component in the LHCII aggregates, *cf.* dots

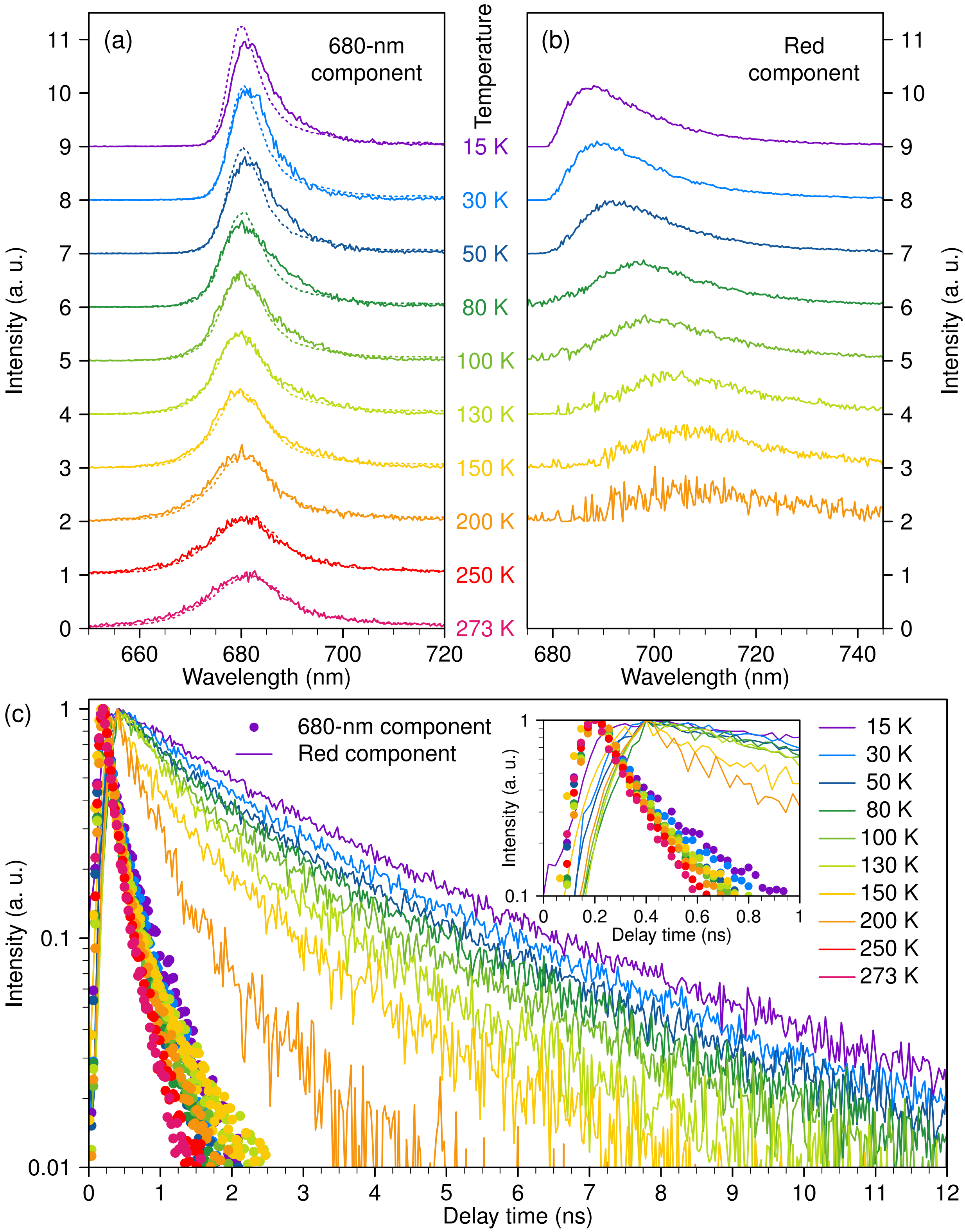

Figure 3.3 | (a–b) Temperature-dependent fluorescence spectra of the extracted 680-nm and red components in the LHCII aggregate. Spectra at different temperatures are shifted vertically for clarity. For comparison, dots in panel (a) represent the fluorescence spectra from Fig. 3.4a, obtained for the LHCII trimers. At highest temperatures, only one spectral component was sufficient to reproduce experimental results. (**c**) Normalized fluorescence decay kinetics of the decomposed two components at various temperatures. **Inset**: the enlarged initial part of the decay kinetics.

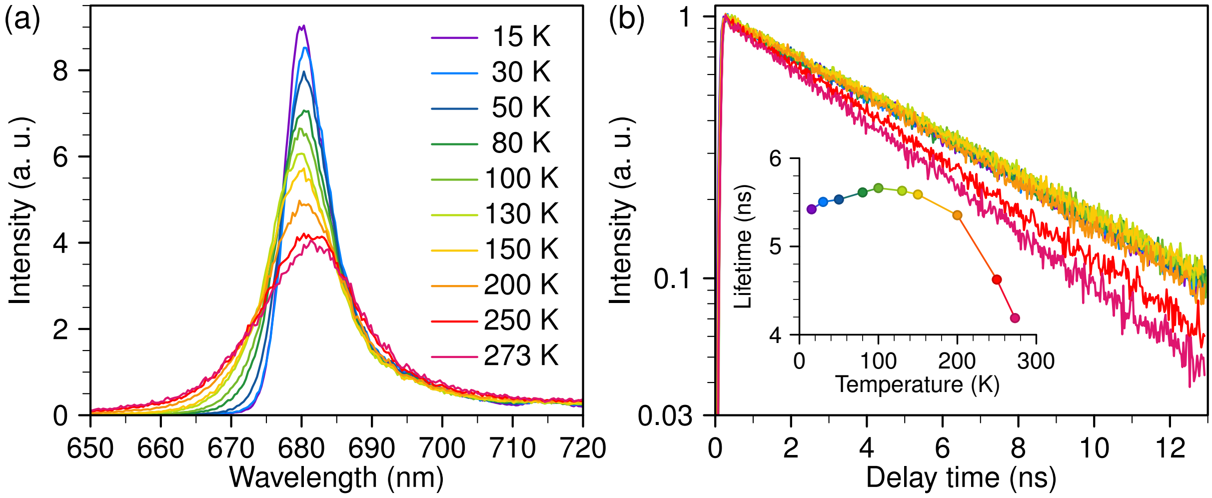

Figure 3.4 | (**a**) Temperature-dependent fluorescence spectra of LHCII trimers, normalized to have equal area below them. Only this single spectral component was sufficient to reproduce experimentally obtained time-resolved fluorescence intensity map similar to that presented in Fig. 3.1a. (**b**) Normalized fluorescence decay kinetics from the LHCII trimers at different temperatures. **Inset**: mean excitation lifetimes in the LHCII trimers at various temperatures, determined from the single-exponential reconvolution fit of the fluorescence kinetics.

and solid lines in Fig. 3.3a, further supporting our used decomposition method. Although some slight variations can be noted at the temperature below ~130 K, these discrepancies might be related to the state transitions experienced by the buffer solution at this temperature region.

In accordance with the results presented in Section 2.3, the fluorescence kinetics of the LHCII trimers exhibited a mono-exponential decay behavior and were further analyzed by fitting them with the convolution of the instrument response function (IRF, approximated with a Gaussian function with FWHM of 110 ps) and a single-exponential function. From that fit, temperature-dependent fluorescence decay rates in the LHCII trimers were obtained (see inset in Fig. 3.4b). We will use these values later in our simulations of the excitation dynamics in the LHCII aggregate.

Contrarily, the obtained fluorescence decay kinetics of both components in LHCII aggregate clearly demonstrate non-exponential behavior (see Figure 3.3c). In Section 2.3, we showed that bi-exponential fluorescence decay kinetics in the LHCII trimers arises from the varying number of the generated triplet states (either one or no at all). Similar explanation should also hold for the LHCII aggregates. However, since no dependence on excitation intensity was observed, the multi-exponentiality of the fluorescence decay kinetics in the LHCII aggregate should be attributed not to the exciton–exciton annihilation effect but to the varying number of the LHCII complexes that have switched into their red-emitting or quenched state.

Interestingly, fluorescence kinetics of the red LHCII species exhibited much slower decay rate and much more pronounced temperature dependence comparing to those of the 680-nm component. This effect confirms very slow excitation back-transfer rate from the red to the dominating LHCII species that was proposed above from the simple analysis of the fluorescence intensity map—in the opposite case, the decay rate of the kinetics of both components would be comparable. Another important point is the fact that the fluorescence of the red component reaches its maximum about 200 ps later than the fluorescence of the 680-nm component (see inset in Figure 3.3c). This means that just after the initial excitation the total energy population of "red" LHCIIs still increases due to incoming excitation energy transfer from the nearby complexes. Such behavior, however, contradicts the so-called excitation radical-pair equilibrium (ERPE) model, which postulates infinitely fast excitation equilibration over the whole photosynthetic antenna and has been widely used in the past [22, 184], thus providing an independent support for the *diffusion-limited* regime of excitation energy transfer in light-harvesting antenna. We will further discuss this issue in the next chapter.

3.3 Excitation dynamics in LHCII aggregate

3.3.1 Coarse-grained model

By summarizing the results obtained from the measured time-resolved fluorescence spectra (see Fig. 3.1 and [174]), the performed multivariate curve resolution analysis (Fig. 3.3) as well as single-molecule spectroscopy studies of single LHCII trimers [107], several important conclusions about the exciton dynamics in the LHCII aggregate can be drawn: (i) at any given time each LHCII monomer can be found in one of at least 3 possible distinct conformational states corresponding to the strong emission around 680 nm, the red-shifted emission, or no emission at all; (ii) the switching between these states is a random process occurring on a micro- to millisecond timescale; (iii) excitation transfer in the aggregate is a diffusion-limited process. All these results can be summarized in the aggregate model schematically presented in Fig. 3.5a. Due to trimeric structure of LHCII, the most favorable arrangement of the pigment–proteins within the aggregate should resemble a hexagonal lattice; such a composition of LHCII oligomers was indeed observed previously by means of electron microscopy [185].

Structure-based calculations of the inter-pigment excitation dynamics within an LHCII monomer have revealed a relatively fast (of the order of several picoseconds) excitation transfer from chlorophyll *b* to chlorophyll *a* and subsequent equilibration [40,42,43,75] (see also Section 1.3). On the other hand, inter-complex

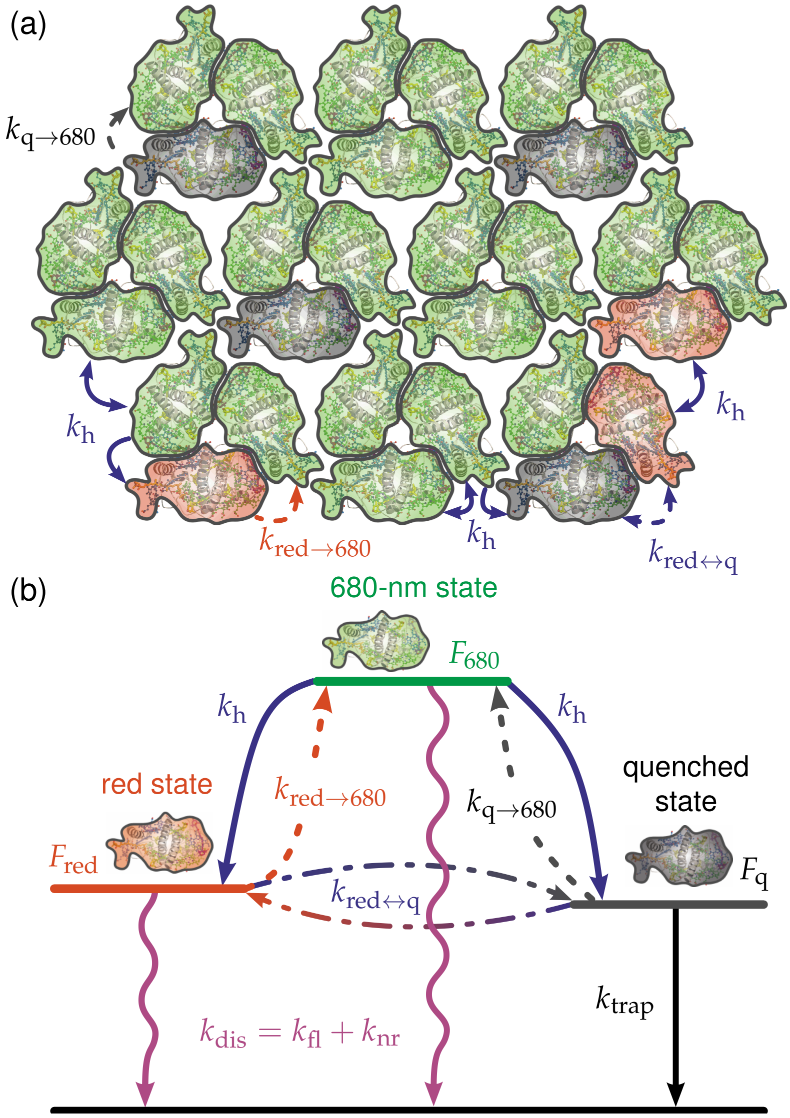

Figure 3.5 | Model for excitation energy transfer in the LHCII aggregate. (**a**) Proposed hexagonal arrangement of the LHCII monomers within the aggregate. Depending on the conformational state of its protein, each LHCII monomer can be in one of the three different states—the 680-nm-emitting one (the most probable, indicated with green), the red-emitting one (indicated with red), and the quenched one (indicated with gray). Inter-monomer excitation hopping rates are indicated with arrows. (**b**) Schematic energy level diagram of different states of the LHCII monomers. Possible transitions and excitation transfer routes between neighboring complexes are indicated with arrows.

excitation transfer rate is supposed to be about an order of magnitude slower [96], so that we can use a coarse-grained model [99–103] to simulate excitation dynamics in the LHCII aggregate. For simplicity, we assume that the LHCII monomer in each state can be described by a single value of (temperature-dependent) free energy $F(T)$, as shown in Fig. 3.5b. Excitation hopping rates between the neighboring complexes of the same free energy as well as those corresponding to a downward energy transfer are assumed to be the same and are denoted as k_h.

The rates of the energetically upward transitions are then rescaled by taking into account the Boltzmann factor. For example, the rate

$$k_{\text{red}\to 680} = k_{\text{h}} \exp\left(-\frac{F_{680} - F_{\text{red}}}{k_{\text{B}}T}\right), \tag{3.2}$$

where k_{B} is Boltzmann constant and T is absolute temperature. The hopping rate k_{h} itself is assumed to similarly depend on temperature:

$$k_{\text{h}} = k_{\text{h}0} \exp\left(-\frac{\Delta E}{k_{\text{B}}T}\right), \tag{3.3}$$

where ΔE is some *activation energy* determining inter-complex excitation transfer that was evaluated by fitting fluorescence excitation kinetics. The parameter $k_{\text{h}0}$ was then chosen in such a way to ensure $k_{\text{h}}^{-1} = 25\,\text{ps}$ at room (300 K) temperature [96,148].

Given all these possible excitation hopping rates between the adjacent monomers, shown in Fig. 3.5, we construct a hexagonal aggregate of 100 complexes, some of which are randomly chosen to be in the red-emitting state and some—in the quenched one. Assuming the homogeneous distribution of the initial excitation over the whole aggregate, its dynamics can be calculated by solving the system of Pauli Master equations:

$$\begin{aligned}\frac{\mathrm{d}}{\mathrm{d}t}P_i(t) = \sum_j k_{j\to i}P_j\left(t\right) - \sum_j k_{i\to j}P_i\left(t\right) - P_i\left(t\right) \times \\ \times \begin{cases} k_{\text{dis}}, & i\text{th complex is in the emitting state,} \\ k_{\text{trap}}, & i\text{th complex is in the quenched state,} \end{cases}\end{aligned} \tag{3.4}$$

where $P_i\left(t\right)$ is the population of the ith complex, $k_{i\to j}$ is the inter-complex excitation hopping rate discussed above, k_{trap} is the excitation trapping time by the quenched LHCIIs (*cf.* Fig. 3.5), and $k_{\text{dis}} = k_{\text{fl}} + k_{\text{nr}}$ is the total excitation dissipation rate due to fluorescence or non-radiative relaxation to the ground state. As discussed in the previous section, this dissipation rate was assumed to be the same for both emitting states (the 680-nm and the red ones) and was determined from our analysis of non-aggregated LHCIIs (see inset in Fig. 3.4b for the temperature dependence of this dissipation rate). The total excitation populations of the 680-nm and red components can then be calculated as the sum of the population of LHCIIs being in a corresponding emitting state. The almost mono-exponential excitation decay kinetics, obtained in such a way, should then be averaged over different random arrangements of red-emitting and quenched LHCIIs within the aggregate as well as over various numbers of such complexes per aggregate. The latter were assumed to be distributed according to Poisson statistics:

$$W_{N_{\mathrm{red}}}^{\langle N_{\mathrm{red}}\rangle} = \frac{\langle N_{\mathrm{red}}\rangle^{N_{\mathrm{red}}} \cdot \mathrm{e}^{-\langle N_{\mathrm{red}}\rangle}}{N_{\mathrm{red}}!}, \quad W_{N_{\mathrm{q}}}^{\langle N_{\mathrm{q}}\rangle} = \frac{\langle N_{\mathrm{q}}\rangle^{N_{\mathrm{q}}} \cdot \mathrm{e}^{-\langle N_{\mathrm{q}}\rangle}}{N_{\mathrm{q}}!}, \tag{3.5}$$

where N_{red} and N_{q} are the actual numbers of the red and quenched complexes during the current realization while $\langle N_{\mathrm{red}}\rangle$ and $\langle N_{\mathrm{q}}\rangle$ denote the corresponding (temperature-dependent) mean values that describe the dynamic equilibrium of the conformational switching between the 3 possible states; $W_{N_{\mathrm{red}}}^{\langle N_{\mathrm{red}}\rangle}$ $(W_{N_{\mathrm{q}}}^{\langle N_{\mathrm{q}}\rangle})$ is the probability to have N_{red} (N_{q}) complexes in the aggregate. By taking into account these random fluctuations of the LHCII aggregate, the desired multi-exponential excitation decay kinetics are obtained that can be further convoluted with a Gaussian function (FWHM = 90 ps) representing the IRF of the experimental setup and then then simultaneously fitted to the decomposed fluorescence kinetics of the two LHCII species shown in Fig 3.3c[9].

3.3.2 Calculated excitation decay kinetics

Fluorescence decay kinetics at different temperatures were fitted independently, thus allowing us to obtain the temperature dependence of the model parameters—the mean numbers of the red and quenched complexes as well as energetically upward excitation transfer rates. For the latter, only rates $k_{\mathrm{red}\to 680}$ and $k_{\mathrm{q}\to 680}$ were considered as independent parameters, while transfer rates between the red and quenched complexes were chosen by setting the downward transfer rate to k_{h} and the upward transfer rate being calculated similarly to Eq. 3.2. To minimize ambiguity of the fitting results, the excitation trapping rate k_{trap} was fixed to be the same at all the temperatures. Moreover, the determined relative amplitudes of the 680-nm and red component kinetics (see Fig 3.2b) were also taken into account, thus additionally restricting possible ranges for the $\langle N_{\mathrm{red}}\rangle$ values. All the kinetics were calculated for the time delays up to 3 ns, where our decomposition is valid (*cf.* Fig. 3.1c) and the generation of any additional states (possibly occurring at later times) can be neglected.

The best-fitted excitation decay kinetics of both states, the 680-nm-emitting and the red one, are presented Fig. 3.6 and reveal a good reproduction of all the decomposed fluorescence kinetics at various temperatures as well as the relative amplitudes of both kinetics. Some discrepancies with the initial rise part of the kinetics from the red complexes can be noted, but they can be attributed to the mis-fitting of the multivariate curve resolution procedure at this region of the strong domination of the 680-nm component; nevertheless, the maximum of the

---

[9] These calculations were carried out by A. Gelzinis from Vilnius University. See [174] for further details.

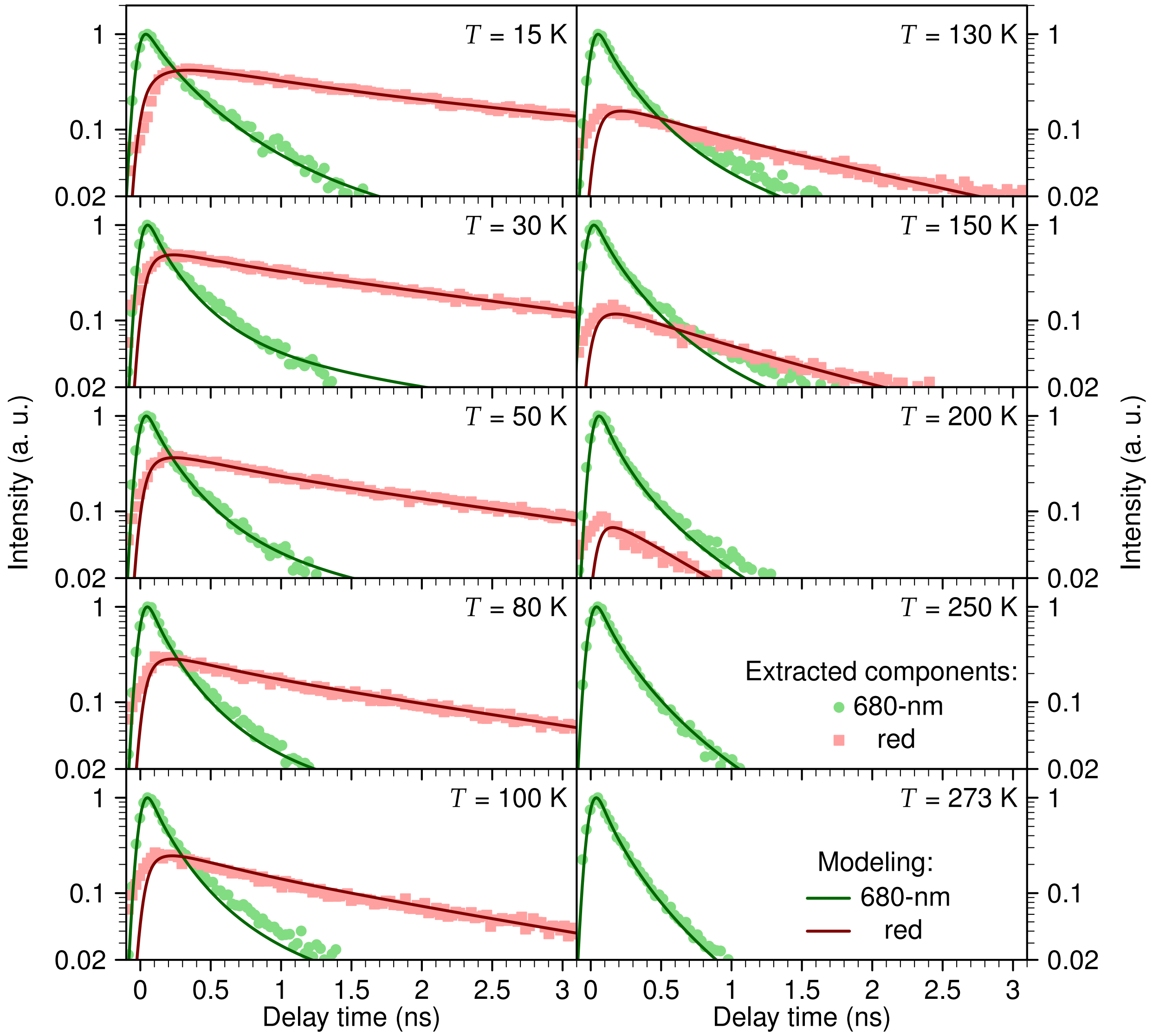

Figure 3.6 | Fitted fluorescence kinetics of the 680-nm and red components in the LHCII aggregate at various temperatures.

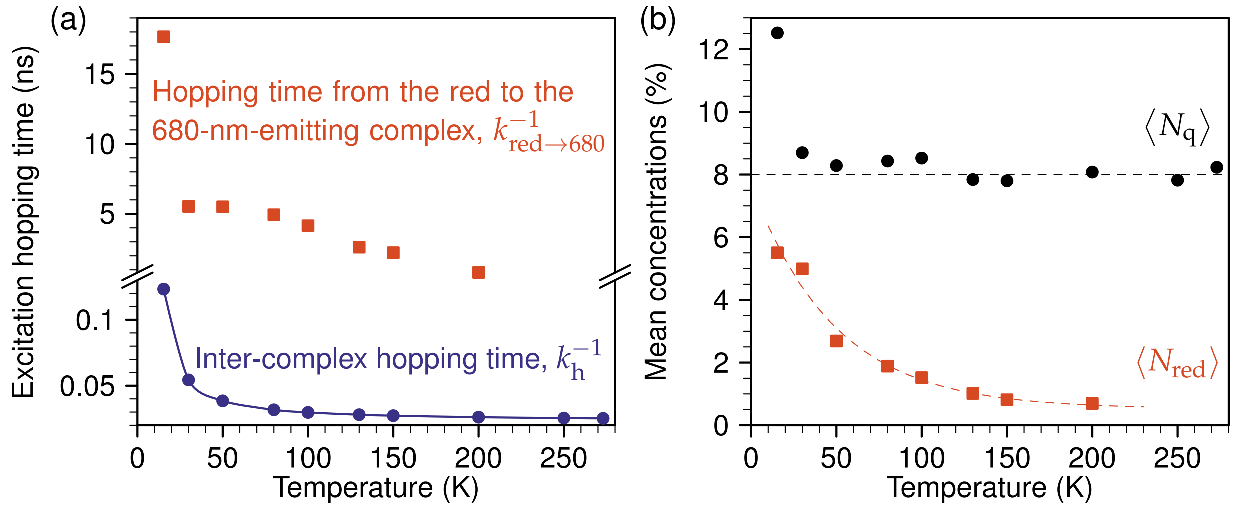

Figure 3.7 | Obtained temperature dependence of the inter-complex excitation hopping times (**a**) and the mean concentrations of the red-emitting and quenched states (**b**).

kinetics of red component was captured by our model at the correctly delayed position.

The kinetics shown in Fig. 3.6 were calculated using the model parameters listed in Fig. 3.7. For the temperature dependence of the inter-complex excitation hopping rate, defined in Eq. 3.3, the activation energy $\Delta E = 18\,\text{cm}^{-1}$ was used (which leads to the temperature dependence of k_h rates as shown Fig. 3.7a), although somewhat similar kinetics can be obtained with any value within the interval from 16 to $22\,\text{cm}^{-1}$. In the latter cases, other fitted model parameters had to be rescaled; nevertheless, their relative dependence on temperature remained the same as shown in Fig. 3.7. Similarly, we found that virtually the same results can be obtained by choosing any value for the trapping rate k_trap within the interval from $(25\,\text{ps})^{-1}$ to $(75\,\text{ps})^{-1}$, while larger discrepancies from the experimental results are faced for the k_trap values lying outside this interval. Such insensitivity of the calculated kinetics to the variations of the trapping rate can be explained by the fact that the quencher was found to be almost irreversible: in all cases, the excitation de-trapping time, $k^{-1}_{\text{q}\to 680}$, was of the order of several ns. Consequently, we get $k_{\text{q}\to 680} \gg k_\text{trap}$, which results in rather undefined specific values for both rates. The situation is completely different for the excitation back-transfer rates from the red-emitting complexes: at all the temperatures except the lowest one, the fitting algorithm has convincingly converged to the $k^{-1}_{\text{red}\to 680}$ values being between 0.8 ns (at 200 K) and 5.5 ns (at 30 K), as demonstrated in Fig. 3.7a. Although being very slow (we have already discussed the requirement for the energetic "deepness" of the red state in a qualitative manner in previous sections), this transfer rate is still faster than or comparable to the intrinsic dissipation rate due to fluorescence or non-radiative decay (*cf.* inset in Fig. 3.4b), leading to its small uncertainty compared with the de-trapping rate from the quenched complexes.

An important outcome from our simulations was very strong dependence of the obtained mean concentration of the red-emitting LHCII states on temperature, yielding an almost 8-fold drop as temperature increases from 15 K to 200 K, see red squares in Fig. 3.7b. At higher temperatures, this dependence can be extrapolated to even smaller values, $\langle N_\text{red} \rangle < 0.6$, that together with the increased backward excitation transfer rate explains why the red-emitting component was not revealed from the multivariate curve resolution analysis at two highest temperatures. Therefore, for simplicity the red states were completely neglected while simulating fluorescence decay kinetics at 250 K and 273 K. Nevertheless, the obtained mean concentrations of the quenched complexes, $\langle N_\text{q} \rangle$, did not differ from those determined at lower temperatures. Differently from the red-emitting states, $\langle N_\text{q} \rangle$ did not demonstrate any pronounced dependence on temperature, exhibiting just some small fluctuation around the value $\langle N_\text{q} \rangle \approx 8\,\%$ (see black circles

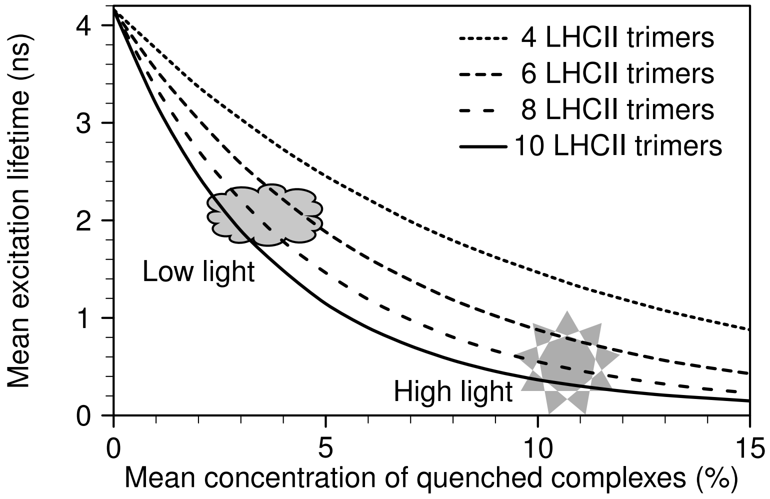

Figure 3.8 | Calculated dependence of the mean excitation lifetime on the mean concentration of the quenched monomers in the small variously sized LHCII aggregates resembling the size of light-harvesting antenna of PSII in intact thylakoid membranes. Shaded regions correspond to the low-light and high-light conditions, respectively.

in Fig. 3.7b). The lowest temperature, $T = 15\,\mathrm{K}$, again falls out of this pattern indicating that at such low temperatures either additional conformational states of LHCIIs become available or the activational temperature dependence of the excitation hopping rate (Eq. 3.3) is violated.

3.3.3 Mimicking PSII antenna in thylakoid membranes

All the results presented so far are related either to the individual LHCII trimers or to their large aggregate. In thylakoid membranes, however, LHCIIs are found to form moderately sized clusters, typically about 3–4 LHCII trimers per RC. Thus the pool of the light-harvesting complexes, separated by the RCs of different PSIIs is composed on average of 6–10 LHCII trimers. To evaluate quenching efficiency in such small antenna systems, the mean excitation lifetime was calculated as a function of the aggregate size and the mean concentration of the quenched complexes within the aggregate:

$$\langle \tau \rangle = \int_0^\infty P(t)\, \mathrm{d}t,$$

where $P(t)$ is the total time-dependent population of the 680-nm-emitting complexes, normalized to 1 at time $t = 0$. For these calculations, we used the parameters extracted from our analysis presented above and corresponding to 273 K, the highest temperature for which intrinsic dissipation rate was determined from the time-resolved fluorescence in LHCII trimers ($k_{\mathrm{dis}}^{-1} = 4.2\,\mathrm{ns}$, *cf.* inset in Fig. 3.4b).

Other rates were chosen to be equal $k_{\mathrm{h}}^{-1} = 25\,\mathrm{ps}$, $k_{\mathrm{trap}}^{-1} = 50\,\mathrm{ps}$, and $k_{\mathrm{q}\to 680}^{-1} = 2\,\mathrm{ns}$ (the calculations were not sensitive to the variations of the latter two rates). For simplicity, no red-emitting complexes were included in this analysis since, as already mentioned, the above calculations suggest vanishingly small concentration of the red-emitting states at higher temperatures.

By changing the size of the aggregate and the mean number of LHCII monomers being in the quenched state, the obtained variations in the mean excitation lifetime are presented in Fig. 3.8. From these dependencies we can see that the probability of just several percent for LHCII to switch into its quenched state is enough to reduce the mean fluorescence lifetime from ~4 ns seen in the LHCII trimers down to ~2 ns observed in intact thylakoids with the closed RCs [166] or even smaller values in the LHCII liposomes [139]. Interestingly, the analysis of fluorescence blinking in single LHCII trimers, discussed in Section 2.2, has also revealed the probability of quenched states being of the order of several percent. Any further environmentally induced slight increase of the concentration of the quenched complexes, potentially accompanied with a physical increase of the antenna size [15], can provide additional 3–4-fold drop of the fluorescence quantum yield, typically observable under NPQ conditions (*cf.* shaded regions in Fig. 3.8).

3.4 Towards the underlying molecular mechanisms

From the fluorescence measurements and simulations of excitation decay kinetics presented above, several important features of the *red-emitting states* are revealed: (i) their fluorescence spectra (Fig. 3.3b) are much broader than those of the dominating 680-nm-emitting states and exhibit a considerable blue shift upon temperature decrease, (ii) the mean concentration of the red-emitting complexes strongly varies with temperature (Fig. 3.7b), and (iii) the fluorescence from the red states decays on a nanosecond timescale (Fig. 3.3c). All these observations together provide a deep insight into the molecular mechanism that is responsible for the red-shifted LHCII fluorescence. Recent studies revealed that the formation of mixed excitonic and charge transfer (CT) states having strong interactions with the unharmonic environment [186] might lead to the significant temperature-dependent variations of the peak position of absorption (and, thus, fluorescence) spectrum. The same effect can also readily explain our second observation. Indeed, depending on local environmental conditions, numerous Chl–Chl CT states with varying energies can be formed in distinct LHCII complexes, but only some of them (those enclosed into a box in Fig. 3.9) are mixed with other Chl excitonic states and can efficiently collect excitation coming from the antenna. The increase of the energy of all the CT states, induced at lower temperatures by the unharmonic environment, results in both the blue-shifted peak position of the fluorescence spectrum

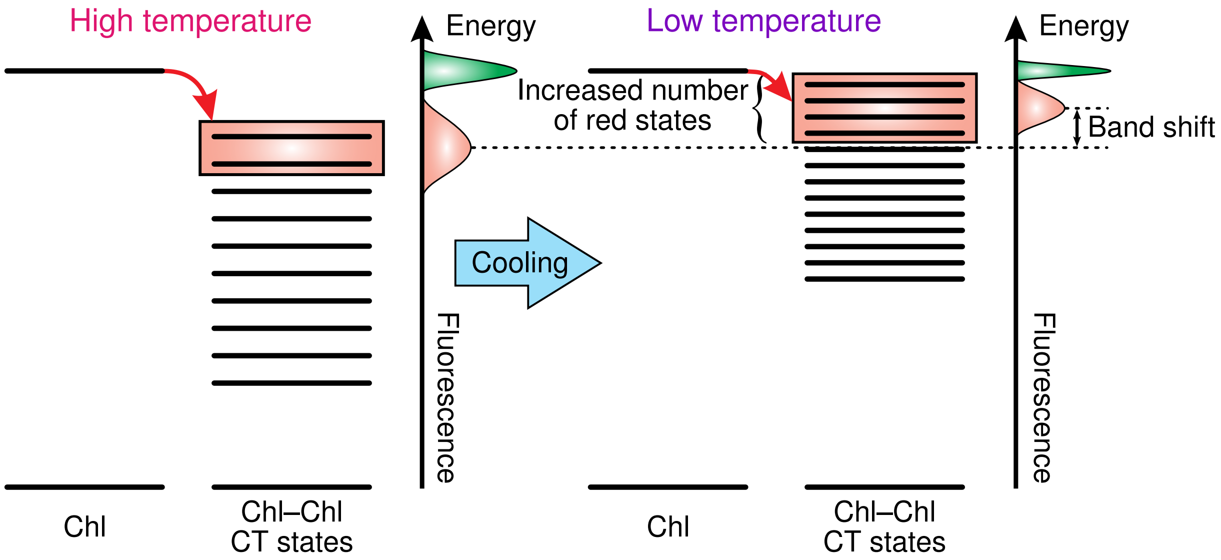

Figure 3.9 | Illustration of the effect of Chl–Chl charge transfer state that can explain both the blue shift of the fluorescence peak as well as the increased concentration of the red-emitting states at lower temperature.

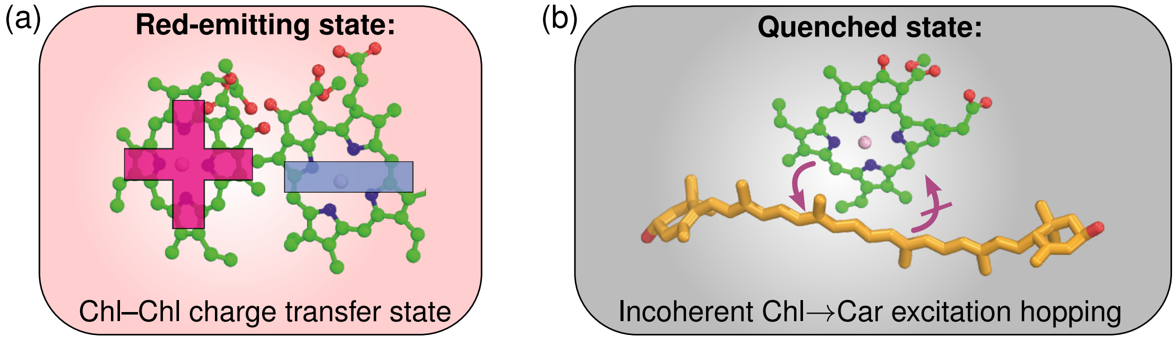

Figure 3.10 | Proposed molecular mechanisms responsible for the formation of the red-emitting (**a**) and quenched (**b**) states of LHCII complexes.

of red component as well as in the increased concentration of the red states per aggregate, *i.e.* the number of CT states that can be significantly mixed with the excitonic ones. Finally, the slow excitation decay from the red state excludes the participation of the short-lived carotenoid states. Therefore our results provide an independent confirmation that the physical origin of the red-shifted fluorescence is related to the formation of the *Chl–Chl CT states* (schematically shown in Fig. 3.10a), as proposed earlier on the basis of the Stark spectroscopy applied to the LHCII complexes [104].

Even more importantly, our simulations also uncovered some properties of the *quenched* LHCII complexes that can help to distinguish between distinct mechanisms proposed so far to govern NPQ [12]. First, contrarily to the case of the red-emitting complexes, the obtained mean concentration of the quenched states did not exhibit any notable dependence on temperature (*cf.* Fig. 3.7b), meaning that the physical origin of both states is totally different. This implies that pronounced excitation quenching is unrelated to the formation of any CT states (either chlorophyll or carotenoid), in contrast to some earlier proposals [22]. Second, the simulation results show that the quenched states of LHCIIs are energetically deep, with excitation de-trapping generally taking several ns. This observation indicates a relatively fast unidirectional excitation transfer within the quenched complex from the Chl pigments to the intrinsic trapping centers and rules out the quenching mechanism based on the coherent mixing between the Chl and Car S_1 states [52]. Indeed, since the excitation flows between coherently coupled states more freely, it could also easily escape from the quenched complex itself back to the antenna, contradicting our determined minor reversibility of NPQ. As a result, the only remaining mechanism that is consistent with all our data is an *incoherent* excitation energy transfer to the short-lived S_1 state of the Car molecules (schematically shown in Fig. 3.10b).

Based on the structure-based quantum chemistry calculations that were discussed in Chapter 1, the most probable candidate for the quenching site is one (or both) of two luteins located in the very heart of the LHCII monomer. Interestingly, in our all-pigment model of the crystallized LHCIIs, formulated in Section 1.3, the mean excitation lifetime in the quenched monomer was just 65 ps, which resembles the possible trapping-times k_{trap}^{-1} determined from the coarse-grained model of LHCII aggregate. This fact provides an additional support for the revealed NPQ mechanism. However, further experiments, *e.g.* on LHCII mutants lacking some specific Cars, are required to pinpoint the exact spatial location of the quenching site more accurately. Similarly, the identification of the exact pigments involved in the formation of CT states may clarify the functional importance of the red-emitting state of LHCII, which seems questionable in PSII–LHCII supercomplexes but might facilitate light harvesting and excitation energy transfer when LHCIIs become associated with photosystem I, as observed during state transitions [16].

3.5 Summarizing remarks

Despite being relatively simple, time-resolved fluorescence measurements have proven to reveal a lot of information on excitation energy transfer in molecular systems. The obtained fluorescence decay kinetics usually lack any exciton–exciton annihilation that cannot be avoided in transient absorption or nonlinear spectroscopy measurements, therefore the registered data can be rather easily and straightforwardly interpreted. In this chapter, we employed the advantage of the streak-camera spectrograph being able to simultaneously measure both temporal and spectral characteristics of the fluorescence signal. The experimentally collected data was analyzed in terms of multivariate curve resolution that allowed us to reveal multiple functionally distinct states of LHCII complexes co-existing within their aggregate. While the multi-exponential decay behavior of the fluorescence kinetics was readily described by the dynamic variations of the number of antenna complexes being in different states, the temperature dependence of the concentrations of these states provided possibility to unambiguously connect each state with its underlying molecular nature. As a result, the red-shifted fluorescence was attributed to a formation of Chl–Chl charge transfer state whereas the excitation quenching was found to be related to the incoherent Chl-to-Car energy transfer.

Based on these results, the significant fluorescence quenching in LHCII aggregates was demonstrated to be a collective phenomenon arising from the interconnectivity of many conformationally fluctuating LHCII complexes, only several of them being in quenched state. This observation leads to a conclusion that the same mechanism plays a major role in NPQ in intact thylakoid membranes, where much smaller number of LHCII trimers are closely inter-connected within the light-harvesting antenna of PSII. Exposure to any ambient stress (like temperature, pH level, or even different levels of aggregation) shifts the dynamic equilibrium between the possible conformational states of a single LHCII, thus varying the relative concentrations of these states in the ensemble. In relatively small antenna systems, a slight variation of the concentration of the quenched complexes can significantly reduce the mean excitation lifetime and the resulting fluorescence quantum yield. The physical increase of the antenna size by just a single LHCII trimer provides an additional possibility to enhance quenching efficiency. As a result, NPQ traps that can be (even with a very low probability of several percent) generated anywhere in the antenna allow photosynthetic organisms to *gradually* adapt to the varying light conditions and adjust NPQ efficiency by a certain degree that prevents photodamage but at the same time is not too high to negatively affect photochemistry in the RCs. We will turn back to this property of NPQ traps in Chapter 5.

> “ *Whatever appears as a motion of the Sun is really due rather to the motion of the Earth.*
>
> NICOLAUS COPERNICUS

Chapter 4

Light harvesting in fluctuating antenna systems

In the previous chapters, several cases of non-exponential fluorescence decay kinetics in the photosynthetic light-harvesting complexes were faced—the obvious bi-exponential kinetics in single LHCII trimers were attributed to the varying number of the generated triplet states, and the multi-exponential kinetics in LHCII aggregates were readily explained by the varying concentrations of the pigment–proteins being in intrinsically different states. The discussion on the multi-exponentiality in light-harvesting antennae would not be complete without referencing the fully functional photosystems II that posses just a single major quencher with a spatially well-defined position—the reaction center. Nevertheless, PSII was found to also exhibit pronounced non-exponential fluorescence decay kinetics which for decades have been ascribed to reversible charge separation taking place in the RC. However, in this description the protein dynamics is not taken into consideration. The intrinsic dynamic disorder of the light-harvesting proteins along with their fluctuating dislocations within the antenna inevitably result in varying connectivity between pigment–protein complexes and therefore can also lead to non-exponential excitation decay kinetics. Based on this presumption, a simple conceptual model describing excitation diffusion in a continuous medium and accounting for possible variations of the excitation transfer rates is proposed in this chapter. This model is then successfully applied to describe fluorescence kinetics originating from very diverse antenna systems, ranging from PSII of various sizes to the LHCII aggregates and even the entire thylakoid membrane. In all cases, complex multi-exponential fluorescence kinetics are perfectly reproduced on the entire relevant time scale without assuming any radical pair equilibration at the side of the excitation quencher, but using just a few parameters reflecting the mean excitation energy transfer rate as well as the overall average organization of the photosynthetic antenna. Additionally, the proposed fluctuating antenna model in a straightforward way solves various contradictions currently existing in the literature[10].

---

[10] The results presented in this chapter are based on the works published in [187, 188].

4.1 Open questions on excitation dynamics in photosystem II

Among all supramolecular photosynthetic complexes, photosystem II from green plants, algae and cyanobacteria has always attracted a lot of attention due to its outstanding physiological significance: as already mentioned in the Introduction, the reaction center of PSII uses water as primary electron donor and, as a by-product of photochemical reactions, generates molecular oxygen indispensable for all aerobic organisms [4]. Occupying a large part of the thylakoid membrane, PSII supercomplexes are present mainly in dimeric form [185,189]. The schematic mutual arrangement of the pigment–protein complexes in PSII is presented in Fig. 4.1a. The core of PSII—the minimal functionally-independent structural element that is able to perform water splitting—consists of an RC that is bound to the core antenna proteins (CP43 and CP47). The PSII core is surrounded by several LHCII trimers which are coupled to the core via the minor monomeric complexes CP24, CP26 and CP29.

Crystal structures of LHCII [38], CP29 [73] and PSII core complexes [74], obtained with a resolution higher than 3 Å, provided essential information about the structural organization of these complexes. A series of time-resolved spectroscopic measurements, accompanied with structure-based theoretical modeling [40,42–44,75,76,98,190], contributed to a deeper insight into details of excitation energy transfer dynamics in PSII complexes. Recent advances in understanding of these topics as well as the internal organization of PSII from the level of individual complexes to the entire thylakoid membrane are reviewed in [6,9–11]. However, a complete detailed model of light-harvesting in PSII is still a challenge because it requires not only to know the *static* spectroscopic properties and precise mutual arrangement of the pigment molecules, but also to understand how the intrinsic disorder and *dynamic* fluctuations of the considered biological system can influence these properties and the overall excitation dynamics [10].

At the heart of such dynamic fluctuations, which may have a serious impact on the efficiency of photosynthesis and usually cannot be simply ignored, is a high level of flexibility as well as ability of light-harvesting systems to adapt quickly and reversibly to the varying environmental conditions. On the macroscopic level, it was revealed that during the so-called state transitions (occurring under specific excitation conditions) distinct LHCII trimers can diffuse through the thylakoid membrane from PSII towards PSI to optimize the relative fluxes of the incoming light photons in both photosynthetic units [191]. The movement and reorganization of the antenna complexes are also pronounced during protein repair [3,4] and during the adaptation to the increased solar radiation on a sunny day [15,16]. Finally, as already discussed in previous chapters, pigment–protein complexes themselves exhibit intrinsic conformational dynamics occur-

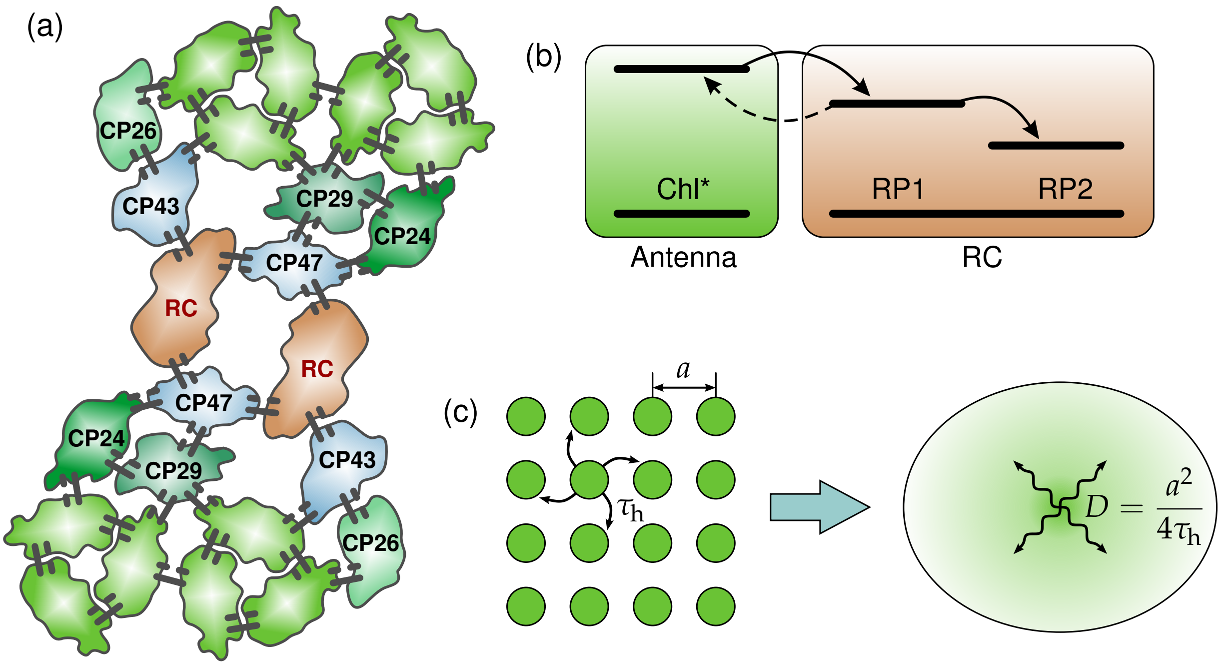

Figure 4.1 | (**a**) Schematic structure of the largest purified PSII supercomplexes ($C_2S_2M_2$, notated below as B11) exhibiting its dimeric nature. LHCII trimers are presented in light green and are not labeled. Thick solid gray bars indicate pathways of inter-complex excitation energy transfer, as used in the coarse-grained (CG) model; on the other hand, broken gray lines demonstrate that due to structural fluctuations of PSII (occurring on a timescale longer than excitation mean lifetime) the efficiency of these pathways is not constant, which results in the varying rates of the excitation energy transfer. This assumption is the prerequisite of fluctuating antenna model. (**b**) Trap-limited ERPE model of excitation dynamics in PSII, assuming instantaneous Boltzmann-equilibration between PSII excited state and first radical-pair (RP1) state in RC. (**c**) Switching from the CG model to the diffusional limit, when excitation migration through the antenna is described by a single diffusion equation (two-dimensional ($d = 2$) case).

ring on a molecular level on a sub-ms timescale and manifesting itself via fluorescence blinking [108, 109] and spectral diffusion [107]. Prior to making a first attempt to phenomenologically account for these fluctuations, we will shortly discuss currently existing theoretical models of excitation energy transfer within the photosynthetic antenna and outline several recent experimental studies that have revealed some contradictions in our current understanding of light-harvesting processes in biological systems.

4.1.1 Trap-limited *vs.* migration-limited regime

Starting from the very first picosecond time-resolved fluorescence measurements, the excitation radical-pair equilibrium (ERPE) model has been suggested and widely used for interpretation of the fluorescence decay kinetics of PSII [155, 171, 184, 192]. In this simple model, summarized in Fig. 4.1b, it is assumed that the initial excitation instantaneously equilibrates over the whole light-harvesting system, so that the overall process of excitation decay depends only on the rate of charge separation in the RC and the energy difference between the thermally equilibrated excited state of PSII and the first radical-pair (RP) state in the RC. Therefore, according to this approach, the excitation dynamics in PSII is a *trap-limited* process. However, this model contradicts the results of singlet–singlet exciton annihilation studies on LHCII aggregates [142,148,149]: in the case of instantaneous excitation equilibration over the whole quenched aggregate, the normalized transient absorption kinetics would be almost independent of the intensity of initial excitation [102], as opposed to the actual observations. In fact, fluorescence measurements [193] as well as structure-based calculations [98, 194] of PSII core predicted a slow (at least several tens of ps) energy transfer between the core antenna complexes (CP43/CP47) and the RC, suggesting a *transfer-to-trap limiting* (TTL) regime.

Later, the theoretical description was extended by taking into account the structural arrangement of the pigment–protein complexes of PSII in a superlattice form, as determined by means of electron microscopy [189,195]. The resulting coarse-grained (CG) model [99–101, 103] (see Fig. 4.1a) assumed an instantaneous excitation equilibration within a given antenna complex only, whereas the inter-complex excitation migration towards the RC was explicitly taken into account and described by a single parameter—the mean excitation hopping time, τ_h. In previous chapter, we used slightly adopted variation of this CG model to model excitation dynamics in the LHCII aggregates. Depending on the antenna size and the excitation migration rate, CG model can either present some perturbation to the *trap-limited* model [196] or describe the excitation dynamics as a *migration-limited* process. In fact, the mean excitation lifetime, $\langle\tau\rangle$, can be split into three terms describing excitation migration through the antenna (τ_mig), its subsequent delivery from the core antenna complexes to the RC (τ_del) followed by the charge separation (τ_CS) [5]:

$$\langle\tau\rangle = \tau_\mathrm{mig} + \tau_\mathrm{del} + \tau_\mathrm{CS}. \tag{4.1}$$

The relative magnitudes of these terms should then define which regime is the most appropriate.

It was found [100] that excitation of the outer antenna in the PSII membranes (so-called BBY particles, on average containing 2.5 LHCII trimers per RC) leads to longer excited-state lifetimes than direct excitation of the core. The excitation kinetics in the entire thylakoid membranes (with 4 LHCII trimers per RC) [197] suggested that at least 50 % of the overall lifetime of excited-state in PSII arises from the migration term. Recently, a first attempt was made to describe the ex-

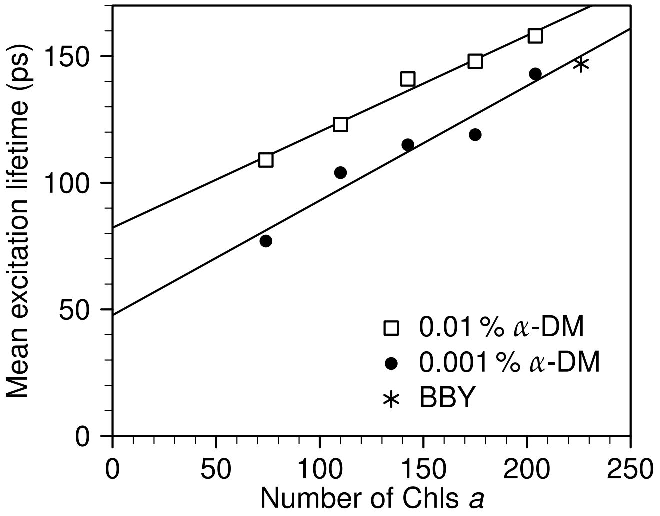

Figure 4.2 | Mean excitation lifetimes *vs.* number of Chl *a* molecules per PSII of different antenna size being solubilized at various detergent concentrations (0.01 or 0.001 % α-DM) as well as in BBY particles. The lines present linear fits that do not approach zero as number of Chl *a* pigments vanishes. Data taken from [103].

citation dynamics within the PSII supercomplex by using a combined Generalized Förster / Modified Redfield approach [96] while merging the existing high-resolution crystal structures of individual pigment–protein complexes with a low-resolution image of the whole PSII supercomplex. As a result, a dominating role of the first two terms in Eq. 4.1, comparable one to another, was demonstrated. However, this conclusion should still be considered rather cautiously since it was obtained for a single static arrangement (*"snapshot"*) of the pigment–proteins and did not take into account any *dynamic* reorganization of PSII structure.

4.1.2 Novel experimental data

Recently performed time-resolved fluorescence measurements of the excitation decay kinetics of variably-sized PSII supercomplexes [103] provided additional data to test the existing models for their response to the changes in antenna size. However, these measurements also cast some doubts on the contemporary fundamental understanding of light-harvesting processes in PSII. First of all, it was shown that the mean excitation lifetime in PSII increases linearly with the number of chlorophyll pigments present in the antenna (see Fig. 4.2). However, upon extrapolation to the systems with vanishing antenna size, the mean excitation lifetime did not converged to zero but to some finite value between 50 and 80 ps. Contrarily, ERPE, CG, and TTL models predict a nearly linear, zero-crossing relationship between both the migration (τ_{mig}) and delivery (τ_{del}) terms of the mean lifetime (see Eq. 4.1) and the number of antenna pigments [5]. Therefore, according to the mentioned models, the extrapolated values might be only related to the intrinsic trapping timescale (τ_{CS}) and for the open RCs are obviously too slow.

Another important issue regarding the excitation energy transfer in PSII is the multi-exponential fluorescence decay kinetics observed in nearly all sample preparations independently of the antenna size [99, 103, 198]. All the models discussed so far predict almost mono-exponential kinetics in the case of irreversible charge separation in the RCs. Therefore, in order to deal with such multi-exponential behavior, all the models had to assume energy equilibration between the radical pair state in the RC and the neighboring antenna pigments. The RC is then treated as a trap with the non-zero possibility of charge recombination. In order to properly describe fluorescence decay kinetics for all the experimental data, it had to be assumed that the intrinsic rate of charge separation in the RC strongly depends on the size of the distant peripheral antenna [103]. Furthermore, the commonly used postulation of radical pair equilibration contradicts another recent claim that initial charge separation in the RC is indeed virtually irreversible [199], which was also proposed in other studies [96, 98]. If so, a fundamental question about the basic properties of the excitation energy dynamics in PSII arises: if not the radical pair equilibration in the RC, then *what* is the origin of the non-monoexponential fluorescence decay kinetics? The possible answer is concealed in the fluctuating properties of light-harvesting antenna, as has been determined by means of electron microscopy [10, 189].

It is well-known that in disordered systems non-exponential behavior sometimes may arise due to statistical averaging of the exponential decay kinetics over some particular distribution of the rate constants [200] and site energies [98], or when dynamic disorder is taken into account [201]. In the previous chapter, for example, the multi-exponential decay kinetics was obtained by averaging over random distribution of LHCIIs being in a particular state within the aggregate as well as Poisson distribution of the exact number of these states. High rate of charge separation by RC, however, excludes such possibility in the case of smaller PSII. On the other hand, a relatively high level of intrinsic disorder along with the mobility of the light-harvesting antenna [10,12] suggest that the internal structure of PSII is not static, so that the distances between the pigment–protein complexes and their mutual orientation constantly vary in time causing temporal fluctuation of the inter-pigment coupling strength and, as a result, of the inter-pigment excitation energy transfer rate. If such conformational dynamics occurring within the same pigment–protein can force it to switch constantly and randomly between different states that are completely opposite in nature and represent light-harvesting and quenched states [109–111], at the level of the entire PSII such intrinsic fluctuations along with the macroscopic reorganization of the antenna complexes might lead to even more drastic and unexpected results. This implies that any *static* model of the PSII antenna described by a fixed set of pigment pools and constant excitation hopping times is most likely not sufficient. For a proper description of light-harvesting processes, the dynamic fluctuations and reorganization of the whole antenna should be taken into consideration. However, this is a challenging task requiring precise time-resolved experimental structural data as well as computationally-expensive molecular dynamics simulations. Therefore, below we propose a simple *conceptual* model of excitation diffusion in a continuous medium taking into account possible variations of inter-complex connectivity. We show that even such an oversimplified approach can perfectly describe the multi-exponential fluorescence decay kinetics without assuming the radical pair equilibration in the RC. Moreover, this model also naturally solves the problem that the excitation mean lifetime does not extrapolate to zero in case of vanishing antenna size. Additionally, it provides some information about the structural organization of the photosynthetic antenna (either planar or stacked) as well as the disturbances in the inter-complex connectivity reflected by the obtained fractional dimensionality of PSII.

4.2 Fluctuating antenna model

As discovered in recent studies, a contribution from long-lived quantum coherence might influence inter-pigment excitation dynamics on a fast, sub-picosecond timescale [7,202,203]. On the other hand, these quantum effects are usually much less pronounced or even disappear on the longer timescale of excitation migration through the whole PSII, which takes from tens to hundreds of ps. Therefore, excitation energy transfer in the light-harvesting antenna is often described by the Pauli Master equations (see, e.g. [204]), which is also the case for the coarse-grained model [99–101,103] and the detailed domain model [96]:

$$\frac{\mathrm{d}}{\mathrm{d}t}p_i\left(t\right)=\sum_j k_{j\to i}p_j\left(t\right)-\sum_j k_{i\to j}p_i\left(t\right). \tag{4.2}$$

Here $p_i\left(t\right)$is the time-dependent probability for the excitation to reside on the ith pigment–protein complex (in the CG model [99]) or in the ith domain of strongly-coupled pigments (in the domain model [96]), and $k_{i\to j}$ is the effective rate of excitation transfer from the ith to the jth complex (or domain), intrinsically taking into account all the quantum effects being relevant within the given complex or domain. For a while, we neglected the dissipation and trapping terms analogical to those introduced in Eqs. 1.8 and 3.4. In the ideal *square lattice* (Fig. 4.1c), where excitation transfer between the adjacent domains only (separated by the distance a) is taken into account (with the constant excitation hopping time $\tau_\mathrm{h}=k_{i\to j}^{-1}$), the system of the Master equations (Eq. 4.2) can be well-approximated by a single equation describing excitation diffusion in a continuous 2-dimensional medium:

$$\frac{\partial}{\partial t} p\left(x, y, t\right) = D \nabla^2 p\left(x, y, t\right). \tag{4.3}$$

Here $\nabla^2 = \frac{\partial^2}{\partial x^2} + \frac{\partial^2}{\partial y^2}$ is the 2-dimensional Laplace operator, $p\left(x, y, t\right)$ is the excitation density at the point $\left(x, y\right)$ at time t, and $D = a^2 / \left(4\tau_{\mathrm{h}}\right)$ is the excitation diffusion constant for this particular square lattice. Below we use a similar approach to describe excitation energy transfer through PSII by a single diffusion equation. However, to account for the varying inter-complex connectivity, additional assumptions by formulating a *fluctuating light-harvesting antenna model* are needed.

4.2.1 Model formulation

As already discussed, in the case of irreversible charge separation the observed multi-exponential excitation decay kinetics in PSII become hardly comprehensible. In the case of PSII, the location of the excitation trap—the RC—is fully determined, whereas due to flexibility of the whole system the inter-connectivity between different subunits remains unresolved. Therefore the fluctuating motion of the protein scaffold can result in varying arrangement of the network of excitation transfer pathways. As will be shown below, the averaging over the ensemble of these distinct pathways will lead to non-exponential excitation decay kinetics.

To deal with a random distribution of excitation transfer pathways, in zero-order approximation one can simplify the task and neglect the discrete nature of mutual arrangement of Chl molecules by considering excitation diffusion in a continuous medium. Such a simplification and the lack of connectivity in some antenna points can then be (at least partially) accounted for by allowing the dimensionality of that continuous medium to be described by a *fractional* number d $\left(1 \leq d \leq 3\right)$ [5, 102, 205]. This approach extends previous studies on non-exponential excitation decay kinetics in 1-dimensional systems arising from the presence of randomly distributed traps [206, 207].

We assume that the initial point-like excitation is completely trapped after diffusing for some random distance R which mimics some particular length of the excitation pathway towards the RC. The time evolution of the excitation in such a system can be described by a diffusion equation similar to Eq. 4.3:

$$\frac{\partial}{\partial t} p\left(\mathbf{r}, t | R\right) = D \nabla_d^2 p\left(\mathbf{r}, t | R\right), \tag{4.4}$$

with the initial condition expressed as $p\left(\mathbf{r}, t = 0 | R\right) = \delta\left(\mathbf{r}\right)$ and the boundary condition given by $p\left(\mathbf{r}, t | R\right) \big|_{|\mathbf{r}| = R} = 0$. Here $p\left(\mathbf{r}, t | R\right)$ is the density of the survived excitation at the time moment t, parametrically depending on R; D is the diffusion constant; and $\delta(\mathbf{r})$ is the Dirac delta-function determining the initial point-like excitation, corresponding to the excitation of some particular complex in the CG model. Due to the spherical symmetry of the excitation migration the Laplacian ∇_d^2 depends on the distance r only, and in a d-dimensional system it is defined as follows [208]:

$$\nabla_d^2 = \frac{\partial^2}{\partial r^2} + \frac{d-1}{r}\frac{\partial}{\partial r}. \tag{4.5}$$

By separating the variables r and t, the solution of Eq. 4.4 can be written as

$$p(\mathbf{r}, t|R) \equiv p(r, t|R) = \sum_n f_n(r|R) \cdot \mathrm{e}^{-\varepsilon_n(R)t}, \tag{4.6}$$

here $f_n(r|R)$ and $\varepsilon_n(R)$ are the eigenfunctions, obeying the boundary condition

$$f_n(r|R)\big|_{r=R} = 0, \tag{4.7}$$

and the eigenvalues of the equation

$$D\nabla_d^2 f_n + \varepsilon_n f_n = 0, \tag{4.8}$$

respectively. By substituting the Laplacian from Eq. 4.5 into Eq. 4.8 we obtain a well-known Bessel equation

$$r^2 f_n''(r|R) + r(d-1) f_n'(r|R) + r^2 \frac{\varepsilon_n}{D} f_n(r|R) = 0. \tag{4.9}$$

The general solution of Eq. 4.9 can be written as a superposition of the linearly independent Bessel functions $J_{\pm\nu}(\xi)$ of the positive and negative non-integer orders $\pm\nu = \pm\left|1 - \frac{d}{2}\right|$. In the case of integer $\nu = 0$ (corresponding to $d = 2$) the solution is expressed as a superposition of Bessel and Neumann functions:

$$f_n(r|R) = \begin{cases} r^{1-\frac{d}{2}}\left[A_n J_{\left|1-\frac{d}{2}\right|}\left(\sqrt{\frac{\varepsilon_n}{D}} \cdot r\right) + B_n J_{-\left|1-\frac{d}{2}\right|}\left(\sqrt{\frac{\varepsilon_n}{D}} \cdot r\right)\right], & d \neq 2, \\ A_n J_0\left(\sqrt{\frac{\varepsilon_n}{D}} \cdot r\right) + B_n N_0\left(\sqrt{\frac{\varepsilon_n}{D}} \cdot r\right), & d = 2, \end{cases} \tag{4.10}$$

where $N_0(\xi)$ is the Neumann function of the 0th order. In order to satisfy the initial condition of Eq. 4.4 and ensure finite values of $f_n(r|R)$ and its derivative at $r = 0$, we should take $B_n = 0$ in the case of $d \geq 2$ and $A_n = 0$ for $d < 2$. As a result, Eq. 4.10 simplifies just to

$$f_n(r|R) = C_n r^{1-\frac{d}{2}} J_{\frac{d}{2}-1}\left(\sqrt{\frac{\varepsilon_n}{D}} r\right), \qquad 0 < d \leq 3. \tag{4.11}$$

By taking into account the boundary condition (Eq. 4.7), the eigenvalues ε_n can be expressed as $\varepsilon_n = D\big(\xi^{(n)}_{d/2-1}/R\big)^2$, where $\xi^{(n)}_{d/2-1}$ is the nth zero of the Bessel function $J_{d/2-1}(\xi)$, obeying the equation

$$J_{d/2-1}\big(\xi^{(n)}_{d/2-1}\big) = 0.$$

Finally, the coefficients C_n in Eq. 4.11 can be obtained, as usual, simply by multiplying both sides of the equation for initial conditions,

$$p\,(\mathbf{r}, t = 0|R) = \sum_n f_n\,(r|R) = \delta(\mathbf{r}),$$

by $f_m\,(r|R)$ and integrating over the whole volume $V(R)$, which in d-dimensional space is given by [208]

$$V(R) = \frac{\pi^{d/2}}{\Gamma\left(\frac{d}{2}+1\right)} R^d. \tag{4.12}$$

Here $\Gamma\,(z)$ stands for the Gamma-function. By taking into account the orthogonality of the functions $f_n\,(r|R)$ and $f_m\,(r|R)$, corresponding to different indices n and m, we finally obtain

$$C_n = \frac{1}{\pi^{d/2}R^2}\frac{1}{\left[J_{d/2}\left(\xi^{(n)}_{d/2-1}\right)\right]^2}\left[\frac{\xi^{(n)}_{d/2-1}}{2R}\right]^{\frac{d}{2}-1}. \tag{4.13}$$

As a result, the total solution for the diffusion equation 4.4 can be written as

$$p\,(r,t|R) = \sum_{n=1}^{\infty} C_n\, r^{1-\frac{d}{2}} \cdot J_{d/2-1}\left(\xi^{(n)}_{d/2-1}\cdot \tfrac{r}{R}\right)\cdot \exp\left[-\big(\xi^{(n)}_{d/2-1}/R\big)^2 Dt\right], \tag{4.14}$$

where coefficients C_n are given by Eq. 4.13. For integer dimensions d this equation simplifies to the well-known expressions [102]:

$$p\,(r,t|R) = \begin{cases} \frac{1}{R}\sum\limits_{n=1}^{\infty}\cos\frac{(2n-1)\pi r}{2R}\exp\left[-\frac{(2n-1)^2\pi^2 Dt}{4R^2}\right], & d=1; \\ \frac{1}{\pi R^2}\sum\limits_{n=1}^{\infty}\frac{J_0\left(\xi^{(n)}_0\cdot\frac{r}{R}\right)}{\left[J_1\left(\xi^{(n)}_0\right)\right]^2}\exp\left[-\frac{\left(\xi^{(n)}_0\right)^2 Dt}{R^2}\right], & d=2; \\ \frac{1}{2R^2}\sum\limits_{n=1}^{\infty}\frac{n}{r}\cdot\sin\frac{n\pi r}{R}\exp\left[-\frac{n^2\pi^2 Dt}{R^2}\right], & d=3. \end{cases}$$

Finally, by integrating Eq. 4.14 over the whole volume $V\,(R)$ confined by the spherical boundary of the radius R, we obtain the total population of the excitation survived in the system until the time t:

$$P\left(t|R\right) = \int\limits_{V(R)} p\left(r,t|R\right)\,\mathrm{d}V = \frac{4}{2^{d/2}\Gamma\left(\frac{d}{2}\right)} \sum_{n=1}^{\infty} \frac{\left(\xi^{(n)}_{d/2-1}\right)^{d/2-2}}{J_{d/2}\left(\xi^{(n)}_{d/2-1}\right)} \cdot \mathrm{e}^{-\left(\xi^{(n)}_{d/2-1}/R\right)^2 Dt}. \tag{4.15}$$

As expected, the proper choice of the coefficients C_n in Eq. 4.14 ensures that $P\left(t=0|R\right) = 1$.

4.2.2 Averaging kinetics

The excitation decay kinetics presented by Eq. 4.15 was obtained by assuming that the excitation has been diffusing in an unperturbed way inside the d-dimensional sphere of radius R and volume V. In other words, this equation corresponds to some specific excitation pathway of the length R on its route towards the RC. Averaging over all possible pathways in this case can be performed similarly as it was done in the previous chapter while analyzing excitation dynamics in the LHCII aggregates with randomly distributed traps. Free diffusion inside the sphere of radius R means that there were no additional traps (*i.e.* RC) inside that sphere. We assume that the traps (or, in other words, the path lengths to the RC) are distributed according to Poisson statistics, so that the probability to obtain k traps inside some volume V is given by

$$W^{(k)}\left(V\right) = \frac{\bar{N}^k}{k!}\mathrm{e}^{-\bar{N}},$$

where $\bar{N} = cV$ is the average number of the traps in the volume V and c is an average concentration of the traps. Then the probability to find no traps inside the sphere of volume V can be written as $W^{(0)}\left(V\right) = \mathrm{e}^{-cV}$. This quantity can be treated as the (non-normalized) probability density $\omega\left(V\right)$ for obtaining the system with some particular value of V. After normalizing the total probability $\int_0^{\infty} \omega(V)\,\mathrm{d}V$ to unity we obtain $\omega\left(V\right) = c\mathrm{e}^{-cV}$. This probability density can be used to average the excitation decay kinetics given by Eq. 4.15 over different realizations of R (or V):

$$\bar{P}\left(t\right) = \int_0^{\infty} P\left(t|R\left(V\right)\right) c\mathrm{e}^{-cV}\,\mathrm{d}V, \tag{4.16}$$

where the relationship between R and V is given by Eq. 4.12. Generally, this integral should be calculated numerically by substituting infinite series from Eq. 4.15. Practically, however, it is usually sufficient to take only the first several terms in Eq. 4.15. Moreover, the asymptotic behavior can even be evaluated analytically.

Long-time kinetics At longer times, the infinite series in Eq. 4.15 is dominated by the single term corresponding to the smallest eigenvalue $\varepsilon_1 = D\big(\xi^{(1)}_{d/2-1}/R\big)^2$, therefore this equation can be approximately rewritten as

$$P\left(t|R\right) \simeq \frac{4}{2^{d/2}\Gamma\left(\frac{d}{2}\right)} \frac{\left(\xi^{(1)}_{d/2-1}\right)^{d/2-2}}{J_{d/2}\left(\xi^{(1)}_{d/2-1}\right)} \cdot \exp\left[-\big(\xi^{(1)}_{d/2-1}/R\big)^2 Dt\right].$$

By substituting this simplified expression into the integral of Eq. 4.16 and applying the steepest-descent method [209] to evaluate it at longer times, we obtain the following asymptotic behavior:

$$\bar{P}\left(t\right) \simeq A_d \left(c^{2/d}Dt\right)^{d/(2d+4)} \exp\left[-\kappa_d \left(c^{2/d}Dt\right)^{d/(d+2)}\right], \tag{4.17}$$

where

$$\kappa_d = \frac{2+d}{d}\left[\frac{\left(\xi^{(1)}_{d/2-1}\sqrt{\pi}\right)^d}{\Gamma\left(\frac{d}{2}\right)}\right]^{\frac{2}{d+2}}$$

and

$$A_d = \frac{8}{2^{d/2}\sqrt{2+d}} \frac{1}{J_{d/2}\left(\xi^{(1)}_{d/2-1}\right)} \left[\frac{\pi^{d+1}\left(\xi^{(1)}_{d/2-1}\right)^{\frac{d^2}{2}-4}}{\left(\Gamma\left(\frac{d}{2}\right)\right)^{d+3}}\right]^{\frac{1}{d+2}}.$$

The non-exponential form of Eq. 4.17 is evident. More importantly, it contains just 2 undetermined parameters: the dimensionality of the system, d, and a simple function of the diffusion coefficient and the mean concentration of the traps, $Dc^{2/d}$, which can be fitted to the experimentally obtained excitation relaxation kinetics in PSII.

The quality of the asymptotic approximation can be evaluated by comparing it with the exact result, obtained by numerically integrating Eq. 4.16. In Fig. 4.3, the total fluorescence kinetics, calculated by assuming $d = 1.7$ and $\left[Dc^{2/d}\right]^{-1} = 1.5\,\mathrm{ns}$ (as will be shown below, these are typical values that can describe fluorescence kinetics in PSII), along with the contribution from the first 4 terms in Eq. 4.15 as well as the asymptotic expression (Eq. 4.17) are shown. We see that the contribution from the first two terms is the most important and that of other terms, affecting only the very initial part of the excitation kinetics, decreases rapidly. Moreover, the steepest-descent approximation is also applicable to describe the excitation kinetics for $t \gtrsim 200\,\mathrm{ps}$. In fact, when we used the asymptotic approximation to fit the fluorescence decay kinetics from variously sized PSIIs within the time win-

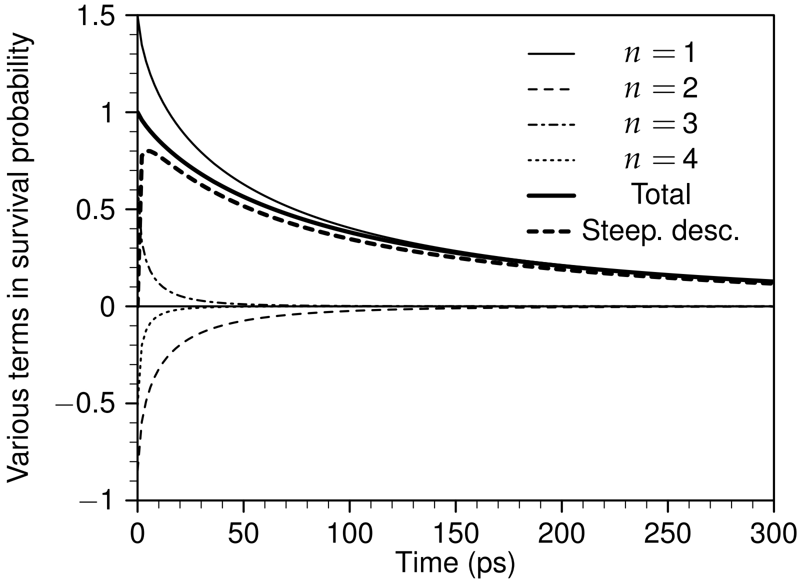

Figure 4.3 | Comparison of the asymptotic steepest-descent approximation (Eq. 4.17, thick dashed line) with the numerically averaged terms in Eq. 4.15 corresponding to $n = 1$–4 (thin lines). Thick solid line is the total probability density evaluated as the sum of the first 30 averaged terms in Eq. 4.15. All the kinetics were calculated using $d = 1.7$ and $\left[Dc^{2/d}\right]^{-1} = 1.5\,\text{ns}$.

dow 200 ps $< t <$ 1000 ps, the resulting error in the obtained model parameters did not exceed 5 % for the dimensionality d and 12 % for the parameter $Dc^{2/d}$, compared with the values given below in Table 4.1.

4.2.3 Excitation mean lifetime

Differently from the excitation kinetics, for which we can obtain a rather simple approximate analytic expression only at longer times, the average lifetime of the excitation can be calculated directly from Eq. 4.15:

$$\tau(R) = \int_0^\infty P(t|R)\,\mathrm{d}t = \frac{R^2}{D}\frac{4}{2^{d/2}\Gamma\left(\frac{d}{2}\right)}\sum_{n=1}^{\infty}\frac{\left(\xi_{d/2-1}^{(n)}\right)^{d/2-4}}{J_{d/2}\left(\xi_{d/2-1}^{(n)}\right)}. \tag{4.18}$$

Interestingly, the total sum of this very complex infinite series converges to a very simple expression:

$$\tau(R) = \frac{R^2}{2dD},$$

i.e. the mean lifetime of the excitation diffusing inside the sphere is just equal to the *diffusion time* needed for the excitation to diffusively reach the distance R. The averaging over various radii R is performed in the same way as it was done before for the excitation kinetics:

$$\langle\tau\rangle = \int_0^\infty \tau\left(R(V)\right)\omega\left(V\right)\,\mathrm{d}V = \frac{\Gamma\left(\frac{2}{d}+1\right)}{2\pi d D c^{2/d}}\left[\Gamma\left(\frac{d}{2}+1\right)\right]^{\frac{2}{d}}. \tag{4.19}$$

This equation gives a rather simple expression for the excitation mean lifetime and, again, depends on the same two parameters, d and $Dc^{2/d}$.

Relationship to the coarse-grained model Turning back to the structural arrangement of the pigment–protein complexes in PSII, the concentration c of the RCs can be expressed as

$$c \simeq \frac{1}{Na^d}, \tag{4.20}$$

where N is the average number of complexes per RC and a^d is the average volume of those complexes (in d-dimensional space, *cf.* Fig. 4.1c for the 2-dimensional case). Similarly, the diffusion constant D is related to the macroscopic excitation hopping time, τ_h, between the adjacent complexes in a similar way as was defined in Eq. 4.3:

$$D \simeq \frac{a^2}{2d\tau_\mathrm{h}}. \tag{4.21}$$

By substituting Eqs. 4.20 and 4.21 into Eq. 4.19 we obtain

$$\langle\tau\rangle = \tau_\mathrm{h} N^{2/d}\cdot\frac{\Gamma\left(\frac{2}{d}+1\right)}{\pi}\left[\Gamma\left(1+\frac{d}{2}\right)\right]^{2/d}, \tag{4.22}$$

which for integer dimensions yields:

$$\langle\tau\rangle = \begin{cases} \frac{1}{2}\tau_\mathrm{h}N^2 = 0.5\tau_\mathrm{h}N^2, & d=1; \\ \frac{1}{\pi}\tau_\mathrm{h}N \approx 0.32\tau_\mathrm{h}N, & d=2; \\ \Gamma\left(\frac{2}{3}\right)\left(\frac{N}{\sqrt{6\pi}}\right)^{2/3}\tau_\mathrm{h} \approx 0.35\tau_\mathrm{h}N^{2/3}, & d=3. \end{cases}$$

We see a strictly linear dependence of $\langle\tau\rangle$ on N only in the case of the ideally two-dimensional arrangement of the pigment–protein complexes. Moreover, for any dimensionality d the mean lifetime approaches zero as $N \to 0$.

4.2.4 Finite trapping rate

Equations 4.15–4.19 describe excitation decay kinetics and mean excitation lifetime in the case of ideal, *i.e.* infinitely fast, trapping by the RCs. To account for the finite rate of charge separation, we can still solve the same diffusion equation 4.4, but supplementing it with slightly modified boundary condition defining the outgoing flux of probability density at the boundary:

$$\frac{\partial}{\partial r} p\left(\mathbf{r}, t|R\right)\Big|_{|\mathbf{r}|=R} = -\frac{\gamma \mathcal{V}_0}{D \cdot S\left(R\right)} p\left(\mathbf{r}, t|R\right)\Big|_{|\mathbf{r}|=R}, \tag{4.23}$$

where γ is the trapping rate by the RC, D is the same diffusion constant as in Eq. 4.4, $S\left(R\right) = V\left(R\right) d/R$ is the "area" of the boundary surrounding the volume $V\left(R\right)$, and $\mathcal{V}_0$ is some characteristic "trapping" volume representing the volume occupied by the RC.

Following the steps presented above, Eq. 4.4 permits a separation of spatial and time variables; therefore, its solution can still be presented in the form of Eq. 4.6, where $f_n\left(r|R\right)$ and $\varepsilon_n\left(R\right)$ are the eigenfunctions and eigenvalues of Eq. 4.9, now obeying the boundary condition of the form

$$\frac{\partial}{\partial r} f_n\left(r|R\right)\Big|_{r=R} + k f_n\left(r|R\right)\Big|_{r=R} = 0.$$

Here, to simplify our notations, we have denoted $k = \frac{\gamma \mathcal{V}_0}{DS(R)}$.

The solution of Eq. 4.9 is again expressed by Eq. 4.11, so that the total excitation density decays in time according to

$$p\left(r, t|R\right) = \sum_{n=1}^{\infty} C_n r^{1-\frac{d}{2}} \cdot J_{d/2-1}\left(\mu_d^{(n)} \cdot \tfrac{r}{R}\right) \exp\left[-\left(\mu_d^{(n)}/R\right)^2 Dt\right], \tag{4.24}$$

where

$$C_n = \frac{1}{\pi R^2}\left(\frac{\mu_d^{(n)}}{2\pi R}\right)^{\frac{d}{2}-1} \cdot \left\{ J_{d/2-1}^2\left(\mu_d^{(n)}\right) \cdot \left[1 - \left(d-2\right)\frac{kR}{\left(\mu_d^{(n)}\right)^2} + \left(\frac{kR}{\mu_d^{(n)}}\right)^2\right]\right\}^{-1}$$

and $\mu_d^{(n)}$ is the n-th solution of the transcendent equation

$$\mu_d \cdot J_{d/2}\left(\mu_d\right) = kR \cdot J_{d/2-1}\left(\mu_d\right). \tag{4.25}$$

By integrating Eq. 4.24 over the whole volume $V\left(R\right)$, we obtain the following expression for the excitation survival probability:

$$P\left(t|R\right) = \frac{4kR}{2^{d/2}\Gamma\left(\frac{d}{2}\right)} \sum_{n=1}^{\infty} \frac{\exp\left[-\left(\mu_d^{(n)}/R\right)^2 Dt\right]}{\left(\mu_d^{(n)}\right)^{1-\frac{d}{2}} J_{d/2-1}\left(\mu_d^{(n)}\right)\left[\left(\mu_d^{(n)}\right)^2 - \left(d-2\right)kR + \left(kR\right)^2\right]}. \tag{4.26}$$

The next step would be to average this expression over R values, as it was defined in Eq. 4.16. However, due to the intrinsic dependence of $\mu_d^{(n)}$ on the radius R (*cf.* Eq. 4.25), this task can not be performed analytically even for the lowest eigenvalue (with $n = 1$), so that the integral may be evaluated only numerically. Nevertheless, we still can calculate the mean excitation lifetime, similarly as it was done in Eq. 4.18:

$$\tau\left(R\right) = \frac{4kR^3}{2^{d/2}\Gamma\left(\frac{d}{2}\right) D} \sum_{n=1}^{\infty} \frac{1}{\left(\mu_d^{(n)}\right)^{3-\frac{d}{2}} J_{\frac{d}{2}-1}\left(\mu_d^{(n)}\right) \left[\left(\mu_d^{(n)}\right)^2 - \left(d-2\right)kR + \left(kR\right)^2\right]}.$$

Numerical evaluations show that, independently of d, k, and R, this complex infinite series converges to a rather simple expression:

$$\tau\left(R\right) = \frac{R^2}{2dD}\left(1 + \frac{2}{kR}\right) = \frac{R^2}{2dD} + \frac{1}{\gamma} \cdot \frac{V\left(R\right)}{\mathcal{V}_0}, \tag{4.27}$$

where the definition of k has been taken into account. As we see, we have obtained the well-known result that the mean excitation lifetime can be decomposed into two terms:

$$\tau\left(R\right) = \tau_{\mathrm{mig}} + \tau_{\mathrm{CS}},$$

where $\tau_{\mathrm{mig}} = R^2 / \left(2dD\right)$ is the time of excitation migration towards the RC, the same as in the case of infinitely fast trapping (*cf.* Eq. 4.18), and $\tau_{\mathrm{CS}} = V\left(R\right) / \left(\gamma \mathcal{V}_0\right)$ is the trapping time by the RC.

The obtained expression of the mean lifetime (Eq. 4.27) can be easily averaged over all values of R (in fact, we have already done that for τ_{mig} term in Eq. 4.19), so that finally we get:

$$\langle\tau\rangle = \frac{\Gamma\left(\frac{2}{d}+1\right)}{2\pi d D c^{2/d}} \left[\Gamma\left(\frac{d}{2}+1\right)\right]^{\frac{2}{d}} + \frac{1}{\gamma c \mathcal{V}_0}. \tag{4.28}$$

We can also relate the obtained result to the coarse-grained model. Since in the notation of Eqs. 4.20–4.22 the volume of the RC is expressed just as $\mathcal{V}_0 \simeq a^d$, the mean excitation lifetime is equal to

$$\langle\tau\rangle = \tau_{\mathrm{h}} N^{2/d} \cdot \frac{2\Gamma\left(\frac{2}{d}\right)}{\pi d} \left[\Gamma\left(1 + \frac{d}{2}\right)\right]^{2/d} + \frac{N}{\gamma}. \tag{4.29}$$

Finally, a short remark regarding the intrinsic dissipation rate is appropriate at this point. In our initial formulation of the diffusional model (Eq. 4.4) we assumed that both excitation migration through the antenna (typically taking up to several hundreds of ps) and charge separation in RC (several ps) are much faster than excitation dissipation due to fluorescence or non-radiative decay to the ground state (several ns). As a result, the latter process was completely ignored so far. In larger antenna systems, however, this assumption might be violated, and Eq. 4.4 should be supplemented with an additional term:

$$\frac{\partial}{\partial t} p\left(\mathbf{r}, t|R\right) = D\nabla_d^2 p\left(\mathbf{r}, t|R\right) - k_{\text{dis}} p\left(\mathbf{r}, t|R\right), \tag{4.30}$$

where k_{dis} is the mentioned mean dissipation rate. It can be shown that addition of this new linear term into the diffusion equation does not change the final solutions significantly [188]. Instead, survival probabilities $P\left(t|R\right)$ given by Eqs. 4.15, 4.17, and 4.26 should be simply multiplied by $\exp\left(-k_{\text{dis}} t\right)$. In such case, the resulting mean excitation lifetimes $\langle \tau \rangle$ cannot be calculated analytically any more, requiring numerical integration in Eq. 4.18.

4.3 Excitation dynamics in various light-harvesting systems

4.3.1 PSII of various size

Until recently, thorough studies on the light-harvesting processes in PSII were limited due to the heterogeneous composition of the preparations of PSII supercomplexes and the lack of their detailed structural maps. Nevertheless, advances in biochemical techniques allowed a reliable purification of various homogeneous PSII species from the thylakoid membranes [189]. It was shown by means of electron microscopy that the largest stable PSII supercomplexes, usually denoted as $C_2S_2M_2$, were composed of the dimeric PSII core (C_2) surrounded by the minor antenna complexes as well as 2 strongly-bound (S_2) and 2 moderately-bound (M_2) LHCII trimers (see Fig. 4.4 for the schematic organization). However, smaller supercomplexes have also been purified, which allowed to study the effect of the antenna size on the overall excitation migration towards the RC. Interestingly, it was revealed that in all these PSII fractions, independently of their size and detergent concentration used for their preparation, the fluorescence kinetics exhibited a multi-exponential decay behavior [103]. Below we use these experimental kinetics to verify whether our fluctuating antenna model can reproduce such a behavior without assuming the presence of additional radical-pair states in the RC.

Following the original suggestion [103], we ignored the longest ns-scale time components in the recorded fluorescence decay traces (arising probably from the closed RCs, free Chls or separated antenna complexes). For the calculations, we used the first 30 terms from the infinite series of Eq. 4.15, all being averaged according to Eq. 4.16. The resulting best-fitted fluorescence decay kinetics are presented in Fig. 4.5, and the corresponding fitting parameters are listed in Table 4.1.

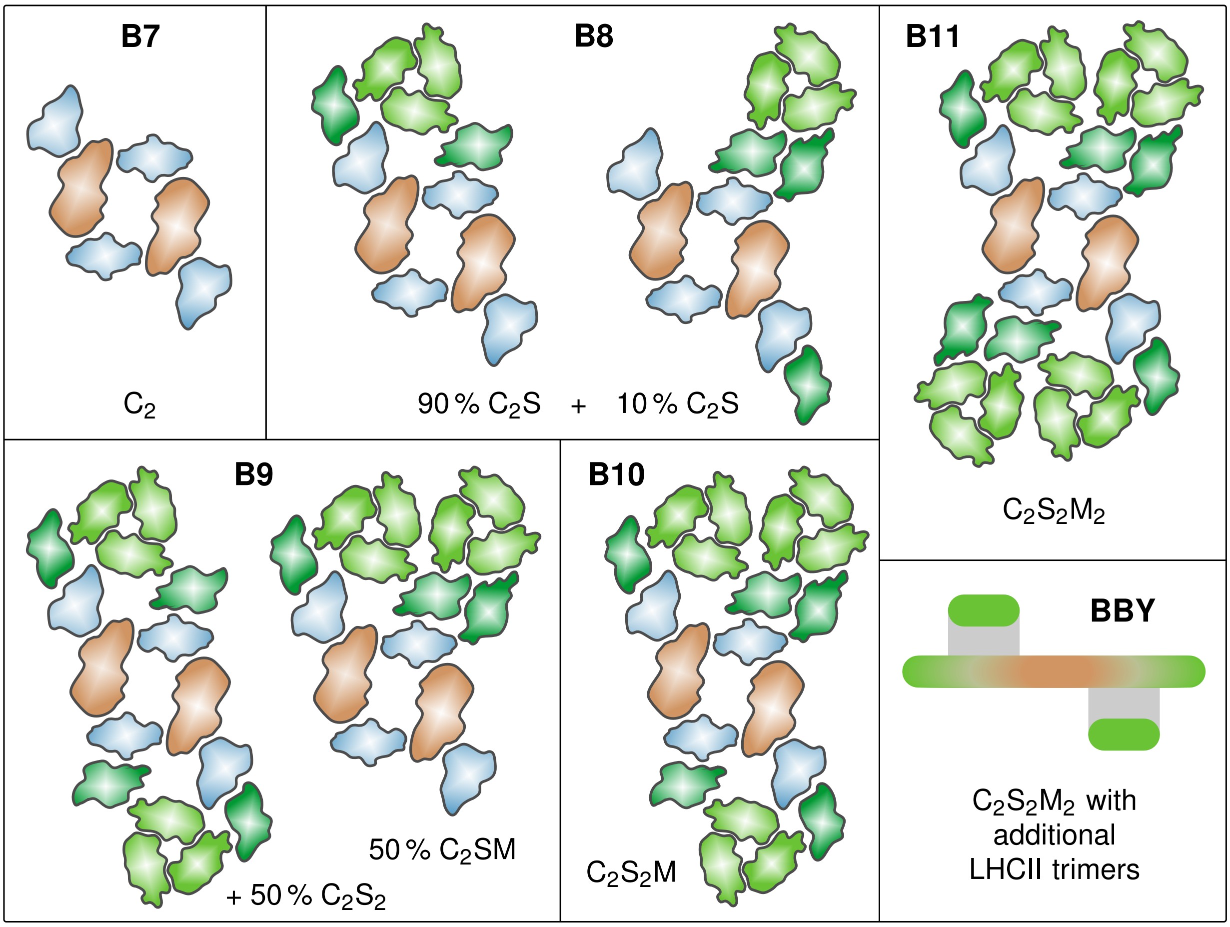

Figure 4.4 | Schematic structures of B7–B11 PSII supercomplexes and the obtained quasi-stacked organization of the BBY particles. Colors and relative position of the pigment–protein complexes are the same as in Fig. 4.1a.

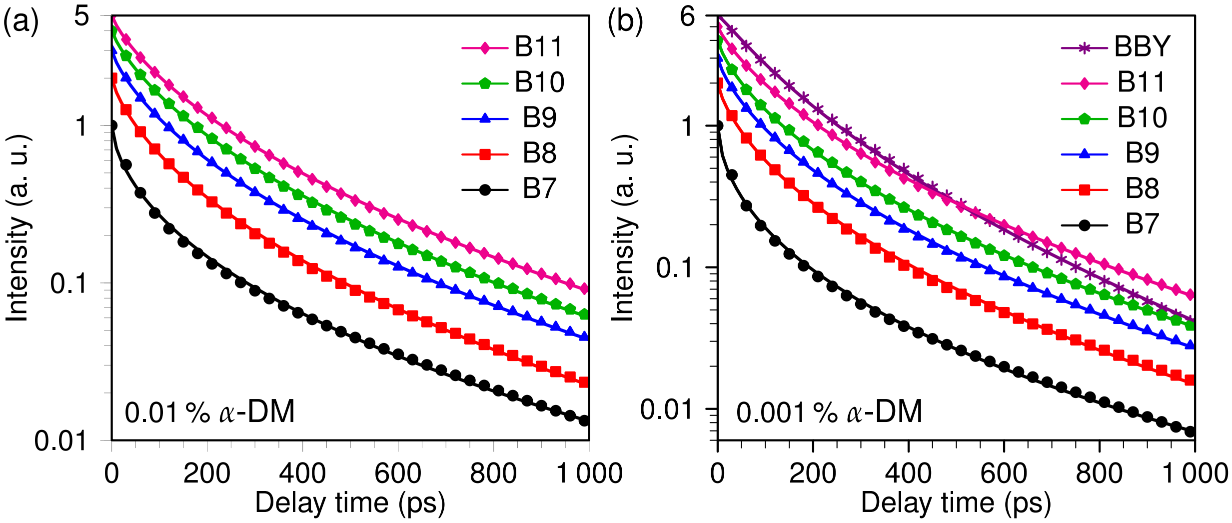

Figure 4.5 | Experimental (symbols) and simulated (lines) fluorescence decay kinetics in PSII of different sizes solubilized in 0.01 % (**a**) and 0.001 % (**b**) α-DM. For comparison, panel (b) also shows kinetics in BBY particles. All the simulated curves were calculated using the fitted parameters presented in Table 4.1. For visual clarity, fluorescence kinetics in B8–BBY supercomplexes were multiplied by integer numbers 2–6, respectively.

Table 4.1 | Fitted model parameters and mean excitation lifetimes obtained for PSII of various size at different detergent concentrations.

PSII	Model parameters		$\langle \tau \rangle$ (ps)	
	d	$\left[D c^{2/d} \right]^{-1}$ (ns)	Model	Experiment
		0.01% α-DM		
B7	1.277	0.759	112	109
B8	1.569	1.170	124	123
B9	1.618	1.395	142	141
B10	1.686	1.544	149	148
B11	1.687	1.656	159	158
		0.001% α-DM		
B7	1.180	0.446	76	77
B8	1.543	0.959	104	104
B9	1.603	1.125	116	115
B10	1.615	1.170	119	119
B11	1.781	1.595	144	143
BBY	2.300	2.103	147	147

In the same table we also present the mean excitation lifetimes $\langle \tau \rangle$, calculated according to Eq. 4.19 using the obtained model parameters, and compare them with the actual experimental values [100, 103].

The fluorescence kinetics in Fig. 4.5 show a perfect agreement between the results proposed by the fluctuating antenna model and the actual experimental observations. Despite being exceptionally simple and dealing merely with an ordinary excitation diffusion in a continuous medium, our model phenomenologically describes the inhomogeneous distribution of the pigment within the antenna and is able to account for the fluctuating nature of the intra- and inter-complex connectivity, thus perfectly reproducing complicated multi-exponential fluorescence decay kinetics in PSII supercomplexes. In contrast to all the existing modifications of the ERPE model, this complex behavior of the fluorescence decay is explained by using just two parameters, both having a simple physical meaning and being in agreement with the current knowledge of excitation dynamics in photosynthetic antennae of PSII.

First of all, the obtained dimensionality of the PSII core is very close to 1, as it is expected for the chain arrangement of CP43 and CP47 core antenna complexes around the RCs. On the other hand, the fractional dimension $1.5 < d < 2$ observed in B8–B12 types of PSII corresponds to the perturbed coordination within the planar distribution of light-harvesting complexes. In other words, it simply reflects the presence of void regions and lack of connectivity between some complexes arranged into two-dimensional aggregates.

Secondly, another model parameter, $Dc^{2/d}$, gives us a direct estimation of the mean excitation transfer times between different pigment–protein complexes provided we know the internal composition of the studied PSII fractions. Indeed, as follows from Eqs. 4.20 and 4.21, the fitted values of the product $Dc^{2/d}$ depend both on the mean excitation inter-complex hopping time, τ_h, and the number of antenna complexes per RC, N, since $\left[Dc^{2/d}\right]^{-1} = 2d\tau_\mathrm{h}N^{2/d}$. In fact, the numbers N represent the amount of subunits participating in the excitation energy transfer and therefore are to some extent an arbitrary choice: they can be chosen to correspond to the number of the pigment–protein complexes, to the number of the domains formed by the strongly coupled pigments, or even to the total number of Chl molecules. Then the corresponding numerical value of τ_h will reflect the mean inter-complex, inter-domain or inter-pigment excitation hopping time, averaged over the whole PSII.

By assuming N representing the number of Chl *a* molecules, the evaluated mean effective inter-pigment transfer time is about 2 ps for all the PSII supercomplexes except the core, for which the value of 1 ps is obtained. However, the excitation energy equilibration within the pigment–protein complex is usually at least by an order of magnitude faster than the energy transfer between the molecules belonging to the different complexes. As a result, the inter-pigment excitation hopping times exhibit much larger variations across the whole PSII comparing to the inter-complex excitation transfer times. The interdependence between N and τ_h for various fractions of PSII is presented in Fig. 4.6. The stars in Fig. 4.6 correspond to the actual number of the pigment–protein complexes per RC in the particular PSII fraction and give us a direct estimate of the corresponding mean inter-complex excitation transfer timescales.

In the case of the smallest PSII fractions, namely PSII core complexes (B7), we find that the mean excitation hopping time from CP43/CP47 complexes to the RC is about 53 ps, which provides independent support for the TTL regime of excitation energy transfer towards the RC [98]. However, upon increasing the antenna size, the mean excitation hopping time decreases quickly. This effect demonstrates much better energetic connectivity between the major antenna complexes as compared to the inter-connectivity of the core complexes: as the antenna grows, the influence of the intra-core migration time becomes less pronounced, leading to the smaller values of the excitation hopping time being averaged over the whole PSII. For the largest PSII supercomplexes, B11, we obtain $\tau_\mathrm{h} \approx 25\,\mathrm{ps}$. When the detergent is removed (0.001 % α-DM), the core complexes get into better contact resulting in a noticeably faster excitation transfer rate. For this low detergent concentration the mean inter-complex excitation hopping times are within the range 20–30 ps, again very close to $\tau_\mathrm{h} \approx 25\,\mathrm{ps}$. This value, in turn, corre-

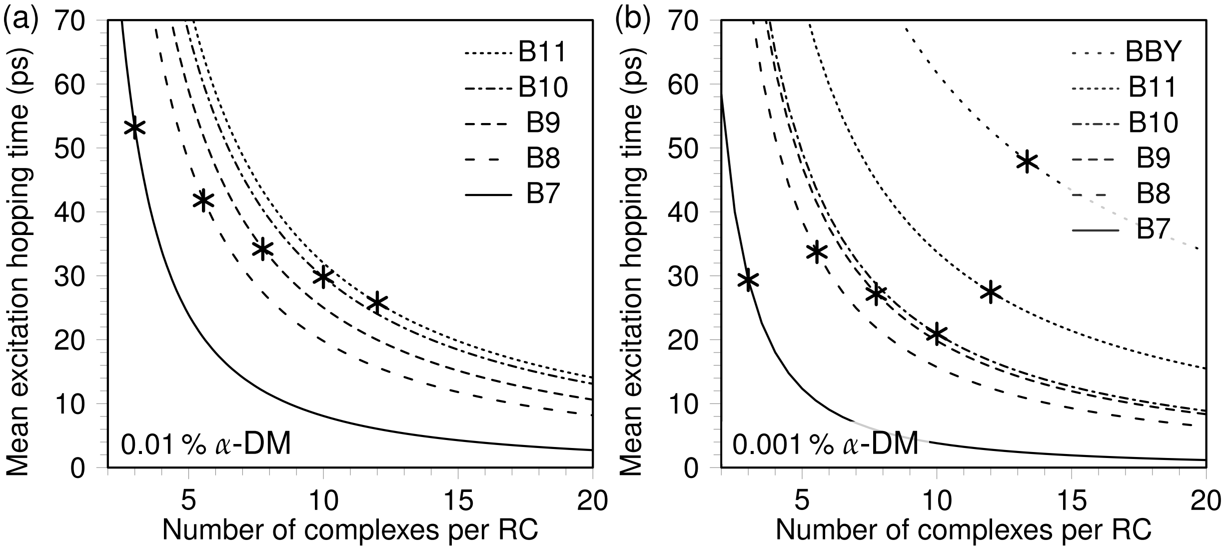

Figure 4.6 | Relationship between the mean inter-complex hopping time and the number of pigment–protein complexes per RC, as obtained for different fractions of PSII solubilized in 0.01 % (**a**) or 0.001 % (**b**) α-DM and ensuring the same fitting parameters as listed in Table 4.1. For comparison, panel (b) also shows data for BBY particles. Stars indicate the hopping times corresponding to the actual number of pigment–protein complexes per RC in the corresponding PSII supercomplex ($N = 3, 5.5, 7.8, 10, 12$, and 13.3 for B7–B11 and BBY complexes, respectively).

sponds to the excitation migration timescale obtained from the singlet–singlet annihilation measurements performed on LHCII aggregates [148]. Moreover, the same value (25 ps) was obtained in recent structure-based calculations [96] for the inter-monomer excitation transfer within the LHCII trimer. Therefore our results provide an additional independent support for the room-temperature value of $\tau_\mathrm{h} \approx 25\,\mathrm{ps}$, chosen in the previous chapter to describe the mean inter-complex excitation hopping rate in the LHCII aggregates.

Another important outcome of our simulations is that we manage to fit all the fluorescence kinetics just by assuming infinitely fast excitation trapping by RCs. This implies that the overall process of light harvesting and a subsequent charge separation is *migration limited*. Of course, this is not entirely true for the core complexes; indeed, for them our fitted fluorescence kinetics were of slightly worse quality when compared to other fitting results, and this has probably led to some overestimation of the mean hopping time in these core complexes. To deal with these drawbacks, our diffusion model can, in principle, be slightly modified by taking into account a finite rate of photochemical excitation trapping, as shortly described in Section 4.2.4. This approach, however, would just complicate the analysis of the experimental data and hardly improve the quality of already well-fitted kinetics. Therefore, we would just like to point out again that, according to this modified model and in agreement with the existing theoretical treat-

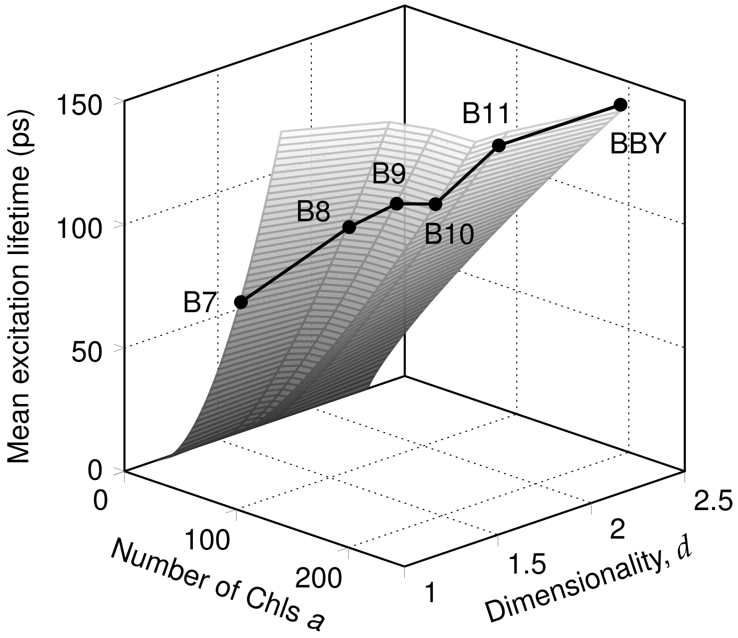

Figure 4.7 | Mean excitation lifetime, presented as a function of the number of Chl *a* molecules and the obtained dimensionality of different fractions of PSII supercomplexes at 0.001 % α-DM. Black dots correspond to the exact lifetimes and structural composition of these PSIIs whereas the d = const thin gray lines depicted on the 3-dimensional surface $\langle\tau\,(N,d)\rangle$ demonstrate the $\langle\tau\,(N)\rangle$ behavior for any given d, approaching zero as $N \to 0$.

ments [5], the mean excitation lifetime is defined as $\langle\tau\rangle = \tau_{\mathrm{mig}} + \tau_{\mathrm{CS}}$ (*cf.* Eq. 4.29), where τ_{mig} is the migration term given by Eq. 4.22 and $\tau_{\mathrm{CS}} = N/\gamma$ is the trapping term depending on the antenna size, N, and the intrinsic rate of the charge separation, γ. Accordingly, a fast but still finite trapping rate would not change our basic conclusions on the fractional dimensionality of the studied systems and the importance of *"fluctuating bridges"* of excitation energy transfer, but just lead to a slightly smaller migration term. Eq. 4.22 then suggests a slight decrease of the mean hopping time τ_{h} and/or increase of system's dimensionality d.

While considering the mean excitation lifetime, we can turn back to Eq. 4.22 for a moment, now treating N as the number of Chl *a* molecules in the given PSII and τ_{h} as an average inter-molecular excitation hopping time. As mentioned above, in the experimental measurements of fluorescence decay kinetics [103] it was observed that the mean excitation lifetime linearly depends on the number of Chl *a* per PSII. However, this dependence does not cross zero when extrapolating towards $N \to 0$ (see Fig. 4.2), as it obviously should do [5]. This behavior can not be understood from the point of view of any existing model of PSII; nevertheless, our proposed diffusion-based fluctuating antenna model can clarify this puzzle as well. Indeed, as follows from Eq. 4.22, the mentioned experimentally observed linear dependency $\langle\tau\,(N)\rangle$ is just a projection of the multivariable function $\langle \tau(N,d) \rangle$ onto a single axis N. For any given dimensionality d we have a proper relation $\langle \tau(N \to 0, d) \rangle \to 0$, as demonstrated in Fig. 4.7.

4.3.2 BBY complexes

For comparison, we have also applied our model to describe fluorescence kinetics of PSII grana membranes (BBY preparations), on average containing 13.2 complexes per RC. [100]. The obtained model parameters are presented at the bottom of Table 4.1, and the corresponding excitation decay kinetics are shown in Fig. 4.5b. First of all, the excitation kinetics notably differs from those of the B7–B11 supercomplexes, even in a qualitative manner. The origin of this difference becomes clear from the obtained model parameters listed in Table 4.1: the dimensionality of the BBY particles is notably larger, $d \approx 2.3$, and reflects the known quasi-3D, or stacked, structure of the purified PSII grana membranes, as schematically demonstrated in Fig. 4.4 [185]. A similar quasi-stacked distribution of antenna complexes was also assumed in previous coarse-grained modeling of the excitation transfer in BBY complexes [101].

The measured Chl a / Chl b ratio in the BBY complexes predicted that there are on average 2.45 LHCII trimers per RC, so that there is one more trimer as compared to the B11 supercomplex. Combining this information with the modeling results shown in Fig. 4.6b, we obtain a rather slow mean excitation hopping time, $\tau_\mathrm{h} \approx 48\,\mathrm{ps}$. If the quasi-stacked structural arrangement of the antenna complexes in the BBY preparations is taken into account, the interpretation of such a slow transfer becomes clear: it predicts much slower rates of inter-layer excitation migration, raising the average hopping time. However, better inter-connectivity (the increased coordination number of the antenna complexes) ensures faster decay of the overall fluorescence kinetics. In fact, the efficiency of excitation energy transfer between different layers of the thylakoid membrane is still unknown, and our simple model seems to be able to indirectly estimate it. Finally, we have also studied the application of our model to analyze fluorescence kinetics originating from even larger and more heterogeneous systems like the whole thylakoid membrane [15].

4.3.3 Thylakoid membranes

Recent studies on time-resolved fluorescence from the thylakoid membranes of green plants [15] have provided us with another opportunity to test the applicability of the presented fluctuating antenna model. Since the thylakoid membranes contain not only PSII, but also PSI and possibly aggregates of LHCII complexes in poor energetic contact with the RCs, the interpretation of the fluorescence kinetics from the whole thylakoid is not as straightforward as for the purified PSII fractions or BBY particles. However, different spectroscopic and structural properties of PSI and PSII can help to disentangle their relative input to the overall kinetics. First of all, the peak of the fluorescence spectrum of PSII is centered at 680 nm, whereas that of PSI is located near 720 nm [210]. Secondly, the fluorescence kinetics of PSI is much faster than that of PSII [8,9], revealing extremely efficient (about 99 %) excitation energy transfer towards the PSI RC, which results in multi-exponential excitation decay with an average lifetime of around 50 ps for isolated PSI [211, 212]. The average lifetime can be longer when measured with time-correlated single photon counting on thylakoid membranes; then the multi-exponentiality is less apparent [15, 197]. PSII, on the contrary, possesses a several times larger light-harvesting antenna exhibiting non-exponential fluorescence kinetics with a mean lifetime of the order of several hundreds of ps.

These mentioned differences in the fluorescence decay rates of both photosystems allow calculating the decay-associated spectra based on the fluorescence kinetics detected at several different wavelengths and thus to distinguish between the fluorescence signal arising from different photosystems [15]. In this analysis, however, it is not entirely clear which part of the fast decay component (around 50–70 ps) should be attributed to PSI and which—to the multi-exponential excitation decay in PSII. Therefore the best way to extract the pure kinetics of each photosystem would be to simultaneously measure both spectral and time-resolved features of the fluorescence signal and then to apply multivariate curve resolution analysis, as demonstrated in the previous chapter for multiple distinct states in the LHCII aggregates. Such a full experimental data, however, is not always accessible. On the other hand, the structural and spectral diversity of both photosynthetic units also suggests an alternative way to analyze data by applying our model while utilizing only several spectral points.

As an example, below we analyze 3 fluorescence decay kinetics in thylakoid membranes acclimated to low light conditions that were detected at 680, 700, and 720 nm [15]. Arising from the both photosystems, these kinetics can be approximately expressed as the sum of two terms:

$$P\left(t,\lambda\right)=A_{\lambda}P_{\mathrm{PSII}}\left(t\right)+\left(1-A_{\lambda}\right)P_{\mathrm{PSI}}\left(t\right), \tag{4.31}$$

where $P_{\mathrm{PSII}}\left(t\right)$ is the normalized long-lived fluorescence coming from PSII, $P_{\mathrm{PSI}}\left(t\right)$ is the fluorescence from PSI, and A_{λ} is the wavelength-dependent amplitude reflecting relative differences in the steady-state fluorescence spectra of both photosystems. Since PSII possesses a large and flexible light-harvesting antenna, this fluorescence signal can be described by Eqs. 4.15 and 4.16 of our fluctuating diffusion model. On the other hand, as already mentioned, PSI has a smaller antenna which is strongly-bound to its RC and exhibits a fluorescence that on the corre-

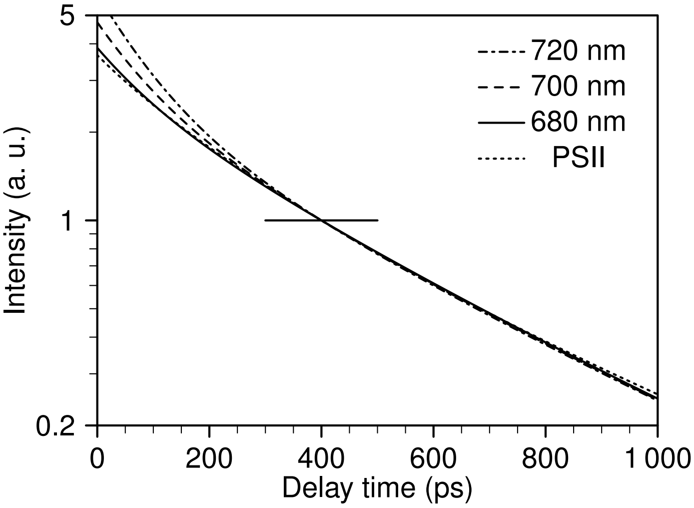

Figure 4.8 | Fluorescence kinetics in low-light-adapted thylakoid membranes [15], detected at different wavelengths and normalized at 400 ps (indicated with horizontal line). The dotted line represents the deconvoluted kinetics of PSII (shown in the inset of Fig. 4.9a), also normalized at 400 ps.

sponding timescale can be approximated relatively well with a single-exponential function:

$$P_{\mathrm{PSI}} = \exp\left(-t/\tau_{\mathrm{PSI}}\right), \tag{4.32}$$

where a lifetime τ_{PSI} is of the order of 70 ps. Such a pronounced difference between the characteristic timescales of excitation decay in both photosystems means that on the timescale of several hundreds of ps only the fluorescence from PSII remains. Therefore, Eq. 4.31 predicts that, asymptotically, the fluorescence kinetics should not depend upon the detection wavelength. This effect was indeed observed experimentally, as demonstrated in Fig. 4.8, where 3 different kinetics exhibit almost the same decay behavior after normalizing them at 400 ps.

To extract the parameters of the PSI and PSII kinetics, we used Eq. 4.31 to perform the global fit analysis by simultaneously fitting all 3 experimental kinetics detected at 3 different wavelengths while using 6 variable parameters—d and $Dc^{2/d}$ for PSII, τ_{PSI} for PSI, and 3 amplitudes A_λ. Since the antenna size of PSII in thylakoid membranes is expected to be somewhat larger than in the purified supercomplexes discussed above, the total excitation migration time may significantly increase. Therefore Eqs. 4.15 and 4.16 were multiplied by the term $\exp\left(-k_{\mathrm{dis}}t\right)$ (see Eq. 4.30 and the comment thereupon), where a mean time constant $k_{\mathrm{dis}}^{-1} \approx 2\,\mathrm{ns}$ accounts for the intrinsic excitation dissipation due to fluorescence, non-radiative relaxation to the ground state, or the occurrence of some quenched LHCIIs with the antenna. The fitting results are shown in Fig. 4.9a, where the simulated fluorescence kinetics are almost indistinguishable from the measured ones, while the obtained parameters are outlined in Table 4.2. The ob-

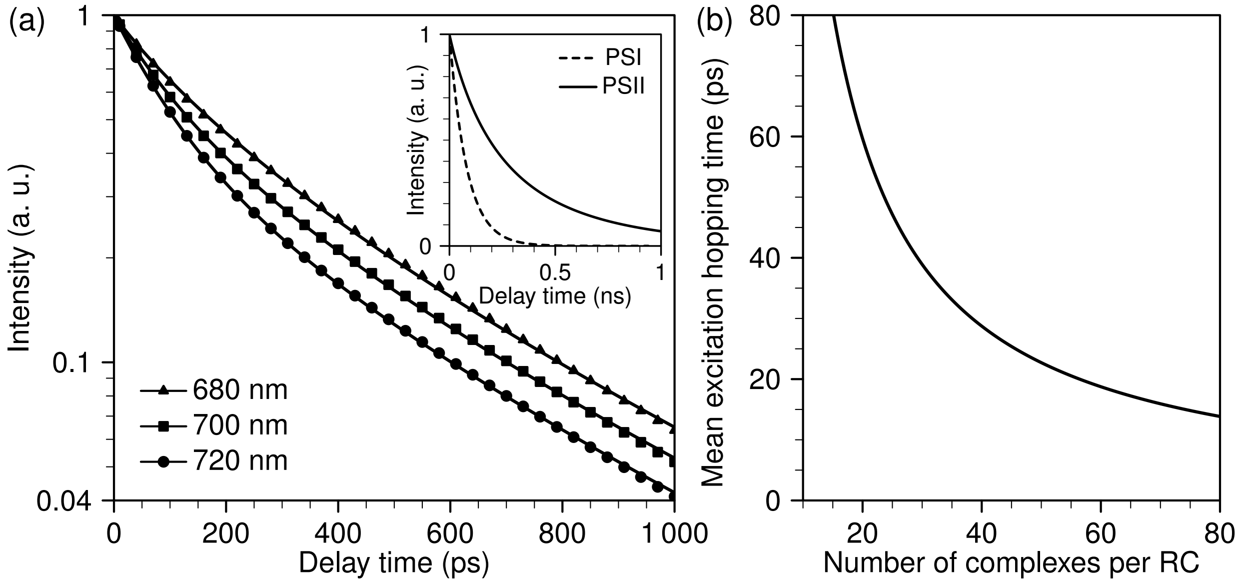

Figure 4.9 | (**a**) Experimental (symbols) and simulated (lines) fluorescence decay kinetics in thylakoid membranes at different detection wavelengths. **Inset**: extracted kinetics of PSI and PSII. The latter can be described by three exponents: $P_{\mathrm{PSII}}(t) = 0.12\mathrm{e}^{-t/78} + 0.55\mathrm{e}^{-t/240} + 0.33\mathrm{e}^{-t/592}$. (**b**) Mean inter-complex hopping time in PSII *vs.* number of pigment complexes per RC, ensuring the same $Dc^{2/d}$ parameter as shown in Table 4.2.

tained dimension of PSII, $d = 1.9$, indicates a more homogeneous distribution of the light-harvesting complexes over the flat photosynthetic membrane as compared to the somewhat distorted fractions of PSII analyzed above. Being only slightly smaller than 2, this dimension might also represent a distorted 3D organization with the absence of the pronounced stacked regions, as detected in the case of BBY particles.

The calculated deconvoluted fluorescence kinetics originating from PSI and PSII are presented in the inset of Fig. 4.9a. while the obtained mean lifetime of PSI is $\tau_{\mathrm{PSI}} = 82\,\mathrm{ps}$, close to what has been observed in earlier studies. The PSII fluorescence decays much slower in a multi-exponential way, with the fastest lifetime component (78 ps) resembling that of PSI. Therefore the resulting relative amplitudes A_λ somewhat differ from those obtained from the DAS analysis [15], were relative attribution of the fast component to the particular photosystem is not so straightforward. The total excitation mean lifetime in PSII of ~340 ps is more than 2 times longer as compared to that of BBY complexes and can be related to the longer excitation transfer to the RC because of the increased antenna size and possibly existing pools of loosely bound LHCII aggregates. This effect is indeed reflected in the obtained $\left[Dc^{2/d}\right]^{-1} = 2d\tau_{\mathrm{h}}N^{2/d} = 5.3\,\mathrm{ns}$ parameter, relating the mean excitation hopping time, averaged over the whole antenna, to the PSII size. This relationship is demonstrated in Fig. 4.9b. If one assumes the

Table 4.2 | Model parameters, obtained from a global fit of fluorescence decay kinetics of thylakoid membranes, measured at different detection wavelengths.

PSII	PSI	A_λ
$d = 1.90$	$\tau_{\mathrm{PSI}} = 82\,\mathrm{ps}$	$A_{680} = 93.5\%$
$\left[Dc^{2/d}\right]^{-1} = 5.32\,\mathrm{ns}$		$A_{700} = 76.2\%$
$\langle\tau\rangle_{\mathrm{PSII}} = 338\,\mathrm{ps}$		$A_{720} = 60.6\%$

same mean hopping time of 25 ps as obtained above for the B11 PSII species, the required number of the pigment–protein complexes is ~45 per RC. Structurally, that would correspond to the $C_2S_2M_2$ supercomplex being surrounded with 13 additional LHCII trimers. In fact, the freeze-fracture electron microscopy images of the PSII-containing thylakoid membranes reveal high level of the heterogeneity in PSII antenna sizes [167], with some PSII–LHCII megacomplexes binding more than 400 Chl pigments per RC. On the other hand, some remote pools of LHCII aggregates may be in worse energetic contact with the RC, which would increase the mean excitation hopping time and therefore require a somewhat smaller number of antenna complexes per RC [103, 197].

4.3.4 LHCII aggregates

The story about the excitation energy migration through the fluctuating antenna would not be complete without turning back to the LHCII aggregates, thoroughly discussed in the previous chapter. Indeed, the non-exponential fluorescence decay of LHCII aggregates as well as the presumed random distribution of NPQ traps suggest that our fluctuating antenna model might also be applied in this case. To test this, we analyzed the fluorescence decay kinetics from Fig. 3.3c, corresponding to the 273 K temperature (as it was shown in the previous chapter, at this high temperature the influence of the red-emitting LHCII species can be neglected, which allow application of our model without any special treatment). A somewhat similar attempt to apply a simplified version of the asymptotic expression of Eq. 4.17 to the fluorescence kinetics from the zeaxanthin-deficient LHCII aggregates [22] has already been done earlier [102]. In the current calculations, the intrinsic dissipation rate, extracted from the fluorescence decay kinetics in non-aggregated trimers at the same temperature ($k_{\mathrm{dis}}^{-1} = 4.2\,\mathrm{ns}$, see inset in Fig. 3.4b), was also included. The obtained best-fitted fluorescence kinetics together with the corresponding model parameters are shown in Fig. 4.10a. Similarly to the previously studied PSII supercomplexes, the obtained dimension is $d = 1.7$, which reveals existence of some distortions in the planar distribution and/or connectivity of the light-harvesting complexes within the aggregate. Finally, the calcu-

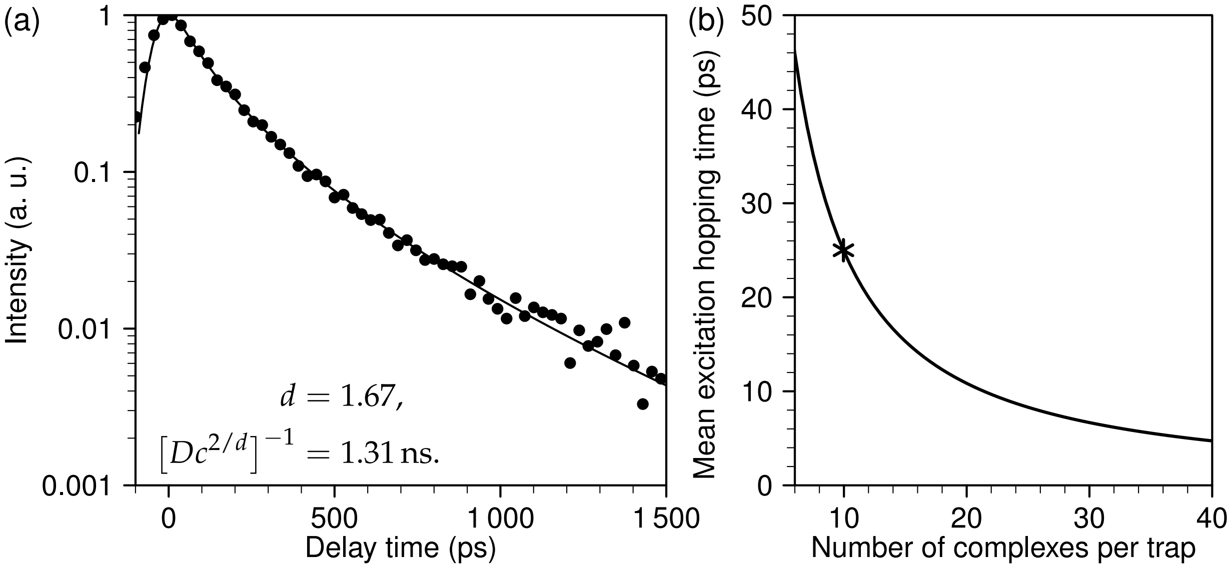

Figure 4.10 | (**a**) Experimental (dots, data taken from Fig. 3.3c at 273 K temperature) and simulated (line) fluorescence decay kinetics in the LHCII aggregate. The obtained model parameters are listed beneath the kinetics. (**b**) The obtained relationship between the mean inter-complex hopping time in the LHCII aggregates and the mean number of pigment–protein complexes per NPQ trap. Star indicates the mean hopping time of 25 ps, corresponding to ~1 trap per 10 complexes.

lated relationship between the mean inter-complex excitation hopping time and the number of complexes per NPQ trap is presented in Fig. 4.10b. By assuming, as previously, $\tau_\mathrm{h} = 25\,\mathrm{ps}$, we obtain that there is on average 1 trap per 10 complexes, which is very close to the mean concentration of the quenched complexes, obtained in the previous chapter from the CG model of LHCII aggregate.

The results shown in Fig. 4.10 were obtained by assuming that excitation traps are perfect quenchers, capable to infinitely quickly convert excess excitation energy into heat. As a result, the overall trapping process is entirely migration-limited. However, recent studies on fluorescence induction kinetics under NPQ conditions that are addressed in the following chapter as well as quantum chemistry-based calculations (*cf.* Section 1.3) suggest that NPQ-traps tend to be rather inefficient and not to compete with the open RCs. Therefore, to preserve the same decay rate of excitation kinetics, a higher concentration of traps should be assumed. In principle, even this more complicated situation can also be studied within the same fluctuating antenna model with some variations of the boundary condition for diffusion equation 4.4, as discussed above in Section 4.2.4.

4.4 Summarizing remarks

While studying excitation energy transfer in various photosynthetic light-harvesting systems, their fluctuating nature and heterogeneity, caused by the macroscopic membrane dynamics (like continuous movement and mutual re-arrangement of the pigment–protein complexes during the repair of the RCs, state transitions or NPQ processes), cannot be under-estimated. In this chapter we developed a simple *conceptual* model of a fluctuating antenna which demonstrates that the origin of the non-exponentiality of the fluorescence decay kinetics, experimentally observed in variously sized and prepared PSII supercomplexes, might be not the reaction center but the fluctuating antenna surrounding it. The demonstrated applicability of this approach to the very diverse light-harvesting antenna systems, ranging from the PSII supercomplexes or LHCII aggregates to the entire thylakoid membrane, provides a strong support for such conclusion.

Despite its simplicity, our approach provides a perfect description of the multi-exponential fluorescence decay kinetics using just two parameters that reflect the mean excitation energy transfer rate and overall organization of the photosynthetic antenna. Although the proposed model can in principle be easily extended to account for the possible excitation “de-trapping” from the RC, perfect reproduction of the fluorescence kinetics in various photosynthetic systems indicates no need for such a complication unless strong independent experimental evidences are collected in favor of the crucial role of the “de-trapping” process. Therefore we believe that our model, presenting an alternative point of view on the origin of the multi-exponential fluorescence kinetics and supporting the importance of the fluctuating properties of the light-harvesting antenna and its proteins, will inspire more detailed future studies on how to account for these fluctuations in a more systematic way.

In the next chapter, we will turn back to the problem of non-photochemical quenching and relate it to the macroscopic reorganization occurring within the thylakoid membrane under high light conditions that have previously just simply proposed to take place.

> *“ Nature always acts slowly, and with economy, as it were.*
>
> CHARLES DE MONTESQUIEU

Chapter 5

Economic photoprotection in photosynthesis

Plant’s adaptation to the varying light intensity includes many stages at different levels of organization—from movement of plant leaves and diffusional motion of chloroplasts within the plant cell to the non-photochemical quenching of excess excitation energy, performed on a molecular level. In the previous chapters, we thoroughly discussed about the possible candidates for governing NPQ process as well as analyzed excitation energy transfer and relaxation in single light-harvesting complexes, their aggregates, and photosynthetic units of various sizes. Based on our results, we managed to identify the most probable underlying NPQ mechanism; beside that, an important fluctuating nature of the pigment–protein complexes was revealed. These fluctuations can also be observed at various organization levels—either within the light-harvesting complex itself, being the result of the conformational dynamics of its protein, or within the photosystem as a consequence of the varying inter-connectivity between different antenna sites.

In this final chapter, we go beyond PSII and analyze macroscopic reorganization of the thylakoid membranes under high light conditions. Based on the results of fluorescence induction measurements in chloroplasts, we show that, in contrast to some earlier suggestions, natural switching to NPQ conditions is accompanied with the enhanced energetic connectivity between the light-harvesting antenna and the reaction center of PSII. As a result, the functional absorption cross-section of the RCs increases. This observation further supports our main conclusions made in Chapter 3 and demonstrates that NPQ mechanism effectively offer protection to closed rather than open RCs. This type of defense preserves the exceptional efficiency of photochemistry in PSII over a broad range of light intensities, simultaneously ensuring high photosynthetic productivity and, under hazardous light conditions, sufficient photoprotection for both the reaction centers and the light harvesting pigments of the antenna[11].

---

[11] The modeling results presented in this chapter are based on the work published in [213].

5.1 Measuring absorption cross-section of PSII reaction centers

It was demonstrated recently that the drop of fluorescence signal due to induced non-photochemical quenching is not the only observed property of the thylakoid membranes being under high light conditions. The electron microscopy studies provided evidences that in detergent-solubilized grana membranes NPQ is accompanied with the the decreased distances between PSII core complexes [214]. Latter, reorganization of the thylakoid membrane occurring in intact chloroplasts exposed to high light and resulting in the formation of clustered domains of the LHCII complexes and PSII reaction centers was demonstrated [167, 215]. It was shown that the monomeric and trimeric antenna complexes as well as the PsbS protein are involved in the observed structural changes, occurring on a timescale consistent with the formation and relaxation of NPQ.

Following these electron microscopy-based observations, it was proposed that under NPQ conditions most of the LHCII trimers of the thylakoid membrane undergo functional separation from the PSII core [216]. Such a conclusion was further supported by the appearance of a red-shifted emission band in the fluorescence spectra of highly illuminated leaves. This red-shifted band, which was absent in the dark, was suggested to originate from the quenched LHCII aggregates energetically separated from the PSII core reaction centers [171]. As a result, two distinct NPQ quenching sites were proposed: one in the detached, aggregated cluster of LHCIIs that is not in energy transfer contact with the RCs, and the other in the remaining antenna complexes still attached to PSII [216]. Therefore, according to this model, PSII absorption cross-section is expected to decrease during NPQ. On the other hand, later studies on the diluted chloroplasts did not reveal any long-wavelength components which could be attributed to the detached LHCII complexes [217]. Moreover, in the same work low-temperature excitation fluorescence spectroscopy did not show any alterations in the absorption cross-section of the PSII core antenna that would be expected to result from the detachment of Chl *b*-enriched LHCII trimers.

In order to understand these discrepancies that are faced in different studies, a few comments should be made regarding the validity of the methods used so far to assess the PSII absorption cross-section. First of all, the mentioned conclusion about a red-shifted emission component arising due to detached LHCIIs was not derived from a direct, genuine measurement of the fluorescence emission spectrum of LHCII in the NPQ state, but were based on a rather complex modeling of the time-resolved fluorescence of PSII and PSI, which required up to 8 fluorescence lifetime components [171, 216]. Moreover, these measurements were performed on intact leaves, giving rise to a whole range of side-effects like photon re-absorption [218] or light scattering [219] that could affect the fluorescence data. Therefore an independent approach is needed to further investigate whether the functional PSII antenna size changes during NPQ.

The absorption cross-section of PSII can be directly estimated during the measurements of fluorescence rise kinetics—the so-called fluorescence induction curves—on a ms timescale during the actinic illumination [220]. Fluorescence quantum yield in PSII obviously depends on the redox state of the RCs. Initially, since all the RCs are open, the energy of the absorbed light photons is predominantly transferred to the RCs and then utilized therein during charge separation. As the RCs become progressively closed due to continuous illumination, more excitation remain within the antenna, giving rise to the increased fluorescence signal. After several hundreds of ms of such actinic excitation nearly all the RCs are closed, which results in the fluorescence intensity approaching its maximum value. The rate of fluorescence induction, determining the shape of the rise kinetics, obviously depends on the antenna size of PSII: the larger is the absorption cross-section of the RC, the smaller time is required under the same excitation light intensities to ultimately close all the reaction centers and thus to reach a steady-state regime.

These features of the fluorescence induction traces are illustrated in Fig. 5.1a, where measurement results on the leaves from wild-type (WT) *Arabidopsis* plant and its two well-characterized mutants, namely antisense *Lhcb2* (*asLhcb2*) and *Chlorina-1* (*Ch1*), are shown[12]. The former mutant possesses a halved PSII antenna compared to the WT [221], while *Ch1* has no LHCII at all and expresses only one monomeric antenna complex [222]. Consequently, the smaller light-harvesting antenna in these mutants results in slower fluorescence rise kinetics compared to the wild-type species.

The same techniques were also applied to measure fluorescence induction in intact spinach chloroplasts after their adaptation to high light conditions, when strong fluorescence quenching was recorded. By turning off the saturating light and waiting until all the RCs become open (but at the same time ensuring that NPQ is still active), fluorescence rise kinetics was recorded. For comparison, the measurements were repeated after ~5 min of dark adaptation, when NPQ had been fully relaxed. The resulting fluorescence traces are presented in Fig. 5.1b. A relative change in the detected fluorescence intensity during both measurements is apparent and can be attributed to the NPQ traps acting in light-adapted samples. Additionally we can note that fluorescence from dark-recovered samples reaches its steady state significantly slower than in the light-adapted ones. Such an observation clearly indicates that besides the formation/relaxation of NPQ,

---

[12] The experimental measurements described in this chapter were performed by E. Belgio from Queen Mary University of London, UK. Further details are presented in [213].

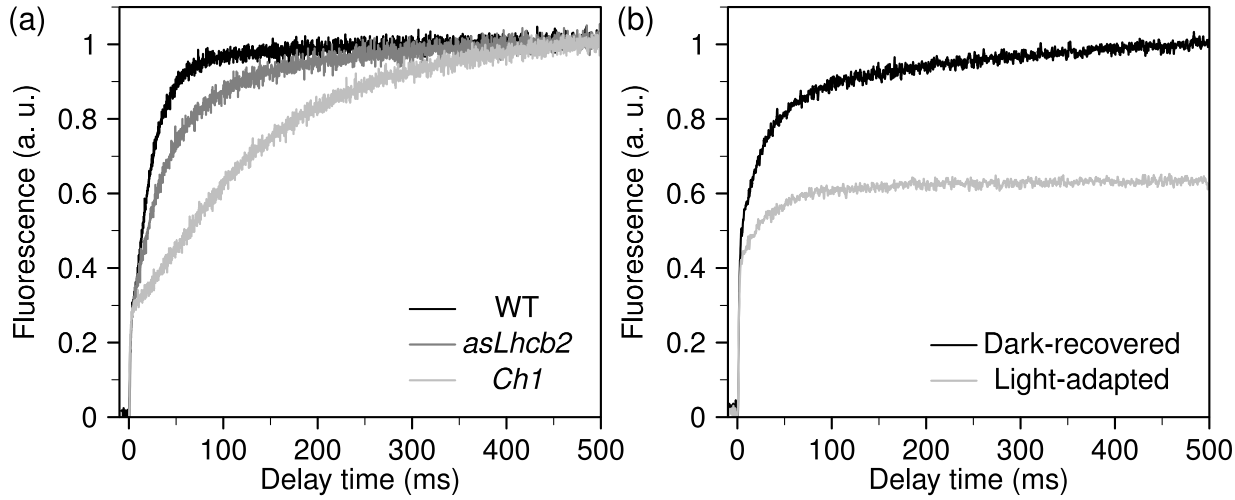

Figure 5.1 | (**a**) Fluorescence induction kinetics, measured in leaves from wild-type (WT) as well as from antisense *Lhcb2* (*asLhcb2*) and *Chlorina-1* (*Ch1*) *Arabidopsis* mutants. (**b**) Fluorescence induction kinetics, obtained from intact spinach chloroplasts after intense illumination inducing NPQ (light-adapted samples) following by the 5-minute dark adaptation period required to recover from NPQ conditions (dark-recovered samples).

some structural reorganization within the thylakoid membranes occurs in response to the varying light conditions, resulting in the dynamically changing absorption cross-section of the PSII reaction centers. To quantitatively evaluate these changes, in the next sections we formulate several models describing fluorescence induction kinetics in thylakoid membranes and adopt them to the previously discussed fluorescence traces from various *Arabidopsis* leaves (shown in Fig. 5.1a). Then we apply the same description for the light- and dark-adapted chloroplasts, which allow us to determine both the changes in the absorption cross-section and the efficiency of NPQ raps.

5.2 Fluorescence induction in light-harvesting antenna

Dependently on the actual distribution of the PSII cores and the LHCII complexes within the thylakoid membrane, several distinct theoretical approaches can be formulated to describe fluorescence rise kinetics during the closure of the reaction centers. In the simplest "lake" model [223–225], PSII is assumed to be a large pool of light-harvesting pigments with randomly distributed reaction centers, so that excitation can freely migrate through the whole system until it reaches any of the RCs. The latter is assumed to be in one of two discrete states: either open or closed. Alternatively, in the so-called "puddle" description, thylakoid membrane is build from many well-separated smaller pools of antenna complexes, each possessing a finite number of the RCs. Both these models are shortly described below.

5.2.1 Lake model

As already mentioned, the lake model describes fluorescence induction in a very large pool of the pigment molecules with, accordingly, a large number of the reaction centers being randomly distributed among them. It is known that excitation energy transfer through the antenna towards the RC occurs on the timescale of several hundreds of ps (*cf.* previous chapter), which is at least 6 orders of magnitude faster than the ms timescale of fluorescence induction. Therefore we can completely neglect inter-pigment and inter-complex excitation energy transfer and describe the state of the system with just two numbers—the total amount of the excited states per RC, $n\left(t\right)$, and the relative concentration of the closed reaction centers, $q\left(t\right)$. The relative concentration of the open RCs, accordingly, is defined as $1-q\left(t\right)$.

If we denote the effective excitation trapping rate by the open RC (taking into account both the photochemical trapping itself and excitation migration through the antenna towards the RC) as k_0, the total excitation trapping rate under conditions of the closed RCs as k_c (it defines mean excitation lifetime in such conditions), and the effective excitation quenching rate by all traps responsible for NPQ, generated per 1 RC under high light conditions, as k_q, then the total amount of excitation per 1 RC under continuous illumination obeys a simple kinetic equation:

$$\frac{\mathrm{d}n\left(t\right)}{\mathrm{d}t}=G-\left[k_0\left(1-q\left(t\right)\right)+k_\mathrm{c}q\left(t\right)+k_\mathrm{q}\right]n\left(t\right), \tag{5.1}$$

where G is the constant rate of generation of excitations (absorption rate) in the system per 1 RC. For optically thin solutions and monochromatic light, G is given by the product of the total absorption cross-section σ of the antenna at the given excitation wavelength and an incoming light intensity I, $G=\sigma I$.

On a millisecond time scale, when the steady-state regime is achieved (*i.e.* when $\mathrm{d}n/\mathrm{d}t=0$), the stationary solution of Eq. 5.1, slowly changing due to increase of $q\left(t\right)$, is

$$n_\mathrm{st}\left(t\right)=\frac{G}{k_0+k_\mathrm{q}-\left(k_0-k_\mathrm{c}\right)q\left(t\right)}=\frac{G/k_0}{1+Q-pq\left(t\right)},$$

where we denoted $p=1-k_\mathrm{c}/k_0$ and $Q=k_\mathrm{q}/k_0$. From the obtained stationary solution we can define the fluorescence yield as

$$F\left(t\right)=\frac{k_\mathrm{f}}{G}\cdot n_\mathrm{st}=\frac{k_\mathrm{f}/k_0}{1+Q-pq\left(t\right)}, \tag{5.2}$$

where k_f is the fluorescence rate. The concentration of the closed RCs increases in time due to photochemistry taking place in the open ones, so that

$$\frac{\mathrm{d}q}{\mathrm{d}t} = k_0 \left(1 - q\left(t\right)\right) n_{\mathrm{st}} = G \frac{1 - q\left(t\right)}{1 + Q - pq\left(t\right)}. \tag{5.3}$$

By numerically solving Eq. 5.3 and substituting its solution, $q\left(t\right)$, into Eq. 5.2 we can obtain the time-dependent fluorescence induction curves $F\left(t\right)$. Accordingly, the minimal (F_0) and maximal (F_{m}) values of the fluorescence yield, corresponding respectively to the cases of $q = 0$ and $q = 1$, are equal to

$$F_0 = \frac{k_{\mathrm{f}}/k_0}{1 + Q}, \qquad F_{\mathrm{m}} = \frac{k_{\mathrm{f}}/k_0}{1 + Q - p}. \tag{5.4}$$

The fluorescence rise kinetics, set to 0 at time $t = 0$ and normalized to 1 at its maximum, *i.e.* the one given by

$$\Phi\left(t\right) = \frac{F\left(t\right) - F_0}{F_{\mathrm{m}} - F_0} = \frac{1 + Q - p}{1 + Q - pq\left(t\right)} q\left(t\right), \tag{5.5}$$

can be used to evaluate the absorption cross-section of the studied system. Indeed, by taking into account Eq. 5.3, the complementary area above the normalized fluorescence induction curve is equal to

$$A = \int_0^{\infty} \left(1 - \Phi\left(t\right)\right) \mathrm{d}t = \frac{1 + Q}{G} \tag{5.6}$$

and for the dark-adapted samples (when $Q = 0$) can be straight-forwardly related to the absorption cross-section: $\sigma = G/I = 1/\left(AI\right)$. However, due to additional Q term in Eq. 5.6, the direct interpretation of the area above the measured fluorescence induction curve becomes non-trivial, and numerical reproduction of the whole kinetics trace should be carried out in order to evaluate the change of the total physical cross-section of the photosynthetic antenna.

5.2.2 Puddle model

In the lake model described above, the system is supposed to be very large and interconnected, therefore consisting of many RCs. As a result, the relative concentration of the closed RCs, $q\left(t\right)$, continuously increases in time. In real systems, however, various PSIIs might become more separated, resulting in the number of RCs per PSII being finite, which leads to the changes of q happening in a discrete manner. This effect can be accounted for in a slightly more sophisticated statistical (or "puddle") approach, in agreement with the well-established model of the photosynthetic membrane [160]. A somewhat similar statistical approach was implemented in Section 2.3 to model singlet–triplet annihilation.

Let us analyze the system with N RCs, when i of them are closed. In this case, the excitation density of the whole system, n_i, obeys the following equation:

$$\frac{\mathrm{d}n_i}{\mathrm{d}t} = G - \left[k_0\left(1 - \tfrac{i}{N}\right) + k_\mathrm{c}\tfrac{i}{N} + k_\mathrm{q}\right] n_i = G - \left[k_0\left(1 - \tfrac{i}{N}p\right) + k_\mathrm{q}\right],$$

where again $p = 1 - k_\mathrm{c}/k_0$, $G = \sigma I$ is the rate of generation of excitations in the whole system, and all the rate constants are the same as defined previously in the lake model (normalized to the whole system). In the stationary regime observed on a ms timescale we obtain:

$$n_i^{(\mathrm{st})} = \frac{G/k_0}{1 + Q - p\frac{i}{N}}, \tag{5.7}$$

where $Q = k_\mathrm{q}/k_0$. From the obtained stationary solutions the following fluorescence yields in each state can be defined similarly to Eq. 5.2:

$$F_i = \frac{k_\mathrm{f}/k_0}{1 + Q - p\frac{i}{N}}. \tag{5.8}$$

In order to calculate the total fluorescence yield, values defined in Eq. 5.8 should be summed up with the time-dependent weighting factors $P_i(t)$ representing probabilities that at a given time t there are exactly i closed RCs in the system. These probabilities can be easily calculated from the following Master equations:

$$\begin{aligned}
\frac{\mathrm{d}P_0}{\mathrm{d}t} &= -k_0 n_0^{(\mathrm{st})} P_0, \\
\frac{\mathrm{d}P_i}{\mathrm{d}t} &= k_0\left[\left(1 - \tfrac{i-1}{N}\right) n_{i-1}^{(\mathrm{st})} P_{i-1} - \left(1 - \tfrac{i}{N}\right) n_i^{(\mathrm{st})} P_i\right], \qquad 1 \le i \le N-1, \\
\frac{\mathrm{d}P_N}{\mathrm{d}t} &= \frac{k_0}{N} n_{N-1}^{(\mathrm{st})} P_{N-1},
\end{aligned}$$

where stationary excitation densities $n_i^{(\mathrm{st})}$ are given in Eq. 5.7. As a result, by numerically solving this system of differential equations, the total fluorescence yield is defined as

$$F(t) = \sum_{i=0}^{N} P_i(t) \cdot \frac{k_\mathrm{f}/k_0}{1 + Q - p\frac{i}{N}}.$$

Since the minimal (F_0) and maximal (F_m) values of the fluorescence yield are the same as in the lake model (see Eq. 5.4), the normalized fluorescence induction kinetics is then given by

$$\Phi(t) = \frac{F(t) - F_0}{F_\mathrm{m} - F_0} = \frac{1 + Q - p}{p}\left[(1 + Q)\sum_{i=0}^{N} \frac{P_i(t)}{1 + Q - p\frac{i}{N}} - 1\right]. \tag{5.9}$$

In the limit $N \gg 1$ this statistical model reproduces the results of the lake model presented before. In more general case of finite N, however, Eq. 5.9 defines more gradual fluorescence rise kinetics than Eq. 5.5. Nevertheless, the complementary area above the normalized fluorescence induction curve given by Eq. 5.9 can be calculated analytically and results in exactly the same expression as obtained previously:

$$A = \int_0^\infty \left(1 - \Phi\left(t\right)\right) \, \mathrm{d}t = \frac{1+Q}{G/N}.$$

In the case of a more realistic heterogeneous photosynthetic membrane, consisting of several types of subsystems of different absorption cross-sections, σ_j, with a relative fraction h_j (so that $\sum_j h_j = 1$), the total fluorescence yield can be simply found as a weighted sum of those produced in all the subsystems separately, each described by its own $k_0^{(j)}$, G_j, N_j, and Q_j values:

$$F\left(t\right) = \sum_j h_j \frac{k_\mathrm{f}}{k_0^{(j)}} \sum_{i=0}^{N} \frac{P_i^{(j)}\left(t\right)}{1 + Q_j - p\frac{i}{N_j}}.$$

The effective trapping rates by the open RCs, $k_0^{(j)}$, are approximately inversely proportional to the antenna size—such a relationship is strictly attained for both trap-limited [5] and two-dimensional migration-limited cases (*cf.* Eq. 4.22). Therefore these rates can be rescaled according to $k_0^{(j)} = k_0^{(1)} G_1 / G_j$. Then the average absorption cross-section is $\sigma \propto G = \sum_j h_j G_j$ and the net value of the average efficiency of NPQ traps, Q, can be evaluated as the ratio of the total number of excitons being trapped per unit time by the NPQ quenchers and the open RCs: $Q = G_\mathrm{NPQ}/G_\mathrm{RC}$, where

$$G_\mathrm{NPQ} = \sum_j h_j G_j \cdot \frac{k_q^{(j)}}{k_0^{(j)} + k_\mathrm{q}^{(j)}} = \sum_j \frac{h_j G_j Q_j}{1 + Q_j}$$

and $G_\mathrm{RC} = G - G_\mathrm{NPQ}$.

5.2.3 Calibrating the models

Prior to analyzing changes in the fluorescence induction traces measured in dark and high light conditions, we used fluorescence kinetics obtained from different *Arabidopsis* plants and presented in Fig. 5.1a to validate both models described above. The analysis of these kinetics provided us several benefits: first of all, the corresponding measurements were performed on the dark-adapted leaves when non-photochemical quenching can be neglected, which leads to simpler interpretation of the modeling results. The known antenna composition of WT species and

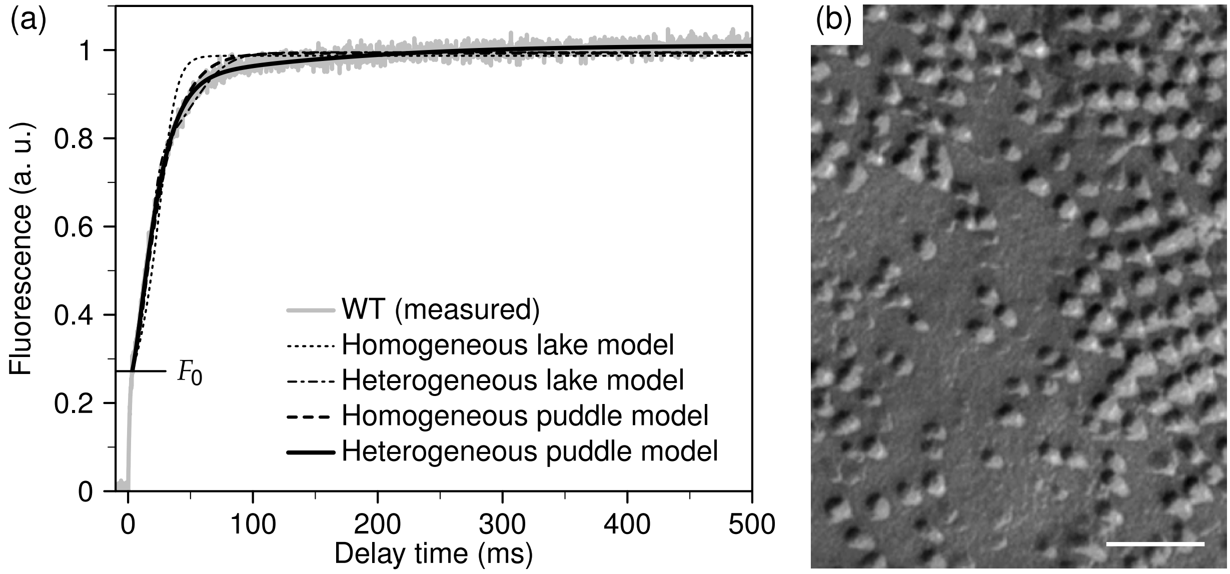

Figure 5.2 | (**a**) Comparison of the best-fitted fluorescence induction curves in wild-type *Arabidopsis* leaves as obtained by using homogeneous and heterogeneous (containing 2 subsystems) lake and puddle models. Horizontal line indicates F_0 fluorescence yield. (**b**) A freeze-fracture electron microscopy image of PSII-containing membranes showing the variations in RC density (LHCIIs are not visible here) as possible grounds for heterogeneity in PSII antenna size. White bar corresponds to 100 nm [213].

different mutants allowed us to further verify these modeling results by comparing the calculated relative absorption cross-section for all the samples with those based on the biochemical composition of PSII in the mentioned plant species.

The comparison of different models used to describe fluorescence kinetics in WT leaves is demonstrated in Fig. 5.2a. Here we see that neither a simple lake model nor a homogeneous puddle model were sufficient to reproduce the experimentally recorded fluorescence kinetics. On the other hand, a satisfactory result was achieved by using the heterogeneous puddle model accounting for just two subsystems that exhibit a 7-fold difference in their absorption cross-sections (see Table 5.1), in agreement with the previously reported existence of PSIIs with different sizes of the light-harvesting antenna (the so-called α- and β-species of PSII) [226]. This result is also supported by the electron microscopy of PSII membranes that clearly reveals their inhomogeneous nature as well as the presence of PSIIs with small antenna (see Fig. 5.2b). The latter obviously cannot be described by the lake model in an appropriate way. We also noted that smaller N_j values resulted in better description of the experimental data; therefore, by taking into account the dimeric nature of PSII, the same number of RCs per PSII supercomplex, $N_j = N = 2$, was assumed for all the subsequent calculations. Accordingly, the heterogeneous puddle model assuming the co-existence of two subsystems with different absorption cross-sections was used throughout.

Table 5.1 | Model parameters, obtained by fitting fluorescence induction kinetics in the WT, *asLhcb2*, and *Ch1 Arabidopsis* leaves with the heterogeneous puddle model (vertical lines separate the parameters obtained for both subsystems).

Parameter	WT	*asLhcb2*	*Ch1*
$p = 1 - k_\mathrm{c}/k_0$	0.728	0.722	0.728
$h_1 \mid h_2$	54.0 % ∣ 46.0 %	26.9 % ∣ 73.1 %	17.3 % ∣ 82.7 %
$G_1 \mid G_2$ (ms^{-1})	0.0969 ∣ 0.0129	0.0819 ∣ 0.0175	0.0277 ∣ 0.0107
$G = \sum_j h_j G_j$ (ms^{-1})	0.0583	0.0348	0.0136
Relative cross-section	**100 %**	**60 %**	**23 %**

As a result of these simplifications, the number of the model parameters used to describe fluorescence induction kinetics in the dark-adapted samples reduced to 4, namely G_1, G_2, h_1 (and $h_2 = 1 - h_1$), and p (the latter describes features of the RC and therefore was assumed to be the same for both subsystem in our heterogeneous puddle model). However, the ambiguity of the fitting results is kept minimal since strong experiment-based restrictions exist for some parameters. For example, the parameter $p = 1 - k_\mathrm{c}/k_0$ can be expressed as $p = 1 - F_0/F_\mathrm{m}$ (see Eq. 5.4 when $Q_j = 0$), where the minimum and maximum fluorescence yields are easily extracted from the recorded fluorescence kinetics. Similarly, the cross-section of the smaller subsystem (say, $G_2 = \min\left\{G_j\right\}$) is also severely restricted by the experimental observations: it can be shown that for the dark-adapted samples at longer times the following asymptotic relation holds:

$$\ln\left(1 - \Phi\left(t\right)\right) = \ln\frac{F_\mathrm{m} - F\left(t\right)}{F_\mathrm{m} - F_0} \overset{\text{large } t}{\simeq} a - b\,t,$$

where b can be simply evaluated from the experimental kinetics and is related to the model parameters: $b = G_2/\left[N - p\left(N-1\right)\right]$. The remaining parameters are strongly inter-connected as well since, as stated above, the complementary area above the normalized kinetics, $A = N/\sum_j\left(h_j G_j\right)$, can also be directly evaluated from the experiment. Similar albeit more complicated restrictions also exist for the kinetics obtained from the light-adapted samples, when $Q_j \neq 0$.

Taking these considerations into account, fluorescence induction kinetics in *Arabidopsis* mutants were analyzed in a similar way as that in WT species discussed above. The normalized measured fluorescence kinetics, $\Phi\left(t\right)$ (see Eq. 5.9 for definition) together with the fitted ones are shown in Fig. 5.3 while the obtained parameters of the heterogeneous puddle model are listed in Table 5.1. From this table we see that $p = 0.73$ was the same in all three different species, indicating that the intrinsic trapping capabilities of the RCs were not affected in the *Arabidopsis* mutants. Secondly, all the three plant species exhibit a high level of

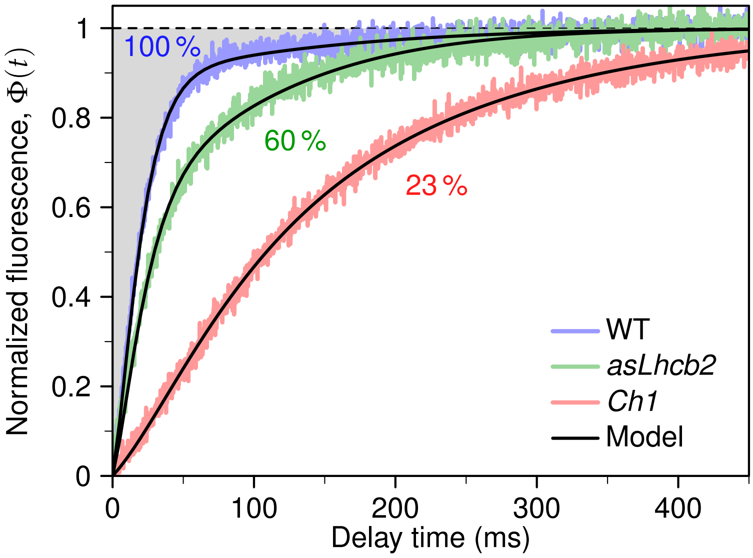

Figure 5.3 | Normalized fluorescence induction kinetics $\Phi(t)$ in various *Arabidopsis* plants (color lines; kinetics are taken from Fig. 5.1a, zeroed at F_0 and normalized to 1 at F_m) together with the simulated ones (black lines). The shaded region indicates the complementary area above the kinetics from WT leaves which is reciprocal to the mean absorption cross-section of the RCs. Numbers correspond to the estimated PSII absorption cross-section in *Arabidopsis* mutants relative to that in WT species.

heterogeneity in PSII absorption cross-section, albeit it is less pronounced in the mutants due to globally reduced antenna size: the ratio G_1/G_2 equals 7.5, 4.7, and 2.6 for WT, *asLhcb2*, and *Ch1* species, respectively. Moreover, if in WT thylakoid membranes both larger and smaller PSIIs are distributed almost equally, the smaller ones dominate in both mutants (*cf.* weighting factors h_j in Table 5.1). Both these effects result in the membrane-averaged PSII absorption cross-sections of the *asLhcb2* and *Ch1* mutants, which are proportional to $G = \sum_j h_j G_j$, being just 60 % and 23 % that of wild-type species, respectively (see last column in Table 5.1). As expected, this observation is fully inline with a direct estimation of the complementary area above the normalized induction kinetics, for WT leaves being indicated by the shaded region in Fig. 5.3.

By taking into account the known biochemical composition of the photosynthetic membranes from various *Arabidopsis* species [221,222,227], it is possible to evaluate the mean number of Chl molecules bound by the PSII monomer. This data is summarized in Table 5.2 and reveals a perfect agreement between the estimated relative numbers of Chl pigments and the mean relative absorption cross-sections evaluated above, thus providing an additional support for our chosen heterogeneous puddle model of fluorescence induction. Therefore in the following section we use this model to measure the dynamic changes in the structural organization of the thylakoid membranes occurring in response to the varying light conditions.

Table 5.2 | Relative PSII absorption cross-sections in different species of *Arabidopsis* plant, estimated from their biochemical composition [221, 222, 227] and from the model fit presented in Fig. 5.3 and Table 5.1.

Species	Antenna proteins per PSII monomer and resulting number of Chl pigments	Estimated cross-section	
		structure-based	model-based
WT	5 LHCII trimers, 1 CP29, 1 CP26, 1 CP24, 1 CP43, 1 CP47, 1 RC $\Longrightarrow$ **277 Chls**	100 %	100 %
asLhcb2	2 Lhcb3 trimers, 1 CP29, 2 CP26, 1 CP24, 1 CP43, 1 CP47, 1 RC $\Longrightarrow$ **159 Chls**	57 %	60 %
Ch1	1 Lhcb2 monomer, 1.5 CP26, 1 CP43, 1 CP47, 1 RC $\Longrightarrow$ **61 Chls**	22 %	23 %

5.3 Determining PSII functional cross-section in NPQ state

The model discussed so far for leaves was applied in a similar way to fluorescence induction traces of intact spinach chloroplasts in the NPQ state and following their dark-recovery. The induction kinetics in the low light conditions was uniquely described with the parameters listed in Table 5.3. Similarly to the WT *Arabidopsis* leaves, the PSII membrane of spinach chloroplasts in the dark state consists of two dominating pools of PSIIs that exhibit an 8-fold difference in their antenna size. Although the larger ones comprise only one fifth of all the PSII supercomplexes, such a pronounced difference in the absorption cross-section ensures that these large photosynthetic units cover about 65 % of the membrane surface area occupied by PSIIs. Moreover, since the measurements of the fluorescence induction kinetics were performed under the same excitation intensities as with *Arabidopsis* leaves discussed above, we can take the advantage of our previous analysis by mapping the model parameters G_j, proportional to the absorption cross-section σ_j and listed in Table 5.1, with the actual chlorophyll composition of the PSII light-harvesting antenna (*cf.* Table 5.2). As a result, we can evaluate that the larger PSII in the dark-adapted state bounds about 430 Chl molecules per RC (structurally that would correspond to the $C_2S_2M_2$ supercomplex shown in Fig. 4.1a with ~13 additional LHCII trimers) whereas the smaller one—only 52 Chls per RC and therefore probably lacks any LHCII trimers.

In order to properly fit the fluorescence induction trace in the light-adapted state, besides G_j and h_j parameters, an additional degree of freedom was added—the quenching efficiency of each subsystems (Q_1 and Q_2). Such complication, however, introduced some ambiguity in determining model parameters. Therefore in order to avoid over-fitting, two approaches were used. First, we let the in-

Table 5.3 | Model parameters (p, h_j, G_j, and Q_j), obtained by fitting fluorescence induction in light-adapted and dark-recovered intact spinach chloroplasts (vertical lines separate the parameters obtained for both subsystems). Other quantities were calculated from these mentioned parameters. For the light-adapted samples, the parameters p and h_j were fixed to be the same as obtained for the dark-recovered chloroplasts.

Parameter	Dark-recovered	Light-adapted
$p = 1 - k_c/k_0$	0.5069	0.5069
h_1 ∣ h_2	18.7 % ∣ 81.3 %	18.7 % ∣ 81.3 %
G_1 ∣ G_2 (ms^{-1})	0.0904 ∣ 0.0110	0.0944 ∣ 0.0268
Number of Chls per RC	430 ∣ 52	449 ∣ 127
$G = \sum_j h_j G_j$ (ms^{-1})	0.0258	0.0394
Relative cross-section	**100 %**	**152 %**
$Q_j = k_q^{(j)}/k_0^{(j)}$	—	0.29 ∣ 1.53
Weighted NPQ efficiency (relative to RC)	—	0.75

coming excitation densities, G_j, of both subsystems vary while their corresponding weighting factors h_j and the parameter $p = 1 - k_c/k_0$ were fixed to the same values as obtained from the previously-fitted dark-adapted samples, thus again minimizing the number of undefined model parameters. From this approach it followed that under NPQ conditions, the antenna of the larger PSII was increased by a single LHCII trimer whereas the smaller pool of PSII complexes increased their absorption cross-section more than two-fold (see Table 5.3). On average, a ~52% increase of PSII mean antenna size was observed.

For the sake of completeness, we also analyzed less probable situation when in response to the increased light intensity the weighting factors h_j can also vary. The dependence of the obtained model parameters on the weighting factor h_1 of the larger PSII is demonstrated in Fig. 5.4, where we see that independently of the chosen h_1 value, there is a significant (more than 30 %) increase in cross-section under light conditions comparing to the dark-recovery state. The effect of these variation in model parameters on the quality of the fit is, however, negligible: for any given h_1 value, a corresponding set of G_j and Q_j parameters exists, which yields exactly same induction kinetics, as shown in Fig. 5.5.

As a result, fluorescence induction measurements and our modeling results provide a direct demonstration that the functional antenna size of PSII increases during NPQ. This result disproves previous hypothesis of energetic uncoupling of LHCIIs from the PSII reaction centers during NPQ as a consequence of the increased clustering of the LHCII complexes [167]. It also contradicts the model proposing functional detachment of up to 50 % of the peripheral PSII antenna un-

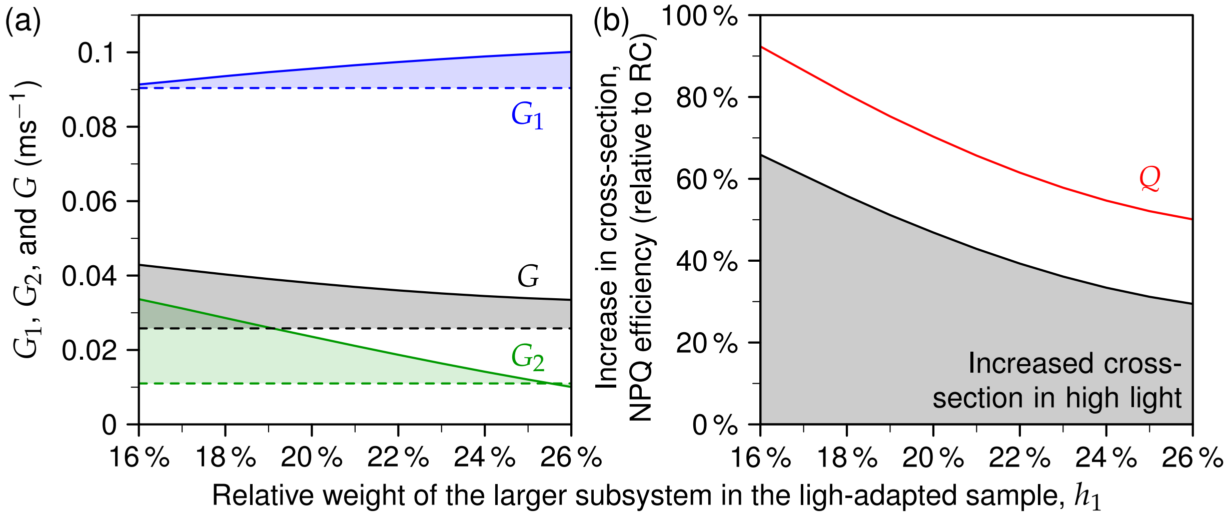

Figure 5.4 | Fitted model parameters, obtained for the light-adapted chloroplasts by fixing the relative weighting factor h_1 of the larger subsystem. (**a**) Parameters G_1, G_2, and G, proportional to the absorption cross-section (solid lines). For reference, corresponding values for the dark-recovered chloroplasts (see Table 5.3) are indicated with the dashed lines; shaded areas highlight the observed change between the high and the low light conditions. (**b**) Weighted mean NPQ efficiency relative to RC (red line) and the relative increase of cross-section in high light conditions (shaded region).

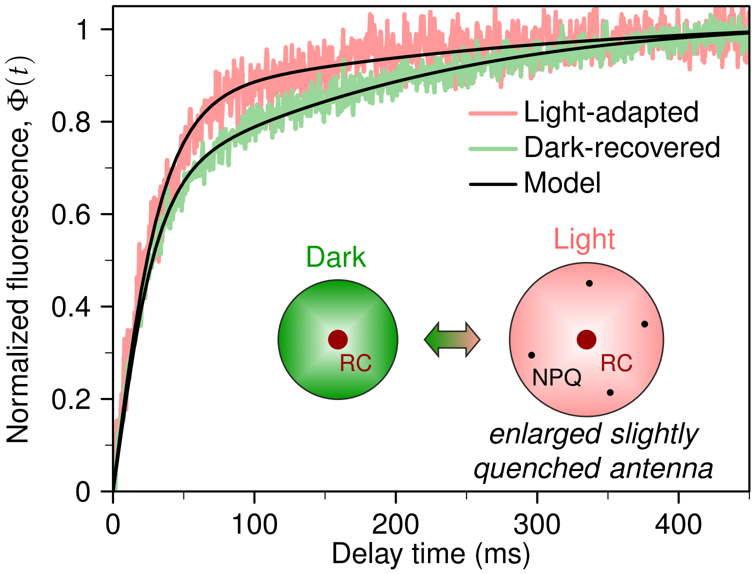

Figure 5.5 | Normalized fluorescence induction kinetics $\Phi(t)$ in the light-adapted and dark-recovered spinach chloroplasts (color lines, taken from Fig. 5.1b, zeroed at F_0 and normalized to 1 at F_m) together with the simulated ones (black lines). The inset illustrates the main conclusion that under high light conditions the generation of NPQ states is accompanied with a considerable increase of the PSII light-harvesting antenna.

der high light conditions [216] and fundamentally changes our understanding of the nature of the NPQ and its concomitant processes. Indeed, it has been widely assumed so far that for the efficient photoprotection the non-photochemical quenchers in the antenna must effectively "compete" with excitation trapping by the RC [101]. In this "strong trap" scenario the probability that an exciton reaches a RC is significantly undermined by the appearance of traps within the antenna. Since such strong traps should significantly reduce the functional size of the PSII antenna, one would expect the fluorescence induction in light-adapted chloroplasts to be notably slower than in the dark-adapted ones. Nevertheless, our results explicitly indicate that this is not the case, and PSII antenna size is not reduced in the NPQ state.

Under NPQ conditions, even when all RCs are open, part of the excitation is quenched by the NPQ-traps. According to our simulations, total non-photochemical quenching in the larger PSIIs is about 3 times less efficient than photochemical quenching (see Table 5.3). This result also indicates that the "strong trap" picture of NPQ is not realistic since the exciton traps that form within the PSII antenna appear to be rather inefficient, meaning that they hardly prevent excitation energy from reaching open RCIIs. If we account also for the smaller PSII units, the average net efficiency of all NPQ centers in the photosynthetic membrane is notably (about 25 %) lower than that of photochemical quenching. That means that only $k_0/\left(k_0+k_\mathrm{q}\right) = 1/\left(1+Q\right) = 57\,\%$ of the light-generated excitation is trapped by the open RCs. However, since the physical antenna size has increased by 52 %, the mean efficiency of the antenna in collecting and delivering excitations to the RC becomes $0.57 \times 1.52 = 87\,\%$ compared with the dark state. The results exhibit some slight variations if different h_1 values are used (see Fig. 5.4b) but do not change our basic conclusions. More important, independently of the chosen h_1, the quantum yield of the photochemical quenching, as it was defined above, remains exactly the same—about 87 % of that in the dark state. Thus upon switching to NPQ conditions the efficiency of trapping by the open reaction centers decreased by only ~13 %. Without such an adjustment of the antenna size, the drop in RC efficiency would exceed 40 %.

5.4 Summarizing remarks

Fluorescence induction measurements have proven to be a sensitive method capable to reveal even small variations in the PSII absorption cross-section in thylakoid membranes. The observed fluorescence rise kinetics from its minimum value F_0 to the steady-state intensity F_m can be viewed in terms of the probability that light photons are harvested in the antenna before steady-state equilibration is reached: the bigger the antenna size, the higher the probability of photon absorption, which consequently shortens the time taken to close all the PSII reaction centers. In this chapter, we demonstrated that due to light-induced structural rearrangements occurring within the photosynthetic membranes the total PSII antenna size increases by 40–50 %, resulting in faster fluorescence induction kinetics. Remembering the collective nature of the non-photochemical quenching that arises from the inter-connectivity of many conformationally fluctuating LHCII complexes, as determined in Chapter 3, the increased antenna has double effect on the processes happening under high light conditions. First, larger antenna means higher probability for LHCII to switch into its quenched state, so that on average more quenchers can be formed even without intrinsically shifting the dynamic equilibrium between distinct states of the pigment–protein complex. Second, increased PSII absorption cross-section helps photosynthetic organism to minimize the drop in excitation delivery to the RC. As a result, NPQ traps do not effectively prevent excitation energy from reaching the reaction centers prior to their closure. Therefore even surrounded by the quenched antenna, open reaction centers are still efficiently supplied with the excitation energy necessary for photochemistry.

The slow quenchers that are formed in antenna act only once energetic equilibration has been reached, serving to relieve the excitation pressure felt by the vulnerable closed reaction centers but not impeding the functionality of the open ones. As a result, slow traps capable of being generated anywhere in the antenna provide a flexible way to gradually adjust the overall efficiency of NPQ. This subtle mechanism is an exceptional example of the *economic* photoprotection implemented by Nature that is sufficient to protect the plant from photodamage while not interfering with the photosynthetic productivity.

Epilogue

In this Thesis, we studied various aspects of excitation dynamics and relaxation in photosynthetic light-harvesting systems, at every step making an attempt to approach a better understanding of one of the today's most puzzling photoprotective mechanisms implemented by Nature in the living organism—the non-photochemical quenching. This term combines a whole set of various processes occurring in the thylakoid membranes of green plants and algae during the short-term acclimation to the increased solar radiation. Over the last two decades, the main concepts of the photosynthetic light harvesting and self-regulation have been formulated, providing a strong foundation for the later studies implementing modern spectroscopic techniques and taking advantages of the cooperation of many people from different fields working together to solve the mystery of NPQ. The author of this Thesis unpretentiously believes that the study covered herein has also made its small contribution towards our deeper understanding of the molecular origin of the self-regulatory processes in photosynthesis.

We began our adventure in the world of light-harvesting systems from the structure-based calculations of the exciton evolution in the LHCII complex. Particularly, by accounting for the quantum-chemistry calculations of the dipole-forbidden S_1 state of carotenoids, we identified lutein molecules as the most efficient excitation quencher in LHCII crystals. Then, based on the fluorescence measurements in single light-harvesting complexes, we provided strong evidences that NPQ state in LHCII is not formed under some particular environment conditions but is rather one of the intrinsic states of the pigment–protein that randomly becomes available as a result of the protein's subtle conformational dynamics. Exposure to any ambient stress, like variations of the detergent concentration, pH level, temperature, *etc.*, in fact does not produce new states itself but just modulates the energy landscape of the pigment–protein complex thus shifting the dynamic equilibrium towards one or another state. Consequently, the probability of that particular state increases leading to the observed variations in fluorescence spectrum and/or intensity.

Our thorough analysis of the temperature-dependent time-resolved fluorescence spectra of LHCII trimers and aggregates allowed us to independently identify at least three distinct functional states of these pigment–protein complexes that were previously observed by means of single-molecule spectroscopy. Namely, besides the dominating state corresponding to strong fluorescence around the 680-nm spectral region, the state responsible for the fluorescence signal at longer wavelengths as well as the quenched states were revealed. Calculations of excitation energy dynamics in the LHCII aggregate allowed us to associate each state with a specific underlying molecular mechanism. In particular, we showed that the red-emitting state arises due to partial mixing of excitonic and chlorophyll–chlorophyll charge transfer states. On the other hand, the nature of the quenched state was demonstrated to be totally different and related to the incoherent excitation transfer to the short-lived carotenoid excited states. Based on our previous structure-based calculations on LHCII crystals, lutein molecule is the most probable candidate for this role.

Turning back to the non-photochemical quenching, we showed that all our conclusions based on the analysis of artificially made LHCII crystals or aggregates can be in a straightforward way generalized to the processes occurring *in vivo*. We demonstrated that in a relatively small light-harvesting antenna of PSII, even slight variation of the concentration of the quenched complexes can significantly reduce fluorescence quantum yield. The physical increase of the PSII absorption cross-section, revealed from the fluorescence induction kinetics, ensures even better photoprotection due to higher probability for the generation of NPQ centers within the antenna and, at the same time, minimizes the drop in excitation delivery to the open reaction centers. This effect gives us a perfect example of the economic design principles of the natural photosynthesis that might be learned and implemented in the mankind's attempts to build up artificial photosynthetic devices.

Finally, we have demonstrated that the multi-exponential fluorescence decay kinetics, observed in various antenna systems—from the single LHCII trimers to their aggregates, variously sized photosystems, or even thylakoid membranes—is just a manifestation of the fluctuating properties of the light-harvesting antenna and its proteins. We believe that this conclusion, breaking the long-existed dogma of the important role of the radical pair equilibration at the side of the excitation quencher and presenting a simple alternative explanation to the known experimental facts, will inspire more detailed future studies, further broadening the current understanding of light-harvesting processes in photosynthesis.

Bibliography

[1] R. E. Blankenship, D. M. Tiede, J. Barber, *et al.*, "Comparing photosynthetic and photovoltaic efficiencies and recognizing the potential for improvement," *Science*, 2011, **332**, 805–809.

[2] L. Taiz and E. Zeiger, *Plant Physiology*. Sunderland, Mass.: Sinauer Associates, 4th ed., 2006.

[3] A. Ruban, *The Photosynthetic Membrane: Molecular Mechanisms and Biophysics of Light Harvesting*. Chichester: John Wiley & Sons, Ltd, 2013.

[4] R. E. Blankenship, *Molecular Mechanisms of Photosynthesis*. Chichester: Wiley Blackwell, 2nd ed., 2014.

[5] H. van Amerongen, L. Valkunas, and R. van Grondelle, *Photosynthetic Excitons*. Singapore: World Scientific, 2000.

[6] R. Croce and H. van Amerongen, "Light-harvesting and structural organization of photosystem II: from individual complexes to thylakoid membrane," *J. Photochem. Photobiol. B*, 2011, **104**, 142–153.

[7] G. D. Scholes, G. R. Fleming, A. Olaya-Castro, and R. van Grondelle, "Lessons from nature about solar light harvesting," *Nat. Chem.*, 2011, **3**, 763–774.

[8] R. Croce and H. van Amerongen, "Light-harvesting in photosystem I," *Photosynth. Res.*, 2013, **116**, 153–166.

[9] H. van Amerongen and R. Croce, "Light harvesting in photosystem II," *Photosynth. Res.*, 2013, **116**, 251–263.

[10] C. D. P. Duffy, L. Valkunas, and A. V. Ruban, "Light-harvesting processes in the dynamic photosynthetic antenna," *Phys. Chem. Chem. Phys.*, 2013, **15**, 18752–18770.

[11] R. Croce and H. van Amerongen, "Natural strategies for photosynthetic light harvesting," *Nat. Chem. Biol.*, 2014, **10**, 492–501.

[12] A. V. Ruban, M. P. Johnson, and C. D. P. Duffy, "The photoprotective molecular switch in the photosystem II antenna," *Biochim. Biophys. Acta, Bioenerg.*, 2012, **1817**, 167–181.

[13] A. O. Goushcha, V. N. Kharkyanen, G. W. Scott, and A. R. Holzwarth, "Self-regulation phenomena in bacterial reaction centers. I. General theory," *Biophys. J.*, 2000, **79**, 1237–1252.

[14] A. O. Goushcha, A. J. Manzo, G. W. Scott, *et al.*, "Self-regulation phenomena applied to bacterial reaction centers: 2. Nonequilibrium adiabatic potential: Dark and light conformations revisited," *Biophys. J.*, 2003, **84**, 1146–1160.

[15] E. Wientjes, H. van Amerongen, and R. Croce, "Quantum yield of charge separation in photosystem II: Functional effect of changes in the antenna size upon light acclimation," *J. Phys. Chem. B*, 2013, **117**, 11200–11208.

[16] E. Wientjes, H. van Amerongen, and R. Croce, "LHCII is an antenna of both photosystems after long-term acclimation," *Biochim. Biophys. Acta, Bioenerg.*, 2013, **1827**, 420–426.

[17] J. Zaks, K. Amarnath, D. M. Kramer, K. K. Niyogi, and G. R. Fleming, "A kinetic model of rapidly reversible nonphotochemical quenching," *Proc. Natl. Acad. Sci. U. S. A.*, 2012, **109**, 15757–15762.

[18] N. E. Holt, D. Zigmantas, L. Valkunas, X. P. Li, K. K. Niyogi, and G. R. Fleming, "Carotenoid cation formation and the regulation of photosynthetic light harvesting," *Science*, 2005, **307**, 433–436.

[19] A. A. Pascal, Z. F. Liu, K. Broess, *et al.*, "Molecular basis of photoprotection and control of photosynthetic light-harvesting," *Nature*, 2005, **436**, 134–137.

[20] A. V. Ruban, R. Berera, C. Ilioaia, *et al.*, "Identification of a mechanism of photoprotective energy dissipation in higher plants," *Nature*, 2007, **450**, 575–578.

[21] T. K. Ahn, T. J. Avenson, M. Ballottari, Y. C. Cheng, K. K. Niyogi, R. Bassi, and G. R. Fleming, "Architecture of a charge-transfer state regulating light harvesting in a plant antenna protein," *Science*, 2008, **320**, 794–797.

[22] M. G. Müller, P. Lambrev, M. Reus, E. Wientjes, R. Croce, and A. R. Holzwarth, "Singlet energy dissipation in the photosystem II light-harvesting complex does not involve energy transfer to carotenoids," *ChemPhysChem*, 2010, **11**, 1289–1296.

[23] X.-G. Zhu, D. R. Ort, J. Whitmarsh, and S. P. Long, "The slow reversibility of photosystem II thermal energy dissipation on transfer from high to low light may cause large losses in carbon gain by crop canopies: A theoretical analysis," *J. Exp. Bot.*, 2004, **55**, 1167–1175.

[24] X.-G. Zhu, S. P. Long, and D. R. Ort, "Improving photosynthetic efficiency for greater yield," *Annu. Rev. Plant Biol.*, 2010, **61**, 235–261.

[25] D. Gust and T. A. Moore, "Mimicking photosynthesis," *Science*, 1989, **244**, 35–41.

[26] P. A. Liddell, D. Kuciauskas, J. P. Sumida, *et al.*, "Photoinduced charge separation and charge recombination to a triplet state in a carotene–porphyrin–fullerene triad," *J. Am. Chem. Soc.*, 1997, **119**, 1400–1405.

[27] D. Gust, T. A. Moore, and A. L. Moore, "Realizing artificial photosynthesis," *Faraday Discuss.*, 2012, **155**, 9–26.

[28] I. Carmeli, I. Lieberman, L. Kraversky, Z. Fan, A. O. Govorov, G. Markovich, and S. Richter, "Broad band enhancement of light absorption in photosystem I by metal nanoparticle antennas," *Nano Lett.*, 2010, **10**, 2069–2074.

[29] K. J. Young, L. A. Martini, R. L. Milot, *et al.*, "Light-driven water oxidation for solar fuels," *Coord. Chem. Rev.*, 2012, **256**, 2503–2520.

[30] Y. Zhao, J. R. Swierk, J. D. Megiatto, Jr, *et al.*, "Improving the efficiency of

water splitting in dye-sensitized solar cells by using a biomimetic electron transfer mediator," *Proc. Natl. Acad. Sci. U. S. A.*, 2012, **109**, 15612–15616.

[31] C. Liu, J. Tang, H. M. Chen, B. Liu, and P. Yang, "A fully integrated nanosystem of semiconductor nanowires for direct solar water splitting," *Nano Lett.*, 2013, **13**, 2989–2992.

[32] S. Y. Reece, J. A. Hamel, K. Sung, T. D. Jarvi, A. J. Esswein, J. J. H. Pijpers, and D. G. Nocera, "Wireless solar water splitting using silicon-based semiconductors and earth-abundant catalysts," *Science*, 2011, **334**, 645–648.

[33] D. G. Nocera, "The artificial leaf," *Acc. Chem. Res.*, 2012, **45**, 767–776.

[34] A. Azarpira, M. Lublow, A. Steigert, *et al.*, "Efficient and stable TiO_2:Pt–Cu(In,Ga)Se_2 composite photoelectrodes for visible light driven hydrogen evolution," *Adv. Energy Mater.*, 2015, 1402148.

[35] C. Liu, J. J. Gallagher, K. K. Sakimoto, E. M. Nichols, C. J. Chang, M. C. Y. Chang, and P. Yang, "Nanowire-bacteria hybrids for unassisted solar carbon dioxide fixation to value-added chemicals," *Nano Lett.*, 2015, **15**, 3634–3639.

[36] W. Kühlbrandt and D. N. Wang, "Three-dimensional structure of plant light-harvesting complex determined by electron crystallography," *Nature*, 1991, **350**, 130–134.

[37] W. Kühlbrandt, D. N. Wang, and Y. Fujiyoshi, "Atomic model of plant light-harvesting complex by electron crystallography," *Nature*, 1994, **367**, 614–621.

[38] Z. F. Liu, H. C. Yan, K. B. Wang, *et al.*, "Crystal structure of spinach major light-harvesting complex at 2.72 Å resolution," *Nature*, 2004, **428**, 287–292.

[39] C. D. P. Duffy, A. V. Ruban, and W. Barford, "Theoretical investigation of the role of strongly coupled chlorophyll dimers in photoprotection of LHCII," *J. Phys. Chem. B*, 2008, **112**, 12508–12515.

[40] F. Müh, M. E.-A. Madjet, and T. Renger, "Structure-based identification of energy sinks in plant light-harvesting complex II," *J. Phys. Chem. B*, 2010, **114**, 13517–13535.

[41] C. D. P. Duffy, L. Valkunas, and A. V. Ruban, "Quantum mechanical calculations of xanthophyll–chlorophyll electronic coupling in the light-harvesting antenna of photosystem II of higher plants," *J. Phys. Chem. B*, 2013, **117**, 7605–7614.

[42] C. D. P. Duffy, J. Chmeliov, M. Macernis, J. Sulskus, L. Valkunas, and A. V. Ruban, "Modeling of fluorescence quenching by lutein in the plant light-harvesting complex LHCII," *J. Phys. Chem. B*, 2013, **117**, 10974–10986.

[43] J. Chmeliov, W. P. Bricker, C. Lo, E. Jouin, L. Valkunas, A. V. Ruban, and C. D. P. Duffy, "An 'all pigment' model of excitation quenching in LHCII," *Phys. Chem. Chem. Phys.*, 2015, **17**, 15857–15867.

[44] F. Müh, M. E.-A. Madjet, and T. Renger, "Structure-based simulation of linear optical spectra of the CP43 core antenna of photosystem II," *Photosynth. Res.*, 2012, **111**, 87–101.

[45] T. Polívka and V. Sundström, "Ultrafast dynamics of carotenoid excited

states – from solution to natural and artificial systems," *Chem. Rev.*, 2004, **104**, 2021–2071.

[46] J. T. Landrum, ed., *Carotenoids: Physical, Chemical, and Biological Functions and Properties*. Boca Raton: CRC Press, 2010.

[47] P. Jahns, D. Latowski, and K. Strzalka, "Mechanism and regulation of the violaxanthin cycle: the role of antenna proteins and membrane lipids," *Biochim. Biophys. Acta, Bioenerg.*, 2009, **1787**, 3–14.

[48] F. G. Plumley and G. W. Schmidt, "Reconstitution of chlorophyll a/b light-harvesting complexes: Xanthophyll-dependent assembly and energy transfer," *Proc. Natl. Acad. Sci. U. S. A.*, 1987, **84**, 146–150.

[49] H. A. Frank, J. A. Bautista, J. S. Josue, and A. J. Young, "Mechanism of non-photochemical quenching in green plants: Energies of the lowest excited singlet states of violaxanthin and zeaxanthin," *Biochemistry*, 2000, **39**, 2831–2837.

[50] J. S. Josue and H. A. Frank, "Direct determination of the S_1 excited-state energies of xanthophylls by low-temperature fluorescence spectroscopy," *J. Phys. Chem. A*, 2002, **106**, 4815–4824.

[51] T. Polívka, D. Zigmantas, V. Sundström, E. Formaggio, G. Cinque, and R. Bassi, "Carotenoid S_1 state in a recombinant light-harvesting complex of photosystem II," *Biochemistry*, 2002, **41**, 439–450.

[52] P. J. Walla, P. A. Linden, K. Ohta, and G. R. Fleming, "Excited-state kinetics of the carotenoid S_1 state in LHC II and two-photon excitation spectra of lutein and β-carotene in solution: Efficient Car $S_1 \rightarrow$ Chl electronic energy transfer via hot S_1 states?," *J. Phys. Chem. A*, 2002, **106**, 1909–1916.

[53] E. E. Ostroumov, R. M. Mulvaney, R. J. Cogdell, and G. D. Scholes, "Broadband 2D electronic spectroscopy reveals a carotenoid dark state in purple bacteria," *Science*, 2013, **340**, 52–56.

[54] H. Kramer and P. Mathis, "Quantum yield and rate of formation of the carotenoid triplet state in photosynthetic structures," *Biochim. Biophys. Acta*, 1980, **593**, 319–329.

[55] P. G. Bowers and G. Porter, "Quantum yields of triplet formation in solutions of chlorophyll," *Proc. R. Soc. Lond. A*, 1967, **296**, 435–441.

[56] J. Breton, N. E. Geacintov, and C. E. Swenberg, "Quenching of fluorescence by triplet excited states in chloroplasts," *Biochim. Biophys. Acta*, 1979, **548**, 616–635.

[57] H. J. den Blanken, A. J. Hoff, A. P. J. M. Jongenelis, and B. A. Diner, "High-resolution triplet-minus-singlet absorbance difference spectrum of photosystem II particles," *FEBS Lett.*, 1983, **157**, 21–27.

[58] K. Apel and H. Hirt, "Reactive oxygen species: Metabolism, oxidative stress, and signal transduction," *Annu. Rev. Plant Biol.*, 2004, **55**, 373–399.

[59] D. Siefermann-Harms, "The light-harvesting and protective functions of carotenoids in photosynthetic membranes," *Physiol. Plant.*, 1987, **69**, 561–568.

[60] E. J. G. Peterman, F. M. Dukker, R. van Grondelle, and H. van Amerongen, "Chlorophyll *a* and carotenoid triplet states in light-harvesting complex II of higher plants," *Biophys. J.*, 1995, **69**, 2670–2678.

[61] V. Barzda, E. J. Peterman, R. van Grondelle, and H. van Amerongen, "The influence of aggregation on triplet formation in light-harvesting chlorophyll *a*/*b* pigment–protein complex II of green plants," *Biochemistry*, 1998, **37**, 546–551.

[62] G. H. Krause and U. Behrend, "ΔpH-dependent chlorophyll fluorescence quenching indicating a mechanism of protection against photoinhibition of chloroplasts," *FEBS Lett.*, 1986, **200**, 298–302.

[63] G. Noctor, D. Rees, A. Young, and P. Horton, "The relationship between zeaxanthin, energy-dependent quenching of chlorophyll fluorescence, and trans-thylakoid pH gradient in isolated chloroplasts," *Biochim. Biophys. Acta, Bioenerg.*, 1991, **1057**, 320–330.

[64] B. Demmig-Adams, "Carotenoids and photoprotection in plants: A role for the xanthophyll zeaxanthin," *Biochim. Biophys. Acta, Bioenerg.*, 1990, **1020**, 1–24.

[65] X. P. Li, O. Bjorkman, C. Shih, A. R. Grossman, M. Rosenquist, S. Jansson, and K. K. Niyogi, "A pigment-binding protein essential for regulation of photosynthetic light harvesting," *Nature*, 2000, **403**, 391–395.

[66] P. Horton, A. Ruban, D. Rees, A. Pascal, G. Noctor, and A. Young, "Control of the light-harvesting function of chloroplast membranes by aggregation of the LHCII chlorophyll–protein complex," *FEBS Lett.*, 1991, **292**, 1–4.

[67] B. van Oort, A. van Hoek, A. V. Ruban, and H. van Amerongen, "Aggregation of light-harvesting complex II leads to formation of efficient excitation energy traps in monomeric and trimeric complexes," *FEBS Lett.*, 2007, **581**, 3528–3532.

[68] H. A. Frank, A. Cua, V. Chynwat, A. Young, D. Gosztola, and M. R. Wasielewski, "Photophysics of the carotenoids associated with the xanthophyll cycle in photosynthesis," *Photosynth. Res.*, 1994, **41**, 389–395.

[69] S. Amarie, L. Wilk, T. Barros, W. Kuhlbrandt, A. Dreuw, and J. Wachtveitl, "Properties of zeaxanthin and its radical cation bound to the minor light-harvesting complexes CP24, CP26 and CP29," *Biochim. Biophys. Acta, Bioenerg.*, 2009, **1787**, 747–752.

[70] Y.-Z. Ma, N. E. Holt, X.-P. Li, K. K. Niyogi, and G. R. Fleming, "Evidence for direct carotenoid involvement in the regulation of photosynthetic light harvesting," *Proc. Natl. Acad. Sci. U. S. A.*, 2003, **100**, 4377–4382.

[71] S. Bode, C. C. Quentmeier, P.-N. Liao, *et al.*, "On the regulation of photosynthesis by excitonic interactions between carotenoids and chlorophylls," *Proc. Natl. Acad. Sci. U. S. A.*, 2009, **106**, 12311–12316.

[72] H. Staleva, J. Komenda, M. K. Shukla, V. Šlouf, R. Kaňa, T. Polívka, and R. Sobotka, "Mechanism of photoprotection in the cyanobacterial ancestor of plant antenna proteins," *Nat. Chem. Biol.*, 2015, **11**, 287–291.

[73] X. Pan, M. Li, T. Wan, *et al.*, "Structural insights into energy regulation of light-harvesting complex CP29 from spinach," *Nat. Struct. Mol. Biol.*, 2011, **18**, 309–315.

[74] Y. Umena, K. Kawakami, J.-R. Shen, and N. Kamiya, "Crystal structure of oxygen-evolving photosystem II at a resolution of 1.9 Å," *Nature*, 2011, **473**, 55–60.

[75] V. I. Novoderezhkin, M. A. Palacios, H. van Amerongen, and R. van Grondelle, "Excitation dynamics in the LHCII complex of higher plants: Modeling based on the 2.72 Å crystal structure," *J. Phys. Chem. B*, 2005, **109**, 10493–10504.

[76] V. Novoderezhkin, A. Marin, and R. van Grondelle, "Intra- and intermonomeric transfers in the light harvesting LHCII complex: the Redfield–Förster picture," *Phys. Chem. Chem. Phys.*, 2011, **13**, 17093–17103.

[77] V. I. Novoderezhkin, M. A. Palacios, H. van Amerongen, and R. van Grondelle, "Energy-transfer dynamics in the LHCII complex of higher plants: Modified Redfield approach," *J. Phys. Chem. B*, 2004, **108**, 10363–10375.

[78] F. Müh, T. Renger, and A. Zouni, "Crystal structure of cyanobacterial photosystem II at 3.0 Å resolution: a closer look at the antenna system and the small membrane-intrinsic subunits," *Plant Physiol. Biochem.*, 2008, **46**, 238–264.

[79] K. Schulten, I. Ohmine, and M. Karplus, "Correlation effects in the spectra of polyenes," *J. Chem. Phys.*, 1976, **64**, 4422–4441.

[80] T. Kusumoto, D. Kosumi, C. Uragami, H. A. Frank, R. R. Birge, R. J. Cogdell, and H. Hashimoto, "Femtosecond transient absorption spectroscopic study of a carbonyl-containing carotenoid analogue, 2-(all-*trans*-retinylidene)-indan-1,3-dione," *J. Phys. Chem. A*, 2011, **115**, 2110–2119.

[81] B. P. Krueger, G. D. Scholes, and G. R. Fleming, "Calculation of couplings and energy-transfer pathways between the pigments of LH2 by the *ab initio* transition density cube method," *J. Phys. Chem. B*, 1998, **102**, 5378–5386.

[82] W. P. Bricker and C. S. Lo, "Excitation energy transfer in the peridinin-chlorophyll *a*-protein complex modeled using configuration interaction," *J. Phys. Chem. B*, 2014, **118**, 9141–9154.

[83] M. J. S. Dewar and W. Thiel, "Ground states of molecules. 38. the MNDO method. approximations and parameters," *J. Am. Chem. Soc.*, 1977, **99**, 4899–4907.

[84] J. J. P. Stewart, "MOPAC2006," 2008.

[85] R. S. Knox and B. Q. Spring, "Dipole strengths in the chlorophylls," *Photochem. Photobiol.*, 2003, **77**, 497–501.

[86] T. Förster, "Zwischenmolekulare energiewanderung und fluoreszenz," *Ann. Phys.*, 1948, **437**, 55–75.

[87] T. Förster, "10th spiers memorial lecture. transfer mechanisms of electronic excitation," *Discuss. Faraday Soc.*, 1959, **27**, 7–17.

[88] M. Şener, J. Strümpfer, J. Hsin, D. Chandler, S. Scheuring, C. N. Hunter, and K. Schulten, "Förster energy transfer theory as reflected in the structures

of photosynthetic light-harvesting systems," *ChemPhysChem*, 2011, **12**, 518–531.

[89] H. C. Yan, P. F. Zhang, C. Wang, Z. F. Liu, and W. R. Chang, "Two lutein molecules in LHCII have different conformations and functions: Insights into the molecular mechanism of thermal dissipation in plants," *Biochem. Biophys. Res. Commun.*, 2007, **355**, 457–463.

[90] E. J. Peterman, C. C. Gradinaru, F. Calkoen, J. C. Borst, R. van Grondelle, and H. van Amerongen, "Xanthophylls in light-harvesting complex II of higher plants: Light harvesting and triplet quenching," *Biochemistry*, 1997, **36**, 12208–12215.

[91] S. Caffarri, R. Croce, J. Breton, and R. Bassi, "The major antenna complex of photosystem II has a xanthophyll binding site not involved in light harvesting," *J. Biol. Chem.*, 2001, **276**, 35924–35933.

[92] A. Ishizaki, T. R. Calhoun, G. S. Schlau-Cohen, and G. R. Fleming, "Quantum coherence and its interplay with protein environments in photosynthetic electronic energy transfer," *Phys. Chem. Chem. Phys.*, 2010, **12**, 7319–7337.

[93] L. Valkunas, S. Kudzmauskas, and G. Juzeliunas, "Excitation transfer in highly concentrated pseudoisocyanine dye solution," *Sov. Phys. Coll.*, 1985, **25**, 41–47.

[94] G. D. Scholes, X. J. Jordanides, and G. R. Fleming, "Adapting the Förster theory of energy transfer for modeling dynamics in aggregated molecular assemblies," *J. Phys. Chem. B*, 2001, **105**, 1640–1651.

[95] T. Renger and R. Marcus, "On the relation of protein dynamics and exciton relaxation in pigment–protein complexes: An estimation of the spectral density and a theory for the calculation of optical spectra," *J. Chem. Phys.*, 2002, **116**, 9997–10019.

[96] D. I. G. Bennett, K. Amarnath, and G. R. Fleming, "A structure-based model of energy transfer reveals the principles of light harvesting in photosystem II supercomplexes," *J. Am. Chem. Soc.*, 2013, **135**, 9164–9173.

[97] M. Yang and G. R. Fleming, "Construction of kinetic domains in energy trapping processes and application to a photosynthetic light harvesting complex," *J. Chem. Phys.*, 2003, **119**, 5614–5622.

[98] G. Raszewski and T. Renger, "Light harvesting in photosystem II core complexes is limited by the transfer to the trap: Can the core complex turn into a photoprotective mode?," *J. Am. Chem. Soc.*, 2008, **130**, 4431–4446.

[99] K. Broess, G. Trinkunas, C. D. van der Weij-de Wit, J. P. Dekker, A. van Hoek, and H. van Amerongen, "Excitation energy transfer and charge separation in photosystem II membranes revisited," *Biophys. J.*, 2006, **91**, 3776–3786.

[100] K. Broess, G. Trinkunas, A. van Hoek, R. Croce, and H. van Amerongen, "Determination of the excitation migration time in photosystem II – consequences for the membrane organization and charge separation parameters," *Biochim. Biophys. Acta, Bioenerg.*, 2008, **1777**, 404–409.

[101] L. Valkunas, G. Trinkunas, J. Chmeliov, and A. V. Ruban, "Modeling of exciton quenching in photosystem II," *Phys. Chem. Chem. Phys.*, 2009, **11**, 7576–7584.

[102] L. Valkunas, J. Chmeliov, G. Trinkunas, C. D. P. Duffy, R. van Grondelle, and A. V. Ruban, "Excitation migration, quenching, and regulation of photosynthetic light harvesting in photosystem II," *J. Phys. Chem. B*, 2011, **115**, 9252–9260.

[103] S. Caffarri, K. Broess, R. Croce, and H. van Amerongen, "Excitation energy transfer and trapping in higher plant photosystem II complexes with different antenna sizes," *Biophys. J.*, 2011, **100**, 2094–2103.

[104] M. Wahadoszamen, R. Berera, A. M. Ara, E. Romero, and R. van Grondelle, "Identification of two emitting sites in the dissipative state of the major light harvesting antenna," *Phys. Chem. Chem. Phys.*, 2012, **14**, 759–766.

[105] P.-N. Liao, C.-P. Holleboom, L. Wilk, W. Kühlbrandt, and P. J. Walla, "Correlation of Car $S_1 \rightarrow$ Chl with Chl $\rightarrow$ Car S_1 energy transfer supports the excitonic model in quenched light harvesting complex II," *J. Phys. Chem. B*, 2010, **114**, 15650–15655.

[106] G. S. Schlau-Cohen, H.-Y. Yang, T. P. J. Krüger, *et al.*, "Single-molecule identification of quenched and unquenched states of LHCII," *J. Phys. Chem. Lett.*, 2015, **6**, 860–867.

[107] T. P. J. Krüger, V. I. Novoderezkhin, C. Ilioaia, and R. van Grondelle, "Fluorescence spectral dynamics of single LHCII trimers," *Biophys. J.*, 2010, **98**, 3093–3101.

[108] T. P. J. Krüger, C. Ilioaia, and R. van Grondelle, "Fluorescence intermittency from the main plant light-harvesting complex: Resolving shifts between intensity levels," *J. Phys. Chem. B*, 2011, **115**, 5071–5082.

[109] T. P. J. Krüger, C. Ilioaia, L. Valkunas, and R. van Grondelle, "Fluorescence intermittency from the main plant light-harvesting complex: Sensitivity to the local environment," *J. Phys. Chem. B*, 2011, **115**, 5083–5095.

[110] L. Valkunas, J. Chmeliov, T. P. J. Krüger, C. Ilioaia, and R. van Grondelle, "How photosynthetic proteins switch," *J. Phys. Chem. Lett.*, 2012, **3**, 2779–2784.

[111] J. Chmeliov, L. Valkunas, T. P. J. Krüger, C. Ilioaia, and R. van Grondelle, "Fluorescence blinking of single major light-harvesting complexes," *New J. Phys.*, 2013, **15**, 085007.

[112] J. M. Gruber, J. Chmeliov, T. P. J. Krüger, L. Valkunas, and R. van Grondelle, "Singlet-triplet annihilation in single LHCII complexes," *Phys. Chem. Chem. Phys.*, 2015, **17**, 19844–19853.

[113] W. E. Moerner and L. Kador, "Optical detection and spectroscopy of single molecules in a solid," *Phys. Rev. Lett.*, 1989, **62**, 2535–2538.

[114] W. P. Ambrose, P. M. Goodwin, J. C. Martin, and R. A. Keller, "Single-molecule detection and photochemistry on a surface using near-field optical-excitation," *Phys. Rev. Lett.*, 1994, **72**, 160–163.

[115] X. S. Xie and R. C. Dunn, "Probing single-molecule dynamics," *Science*, 1994, **265**, 361–364.

[116] M. Nirmal, B. O. Dabbousi, M. G. Bawendi, J. J. Macklin, J. K. Trautman, T. D. Harris, and L. E. Brus, "Fluorescence intermittency in single cadmium selenide nanocrystals," *Nature*, 1996, **383**, 802–804.

[117] R. M. Dickson, A. B. Cubitt, R. Y. Tsien, and W. E. Moerner, "On/off blinking and switching behaviour of single molecules of green fluorescent protein," *Nature*, 1997, **388**, 355–358.

[118] M. A. Bopp, Y. W. Jia, L. Q. Li, R. J. Cogdell, and R. M. Hochstrasser, "Fluorescence and photobleaching dynamics of single light-harvesting complexes," *Proc. Natl. Acad. Sci. U. S. A.*, 1997, **94**, 10630–10635.

[119] J. Hofkens, W. Schroeyers, D. Loos, *et al.*, "Triplet states as non-radiative traps in multichromophoric entities: Single molecule spectroscopy of an artificial and natural antenna system," *Spectrochim. Acta A*, 2001, **57**, 2093–2107.

[120] D. Rutkauskas, V. Novoderezkhin, R. J. Cogdell, and R. van Grondelle, "Fluorescence spectral fluctuations of single LH2 complexes from *Rhodopseudomonas acidophila* strain 10050," *Biochemistry*, 2004, **43**, 4431–4438.

[121] L. Valkunas, J. Janusonis, D. Rutkauskas, and R. van Grondelle, "Protein dynamics revealed in the excitonic spectra of single LH2 complexes," *J. Lumin.*, 2007, **127**, 269–275.

[122] T. P. J. Krüger, C. Ilioaia, M. P. Johnson, A. V. Ruban, E. Papagiannakis, P. Horton, and R. van Grondelle, "Controlled disorder in plant light-harvesting complex II explains its photoprotective role," *Biophys. J.*, 2012, **102**, 2669–2676.

[123] S. Weiss, "Fluorescence spectroscopy of single biomolecules," *Science*, 1999, **283**, 1676–1683.

[124] C. Joo, H. Balci, Y. Ishitsuka, C. Buranachai, and T. Ha, "Advances in single-molecule fluorescence methods for molecular biology," *Annu. Rev. Biochem.*, 2008, **77**, 51–76.

[125] M. Kuno, D. P. Fromm, S. T. Johnson, A. Gallagher, and D. J. Nesbitt, "Modeling distributed kinetics in isolated semiconductor quantum dots," *Phys. Rev. B*, 2003, **67**, 125304.

[126] F. Cichos, C. von Borczyskowski, and M. Orrit, "Power-law intermittency of single emitters," *Curr. Opin. Colloid Interface Sci.*, 2007, **12**, 272–284.

[127] T. Basche, S. Kummer, and C. Brauchle, "Direct spectroscopic observation of quantum jumps of a single-molecule," *Nature*, 1995, **373**, 132–134.

[128] F. D. Stefani, J. P. Hoogenboom, and E. Barkai, "Beyond quantum jumps: Blinking nanoscale light emitters," *Physics Today*, 2009, **62**, 34–39.

[129] I. H. Chung and M. G. Bawendi, "Relationship between single quantum-dot intermittency and fluorescence intensity decays from collections of dots," *Phys. Rev. B*, 2004, **70**, 165304.

[130] M. Kuno, D. P. Fromm, H. F. Hamann, A. Gallagher, and D. J. Nesbitt, "Non-exponential "blinking" kinetics of single CdSe quantum dots: A universal power law behavior," *J. Chem. Phys.*, 2000, **112**, 3117–3120.

[131] R. Verberk, A. M. van Oijen, and M. Orrit, "Simple model for the power-law blinking of single semiconductor nanocrystals," *Phys. Rev. B*, 2002, **66**, 233202.

[132] J. Tang and R. A. Marcus, "Diffusion-controlled electron transfer processes and power-law statistics of fluorescence intermittency of nanoparticles," *Phys. Rev. Lett.*, 2005, **95**, 107401.

[133] J. Tang and R. A. Marcus, "Mechanisms of fluorescence blinking in semiconductor nanocrystal quantum dots," *J. Chem. Phys.*, 2005, **123**, 054704.

[134] L. Christophorov, A. Holzwarth, V. Kharkyanen, and F. van Mourik, "Structure–function self-organization in nonequilibrium macromolecular systems," *Chem. Phys.*, 2000, **256**, 45–60.

[135] L. N. Christophorov and V. N. Kharkyanen, "Synergetic mechanisms of structural regulation of the electron transfer and other reactions of biological macromolecules," *Chem. Phys.*, 2005, **319**, 330–341.

[136] B. Fain, *Irreversibilities in Quantum Mechanics*. Fundamental theories of physics, Dordrecht, London: Kluwer Academic, 2000.

[137] N. Agmon and S. Rabinovich, "Diffusive dynamics on potential-energy surfaces – nonequilibrium co binding to heme-proteins," *J. Chem. Phys.*, 1992, **97**, 7270–7286.

[138] H. Ihee, S. Rajagopal, V. Srajer, *et al.*, "Visualizing reaction pathways in photoactive yellow protein from nanoseconds to seconds," *Proc. Natl. Acad. Sci. U. S. A.*, 2005, **102**, 7145–7150.

[139] I. Moya, M. Silvestri, O. Vallon, G. Cinque, and R. Bassi, "Time-resolved fluorescence analysis of the photosystem II antenna proteins in detergent micelles and liposomes," *Biochemistry*, 2001, **40**, 12552–12561.

[140] B. van Oort, A. van Hoek, A. V. Ruban, and H. van Amerongen, "Equilibrium between quenched and nonquenched conformations of the major plant light-harvesting complex studied with high-pressure time-resolved fluorescence," *J. Phys. Chem. B*, 2007, **111**, 7631–7637.

[141] C. Ilioaia, M. P. Johnson, P. Horton, and A. V. Ruban, "Induction of efficient energy dissipation in the isolated light-harvesting complex of photosystem II in the absence of protein aggregation," *J. Biol. Chem.*, 2008, **283**, 29505–29512.

[142] D. Rutkauskas, J. Chmeliov, M. Johnson, A. Ruban, and L. Valkunas, "Exciton annihilation as a probe of the light-harvesting antenna transition into the photoprotective mode," *Chem. Phys.*, 2012, **404**, 123–128.

[143] J.-P. Bouchaud and A. Georges, "Anomalous diffusion in disordered media: Statistical mechanisms, models and physical applications," *Phys. Rep.*, 1990, **195**, 127–293.

[144] J. P. Connelly, M. G. Muller, M. Hucke, *et al.*, "Ultrafast spectroscopy of

trimeric light-harvesting complex II from higher plants," *J. Phys. Chem. B*, 1997, **101**, 1902–1909.

[145] R. Metzler and J. Klafter, "The restaurant at the end of the random walk: Recent developments in the description of anomalous transport by fractional dynamics," *J. Phys. A: Math. Gen.*, 2004, **37**, R161–R208.

[146] M. Weiss, H. Hashimoto, and T. Nilsson, "Anomalous protein diffusion in living cells as seen by fluorescence correlation spectroscopy," *Biophys. J.*, 2003, **84**, 4043–4052.

[147] H. M. Visser, F. J. Kleima, I. H. M. van Stokkum, R. van Grondelle, and H. van Amerongen, "Probing the many energy-transfer processes in the photosynthetic light-harvesting complex II at 77 K using energy-selective sub-picosecond transient absorption spectroscopy," *Chem. Phys.*, 1996, **210**, 297–312.

[148] V. Barzda, V. Gulbinas, R. Kananavicius, V. Cervinskas, H. van Amerongen, R. van Grondelle, and L. Valkunas, "Singlet-singlet annihilation kinetics in aggregates and trimers of LHCII," *Biophys. J.*, 2001, **80**, 2409–2421.

[149] L. Valkunas, I. H. M. van Stokkum, R. Berera, and R. van Grondelle, "Exciton migration and fluorescence quenching in LHCII aggregates: Target analysis using a simple nonlinear annihilation scheme," *Chem. Phys.*, 2009, **357**, 17–20.

[150] Y. Zaushitsyn, K. G. Jespersen, L. Valkunas, V. Sundström, and A. Yartsev, "Ultrafast dynamics of singlet-singlet and singlet-triplet exciton annihilation in poly(3-2′-methoxy-5′octylphenyl)thiophene films," *Phys. Rev. B*, 2007, **75**, 195201.

[151] R. Schödel, K. D. Irrgang, J. Voigt, and G. Renger, "Quenching of chlorophyll fluorescence by triplets in solubilized light-harvesting complex II (LHCII)," *Biophys. J.*, 1999, **76**, 2238–2248.

[152] R. Croce, R. Remelli, C. Varotto, J. Breton, and R. Bassi, "The neoxanthin binding site of the major light harvesting complex (LHCII) from higher plants," *FEBS Lett.*, 1999, **456**, 1–6.

[153] L. Valkunas, V. Liuolia, and A. Freiberg, "Picosecond processes in chromatophores at various excitation intensities," *Photosynth. Res.*, 1991, **27**, 83–95.

[154] G. Paillotin, C. E. Swenberg, J. Breton, and N. E. Geacintov, "Analysis of picosecond laser induced fluorescence phenomena in photosynthetic membranes utilizing a master equation approach," *Biophys. J.*, 1979, **25**, 513–533.

[155] R. van Grondelle, "Excitation energy transfer, trapping and annihilation in photosynthetic systems," *Biochim. Biophys. Acta, Rev. Bioenerg.*, 1985, **811**, 147–195.

[156] L. Valkunas, G. Trinkunas, V. Liuolia, and R. van Grondelle, "Nonlinear annihilation of excitations in photosynthetic systems," *Biophys. J.*, 1995, **69**, 1117–1129.

[157] T. Kolubayev, N. E. Geacintov, G. Paillotin, and J. Breton, "Domain sizes in chloroplasts and chlorophyll–protein complexes probed by fluorescence

yield quenching induced by singlet–triplet exciton annihilation," *Biochim. Biophys. Acta, Bioenerg.*, 1985, **808**, 66–76.

[158] M. Pope and C. E. Swenberg, *Electronic Processes in Organic Crystals and Polymers*. Monographs on the Physics and Chemistry of Materials, New York: Oxford University Press, 2nd ed., 1999.

[159] J. G. C. Bakker, R. van Grondelle, and W. T. F. den Hollander, "Trapping, loss and annihilation of excitations in a photosynthetic system: II. experiments with the purple bacteria *Rhodospirillum rubrum* and *Rhodopseudomonas capsulata*," *Biochim. Biophys. Acta, Bioenerg.*, 1983, **725**, 508–518.

[160] L. Valkunas, V. Cervinskas, and F. van Mourik, "Energy transfer and connectivity in chloroplasts: Competition between trapping and annihilation in pulsed fluorescence induction experiments," *J. Phys. Chem. B*, 1997, **101**, 7327–7331.

[161] M. W. Graham, J. Chmeliov, Y.-Z. Ma, *et al.*, "Exciton dynamics in semiconducting carbon nanotubes," *J. Phys. Chem. B*, 2011, **115**, 5201–5211.

[162] C. Hofmann, T. J. Aartsma, H. Michel, and J. Kohler, "Direct observation of tiers in the energy landscape of a chromoprotein: A single-molecule study," *Proc. Natl. Acad. Sci. U. S. A.*, 2003, **100**, 15534–15538.

[163] R. van Grondelle, J. P. Dekker, T. Gillbro, and V. Sundstrom, "Energy transfer and trapping in photosynthesis," *Biochim. Biophys. Acta, Bioenerg.*, 1994, **1187**, 1–65.

[164] E. C. M. Engelmann, G. Zucchelli, F. M. Garlaschi, A. P. Casazza, and R. C. Jennings, "The effect of outer antenna complexes on the photochemical trapping rate in barley thylakoid photosystem II," *Biochim. Biophys. Acta*, 2005, **1706**, 276–286.

[165] W. Leibl, J. Breton, J. Deprez, and H. W. Trissl, "Photoelectric study on the kinetics of trapping and charge stabilization in oriented PS II membranes," *Photosynth. Res.*, 1989, **22**, 257–275.

[166] E. Belgio, M. P. Johnson, S. Jurić, and A. V. Ruban, "Higher plant photosystem II light-harvesting antenna, not the reaction center, determines the excited-state lifetime—both the maximum and the nonphotochemically quenched," *Biophys. J.*, 2012, **102**, 2761–2771.

[167] M. P. Johnson, T. K. Goral, C. D. P. Duffy, A. P. R. Brain, C. W. Mullineaux, and A. V. Ruban, "Photoprotective energy dissipation involves the reorganization of photosystem II light-harvesting complexes in the grana membranes of spinach chloroplasts," *Plant Cell*, 2011, **23**, 1468–1479.

[168] A. V. Ruban, J. P. Dekker, P. Horton, and R. van Grondelle, "Temperature dependence of chlorophyll fluorescence from the light harvesting complex II of higher plants," *Photochem. Photobiol.*, 1995, **61**, 216–221.

[169] A. Ruban, F. Calkoen, S. Kwa, R. van Grondelle, P. Horton, and J. Dekker, "Characterisation of LHC II in the aggregated state by linear and circular dichroism spectroscopy," *Biochim. Biophys. Acta, Bioenerg.*, 1997, **1321**, 61–70.

[170] P. Horton, M. Wentworth, and A. Ruban, "Control of the light harvesting

function of chloroplast membranes: The LHCII-aggregation model for non-photochemical quenching," *FEBS Lett.*, 2005, **579**, 4201–4206.

[171] Y. Miloslavina, A. Wehner, P. H. Lambrev, *et al.*, "Far-red fluorescence: A direct spectroscopic marker for LHCII oligomer formation in non-photochemical quenching," *FEBS Lett.*, 2008, **582**, 3625–3631.

[172] P. H. Lambrev, F.-J. Schmitt, S. Kussin, *et al.*, "Functional domain size in aggregates of light-harvesting complex II and thylakoid membranes," *Biochim. Biophys. Acta, Bioenerg.*, 2011, **1807**, 1022–1031.

[173] N. M. Magdaong, M. M. Enriquez, A. M. LaFountain, L. Rafka, and H. A. Frank, "Effect of protein aggregation on the spectroscopic properties and excited state kinetics of the LHCII pigment–protein complex from green plants," *Photosynth. Res.*, 2013, **118**, 259–276.

[174] J. Chmeliov, A. Gelzinis, E. Songaila, R. Augulis, C. D. P. Duffy, A. V. Ruban, and L. Valkunas, "The nature of self-regulation in photosynthetic light-harvesting antenna," 2015. Under review in *Nature*.

[175] A. V. Ruban and P. Horton, "Mechanism of ΔpH-dependent dissipation of absorbed excitation energy by photosynthetic membranes. I. Spectroscopic analysis of isolated light-harvesting complexes," *Biochim. Biophys. Acta, Bioenerg.*, 1992, **1102**, 30–38.

[176] P. Xu, L. Tian, M. Kloz, and R. Croce, "Molecular insights into zeaxanthin-dependent quenching in higher plants," *Sci. Rep.*, 2015, **5**, 13679.

[177] A. V. Ruban, D. Phillip, A. J. Young, and P. Horton, "Carotenoid-dependent oligomerization of the major chlorophyll a/b light harvesting complex of photosystem II of plants," *Biochemistry*, 1997, **36**, 7855–7859.

[178] A. V. Ruban, A. Young, and P. Horton, "Modulation of chlorophyll fluorescence quenching in isolated light harvesting complex of photosystem II," *Biochim. Biophys. Acta, Bioenerg.*, 1994, **1186**, 123–127.

[179] A. M. Gilmore and M. C. Ball, "Protection and storage of chlorophyll in overwintering evergreens," *Proc. Natl. Acad. Sci. U. S. A.*, 2000, **97**, 11098–11101.

[180] A. M. Gilmore, S. Matsubara, M. C. Ball, D. H. Barker, and S. Itoh, "Excitation energy flow at 77 K in the photosynthetic apparatus of overwintering evergreens," *Plant Cell Environ.*, 2003, **26**, 1021–1034.

[181] G. Oquist and N. P. A. Huner, "Photosynthesis of overwintering evergreen plants," *Annu. Rev. Plant Biol.*, 2003, **54**, 329–355.

[182] W. H. Lawton and E. A. Sylvestre, "Self modeling curve resolution," *Technometrics*, 1971, **13**, 617–633.

[183] M. W. Berry, M. Browne, A. N. Langville, V. P. Pauca, and R. J. Plemmons, "Algorithms and applications for approximate nonnegative matrix factorization," *Comput. Stat. Data Anal.*, 2007, **52**, 155–173.

[184] G. H. Schatz, H. Brock, and A. R. Holzwarth, "Picosecond kinetics of fluorescence and absorbance changes in photosystem II particles excited at low photon density," *Proc. Natl. Acad. Sci. U. S. A.*, 1987, **84**, 8414–8418.

[185] J. P. Dekker and E. J. Boekema, “Supramolecular organization of thylakoid membrane proteins in green plants,” *Biochim. Biophys. Acta, Bioenerg.*, 2005, **1706**, 12–39.

[186] T. Mančal, L. Valkunas, and G. R. Fleming, “Theory of exciton-charge transfer state coupled systems,” *Chem. Phys. Lett.*, 2006, **432**, 301–305.

[187] J. Chmeliov, G. Trinkunas, H. van Amerongen, and L. Valkunas, “Light harvesting in a fluctuating antenna,” *J. Am. Chem. Soc.*, 2014, **136**, 8963–8972.

[188] J. Chmeliov, G. Trinkunas, H. van Amerongen, and L. Valkunas, “Excitation migration in fluctuating light-harvesting antenna systems,” *Photosynth. Res.*, 2015. Doi:10.1007/s11120-015-0083-3.

[189] S. Caffarri, R. Kouril, S. Kereïche, E. J. Boekema, and R. Croce, “Functional architecture of higher plant photosystem II supercomplexes,” *EMBO J.*, 2009, **28**, 3052–3063.

[190] A. Gelzinis, L. Valkunas, F. D. Fuller, J. P. Ogilvie, S. Mukamel, and D. Abramavicius, “Tight-binding model of the photosystem II reaction center: Application to two-dimensional electronic spectroscopy,” *New J. Phys.*, 2013, **15**, 075013.

[191] J. F. Allen, “Protein phosphorylation in regulation of photosynthesis,” *Biochim. Biophys. Acta, Bioenerg.*, 1992, **1098**, 275–335.

[192] G. H. Schatz, H. Brock, and A. R. Holzwarth, “Kinetic and energetic model for the primary processes in photosystem II,” *Biophys. J.*, 1988, **54**, 397–405.

[193] N. P. Pawlowicz, M.-L. Groot, I. H. M. van Stokkum, J. Breton, and R. van Grondelle, “Charge separation and energy transfer in the photosystem II core complex studied by femtosecond midinfrared spectroscopy,” *Biophys. J.*, 2007, **93**, 2732–2742.

[194] S. Vasil’ev, P. Orth, A. Zouni, T. G. Owens, and D. Bruce, “Excited-state dynamics in photosystem II: Insights from the X-ray crystal structure,” *Proc. Natl. Acad. Sci. U. S. A.*, 2001, **98**, 8602–8607.

[195] E. J. Boekema, H. van Roon, F. Calkoen, R. Bassi, and J. P. Dekker, “Multiple types of association of photosystem II and its light-harvesting antenna in partially solubilized photosystem II membranes,” *Biochemistry*, 1999, **38**, 2233–2239.

[196] O. J. G. Somsen, L. Valkunas, and R. van Grondelle, “A perturbed two-level model for exciton trapping in small photosynthetic systems,” *Biophys. J.*, 1996, **70**, 669–683.

[197] B. van Oort, M. Alberts, S. de Bianchi, *et al.*, “Effect of antenna-depletion in photosystem II on excitation energy transfer in *Arabidopsis thaliana*,” *Biophys. J.*, 2010, **98**, 922–931.

[198] J. Veerman, M. D. McConnell, S. Vasil’ev, F. Mamedov, S. Styring, and D. Bruce, “Functional heterogeneity of photosystem II in domain specific regions of the thylakoid membrane of spinach (*Spinacia Oleracea L.*),” *Biochemistry*, 2007, **46**, 3443–3453.

[199] C. D. van der Weij-de Wit, J. P. Dekker, R. van Grondelle, and I. H. M. van Stokkum, “Charge separation is virtually irreversible in photosystem II core

complexes with oxidized primary quinone acceptor," *J. Phys. Chem. A*, 2011, **115**, 3947–3956.

[200] M. N. Berberan-Santos and B. Valeur, "Luminescence decays with underlying distributions: General properties and analysis with mathematical functions," *J. Lumin.*, 2007, **126**, 263–272.

[201] G. Trinkunas and A. R. Holzwarth, "A model for dynamic protein control of energy transfer to photosynthetic reaction centers," *J. Phys. Chem. B*, 1997, **101**, 7271–7274.

[202] J. Wu, F. Liu, J. Ma, R. J. Silbey, and J. Cao, "Efficient energy transfer in light-harvesting systems: Quantum-classical comparison, flux network, and robustness analysis," *J. Chem. Phys.*, 2012, **137**, 174111.

[203] R. Hildner, D. Brinks, J. B. Nieder, R. J. Cogdell, and N. F. van Hulst, "Quantum coherent energy transfer over varying pathways in single light-harvesting complexes," *Science*, 2013, **340**, 1448–1451.

[204] J.-H. Kim and J. Cao, "Optimal efficiency of self-assembling light-harvesting arrays," *J. Phys. Chem. B*, 2010, **114**, 16189–16197.

[205] A. Bunde and S. Havlin, *Fractals and Disordered Systems*. Berlin: Springer-Verlag, 1991.

[206] B. Y. Balagurov and V. Vaks, "Random walks of a particle on lattices with traps," *Zh. Eksper. Teoret. Fiz.*, 1973, **65**, 1939–1946.

[207] N. Agmon, "Diffusion with random traps: Transient one-dimensional kinetics in a linear potential," *J. Stat. Phys.*, 1986, **43**, 537–559.

[208] F. H. Stillinger, "Axiomatic basis for spaces with noninteger dimension," *J. Math. Phys.*, 1977, **18**, 1224–1234.

[209] J. Mathews and R. L. Walker, *Mathematical Methods of Physics*. New York: W. A. Benjamin, 2nd ed., 1970.

[210] F. Franck, P. Juneau, and R. Popovic, "Resolution of the photosystem I and photosystem II contributions to chlorophyll fluorescence of intact leaves at room temperature," *Biochim. Biophys. Acta, Bioenerg.*, 2002, **1556**, 239–246.

[211] B. van Oort, A. Amunts, J. W. Borst, A. van Hoek, N. Nelson, H. van Amerongen, and R. Croce, "Picosecond fluorescence of intact and dissolved PSI–LHCI crystals," *Biophys. J.*, 2008, **95**, 5851–5861.

[212] E. Wientjes, I. H. M. van Stokkum, H. van Amerongen, and R. Croce, "The role of the individual Lhcas in photosystem I excitation energy trapping," *Biophys. J.*, 2011, **101**, 745–754.

[213] E. Belgio, E. Kapitonova, J. Chmeliov, C. D. P. Duffy, P. Ungerer, L. Valkunas, and A. V. Ruban, "Economic photoprotection in photosystem II that retains a complete light-harvesting system with slow energy traps," *Nat. Commun.*, 2014, **5**, 4433.

[214] N. Betterle, M. Ballottari, S. Zorzan, *et al.*, "Light-induced dissociation of an antenna hetero-oligomer is needed for non-photochemical quenching induction," *J. Biol. Chem.*, 2009, **284**, 15255–15266.

[215] T. K. Goral, M. P. Johnson, C. D. P. Duffy, A. P. R. Brain, A. V. Ruban, and C. W. Mullineaux, "Light-harvesting antenna composition controls the macrostructure and dynamics of thylakoid membranes in arabidopsis," *Plant J.*, 2012, **69**, 289–301.

[216] A. R. Holzwarth, Y. Miloslavina, M. Nilkens, and P. Jahns, "Identification of two quenching sites active in the regulation of photosynthetic light-harvesting studied by time-resolved fluorescence," *Chem. Phys. Lett.*, 2009, **483**, 262–267.

[217] M. P. Johnson and A. V. Ruban, "Photoprotective energy dissipation in higher plants involves alteration of the excited state energy of the emitting chlorophyll(s) in the light harvesting antenna II (LHCII)," *J. Biol. Chem.*, 2009, **284**, 23592–601.

[218] M. Kaplanová and K. Čermák, "Effect of reabsorption on the concentration dependence of fluorescence lifetimes of chlorophyll *a*," *J. Photochem.*, 1981, **15**, 313–319.

[219] E. Schäfer, L. Fukshansky, and J. Shropshire, W., *Action Spectroscopy of Photoreversible Pigment Systems*, vol. 16 of *Encyclopedia of Plant Physiology*, 39–68. Springer Berlin Heidelberg, 1983.

[220] D. Lazár, "Chlorophyll *a* fluorescence induction," *Biochim. Biophys. Acta, Bioenerg.*, 1999, **1412**, 1–28.

[221] A. V. Ruban, M. Wentworth, A. E. Yakushevska, *et al.*, "Plants lacking the main light-harvesting complex retain photosystem II macro-organization," *Nature*, 2003, **421**, 648–652.

[222] M. Havaux, L. Dall'osto, and R. Bassi, "Zeaxanthin has enhanced antioxidant capacity with respect to all other xanthophylls in arabidopsis leaves and functions independent of binding to PSII antennae," *Plant Physiol.*, 2007, **145**, 1506–1520.

[223] J. Lavorel and P. Joliot, "A connected model of the photosynthetic unit," *Biophys. J.*, 1972, **12**, 815–831.

[224] G. Paillotin, "Movement of excitations in the photosynthetic domains of photosystem II," *J. Theor. Biol.*, 1976, **58**, 237–252.

[225] L. Valkunas, N. E. Geacintov, L. France, and J. Breton, "The dependence of the shapes of fluorescence induction curves in chloroplasts on the duration of illumination pulses," *Biophys. J.*, 1991, **59**, 397–408.

[226] D. Lazár, P. Tomek, P. Ilík, and J. Naus, "Determination of the antenna heterogeneity of photosystem II by direct simultaneous fitting of several fluorescence rise curves measured with DCMU at different light intensities," *Photosynth. Res.*, 2001, **68**, 247–257.

[227] S. Caffarri, K. Broess, R. Croce, and H. van Amerongen, "Excitation energy transfer and trapping in higher plant photosystem II complexes with different antenna sizes," *Biophys. J.*, 2011, **100**, 2094–2103.